IECO

Volume 6 No 4 Year 2023

■ Volume 6

■ No 4

■ Year 2023

University of Sistan and Baluchestan

Iranian Association of Electrical and Electronics Engineers

International Journal Of

Industrial Electronics Control and Optimization

In This Issue:

Research Articles:

IECO

International Journal Of
Industrial Electronics Control and Optimization

About Journal

The University of Sistan and Baluchestan entered into strategic partnership with Iranian Association of Electrical and Electronic Engineers (IAEEE) to publish the **International Journal of Industrial Electronics Control and Optimization (IECO)**. The IECO is a refereed international journal which presents to the international scientific community important results of work in these fields, whether in the form of modeling simulation, analysis, fundamental research, development, application, design or real-time implementation. The scope of IECO is broad, encompassing all aspects of Industrial Electronics, Control and Optimization.

Note: International Journal of Industrial Electronics, Control and Optimization (IECO) has qualified to **ACADEMIC RESEARCH JOURNAL (ELMI-PAJOHESHI)** status certified by the ministry of Science, Research and Technology of Iran (No. 231566/3/18 dated 1396/10/09), and is published by the University of Sistan and Baluchestan through a formal partnership (No. 952/2/1500 dated 1395/11/04) with Iranian Association of Electrical and electronic Engineers (IAEEE) in order to develop scientific and research cooperation.

Aims and Scope

International Journal of Industrial Electronics, Control and Optimization (IECO) is a Peer reviewed journal of advanced and state-of-the-art in the science and engineering of Industrial Electronics, Control and Optimization. Its Scope encompasses the applications of Industrial Electronics, power systems, control, optimization and computational intelligence for the enhancement of industrial and manufacturing system and processes. The scope of the journal include the following:

I. Industrial Electronics

- Low and high-power converters
- Renewable energy
- Drive control techniques
- Techniques for advanced power semiconductor devices
- Power quality and utility applications
- Communications
- Flexible AC Transmission Systems (FACTS)
- Control in power electronics
- Electromagnetic and thermal performance of electronic power converters
- Motion control, robotics, sensors and actuators
- Fault detection and diagnosis
- Power systems
- Factory automation, communication, and computer networks

II. Control

- Adaptive control
- Control of process systems
- Control theory
- Data processing
- Design of control systems
- Hybrid systems
- Identification and observation
- Intelligent systems
- Model-predictive control
- Optimal control

- Robust control
- Fractional order systems

III. Optimization

- Ant Colony
- Chaos Theory
- Evolutionary Computing
- Fuzzy Computing
- Hybrid Methods
- Immunological Computing
- Neuro Computing
- Particle Swarm
- Probabilistic Computing
- Rough Sets
- Wavelet

International Journal Of
Industrial Electronics Control and Optimization
Print ISSN: 3517-2645
Online ISSN: 3568-2645
Homepage: https://ieco.usb.ac.ir/

Simultaneous Optimal Design of PID and MATMD Considering their Proposed Elevation Placement for Seismic Control of Tall Buildings on Soft Soil

Mohammad shahi[1] | Mohammad Reza Sohrabi[1] | Sadegh Etedali[2] | Abbas-Ali Zamni[3]

Department of Civil Engineering, University of Sistan and Baluchestan, Zahedan, Iran.[1]
Department of Civil Engineering, Birjand University of Technology, P.O. Box 97175-569, Birjand, Iran.[2]
Department of Electrical Engineering, Technical and Vocational University (TVU), Tehran, Iran.[3]
Corresponding author's email: etedali@birjandut.ac.ir

Article Info

Article type:
Research Article

Article history:
Received: 21-July-2023
Received in revised form: 26-October-2023
Accepted: 28-October-2023
Published online: 30-October-2023

Keywords:
MATMD,
PID controller,
SATMD,
SSI effects,
Tall buildings,

ABSTRACT

This research proposes an innovative process to locate devices in elevation using structural results in uncontrolled and controlled (passive and active) states, considering Soil-Structure Interaction (SSI) effects, especially for soft soil. Also, a Proportional Integral Derivative (PID) controller with active single and multiple control devices is used for tall buildings under earthquakes. In addition, the simultaneous and non-simultaneous tuning of the design parameters are examined. The results of applying PID with a Multiple Active Tuned Mass Damper (MATMD) compared with the Single-Active Tuned Mass Damper (SATMD) show that the proposed process of locating the control devices reduces responses significantly. It also reduces the computational efforts of the optimization noticeably. The results of the non-simultaneous tuning of design parameters in all states also indicate an increase in the instability potential of the structure compared with simultaneous tuning. On the other hand, the reduction of the Root Mean Square (RMS) of the responses compared with the uncontrolled state confirms the effective performance of the system during earthquakes. Therefore, this research helps researchers gain a new design vision of how to locate control devices in tall buildings without optimization calculations and how to set parameters in the presence of SSI effects.

I. Introduction

Control strategies for tall buildings have received more attention in recent years. The growth of high-rise construction, efforts to reduce costs and alleviate implications for people's lives, are among the most important reasons for this attention. The tuned mass damper (TMD) is one of the conventional devices for controlling tall buildings by reducing the dynamic responses of the structure [1-5]. The single passive tuned mass damper (SPTMD) has many benefits but also some drawbacks. For instance, its performance is restricted to a specific frequency band. A common solution to overcome this problem is using a single active tuned mass damper (SATMD) [5]. Furthermore, to determine the best control force to be applied to the system without increasing the risk of instability, it is necessary to use a reliable control device and a reliable control algorithm. So far, researchers have focused on various types of controllers in their previous studies. Some classical controllers used in the control of

structures, especially for tall structures, include LQG [6,7], LQR [5,8,9], H2 and H_∞ [10-12]. The controller PID [4,16,17] and its variants like fractional order PID [18-20] are a classic controller that is almost the most widely used controller in the industry. The accuracy, stability, ease of implementation, versatility, and real-time control capabilities are the PID advantages in structural control. In addition, fuzzy logic controller (FLC) [13,14,44,48] and its compounds like neuro-fuzzy logic (NFLC) [15] have been widely used in structures against excitations by significantly reducing their dynamic responses and their potential instability [21,22]. In addition, determining the best location of MPTMD in the plan and elevation and finding the best ways to adjust its parameters have been examined [23,24]. Similar to SPTMD, the performance of MPTMD is restricted to a small range of applied frequencies. Therefore, the development of the multiple active tuned mass damper device (MATMD) has been suggested as a solution to this restriction. Structures equipped with MATMD show lower response than those equipped with SATMD, providing the best method for locating the device and the best mass value of each TMD have also been considered [21]. The reduction of the responses may result in a compromise among the displacement, acceleration, or even the relative drift ratio of the floors. An analysis of prior studies reveals that the conventional method for the best placement of multi-devices is generally the placement based on the mode shapes. [21,24,25]. Optimization methods are also used to find the optimal location in elevation [45]. At the same time, this method has a high computational cost for high-rise structures. Also, the optimal placement of TMDs in the plan has been investigated using optimization methods [47], which shows that the frequency content of the earthquake affects the optimal position of the installation of the control device. The results of using two ATMD on an 11-story structure also show that the distributed MATMD with equal mass is better than MATMD with unequal mass and single active TMD in reduction of responses [24]. TMD and controller settings are typically based on the first mode shape; It almost always guarantees a reduction in the maximum displacement of the roof but does not ensure a significant reduction in other responses. Also, the results are reasonable when most of the parameters are designed with real conditions. For example, since the soil-structure interaction (SSI) effect is one of the most important design factors, neglecting it, particularly in the case of soft soil, may increase the structure's potential for instability [4,5,26,27]. Additionally, the simultaneous or non-simultaneous-tuning of the parameters of the control device and the controller can also be one of them [14].

Also, the conditions of other items that impact the system can be considered as follows: locating the control device, changing the structure responses in elevation after applying the control, and examining the effectiveness of the control algorithm regarding the design goals.

structural control topics. The advantages of fuzzy logic controllers in structural control include flexibility, ease of implementation, robustness, and interpretability, and their disadvantages of fuzzy logic controller include dependence on human expertise, difficulty in tuning, limited accuracy and computational complexity [46].

Past studies have also applied multiple passive-tuned mass dampers (MPTMD) to enhance the performance of high-rise

To the best knowledge of the authors, no comprehensive research has so far been done on seismic control of high-rise buildings equipped with MPTMD or MATMD, in which the following criteria were considered together: the modes shapes, SSI effects, the placement of the devices based on the outcomes of the responses after the control of the structure by a single device, and the simultaneous and non-simultaneous tuning of design parameters.

Therefore, in this research, while examining the seismic effects of SPTMD and SATMD control devices and simultaneous and non-synchronous adjustment of design parameters, MPTMD and MATMD devices have been used considering SSI effects on a 40-story tall building. Also, an innovative process, is proposed for locating, the devices at the height of the structure. The well-known PID controller has also been used to determine the applying control signal. Then, the parameters of the devices and controller have been optimized using single and multi-objective particle swarm optimization (PSO) algorithms. Finally, the structural dynamic responses in various states and under the application of important earthquake events have been presented and evaluated.

The remainder of the paper is structured as follows. Section II presents the main structural model and the system's dynamic equations. The PID controller and its adjustment parameters are introduced in Section III. Then, Section IV describes, the PSO optimization algorithm. Section V presents the tuning results of the parameters based on artificial earthquakes. Finally Section VI discusses the analysis and evaluation of numerical results of applying real earthquakes to the structure, and Section VII provides some concluding points.

II. Structural Model

An N-story shear structure equipped with an SPTMD SATMD MPTMD or MATMD, located on the top and one other floor and subjected to an earthquake acceleration $\ddot{x}_g(t)$, is assumed.

Equipping the structure with one or two control devices considering the SSI effects added 3 or 4 degrees-of-freedom to

the primary structural system. In the structural system equipped with passive or active devices, the equation of the motion of the system can be expressed as Eq. (1) and. (2), respectively[4]:

$$\boldsymbol{M}\,\ddot{x}(t)+\boldsymbol{C}\,\dot{x}(t)+\boldsymbol{K}\,x(t)=-\boldsymbol{M}^{*}\ddot{x}_{g}(t) \quad (1)$$

$$\boldsymbol{M}\,\ddot{x}(t)+\boldsymbol{C}\,\dot{x}(t)+\boldsymbol{K}\,x(t)=-\boldsymbol{M}^{*}\ddot{x}_{g}(t)+\mathbf{D}u(t) \quad (2)$$

$$\boldsymbol{C}=\begin{bmatrix}[c] & [0]^{T} & [0]^{T}\\ [0] & c_{s} & 0\\ [0] & 0 & c_{r}\end{bmatrix} \quad (4)$$

in which M, C, and K are the (N+3)× (N+3) mass, damping, and stiffness matrices of the whole system for SPTMD and SATMD and (N+4)×(N+4) for MPTMD and MATMD [4,24]; Also, $x(t)=\{x_1(t),x_2(t),\ldots,x_{N-1}(t),x_N(t),x_{d1}(t),x_0(t),\theta_0(t)\}^{T}$ represents the (N+3)× 1 displacement of the whole system for a single device and $x(t)=\{x_1(t),x_2(t),\ldots,x_{N-1}(t),x_N(t),x_{d1}(t),x_{d2}(t),x_0(t),\theta_0(t)\}^{T}$, represents the (N+4)× 1 displacement for two devices installed on the various floors, where $x_j(t)$ (j=1,..., N) are the displacement of the jth floor of the structure. $x_{d1}(t)-x_{d2}(t), x_0(t), \theta_0(t)$ refer to the TMDs stroke, displacement, and foundation rotation, respectively. In addition,

$$\boldsymbol{M}^{*}=\left\{m_1,m_2,\ldots,m_{N-1},m_N,m_{d1},m_0+\Sigma_{j=1}^{N}M_j+m_{d1},\Sigma_{j=1}^{N}m_jz_j+m_{d1}z_N\right\}^{T}$$

or $\boldsymbol{M}^{*}=\left\{m_1,m_2,\ldots,m_{N-1},m_N,m_{d1},m_{d2},m_0+\Sigma_{j=1}^{N}M_j+m_{d1}+m_{d2},\Sigma_{j=1}^{N}m_jz_j+m_{d1}z_N+m_{d1}z_\alpha\right\}^{T}$

are the (N+3)× 1 and (N+4)× 1 acceleration mass vector for the earthquake for a system equipped with 1 and 2 control devices respectively, D is the (N+3)× 1 or (N+4)× 1 location vector of the control force, and *u(t)* is the control force applied by SATMD or MATMD to the main structure. Besides, α is the corresponding floor number on which the second device is installed. Using the Lagrangian equation, the mass matrices of the whole system are obtained as follows:

$$\boldsymbol{M}=\begin{bmatrix}[m] & \{m\} & [m]\{z\}\\ & m_0+\Sigma_{j=1}^{N}m_j+m_{d1}+m_{d2} & \Sigma_{j=1}^{N}m_jz_j+m_{d1}z_N+m_{d2}z_\alpha\\ Sym. & & I_0+\Sigma_{j=1}^{N}\left(I_j+m_jz_j^{2}\right)+m_{d1}z_N^{2}+m_{d2}z_\alpha^{2}\end{bmatrix} \quad (3)$$

where $[m]=diag\left(m_1,m_2,\ldots,m_{N-1},m_N,m_{d1},m_{d2}\right)$ is the (N+2)× (N+2) mass matrix and $\{m\}=\{m_1,m_2,\ldots,m_{N-1},m_N,m_{d1},m_{d2}\}^{T}$ is the (N+2) ×1 mass vector of the structure equipped with MPTMD or MATMD without SSI effects. Also, $\{z\}=\{z_1,z_2,\ldots,z_{N-1},z_N,z_N,z_\alpha\}^{T}$ is the (N+2) ×1 elevation vector of floors. The mass, mass moment of inertia, and evaluation of the jth floor of the structure are represented by m_j, I_j, and z_j (j=1,..., N), respectively. Moreover, m_0, I_0, and m_{d1}, m_{d2} are the mass and mass moment of inertia of the foundation, and mass of TMDs which are installed on different floors, respectively. To reach M, [m], and vectors $\{m\}$ and $\{z\}$ for a system equipped with SPTMD and SATMD, it is enough to vanish m_{d2} and z_α from the above matrices and vectors. The damping and stiffness matrices of the whole system are given by:

$$\boldsymbol{K}=\begin{bmatrix}[k] & [0]^{T} & [0]^{T}\\ [0] & k_{s} & 0\\ [0] & 0 & k_{r}\end{bmatrix} \quad (5)$$

where $[c]$ and $[k]$ are the (N+2)× (N+2) damping and stiffness matrices of the structure equipped with MPTMD or MATMD without SSI effects. c_s and c_r are the rocking damping and swaying damping of the foundation, and k_r and k_s refer to the rocking and swaying stiffness of the foundation. As before, to reach the matrices C and K for a system equipped with SPTMD or SATMD, the components related to device number such as k_{d2} and c_{d2} should be removed from the matrices presented above. Also, matrices $[c]$ and $[k]$ are achieved as follows:

$$[c]=\begin{bmatrix}[c_{st}]_{N\times N}+[c_d]_{N\times N} & -[c_d]_{N\times n}\\ -[c_d]_{n\times N} & [c_d]_{n\times n}\end{bmatrix} \quad (6)$$

$$[k]=\begin{bmatrix}[k_{st}]_{N\times N}+[k_d]_{N\times N} & -[k_d]_{N\times n}\\ -[k_d]_{n\times N} & [k_d]_{n\times n}\end{bmatrix} \quad (7)$$

where $[c_{st}]$ and $[k_{st}]$ are the main structure mass, damping, and stiffness matrices without SSI effects, respectively. Furthermore $[c_d]$ and $[k_d]$ are the damping and stiffness corresponding to the n-number of TMDs to be employed in the main structure. Also, the main structural system's Rayleigh proportional damping is used to calculate the damping matrix.

III. PID Controller

The PID controller has been employed in numerous engineering studies and is particularly useful for controlling tall buildings. The main benefits of this controller are its ease of use in adjusting gains and efficiency in controlling structural vibrations. [4,15,28,29]. A block diagram of the standard-form PID controller is illustrated in Fig. 1.

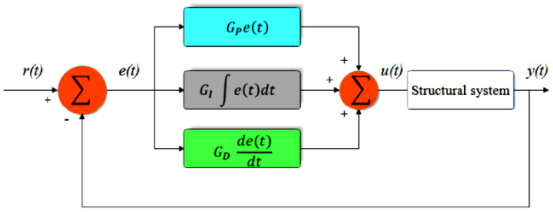

Fig. 1: The block diagram of a standard-form PID controller

According to Fig. 1, the PID controller in the time domain has an error input e(t) and is defined as e(t)= r(t)- y(t) so that r(t) is the reference input and its value is considered equal to zero in structure control issues. In addition, y(t) is the actual output value of the system. The measured error signal is the input of three separate units that create the error multiplier (proportional part), the error rate of change (differential part), and the error sum (integral part).

To determine the amount of applied control force in time t, all three components are added together and weighted by the PID control parameters (G_P, G_I, and G_D). So, the following is how the PID control force can be achieved [4,28].

$$u_{PID}(t)=G_P e(t)+G_I \int_0^t e(t)dt+G_D \frac{de(t)}{dt} \quad (8)$$

where t denotes the length of the control process and Gp, GI, and GD are the proportional, integral, and derivative terms, respectively.

IV. PSO Algorithm

PSO is a population-based stochastic optimization algorithm proposed based on the behavior of swarms in nature such as birds and fish [30]. The PSO algorithm has been used by researchers in the field of vibration control, especially in structural engineering [4,31-36,43]. The advantages of PSO over other optimization algorithms, including the genetic algorithm (GA) and the ant colony algorithm (ACO), include the small number of tuning parameters, ease of application, rapid convergence, and relatively low computational effort [4,31,34-40].

The status of a particle in the search space can be characterized by two factors: position and velocity. Considering a d-dimensional search space, the position and the velocity of the ith particle can be represented by the vectors $x_i = (x_{i1}, x_{i2}, \dots, x_{id})$ and $v_i = (v_{i1}, v_{i2}, \dots, v_{id})$, respectively. Each particle has its own best position (pbest) $p_i = (p_{i1}, p_{i2}, \dots, p_{id})$ corresponding to the personal best objective value obtained so far at time t. The global best particle is also represented as g, which denotes the best position found so far at time t in the whole swarm. The new velocity of each particle and the position of the ith particle are then updated using Eq. (9) and (10), respectively [42].

$$v_{ij}(t+1) = w v_{ij}(t) + c_1 r_1 [p_{ij} - x_{ij}(t)] \dots + c_2 r_2 [g_j - x_{ij}(t)], \quad j = 1, 2, \dots, d \quad (9)$$

$$x_{ij}(t+1) = x_{ij}(t) + v_{ij}(t+1), \quad j = 1, 2, \dots, d \quad (10)$$

where the acceleration coefficients, denoted by the constants c_1 and c_2, are frequently set to 2.0 based on prior knowledge. Moreover, *w* is the inertia weight factor, which is frequently in the range [0.1, 0.9] and can be obtained using the updated following equation to improve convergence: r_1 and r_2 are two independent random numbers uniformly distributed in the range [0, 1].

$$w = w_{max} - n_i \left(\frac{w_{max} - w_{min}}{n_{max}}\right) \quad (11)$$

in which w_{max} and w_{min} denote maximum and minimum weights. Also, n_i and n_{max} are the current generation number, and the maximum number of generations, respectively [41].

V. Numerical Studies

A well-known 40-story benchmark structure has been chosen to investigate how well a tall building performs against earthquakes when equipped with one or more control devices, such as SPTMD, SATMD, MPTMD, or MATMD [1,4].

Because studying SSI effects is more crucial in soft soils than other soils, this state was selected as a construction soil for all designs. The specifications of the main structure are shown in Table 1. Table 2 presents the soft soil parameters.

A. Proposed placement of TMDs

Previous studies have optimally located the control device using mode shapes. In the present research, with an innovative process and according to [4], other items were included in the design process as follows: the results of uncontrolled state and controlled state by SPTMD and SATMD considering SSI effects.

The first eight modes are shown in Fig. 2. Also, the normalized maximum deformation of the modes and the corresponding floors are presented in Table 3. Based on [4], Fig. 3 displays the diagram of the relative displacement, acceleration, and drift ratio of the structure floors under a filtered white noise artificial earthquake for various states in which w/o control, PTMD, and PID1US show, the uncontrolled state, controlled state by a single passive TMD and single ATMD in non-simultaneous tuning, respectively. As was already mentioned, the single device is installed on the top floor. It is evident from Fig. 2 and Table 3, that the top story is where the structure's

maximum displacement occurs. It confirms the 40th floor's selection as the best location to limit the maximum displacement of the structure. This conclusion is confirmed in Fig. 3, containing before and after controlling. Furthermore, for the uncontrolled and SPTMD states, the maximum acceleration has occurred on the 24th floor. On the other hand, it is the 25th floor for the SATMD state. Additionally, the highest value of the relative drift ratio of the floors is related to the 33rd floor for the uncontrolled and SATMD, the 32nd floor for the SPTMD.

TABLE 1
STRUCTURAL PARAMETERS [1,4]

Number of stories	40
Story height	4 m
Breadth and depth of the structure	40 m
Story mass, mass moment of inertia	m_j=9.80e5 kg, I_j=1.31e8 kg.m2
Story stiffness*	k_1= 2.13 e9 N/m, k_{40}=9,98e8 N/m
Foundation radius, mass, moment of inertia	R_0=20m, m_0=1.96e6kg, I_0=1.96e8kg.m2

* The stiffness of each story is linearly decreased as the evaluation of the structure

TABLE 2
THE SOFT SOIL PARAMETERS [1,4]

Soil type	Poisson's ratio (v_s)	Soil density $\rho(kg/m^3)$	Shear wave velocity $V_s(m/s)$	Shear modulus $G_s(N/m^2)$	Swaying damping $(N.s/m)$	Rocking damping $C_r(N.s.m)$	Swaying stiffness $K_s(N/m)$	Rocking stiffness $K_r(N.m)$
Soft	0.49	1800	100	1.80×107	2.19×108	2.26×1010	1.91×109	7.53×1011

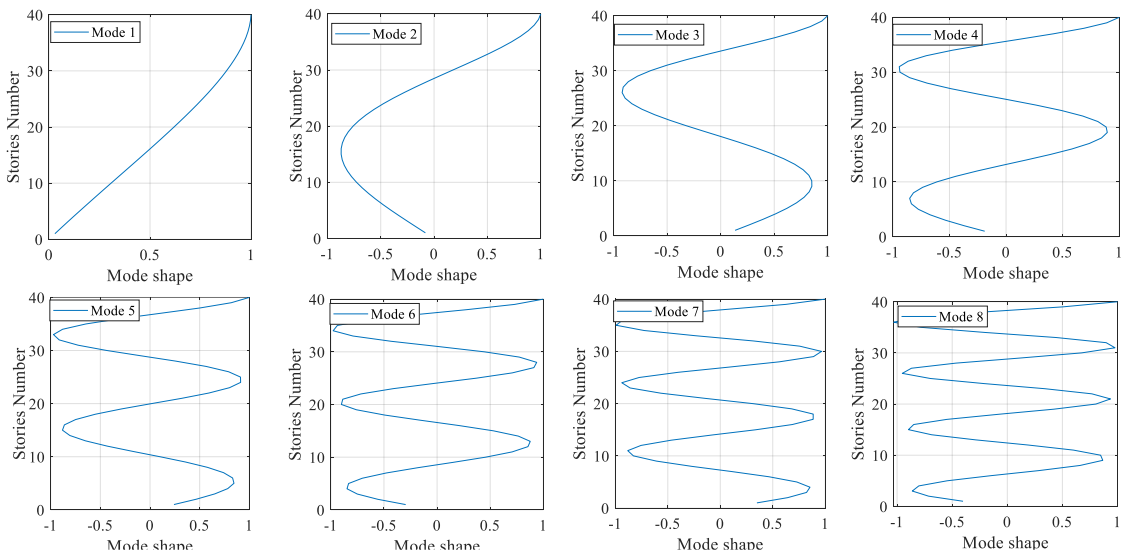

Fig. 2. The 1st to the 8th normalized mode shapes

TABLE 3
THE RESULTS OF THE MODE SHAPES ANALYSIS

Mode number	**1**	**2**	**3**	**4**	**5**	**6**	**7**	**8**
Maximum Deformation(normalized)*	1	1	1	1	1	1	1	1.03
Corresponding floor	40	40	40	40	40	40	40	36

*Max. floor deformation normalized by 40th-story deformation

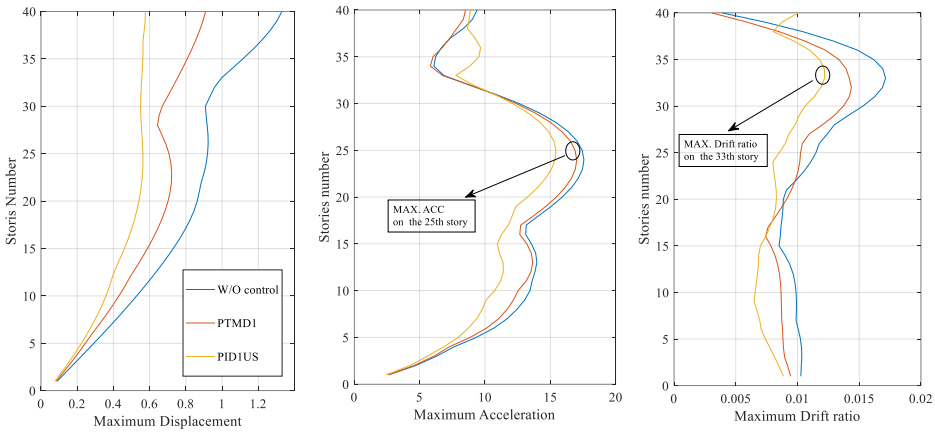

Fig. 3. The maximum responses of a structure subjected to an artificial earthquake [5]

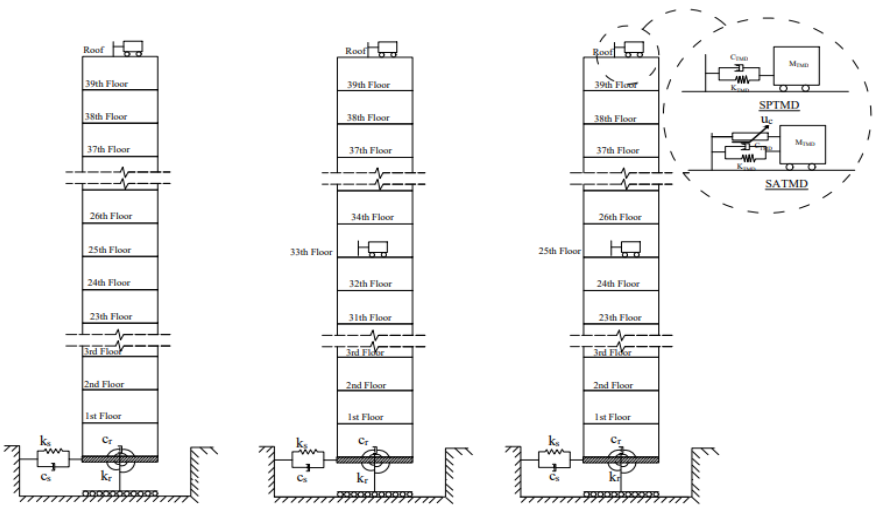

(a) (b) (c)

Fig. 4. The proposed location for installing various control devices on the elevation of the structure: (a) single device, (b) multi-device-case40-33, (c) multi-device-case40-25

According to all the aforementioned factors, it can be proposed that the 40th floor is the fixed best location for one of the control devices. To locate the second device, we should accept the possible compromise between reducing displacement-acceleration and displacement-relative drift which leads to two possible scenarios, henceforth named case 40-33 and case 40-25. The numbers after the case refer to the location of devices on floors. Fig. 4 shows the suggested location for the structure equipped with a single control device (SPTMD or SATMD) and multiple devices (MPTMD or MATMD).

B. Optimal TMD and PID parameters

Different states of controller and control device parameter optimization using the PSO algorithm have been examined. The evaluation of the effects of using one or more control devices(passive or active) and the effect of simultaneous and non-simultaneous tuning of TMDs and PID parameters are among them. In this study, the meaning of non-simultaneous tuning is that first, using the optimization algorithm, the optimal tuning of the parameters TMD and then the optimal tuning of the PID controller parameters is done. On the other hand, simultaneous tuning means tuning the devices and controller parameters at the same time under an artificial earthquake. The first optimization problem involves finding the best TMD parameters for two states of TMD placement. The first state includes SPTMD and SATMD, and the second includes MPTMD and MATMD. The optimal design of TMD parameters for multi-control devices, including frequency ratios, f_1, f_2, and damping ratios, ξ_{T1}, ξ_{T2}, with various mass ratios of TMD is as follows:

$$\begin{cases} Find & x = \{f_1, \xi_{T1}, f_2, \xi_{T2}\} \\ \text{minimize} & F = (Of_1, Of_2) \end{cases} \quad (12)$$

Also, assuming that M_s is the mass of the original structure, the optimum TMDs mass, damping, and stiffness of TMDs are calculated as follows:

$$\begin{cases} M_{tmd1} = \gamma_1 M_s \\ and \\ M_{tmd2} = \gamma_2 M_s \end{cases}, \begin{cases} C_{tmd1} = 2M_{tmd1}\xi_{T1} f_1 \omega_s \\ and \\ C_{tmd2} = 2M_{tmd2}\xi_{T2} f_2 \omega_s \end{cases}, and \begin{cases} K_{tmd1} = M_{tmd1} f_1^2 \omega_s^2 \\ and \\ K_{tmd2} = M_{tmd2} f_2^2 \omega_s^2 \end{cases} \quad (13)$$

where, γ_1 and γ_2 are preselected mass ratios of TMDs. The second optimization problem entails designing a PID controller to adjust the control force for SATMD and MATMD as follows, respectively:

$$\begin{cases} Find & x = \{G_{P1}, G_{I1}, G_{D1}\} \\ \text{minimize} & F = (Of_1) \\ Subjected\ to & \max\|u_{PID1}(t)\| \le 0.05\ W_s \end{cases} \quad (14)$$

$$\begin{cases} Find & x = \{G_{P1}, G_{I1}, G_{D1}, G_{P2}, G_{I2}, G_{D2}\} \\ \text{minimize} & F = (Of_1, Of_2) \\ Subjected\ to & \max\|u_{PIDi}(t)\| \le 0.05\ W_s \quad i = 1, 2 \end{cases} \quad (15)$$

in which, G_{P1}, G_{I1}, G_{D1}, G_{P2}, G_{I2}, G_{D2} are the parameters related to two controllers corresponding to control devices installed in different floors. The total weight of the structure is represented by W_S. Also, the search spaces of f_i, ξ_{Ti} , G_{Pi}, G_{Ii}, G_{Di} parameters for the upper and lower bands are limited, based on previous experience, to [0.5, 1.4], [0.01,0.2], [9e4,12e4], [1.7e8,2.2e8], [0,2e3], respectively.

In Eq. 12-14, only subscript 1 is considered for the state of SPTMD or SATMD and the rest of them are ignored. For SPTMD Eq. 12-13, and for SATMD, Eq. 12-14 are considered a single-objective optimization. In Eq. 12 and 14, only of_1 is considered the single-objective function.

In other words, for MPTMD Eq. 12-13 and for MATMD, Eq. 12-13 and 15 are considered a multi-objective optimization. The population size for single-objective and multi-objective optimization is 50 and 100, respectively; In addition, the prescribed number of iterations is considered equal to 20 for both states.

As mentioned in Section 5.1, cases 40-25 and 40-33 have been proposed to investigate the effects of control device placement. In Eq. 12 and 15, the two-objective function includes minimizing the maximum displacement of the roof floor (Of_1) and the maximum acceleration of the 25th floor (Of_2) corresponding to case 40-25. Similarly, for case 40-33, the multi-objective function includes minimizing the roof displacement (Of_1) and relative drift ratio (Of_2) of 33rd floor.

For the mass ratio of TMDs, three scenarios are proposed. The main constraint for determining the mass of TMDs is $\sum_{i=1}^{i=2} M_{TMD_i} = 0.05 \times M_s$. It has been proposed to compare with the single device state. The recommended mass ratios for the TMD installed on the 40th floor are three values of γ_1=4, 3, and 2.5%. For the device installed on the 25th or 33rd floor, the corresponding values of γ_2=1, 2, and 2.5% are suggested. In other words, the combination of mass ratios of 4%-1%, 3%-2%, and 2.5%-2.5% has been selected for the γ_1 and γ_2 values, respectively.

For generalizing settings and avoiding several time-consuming analyses, an artificial earthquake has been applied for tuning control parameters. The filtered white noise is used as the artificial earthquake. It is generated by passing a Gaussian white noise process through a filter model [4]. The well-known Kanai-Tajimi filter with the following spectral density function is applied for this purpose [4,16].

$$s(\omega) = S_0 \left[\frac{\omega_g^4 + 4\xi_g^2 \omega_g^2 \omega^2}{(\omega^2 - \omega_g^2)^2 + 4\xi_g^2 \omega_g^2 \omega^2} \right], \quad S_0 = \frac{0.03\xi_g}{\pi\omega_g(4\xi_g^2 + 1)} \quad (15)$$

where S_0, ξ_g, and ω_g are the constant spectral density, the ground damping, and frequency, respectively. In this paper, $\xi_g = 0.3$ and $\omega_g = 37.3\ rad/s$ have been used for numerical simulations. The filtered white noise is shown in Fig. 5. The Optimum TMD and PID parameters for SPTMD and SATMD and the non-simultaneous tuning state are inserted in Table 4 [4]. Also, the results of the simultaneous tuning of them are inserted in this table. The best results of optimal design for MATMD, MPTMD, and PID parameters are presented in Tables 5 and 6; They have been extracted based on the Pareto diagram, considering a compromise between the responses. In addition, the optimal parameters with various proposed placements and different mass ratios have been inserted. In Table 5, the optimal PID parameters are obtained in the continuation of fixing the optimal TMD parameters. In contrast, all parameters presented in Table 6 have been optimized simultaneously.

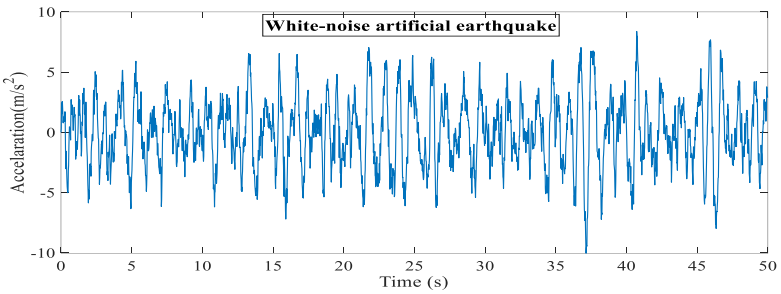

Fig. 5. The filtered white noise artificial earthquake

TABLE 4
OPTIMUM TMD AND PID PARAMETERS FOR SOFT SOIL [4]

Tuning type	TMD parameters		PID parameters		
	frequency ratio (f)	damping ratio (ξ_T)	G_P	G_I	G_D
Non-simultaneous [4]	1.26	0.20	1.10×10^5	1.94×10^8	0.00
Simultaneous	1.22	0.08	1.11×10^5	1.79×10^8	1.06×10^3

TABLE 5
OPTIMUM TMD AND PID PARAMETERS FOR SOFT SOIL (NON-SIMULTANEOUS TUNING)

Case	**TMD location (story)**	**TMD mass ratio**	**TMD parameters**		**PID parameters**		
			frequency ratio (f)	**damping ratio (ξ_T)**	**G_P**	**G_I**	**G_D**
40-33	40	4%	1.3967	0.1996	1.0 e+05	1.7 e+08	0.0
	33	1%	0.7303	0.1956	1.0 e+05	1.7 e+08	0.0
	40	3%	1.3806	0.1965	1.0 e+05	1.7 e+08	1.6788e+03
	33	2%	0.9555	0.1972	1.0 e+05	1.7 e+08	978.5679
	40	2.5%	1.3796	0.1902	1.0 e+05	1.7 e+08	705.4445
	33	2.5%	1.0049	0.0940	1.0 e+05	1.7 e+08	511.3972
40-25	40	4%	1.400	0.1905	1.0243e+05	1.7341e+08	1.7150e+03
	25	1%	0.6137	0.0100	1.0492e+05	1.7043e+08	1.6726e+03
	40	3%	1.3902	0.1992	1.1410e+05	1.7275e+08	518.8052
	25	2%	0.6230	0.1969	1.0131e+05	1.7552e+08	1.7085e+03
	40	2.5%	1.400	0.2000	1.0 e+05	1.7 e+08	240.7838
	25	2.5%	0.6000	0.1854	1.0 e+05	1.7 e+08	673.5438

TABLE 6
OPTIMUM TMD AND PID PARAMETERS FOR SOFT SOIL (SIMULTANEOUS TUNING)

Case	**TMD location (story)**	**TMD mass ratio**			**PID parameters**		
			frequency ratio (f)	**damping ratio (ξ_T)**	**G_P**	**G_I**	**G_D**
40-33	40	4%	1.2298	0.0887	727.6826	1.8569e+08	1.1308e+05
	33	1%	0.7466	0.0274	1.2826e+03	1.8142e+08	1.1072e+05
	40	3%	1.1903	0.0912	1.0 e+05	1.8990e+08	0.0
	33	2%	0.7810	0.1121	1.0 e+05	2.0825e+08	1.1679e+03
	40	2.5%	1.4000	0.2000	1.9240e+03	2.1962e+08	1.0364e+05
	33	2.5%	0.6262	0.1891	2.0 e+03	1.7217e+08	1.2 e+05
40-25	40	4%	1.4000	0.1849	1.0457e+03	1.9321e+08	1.1998e+05
	25	1%	0.6031	0.0494	781.6318	1.9691e+08	1.0 e+05
	40	3%	0.6621	0.1880	470.4099	1.7097e+08	1.1064e+05
	25	2%	1.4000	0.2000	1.7688e+03	1.7 e+08	1.1762e+05
	40	2.5%	0.6382	0.2000	276.8684	1.7409e+08	1.0 e+05
	25	2.5%	1.4000	0.2000	1.9685e+03	1.9258e+08	1.0278e+05

VI. Results and Discussion

The findings of [4] are utilized to assess the effectiveness of the proposed change. The evaluation of the suggestions, such as locating control devices in the elevation, how to choose the best design parameters, simultaneous and non-simultaneous settings of devices and controller parameters, and the TMDs mass various ratios, was explored. Table 8 presents the comparative results under artificial earthquake for all proposed cases. Fig. 6 illustrates the results of a filtered white noise earthquake application for case 40-33 and different mass ratios. All figures depict uncontrolled (w/o control), the structure equipped with an SPTMD (PTMD1), an SATMD and PID controller with non-simultaneous settings (PID1US), an SATMD and PID controller with simultaneous settings (PID1S), MPTMD with two TMDs (PTMD2), MATMD with two devices PID controller with non-simultaneous settings (PID2US), and finally MATMD with two devices and PID controller with simultaneous settings (PID2S), respectively. In Fig. 6, subcase 4-1 is related to the mass ratio of the TMD device, which is located on the 40^{th} and 33^{rd} floors, respectively. Similarly, subcases 3-2 and 2.5-2.5 are also defined. Table 8 shows the maximum displacement response when using the SATMD. Simultaneous tuning is improved by 7.1% compared with the non-simultaneous state. At the same time, there is little change in the maximum acceleration and maximum drift ratio of the floors. Furthermore, there are no appreciable differences in responses when MPTMD is used instead of SPTMD.

As well, the results of the non-simultaneous tuning of MATMD and PID controller show a decrease of up to 14.3% compared with the uncontrolled state, whereas, compared with the SATMD with non-simultaneous tuning, an increase of up to 183.7% can be seen in responses. Of course, in the case of the maximum acceleration of the floors, the results of the answers are almost unchanged. On the other hand, the results of the simultaneous settings show a reduction of the maximum displacement up to 67.7% compared with the uncontrolled case. This decrease is 19.9% compared with SATMD with non-simultaneous tuning, which is related to case 40-33 with a mass ratio of 4%-1%. Also, the improvement of the response of the maximum acceleration and the maximum drift ratio is 25.4% and 40.4% compared with the uncontrolled case. This decrement is 15.3% and 16.4% compared with SATMD with non-simultaneous adjustment, which belongs to case 40-25 with a mass ratio of 4%-1%. The results show that the decrement of the maximum acceleration occurs in all states. At the same time, by considering a trade-off between the reduction of the maximum responses, the best result may belong to case 40-25 or case 40-33 and the mass ratio of 4%-1%. The corresponding percent is up to 19.9%, 15.3%, and 16.4% compared with SATMD, respectively.

Compared to [4], the general evaluation of the results demonstrates significant improvement in responses all over the cases, including structures equipped with SATMD and MATMD with simultaneous tuning. In addition, it shows that the proposed placements of devices were successful compared with the control primary objectives.

The optimal settings were evaluated by two famous Kobe and Northridge (Newhall station) earthquakes. they were reported by [4], and their characteristics are given in Table 7. From now on, the earthquake is referred to as Northridge (Newhall station) abbreviated as Newhall. Also, the data of these earthquakes have been extracted from the PEER Ground Motion Database. Tables 9 and 10 report the results of these earthquakes. Additionally, Fig. 7 displays the results of dynamic responses to the Kobe earthquake. For the simultaneous settings of SATMD and PID compared with non-simultaneous settings [4], the results of applying the Kobe-1995 and Northridge-1994 earthquakes show a reduction of 6.4% and 14.4% in the maximum displacement, respectively. Furthermore, the maximum acceleration for Kobe was almost unchanged and for Newhall, an increase of 8.5% was seen. An increase of 17.5% for Kobe and 16.1% for Newhall occurred in the maximum floor drift.

The examination of the results of the application of MPTMD on the structure for all cases shows insignificant changes compared with the SPTMD state. This general conclusion is true for two earthquakes and all maximum responses. Also, the analysis of the results of the responses of the structure equipped with MATMD with the non-simultaneous tuning reveals decreases of up to 19% and up to 39.4% for the results of the Kobe and Newhall earthquake compared with the uncontrolled state in the maximum displacement, respectively. The maximum acceleration and maximum drift for all cases are almost lower than those in the uncontrolled state, except for Kobe and maximum acceleration for case 40-25.

TABLE 7
THE CHARACTERISTICS OF EARTHQUAKES

Earthquake Name	Year	Magnitude	Station Name	PGA(g)
Kobe	1995	6.9	KJMA	0.82
Northridge	1994	6.69	Newhall	0.59

Almost all responses mentioned above are incremental compared with the SATMD with non-simultaneous settings. Only in Kobe and case 40-25, did the responses improve significantly.

The best results for Kobe are related to the maximum

displacement of MATMD with simultaneous setting, which belongs to case 40-33 with a mass ratio of 3%-2%. Also, a reduction of 53.7% and 26.5% were reported compared with the uncontrolled state and SATMD with non-simultaneous tuning, respectively. In this regard, the maximum decrement for the maximum acceleration and the maximum drift ratio of floors belongs to case 40-33 which are, 11.3% and 16.7% compared with the uncontrolled state and 5.9%, and 4.8% compared with the SATMD and non-simultaneous setting, respective. In contrast, the same increment is reported for case 40-25 so that the maximum acceleration increase by up to 8.4%.

TABLE 8
RESULTS FOR ALL CONTROL CASES UNDER THE ARTIFICIAL EARTHQUAKE

Control case	Subcase	Non-simultaneous tuning			Simultaneous tuning		
		MAX. Disp(m)	MAX. Acc(m/s^2)	MAX. Drift ratio	MAX. Disp(m)	MAX. Acc(m/s^2)	MAX. Drift ratio
Uncontrolled	-	1.33	17.57	0.017	-	-	-
SPTMD [4]	-	0.91(31.7%)	17.02(3.1%)	0.014(15.8%)	-	-	-
SATMD (Un-simultaneous) [4]	-	0.58(56.7%)	15.43(12.18%)	0.012(28.6%)	-	-	-
SATMD (Simultaneous)	-	-	-	-	0.54 (59.7%,7.1%)*	15.46 (12.0%, -0.2%)	0.012 (28.7%, 0.0%)
MPTMD (case 40-33)	4-1	0.91 (31.5%)	17.03(3.1%)	0.014 (17.0%)	-	-	-
	3-2	0.92 (30.8%)	17.25(1.8%)	0.014 (15.8%)	-	-	-
	2.5-2.5	0.93 (30.4%)	17.38(1.8%)	0.015 (14.0%)	-	-	-
MPTMD (case 40-25)	4-1	0.91 (31.3%)	16.80(4.4%)	0.015 (11.7%)	-	-	-
	3-2	0.93 (30.4%)	17.10(2.6%)	0.015 (12.3%)	-	-	-
	2.5-2.5	0.93 (30.0%)	17.16(2.3%)	0.015 (10.5%)	-	-	-
MATMD (case 40-33)	4-1	1.52 (-14.2%, -183.7%)	16.04 (8.7%, -3.7%)	0.016 (3.5%, -35.2%)	**0.43 (67.7%, 19.9%)**	13.88 (21.0%, 10.2%)	0.012 (26.9%, -2.5%)
	3-2	1.48 (-10.9%, -175.5%)	15.92 (9.4%, -2.9%)	0.016 (4.1%, -34.4%)	0.46 (65.5%, 14.2%)	13.92 (20.8%, 10.0%)	0.012 (28.7%, 0.0%)
	2.5-2.5	1.518 (-13.6%, -182.1%)	15.92 (9.4%, -3.0%)	0.016 (4.15, -34.4%)	0.44 (67.2%, 18.6%)	13.67 (22.1%, 11.6%)	0.012 (28.7%, 0.0%)
MATMD (case 40-25)	4-1	1.148 (14.3%, -113.0%)	15.37 (12.5%, 0.6%)	0.015 (9.9%, -26.2%)	0.53 (60.4%, 1.7%)	**13.10 (25.4%, 15.3%)**	**0.010 (40.4%, 16.4%)**
	3-2	1.148 (14.2%, -113.1%)	15.51 (11.7%, -0.3%)	0.016 (9.4%, -27.0%)	0.55 (59.0%, -1.9%)	14.02 (20.2%, 9.4%)	0.012 (27.5%, -1.6%)
	2.5-2.5	1.26 (5.6%, -134.4%)	15.59 (11.35, -0.8%)	0.017 (1.2%, -38.5%)	0.55 (58.8%, -2.4%)	14.24 (18.9%, 7.9%)	0.013 (26.3%, -3.3%)

Note: *The values shown by black ink and red ink inside brackets, represent the reduction percentage of the maximum structural responses compared with the uncontrolled case and the structure equipped with SATMD and non-simultaneous tuning related to [4], respectively.

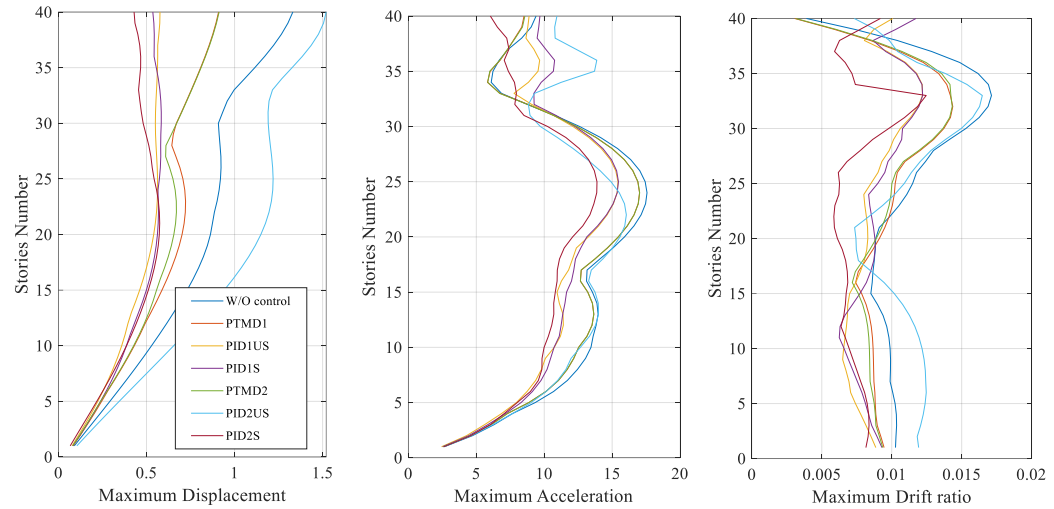

(a)

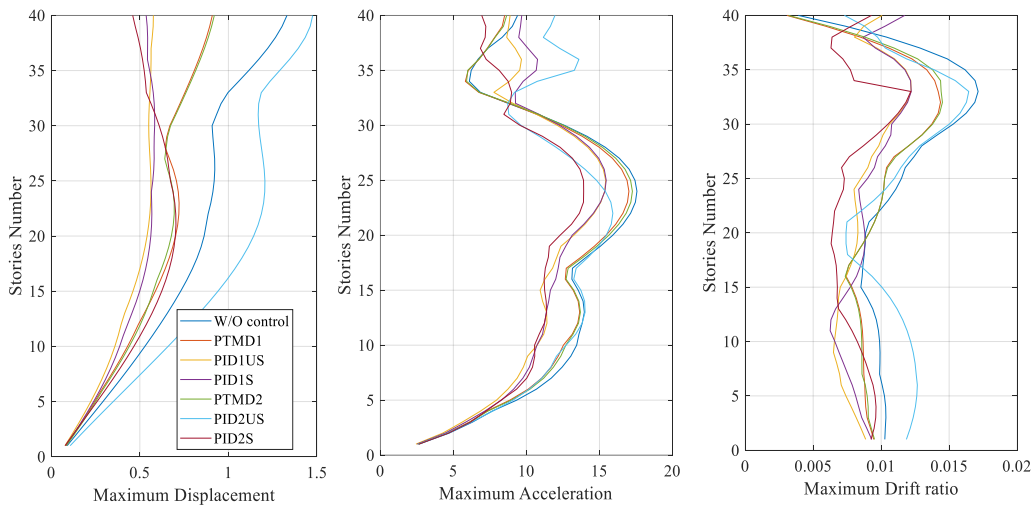

(b)

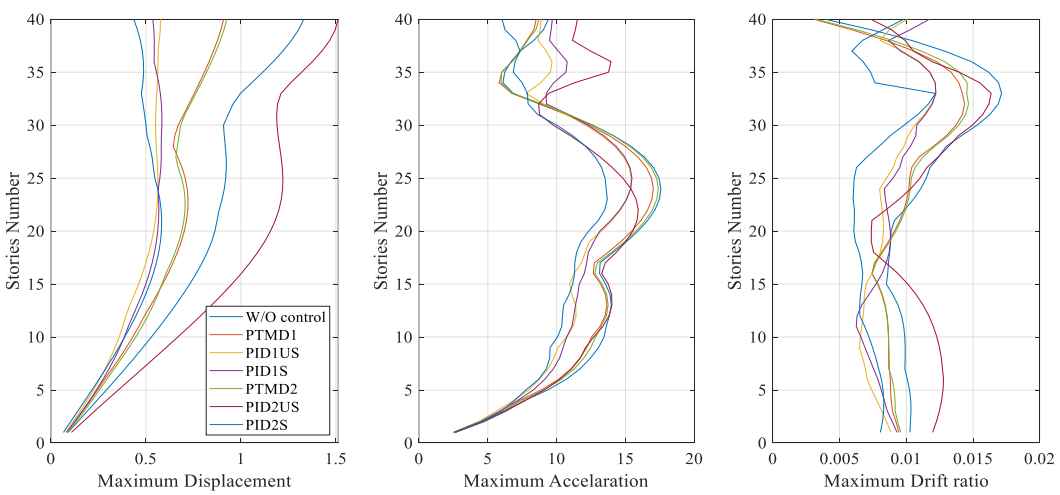

(c)

Fig. 6. Results of case 40-33 under the artificial earthquake: (a) Subcase 4-1, (b) Subcase 3-2, (c) Subcase 2.5-2.5

TABLE 9
RESULTS FOR ALL CASES UNDER THE KOBE EARTHQUAKE CONSIDERING SSI

Control case	Subcase	Non-simultaneous tuning			Simultaneous tuning		
		MAX. Disp(m)	MAX. Acc(m/s^2)	MAX. Drift ratio	MAX. Disp(m)	MAX. Acc(m/s^2)	MAX. Drift ratio
Uncontrolled	-	0.52	9.51	0.007	-	-	-
SPTMD [4]	-	0.47 (8.2%)	9.20 (3.3%)	0.0067 (6.9%)	-	-	-
SATMD (Non-simultaneous) [4]	-	0.33 (%)	8.97 (5.8%)	0.0063 (12.5%)	-	-	-
SATMD (Simultaneous	-	-	-	-	0.30 (41.0%,6.4%)*	8.93 (6.1%,3.3%)	0.0074 (-2.8%,17.5%)
MPTMD (case 40-33)	4-1	0.48 (7.8%)	9.20(3.3%)	0.0067 (6.9%)	-	-	-
	3-2	0.48 (7.2%)	9.25(2.8%)	0.0068 (5.6%)	-	-	-
	2.5-2.5	0.48 (6.9%)	9.29(2.3%)	0.0069 (4.2%)	-	-	-
MPTMD (case 40-25)	4-1	0.48 (7.6%)	9.21(3.2%)	0.0067 (6.9%)	-	-	-
	3-2	0.48 (7.0%)	9.26(2.7%)	0.0068 (5.6%)	-	-	-
	2.5-2.5	0.48 (6.6%)	9.29(2.3%)	0.0069 (4.2%)	-	-	-
MATMD (case 40-33)	4-1	0.42 19.0%, -28.6%)	**8.30 (12.7%, 7.4%)**	**0.0052 (27.8%, 17.5%)**	0.25 (51.5%, 23.0%)	8.55 (10.2%, 4.6%)	**0.006 (16.7%, 4.8%)**
	3-2	0.42 (18.8%, --29.0%)	**8.30 (12.7%, 7.4%)**	**0.0052 (27.8%, 17.5%)**	**0.24 (53.7%, 26.5%)**	8.63 (9.2%, 3.7%)	0.007 (16.7%, -3.2%)
	2.5-2.5	0.42 (18.6%, -29.3%)	**8.30 (12.8%, 7.4%)**	**0.0052 (27.8%, 17.5%)**	0.24 (52.9%, 25.2%)	**8.44 (11.3%, 5.9%)**	0.006 (15.3%, 3.2%)
MATMD (case 40-25)	4-1	0.57 (-9.4%, -73.8%)	10.15 (-6.7%, -11.7%)	0.0067 (6.9%, -6.0%)	0.29 (44.4%, 11.7%)	10.19 (-7.2%, -13.7%)	0.008 (-12.5%, -28.6%)
	3-2	0.57 (-9.3%, -73.6%)	10.18 (-7.0%, -13.5%)	0.0068 (5.6%, -7.9%)	0.33 (35.9%, -1.8%)	10.20 (-7.2%, -13.8%)	**0.006 (16.7%, 4.8%)**
	2.5-2.5	0.56 (-8.8%, -72.8%)	10.16 (-6.8, -13.3%)	0.0067 (6.9%, -6.3%)	0.34 (34.7%, -3.6%)	10.31 (-8.4%, -15.0%)	0.006 (15.3%, -3.2%)

However, the maximum drift ratio of the floors decreases by 15.3% and 16.7% for the mass ratio of 2.5%-2.5% and 3%-2% compared with the uncontrolled state.

Also, the best performance for the Newhall earthquake and all three essential responses is related to the structure equipped with MATMD and case 40-33 with simultaneous adjustment so that the maximum reduction was up to 66.7% for the maximum displacement, up to 14.1% for the maximum acceleration, and up to 26.5% for drift ratio compared with the uncontrolled state. It is noteworthy that this conclusion does not mean that case 40-25 did not improve the responses. For example, a reduction of up to 16.7% in the maximum displacement compared with SATMD with non-simultaneous tuning is observed for it. On the other hand, the responses were evaluated considering a trade-off between them. The selection criteria are based on the reduction of responses compared with the SATMD and non-simultaneous tuning. It shows that for the Kobe earthquake, maybe the best candidates for response improvement are related to MATMD with simultaneous tuning and case 40-33. The first selection may be the mass ratio of 2.5%-2.5% with a reduction of 25.2%, 5.9%, and 3.2% for three main maximum responses, respectively. The second choice is the mass ratio of 3%-2%, which entails a reduction of 26.5%, 3.7%, and 3.2% in the main maximum responses.

Similarly, for the Newhall earthquake, if considering a trade-off between responses, the best selection is the structure equipped with MATMD with simultaneous tuning related to case 40-33. As with the Kobe earthquake, the mass ratio of 2.5%-2.5% and 3%-2% are the best suggestions, and the highest reduction is generally 26.5%, 5.9%, and 4.8% for the main responses, respectively.

TABLE 10
RESULTS FOR ALL CASES UNDER THE NEWHALL EARTHQUAKE CONSIDERING SSI

Control case	Subcase	Non-simultaneous tuning			Simultaneous tuning		
		MAX. Disp	MAX. Acc	MAX. Drift ratio	MAX. Disp	MAX. Acc	MAX. Drift ratio
Uncontrolled	-	0.82	10.19	0.008	-	-	-
SPTMD [4]	-	0.76 (7.9%)	9.99 (2.0%)	0.008 (4.8%)	-	-	-
SATMD (Non-simultaneous) [4]	-	0.38 (53.4%)	8.86 (13.1%)	0.0062 (25.3%)	-	-	-
SATMD (Simultaneous)	-	-	-	-	0.33 (60.0%,14.4%)*	9.61 (5.7%, -8.5%)	0.007 (13.2%, -16.1%)
MPTMD (case 40-33)	4-1	0.76 (7.2%)	9.98(2.0%)	0.008 (6.0%)	-	-	-
	3-2	0.76 (7.9%)	10.02(1.6%)	0.008 (3.6%)	-	-	-
	2.5-2.5	0.75 (9.0%)	10.05(1.4%)	0.008 (2.4%)	-	-	-
MPTMD (case 40-25)	4-1	0.77 (6.1%)	10.00(1.9%)	0.008 (6.0%)	-	-	-
	3-2	0.77 (6.2%)	10.04(1.4%)	0.008 (4.8%)	-	-	-
	2.5-2.5	0.77 (6.3%)	10.06(1.2%)	0.008 (4.8%)	-	-	-
MATMD (case 40-33)	4-1	0.52 (37.1%, -35.0%)	9.51 (6.6%, -7.4%)	0.007 (9.6%, -21.0%)	0.30 (63.0%, 20.7%)	8.83 (13.4%, 0.3%)	**0.006 (26.5%, 1.6%)**
	3-2	0.52 (36.7%, -35.7%)	9.52 (6.6%, -7.4%)	0.007 (9.6%, -21.0%)	**0.27 (66.7%, 28.6%)**	8.93 (12.4%, -0.8%)	0.006 (22.9%, -3.2%)
	2.5-2.5	0.52 (36.3%, -36.5%)	9.52 (6.6%, -7.5%)	0.007 (9.6%, -21.0%)	0.29 (65.1%, 25.3%)	**8.75 (14.1%, 1.2%)**	0.006 (25.3%, 0.0%)
MATMD (case 40-25)	4-1	0.51 (38.7%, -23.9%)	9.87 (3.1%, -10.3%)	0.007 (19.3%, -7.5%)	0.33 (61.1%,16.7%)	9.24 (9.3%, -4.3%)	0.008 (6.0%, -25.8%)
	3-2	0.50 (39.4%, -30.0%)	9.87 (3.2%, -11.4%)	0.007 (19.3%, -8.1%)	0.33 (59.8%, 13.7%)	9.25 (9.2%, -4.4%)	0.007 (20.5%, -6.4%)
	2.5-2.5	0.50 (39.2%, -30.0%)	9.85 (3.3, -11.2%)	0.007 (19.3%, -8.1%)	0.33 (59.9%, 13.9%)	9.21 (9.6%, -4.02%)	0.007 (20.5%, -6.4%)

It is also important to evaluate the responses during the time history of an earthquake. One of the criteria to examine is the root mean square (RMS) presented in Eq. 16 for displacement responses. This equation can be generalized for acceleration and drift ratio responses.

$$x_{RMS} = \sqrt{\frac{{x_1}^2 + {x_2}^2 + \cdots + {x_n}^2}{n}} \quad (16)$$

where x and n are the displacement response at time t and the number of input earthquakes, respectively. RMSs of the three main responses are shown in Figs. 8 and 9 for the Kobe and

Newhall earthquakes, respectively. The average RMS of the responses of floors is also presented as another indicator in Figs. 10 and 11.

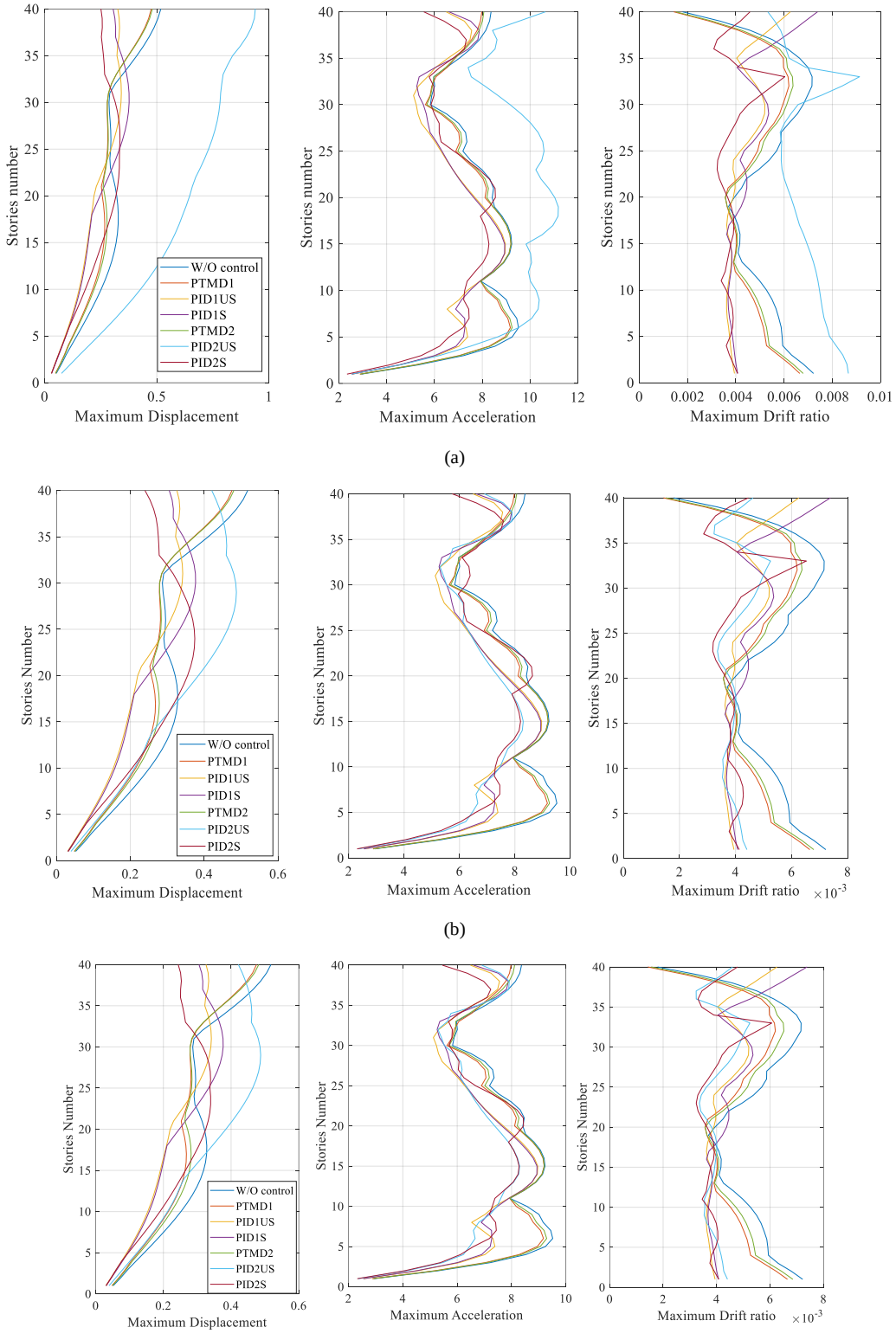

Fig. 7. Results for case 40-33 under the Kobe earthquake: (a) Subcase 4-1, (b) Subcase 3-2, (c) Subcase 2.5-2.5

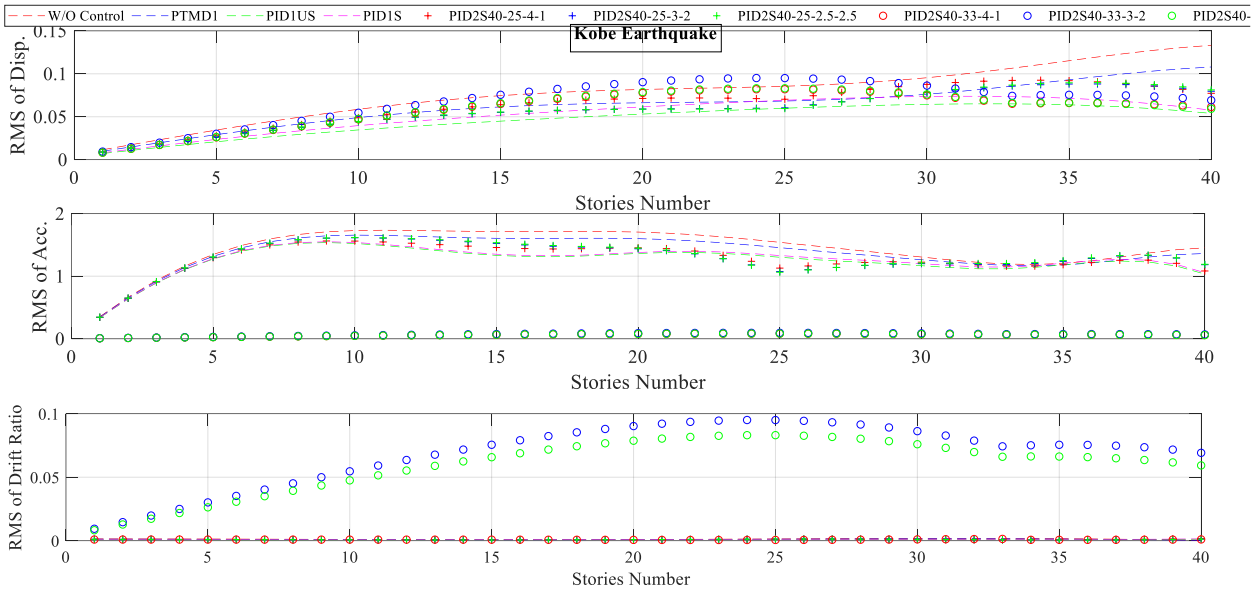

Fig. 8. Results of RMS for all stories under the Kobe earthquake

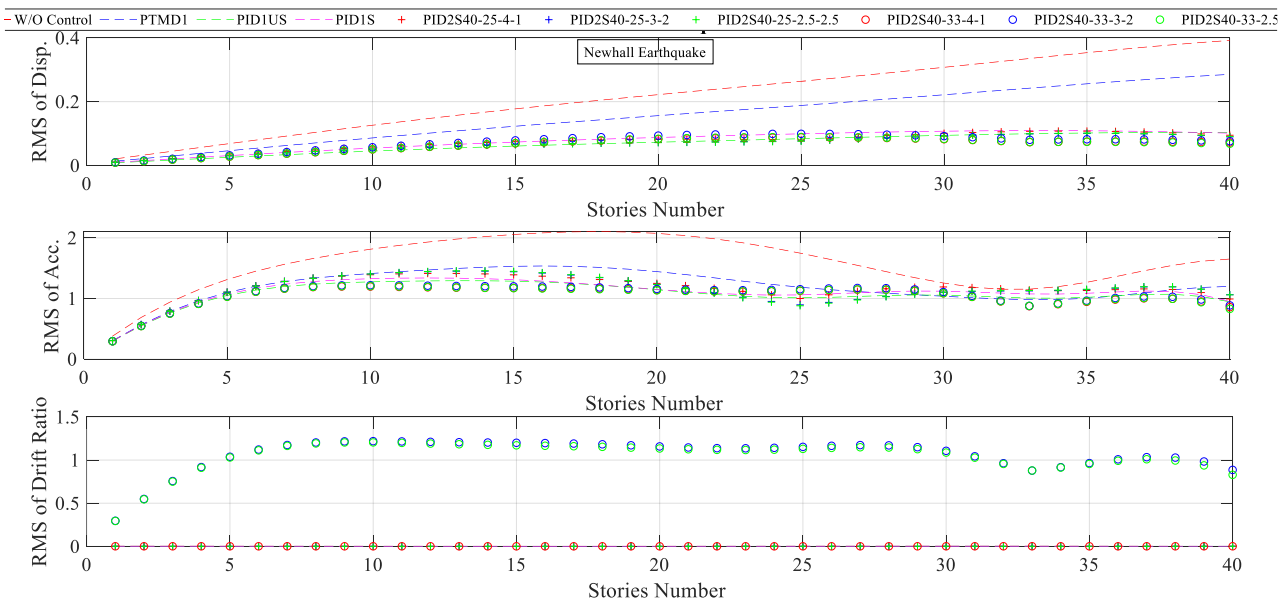

Fig. 9. Results of RMS for all stories under the Newhall earthquake

For the Newhall earthquake, the lowest maximum RMS of displacement and acceleration of the floors are related to MATMD and case 40-33 for which the values of 0.09 and 1.20 were gained, respectively. It belongs to the mass ratio of 4%-1%. In addition, the minimum RMS for the relative drift is 0.0014, related to SATMD with non-simultaneous tuning.

Also, for the Kobe earthquake, the best RMS for displacement and relative drift ratio are 0.065 and 0.0013, respectively. It belongs to SATMD with non-simultaneous tuning. In addition, for acceleration, case 40-33 and the mass ratio of 4%-1% are reported to have the best RMS of 1.514. Also, the lowest average RMS value of the response for the Kobe earthquake is related to SATMD with simultaneous tuning. Of course, the results of other active control states and different mass ratios are also very close to this value. On the contrary, the lowest average RMS is related to case 33-40, and the mass ratio 4%-1% for the Newhall earthquake and for three main responses.

VII. Conclusions

In this research, an innovative application-modification process was suggested. According to this, a new method was presented to find the TMDs' elevation placement position as a control device, could imrove responses and significantly reduces the volume of calculations, especially for the

optimization process. In this regard, a few items were examined as follows: the effects of simultaneous and non-simultaneous designed parameters of PID and devices controller, various devices containing SPTMD, SATMD, MATMD, MPTMD, and different mass ratios. According to this proposed method, the mode shapes of the structure and the maximum responses in uncontrolled states were examined; In addition, the responses of the structure equipped with SPTMD and SATMD were considered taking SSI into account. Based on that, two placement scenarios were proposed. A 40-story tall benchmark structure located on soft soil was selected. For generalizing settings, a filtered white noise was applied as an artificial earthquake to the main structure, and design parameters were optimized using the PSO algorithm. to evaluate of the optimum settings, two famous Kobe-1995 and Northridge-1994 earthquakes were used and the results were presented.

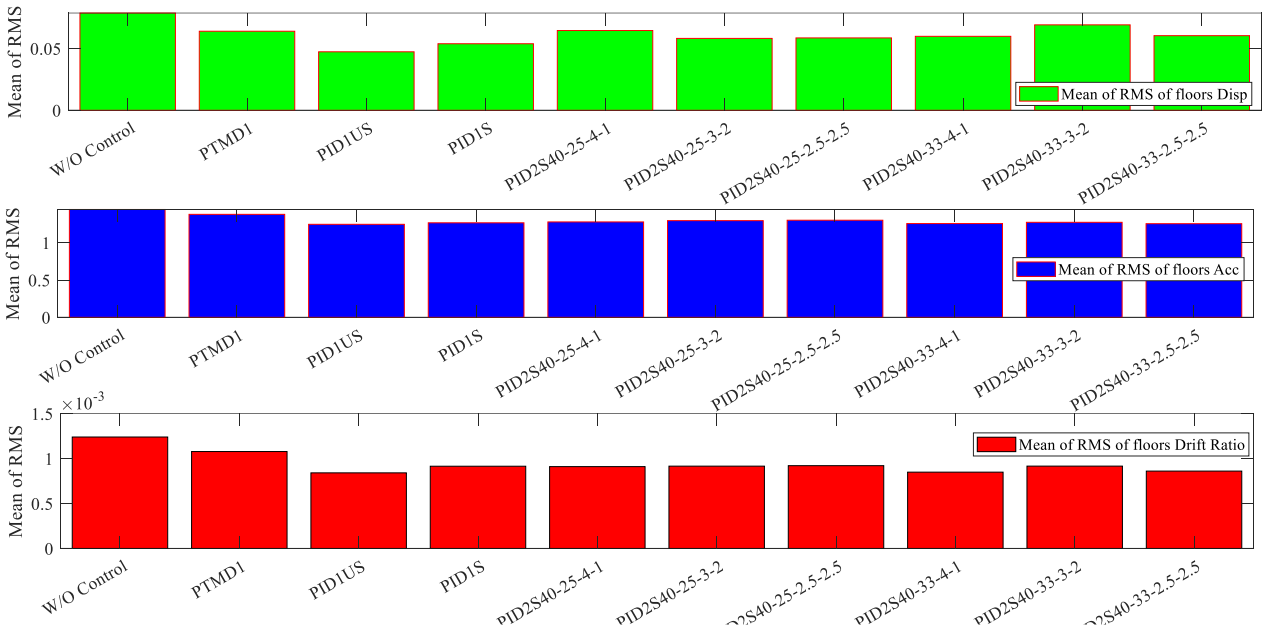

Fig. 10. Results of the mean of RMS of stories under the Kobe earthquake

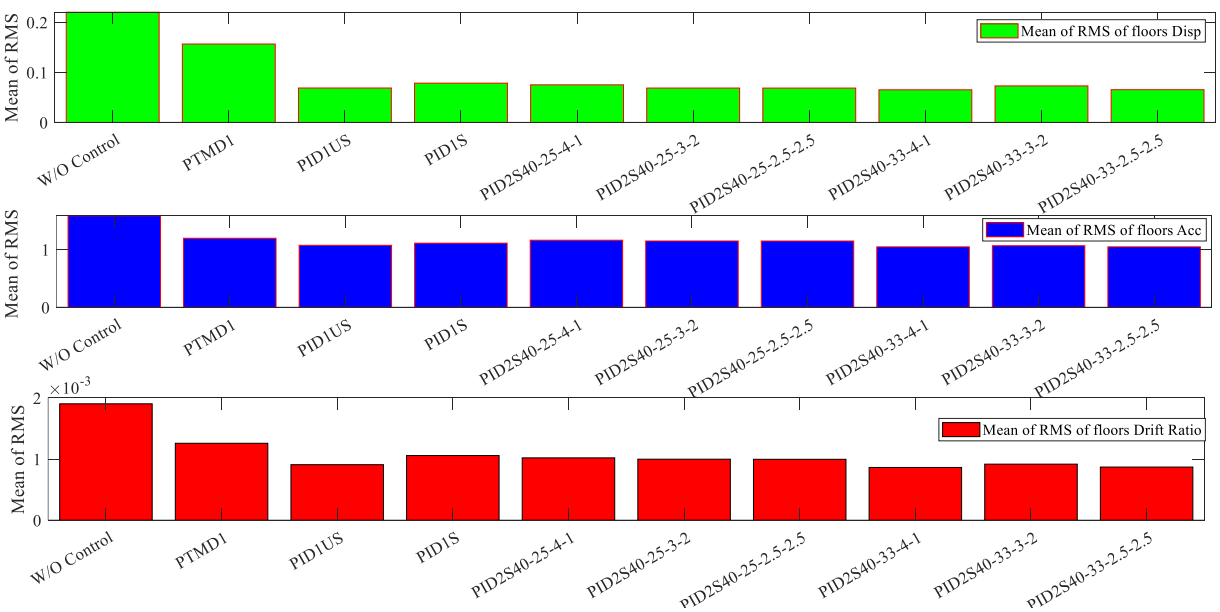

Fig. 11. Results of the mean of RMS of stories under the Newhall earthquake

The results of the application of the simultaneous tuning compared to non-simultaneous showed a significant decrease

in the responses, especially, for the structure equipped with SATMD and MATMD taking SSI into account. It can increase the potential for structural instability. Also, two different scenarios were suggested to evaluate placement control devices. The results of using MPTMD instead of SPTMD were almost unchanged, provided that the total mass of TMDs was limited to 5% of the total mass of the structure. Further, the application of MATMD with PID controller and simultaneous tuning led to a significant improvement in the responses. These responses contained the maximum displacement, maximum acceleration, and maximum drift ratio. Also, to examine the effectiveness, the results were compared with the state of SATMD and PID controller with non-simultaneous tuning. In addition, the RMS of the floors and the average RMS of the total floors were investigated. Its criterion was used to evaluate the performance of the system in reducing the responses during the time history. The results confirmed the higher effectiveness of the controller and MATMD with the proposed elevation placement in improving responses; The general evaluation of the results showed that MATMD with simultaneous tuning in case 40-33 had the best application. Also, these results confirmed the superiority of MATMD and the proposed placements compared with SATMD [4]. Furthermore, the proposed method reduced requirement costs, especially for the optimization process. At last, the results will help designers and researchers to gain a new design vision to find the optimal placement of control devices in tall buildings.

Funding:

The authors received no financial support.

Declarations:

Conflict of interest the authors declare that have no conflict of interest or competing interests.

REFERENCES

[1] Liu, Ming-Yi., Chiang, W.-L., Hwang, J.-H., and Chu, C.-R., "Wind-Induced Vibration of High-Rise Building with Tuned Mass Damper Including Soil–Structure Interaction." Journal of Wind Engineering and Industrial Aerodynamics, vol. 96, no. 6-7, pp. 1092-102, 2008.

[2] Chey, Min-Ho and Jae-Ung Kim. "Parametric Control of Structural Responses Using an Optimal Passive Tuned Mass Damper under Stationary Gaussian White Noise Excitations." Frontiers of Structural and Civil Engineering, vol. 6, pp. 267-80, 2012.

[3] Nigdeli, Sinan Melih and Gebrail Bekdaş. "Optimum Tuned Mass Damper Design in Frequency Domain for Structures." KSCE journal of civil engineering, vol. 21, pp. 912-22, 2017.

[4] Shahi, Mohammad., Sohrabi, M. R., and Etedali, S., "Seismic Control of High-Rise Buildings Equipped with Atmd Including Soil-Structure Interaction Effects." Journal of Earthquake and Tsunami, vol. 12, no. 03, p. 1850010, 2018.

[5] Etedali, Sadegh and Mohammad Shahi. "A Control Scheme for Amd in the Presence of Time-Delays and Ssi Effects for Tall Buildings." Structural Engineering and Mechanics, An Int'l Journal, vol. 79, no. 2, pp. 267-78, 2021.

[6] Samali, Bijan., Al-Dawod, B. M., Kwok, K. C., and Naghdy, F. "Active Control of Cross Wind Response of 76-Story Tall Building Using a Fuzzy Controller." Journal of engineering mechanics, vol. 130, no. 4, pp. 492-98, 2004.

[7] Warsewa, Alexander., Wagner, J. L., Böhm, M., Sawodny, O., and Tarín, C. "Decentralized Lqg Control for Adaptive High-Rise Structures." IFAC-PapersOnLine, vol. 53, no. 2, pp. 9131-37, 2020.

[8] Mac, Thi-Thoa and Hai-Le Bui. "Lqr Control Design in Vibration Control of a Benchmark Building Structure Subjected to Seismic Load." The AUN/SEED-Net Joint Regional Conference in Transportation, Energy, and Mechanical Manufacturing Engineering: Proceeding of RCTEMME2021, Hanoi, Vietnam, Springer, pp. 771-80, 2022.

[9] Jalali, Himan Hojat., Farzam, M. F., Gavgani, S. A. M., and Bekdaş, G. "Semi-Active Control of Buildings Using Different Control Algorithms Considering Ssi." Journal of Building Engineering, vol. 67, p. 105956, 2023.

[10] Huo, Linsheng et al. "Robust Control Design of Active Structural Vibration Suppression Using an Active Mass Damper." Smart materials and structures, vol. 17, no. 1, p. 015021, 2007.

[11] Park, SJ et al. "Numerical and Experimental Investigation of Control Performance of Active Mass Damper System to High-Rise Building in Use." Wind & structures, vol. 12, no. 4, pp. 313-32, 2009.

[12] Li, Zhijun and Hojjat Adeli. "New Adaptive Robust H∞ Control of Smart Structures Using Synchrosqueezed Wavelet Transform and Recursive Least-Squares Algorithm." Engineering Applications of Artificial Intelligence, vol. 116, p. 105473, 2022.

[13] Shariatmadar, Hashem and H Meshkat Razavi. "Seismic Control Response of Structures Using an Atmd with Fuzzy Logic Controller and Pso Method." Struct. Eng. Mech, vol. 51, no. 4, pp. 547-64, 2014.

[14] Lavassani, S. H. H., Ebadijalal,M., Shahrouzi, M., Gharehbaghi, V., Farsangi, E. N., and Yang, T., "Interpretation of Simultaneously Optimized Fuzzy Controller and Active Tuned Mass Damper Parameters under Pulse-Type Ground Motions." Engineering Structures, vol. 261, p. 114286, 2022.

[15] Zamani, A. A., Tavakoli, S., and Etedali, S. "Control of Piezoelectric Friction Dampers in Smart Base-Isolated Structures Using Self-Tuning and Adaptive Fuzzy Proportional–Derivative Controllers." Journal of Intelligent Material Systems and Structures, vol. 28, no. 10, pp. 1287-302, 2017.

[16] Etedali, S., Tavakoli, S., and Sohrabi, M. R. "Design of a Decoupled Pid Controller Via Mocs for Seismic Control of Smart Structures." Earthquakes and Structures, vol. 10, no. 5, pp. 1067-87, 2016.

[17] Kayabekir, A. E., Bekdaş, G., Nigdeli, S. M. "Control of Reinforced Concrete Frame Structures Via Active Tuned Mass Dampers." Proceedings of 7th International Conference on Harmony Search, Soft Computing and Applications: ICHSA 2022, Springer, 2022, pp. 271-77.

[18] Etedali, Sadegh., Zamani, A.-A., and Tavakoli, S. "A Gbmo-Based Piλdμ Controller for Vibration Mitigation of Seismic-Excited Structures." Automation in Construction, vol. 87, pp. 1-12, 2018.

[19] Seghir, Jaballah Mohamed., Bachir, N., Salaheddine, H.,

and Salim, G. "Hybrid Vibration Control of Structures Using Fractional Order Pi^¥Uplambda D^¥Upmu Pi Λ D M Controller." Artificial Intelligence and Heuristics for Smart Energy Efficiency in Smart Cities: Case Study: Tipasa, Algeria, Springer, pp. 569-77, 2022.

[20] Zamani, Abbas-Ali and Sadegh Etedali. "Optimal Fractional-Order Pid Control Design for Time-Delayed Multi-Input Multi-Output Seismic-Excited Structural System." Journal of Vibration and Control, vol. 29, no. 3-4, pp. 802-19, 2023.

[21] Akyürek, Osman. "Analysis of Different Placement Strategies of Multi-Tuned Mass Dampers Placed in Building Height." Arabian Journal for Science and Engineering, pp. 1-19, 2022.

[22] Etedali, Sadegh. "Probabilistic Study on Buildings with Mtmd System in Different Seismic Performance Levels." Structural Engineering and Mechanics, vol. 81, no. 4, pp. 429-41, 2022.

[23] Zhan, Wei., Cui, Y., Feng, Z., Cheung, K., Lam, J., and Gao, H. "Joint Optimization Approach to Building Vibration Control Via Multiple Active Tuned Mass Dampers." Mechatronics, vol. 23, no. 3, pp. 355-68, 2013.

[24] Huu, Thang Pham., Miura, N., and Iba, D. "Multi Active Tuned Mass Dampers for Earthquake-Induced Vibration Response Control of High Rise Building." Journal of Mechanical Science and Technology, vol. 36, no. 4, pp. 1655-66, 2022.

[25] Elias, Said., Matsagar, V., and Datta, T. "Distributed Tuned Mass Dampers for Multi-Mode Control of Benchmark Building under Seismic Excitations." Journal of Earthquake Engineering, vol. 23, no. 7, pp. 1137-72, 2019.

[26] Golnargesi, Siamak et al. "Seismic Control of Buildings with Active Tuned Mass Damper through Interval Type-2 Fuzzy Logic Controller Including Soil–Structure Interaction." Asian Journal of Civil Engineering, vol. 19, no. 2, pp. 177-88, 2018.

[27] Mishra, Abhishek., Shukla, A., Shukla, M., and Vanshaj, K. "Salp Swarm Optimization of Active Tuned Mass Dampers in Asymmetric Plan Buildings Including Ssi Effects." Asian Journal of Civil Engineering, vol. 24, no. 3, pp. 837-48, 2023.

[28] Etedali, Sadegh., Sohrabi, M. R., and Tavakoli, S. "Optimal Pd/Pid Control of Smart Base Isolated Buildings Equipped with Piezoelectric Friction Dampers." Earthquake Engineering and Engineering Vibration, vol. 12, pp. 39-54, 2013.

[29] Ulusoy, Serdar., Nigdeli, S. M., and Bekdaş, G. "Novel Metaheuristic-Based Tuning of Pid Controllers for Seismic Structures and Verification of Robustness." Journal of Building Engineering, vol. 33, p. 101647, 2021.

[30] Kennedy, James and Russell Eberhart. "Particle Swarm Optimization." Proceedings of ICNN'95-international conference on neural networks, vol. 4, IEEE, pp. 1942-48, 1995.

[31] Fourie, PC and Albert A Groenwold. "The Particle Swarm Optimization Algorithm in Size and Shape Optimization." Structural and Multidisciplinary Optimization, vol. 23, no. 4, pp. 259-67, 2002.

[32] Schutte, Jaco F and Albert A Groenwold. "Sizing Design of Truss Structures Using Particle Swarms." Structural and Multidisciplinary Optimization, vol. 25, pp. 261-69, 2003.

[33] Leung, Andrew Yee Tak and Haijun Zhang. "Particle Swarm Optimization of Tuned Mass Dampers." Engineering Structures, vol. 31, no. 3, pp. 715-28, 2009.

[34] Mohan, SC et al. "A Comparative Study on Crack Identification of Structures from the Changes in Natural Frequencies Using Ga and Pso." Engineering Computations, 2014.

[35] Khatir, Samir et al. "Multiple Damage Detection in Composite Beams Using Particle Swarm Optimization and Genetic Algorithm." Mechanics, vol. 23, no. 4, pp. 514-21, 2017.

[36] Ghannadi, Parsa et al. "The Application of Pso in Structural Damage Detection: An Analysis of the Previously Released Publications (2005–2020)." Frattura ed Integrità Strutturale, vol. 16, no. 62, pp. 460-89, 2022.

[37] Saidi, Hanane et al. "Energy Spectra of the Schrödinger Equation and the Differential Quadrature Method: Improvement of the Solution Using Particle Swarm Optimization." Applied mathematics and computation, vol. 182, no. 1, pp. 559-66, 2006.

[38] De Falco, Ivanoe et al. "Facing Classification Problems with Particle Swarm Optimization." Applied Soft Computing, vol. 7, no. 3, pp. 652-58, 2007.

[39] He, Qie and Ling Wang. "An Effective Co-Evolutionary Particle Swarm Optimization for Constrained Engineering Design Problems." Engineering Applications of Artificial Intelligence, vol. 20, no. 1, pp. 89-99, 2007.

[40] Leung, Andrew Yee Tak and Haijun Zhang. "Particle Swarm Optimization of Tuned Mass Dampers." Engineering Structures, vol. 31, no. 3, pp. 715-28, 2009.

[41] Shi, Yuhui and Russell Eberhart. "A Modified Particle Swarm Optimizer." 1998 IEEE international conference on evolutionary computation proceedings. IEEE world congress on computational intelligence (Cat. No. 98TH8360), IEEE, pp. 69-73, 1998.

[42] Eberhart, Russell C and Yuhui Shi. "Tracking and Optimizing Dynamic Systems with Particle Swarms." Proceedings of the 2001 congress on evolutionary computation (IEEE Cat. No. 01TH8546), vol. 1, IEEE, pp. 94-100, 2001.

[43] Mirzaei, Davoud and Saeid Amini. "Design a Novel Ultrasonic Horn Using Electro-Mechanical Circuit Method and Optimization Algorithm." International Journal of Industrial Electronics Control and Optimization, vol. 5, no. 3, pp. 269-77, 2022.

[44] Hosseini Lavassani, Seyed Hossein and Saman Shangapour. "Interval Type-2 Fuzzy Hybrid Control of a High-Rise Building Including Soil–Structure Interaction under near-Field and Far-Field Ground Motions." Structural Engineering International, vol. 32, no. 3, pp. 316-27, 2022.

[45] Arfiadi, Y., & Hadi, M. "Optimum placement and properties of tuned mass dampers using hybrid genetic algorithms." Iran University of Science & Technology, 1(1), 167-187, 2011.

[46] Alberto, P., Sala, A., & Olivares, M. " Fuzzy Logic Controllers. Methodology. Advantages and Drawbacks". In, 2015.

[47] Radmard Rahmani, H., & Könke, C. "Seismic control of tall buildings using distributed multiple tuned mass dampers." Advances in Civil Engineering, pp. 1-19, 2019.

[48] Azizi, M., Talatahari, S., & Sareh, P. (2022). Design optimization of fuzzy controllers in building structures using the crystal structure algorithm (CryStAl). Advanced Engineering Informatics, 52, 101616.

Mohammad Shahi was born in Iran in 1985. He received his B.Sc. degree in Civil Engineering from the Torbat Heydarieh University, Torbat Heydarieh in 2010 and his M.Sc. degree in Structural Engineering from University of Sistan and Baluchestan, Zahedan, Iran in 2017. He is a Ph.D. candidate in Structural Engineering at University of Sistan and Baluchestan , Zahedan. His current research interests include the structural control in smart structures.

Mohammad Reza Sohrabi received B.Sc., M.Sc. degrees in Civil Engineering from the University of Tehran, Tehran, Iran in 1984 and 1986 respectively. His current research interests include the structural control in smart structures. He received Ph.D. degree in structural engineering from University of Newcastle Upon Tyne in 1996. Currently, he is an associated professor at the Engineering Faculty of University of Sistan and Baluchestan, Zahedan, Iran. His research interests include structural contro l, Concrete structure s and structural dynamics.

Sadegh Etedali was born in Zahedan, Iran on January 2, 1983. Sadegh Received his Ph.D. degree in Structural Engineering from the University of Sistan and Baluchestan, Zahedan, Iran in 2014. After graduation, Sadegh Joined the Department of Civil Engineering at the Birjand University of Technology (BUT), Birjabd, Iran. He is currently an associate professor in the Department of Civil Engineering, BUT. Dr. Etedali has more than 8 years of experience in the field of structural vibration and control, soil - structure interaction, smart structures, soft computing, structural optimization, and structural reliability. He has published more than 80 scientific papers in journals and proceedings at national and international levels. He supervised/advised 15 M.Sc. and 5 Ph.D. students.

Abbas -Ali Zamani was born in Isfahan, Iran, in 1986. He received the B.Sc. degree in Electronic Engineering from Hakim Sabzevari University, Sabzevar, Iran 2009. He received the M.Sc. degree from Isfahan University of Technology, Isfahan, Iran 2011, and the Ph.D. degree from the University of Sistan and Baluchestan, Sistan and Baluchestan, Iran, in 2018, in Control Engineering. He is an Assistant Professor in the Department of Electrical Engineering, Technical and Vocational University, Isfahan, Iran. His research interests are Seismic Control, Power System Control, Smart grids, Renewable energies, and Artificial intelligence.

IECO

This page intentionally left blank.

International Journal Of
Industrial Electronics Control and Optimization
Print ISSN: 3517-2645
Online ISSN: 3568-2645
Homepage: https://ieco.usb.ac.ir/

Virtual Inertia Control and Small-Signal Stability Analysis of Electric Vehicle

Mehran Jami

Department of Electrical Engineering, Islamic Azad University, Marivan Branch, Marivan, Iran.[1], Department of Electrical
Corresponding author's email: mehran.jami8@gmail.com

Article Info

Article type:
Research Article

Article history:
Received: 24-July-2023
Received in revised form: 21-September-2023
Accepted: 26-October-23
Published online: 30-October-23

Keywords:
Electric Vehicle, Energy Storage System, Small-Signal Model, Stability, Virtual Inertia

ABSTRACT

In electric vehicles (EVs), the small size of the dc link capacitor results in significant voltage deviations when there are changes in load or uncertain fluctuations from the power resources. This causes a decline in voltage quality. To address the issue of low inertia, this study suggests the use of a fast-responding energy storage system, such as a supercapacitor (SC), which can replicate inertial responses through a specified control algorithm. A virtual capacitor and a virtual conductance are presented in this paper, which are implemented in the inner loop control, specifically the current loop control of SC, to effectively emulate inertia and damping and improves the battery lifetime by reducing the rate of charge and discharge. To assess the stability of the EV, a comprehensive small-signal model is developed, and the acceptable range of inertia response parameters is determined through eigenvalues analysis of the system. Numerical simulations are conducted to demonstrate the performance of the proposed control structure.

I. Introduction

The energy storage system utilized in electric or hybrid vehicles remains a major challenge due to its high cost, limited range, and slow recharge times. Therefore, the primary focus for advancing electric vehicles lies in enhancing onboard energy storage systems to improve range, size specifications, and lifespan [1]. The concept of electric vehicles (EVs) emerged with various energy storage devices such as batteries, fuel cells (FCs), and ultracapacitors (UCs) or supercapacitors (SCs). Modification of these EVs led to the development of hybrid electric vehicles (HEVs), combining the aforementioned sources to enhance efficiency and ensure uninterrupted power supply in vehicles [2]. A combination of fuel cell and battery is proposed in [3]. A similar study on SC and fuel cell is proposed in [4] and a study on fuel cell, SC and battery is proposed in [5]. Energy sources are fully responsible for supplying the required load of hybrid electric vehicles (HEVs) at different voltage levels according to different vehicle speeds. To ensure the correct operation of electronic equipment, it is necessary to adjust the main DC bus voltage. Power converters play a vital role in transportation industry to achieve dynamic voltage regulation and maintain coupling between energy sources and three-phase induction motor. Therefore, various types of power converters have been presented in the past. Many control algorithms for HEV energy management and control have been proposed in previous studies. For efficient energy management, predictive controllers have been proposed for energy control among fuel cells, SC, and batteries [6]. A fuzzy logic controller based on genetic algorithms is introduced to improve the performance and fuel economy of his fuel cell-based HEV [7]. Adaptive fuzzy logic-based controllers are used for energy management in his fuel cell and battery-based HEVs, controlling performance and maintaining battery state of charge [8]. Additionally, a predictive control model was introduced to improve battery performance and prevent battery and fuel cell degradation [9]. According to the various methods that have been presented in the field of using energy storage resources in a hybrid electric vehicle and its control, it is clear that in

these methods, the control objectives considered include improving the inertia of the DC microgrid in the form of reducing the rate of change of voltage (RoCoV) immediately after the change, the increase in DC link voltage response damping, and also the improvement of DC microgrid stability in the presence of constant power loads (CPLs), have not been studied at the same time.

The electric vehicle is an unconventional power system that differs from traditional ones with rotating machines. It is a DC microgrid (DC-MG) that is predominantly controlled by power electronics and can operate independently. By integrating electric vehicles with local renewable sources and loads, the foundation for microgrids involving EVs can be established [10]. The presence of native DC sources like photovoltaic systems and EV batteries facilitates the creation of DC microgrids, which have a shared DC link and can connect to the AC low-voltage network of the local distributor [11]. The inclusion of a bidirectional DC converter (Bi-C) is crucial in linking parallel-energy storage units (ESUs) to the dc buses and achieving voltage conversion. This design characteristic renders the EV a system without inertia [12]. Furthermore, from the perspective of the source bus, a power electronic converter behaves like a constant power load when it precisely regulates its output voltage with a resistance load. Despite having a negative incremental impedance, the CPL has a positive instantaneous impedance. As a result, the system's damping is reduced and its susceptibility to oscillation is increased [13]. In summary, the stability of EV, like other islanded DC-MGs, is at risk due to its negative impedance and low inertia characteristics [14]. This poses a challenge to the reliable and convenient power supply for EVs, ultimately impeding the widespread adoption of electric vehicles. Consequently, it is necessary to enhance the dynamic voltage stability of EV in order to ensure efficient and high-quality charging of EVs [15]. A suggestion has been made in [16] to improve the frequency stability of an islanded MG by using a hybrid ESS (HESS) consisting of both a SC and an electric vehicle battery. Authors in [17] present a method for frequency stabilization of the utility grid by modulating the power level of an inductive electric vehicle charger supplied by the grid. To replace the greater damping coefficient, Huang *et al.* [18] create a dynamic virtual impedance (DVI) based on the damping mechanism of the damping torque analysis. A modified droop control method using Neuro-Fuzzy Inference System (ANFIS) [19] and fuzzy logic [20] are designed based on the inertia injection, which injects adaptive virtual inertia instead of modeling the constant inertia. The work mentioned above, however, focuses on AC-MG rather than DC-MG. A simple method to improve system inertia in DC-MG, such as EV, is adding extra capacitors. These capacitors utilize their stored energy to counteract the rapid fluctuations in voltage. However, it should be noted that while this approach enhances system performance, it also requires additional investment and poses challenges in terms of limited space availability [15]. In [21], the virtual inertia is adaptively adjusted to enhance the stability of the DC-MG by establishing the relationship between the inertia coefficient and rate of change of voltage. In [15], strategies for enhancing the dynamic stability and ensuring a high-quality power supply for electric vehicles are discussed. These strategies, known as inertia droop control (IDC), are specifically designed for bidirectional dc converters. Unlike the virtual inertia and damping control (VIDC), the proposed IDC offers a simpler solution by making slight modifications to the conventional droop control method, eliminating the need for intricate control structures. In comparison to the VIDC discussed in previous literature [22], which was derived using a complex machine model, the simplified control structure of the inertia droop control (IDC) offers greater convenience for practical application and promotion in DC-MG. Additionally, IDC also addresses the voltage deviation issue inherent in droop control, a problem that was not previously considered in the literature The stability mechanism of VIDC has not been extensively explored in previous literature. Typically, the impedance-based method is used to investigate stability mechanisms and evaluate voltage stability [23]. In [22], a feedback analytic approach is introduced to analyze the PD caused by virtual DC machine control, which explains how the voltage behaves when subjected to disturbance current. However, this approach still relies on impedance-based analysis, solely focusing on the port characteristics. The stability of a DC network designed for electric vehicle charging stations (EVCSs) was examined by the authors of [24]. The purpose of this investigation is to provide general recommendations for network planning by demonstrating how the interconnection of EVCSs may affect the stability of the DC network.

According to the various methods that have been presented in the field of using energy storage resources in an electric vehicle and its control, it is clear that in these methods, the control objectives considered include improving the inertia of the DC network in the form of reducing the rate of change of voltage immediately after the change, the increase in DC link voltage response damping, and also the improvement of DC network stability in the presence of CPLs, have not been studied at the same time. Therefore, this research gap is covered in this study. To address the gaps in the existing literature, a virtual impedance control loop including virtual capacitor and virtual resistance by using the virtual inertia concept is proposed in this paper. The salient features of this work can be summarized as:

- Comprehensive modeling of an electric vehicle in the form of a DC microgrid including distributed generation sources, interface converters and loads connected to a common DC link.

- Small signal stability analysis of DC microgrids independent from the main grid considering CPLs and proposed virtual inertial control.
- Investigating the influence of CPLs on the stability of low frequency dominant modes of the studied DC microgrid.
- Improving the dynamic behavior of common DC link voltage by using the proposed virtual inertial control loop.
- The use of SC as a suitable source of energy storage for quick injection of virtual inertia immediately after disturbance.
- The size of capacitors in EV is usually small, because these elements have a large impact on short-circuit current, system reliability, and control system complexity. The use of large capacitors causes problems in the field of fault detection, fault isolation and system protection. Also, the use of large capacitors increases the cost, weight, and volume of the entire system. Increasing the DC link capacitor virtually, using energy storage source and appropriate control method is investigated as the main goal of this research.

The rest of this paper is organized as follows. In Section II, the proposed structure of electric vehicle is introduced. Section III describes the small-signal model of electric vehicle. The stability analysis of the system in the presence of the proposed controller are presented in Section IV. Simulation results are presented in Section V and Section VI concludes the paper.

II. Structure of The Proposed electric Vehicle

Fig. 1 shows the structure of the electric electrical vehicle studied in this research. The battery and SC units are charged or discharged according to the power requirements and working conditions of the vehicle. The solar panel is also controlled based on the tracking of the maximum power point and according to the weather conditions, the maximum power can be produced. The loads in the vehicle are divided into three general categories. The main part of the energy consumed in the car is related to the wheels and the propulsion power that moves the vehicle. For this purpose, we have considered four three-phase induction motors that are placed on the wheels, and connected to the AC link. Other non-motorized AC loads are also assumed to be connected to the AC link. Other loads are considered as DC loads which are connected to the DC link of the system. In order to better control and manage energy consumption each of the auxiliary energy sources is used to connect to the common DC link from an interfaced power electronic converter. In the following, we will study each of these parts in more detail and examine the different working modes of the vehicle.

A. Battery Unit

Lithium-ion batteries with high energy density are the best choice for storing energy in electric vehicles. However, the high charging and discharging cycles that is required during the operation of the vehicle reduces the life of the battery. The

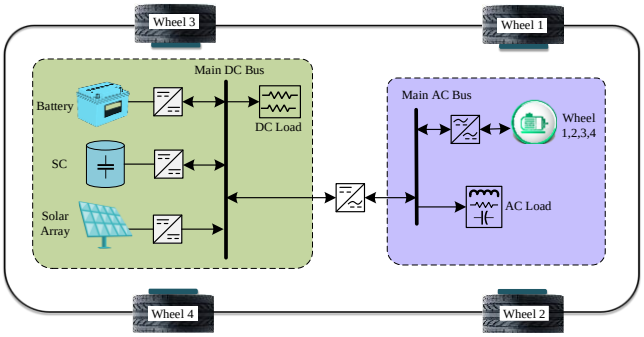

Fig. 1. Structure of the proposed eelctric vehicle.

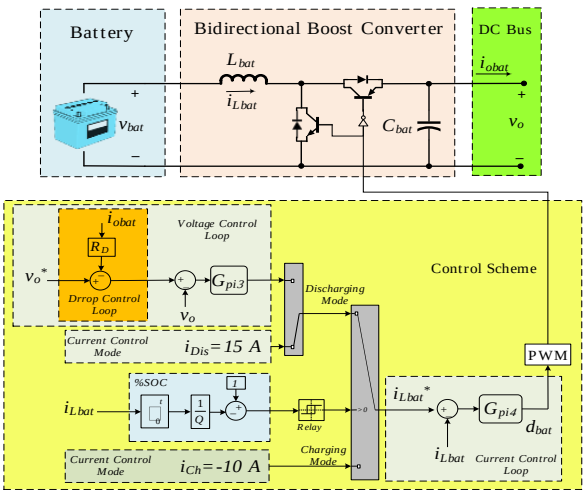

Fig. 2. Configuration and control diagram of battery unit.

main structures for connecting energy storage sources to the DC link are divided into two categories: 1) passive structure and 2) active structure. The passive structure has the simplest structure in which the sources are directly connected to the DC link without an intermediary, and the degree of freedom of its control is zero, and no control algorithm is used in this structure. The charging and discharging control of each power source is obtained based on the value of internal resistance of them. In this method, the battery and other energy sources cannot be used effectively. Although this method is simple and inexpensive, its efficiency is often far from expected. In the active structure, a DC-DC interface converter is used to connect the battery to the DC link. Another great advantage of this interface boost converter is the ability to create a variable DC link voltage. The battery interfaced converter is bidirectional, which makes the power return to the battery in braking mode and charges the battery through the high voltage DC link. In the powertrain of electric vehicles, the output voltage of the battery is in the range of 800 V. The proposed power and control systems for the battery unit is shown in Fig. 2. In general, the battery operates in charging or discharging modes. By calculating the state of charge (SOC), it is determined whether the battery has enough charge or not. If the battery charge is less than the specified range, the charging

mode is activated and it is charged through the DC link and other sources connected to this link. In this case, the battery operates in the current control mode with a fixed current value and remains in this mode until it reaches the specified full charge level. When the battery is fully charged, it goes into discharge mode. According to the system conditions, the battery can be operated in current control or voltage control mode. In the current control mode, the battery is discharged with a constant current and the main DC voltage will be controlled by other units. In addition, if the main source, i.e., the internal combustion engine, is turned off and the vehicle works in full electric mode, the battery operates in voltage control mode and it is responsible for controlling the DC link voltage.

B. Supercapacitor Unit

With the rapid expansion of electric vehicle applications in recent decades, the dynamic performance, cost, and durability of hybrid vehicles still largely depend on the design, component integration, and control of energy storage systems. The high price and short lifetime of pure battery systems are the biggest obstacles to the further adoption of electric vehicles. Energy storage systems are the main components of electric vehicles, which have a great impact on efficiency, driving distance and performance of vehicles. In electric vehicle the size of the battery is obtained based on the characteristics of the vehicle driving distance. The power density of batteries is very low compared to their energy density, and their equivalent series resistance is in the range of several hundred milliohm. Therefore, operating the battery at high power may cause large losses and shorten the lifespan. A simple solution to increase power capacity and reduce losses in energy storage systems is to use a larger battery pack. Although the energy capacity required to transport passengers is close to 100 kWh, a trade-off between weight, driving distance, performance and cost must be considered. Doubling the size of the batteries does not necessarily lead to a linear increase in the driving distance [25]. A solution that prevents the installation of large battery sets is the use of hybrid storages, which a source with high power density is used together with a high energy density battery. SC are the most developed technology in high power, short consumption and light weight applications due to their power density several thousand times larger than lithium-ion batteries. They are less exposed to extreme temperature increase and can be easily connected to power electronic converters in the propulsion system. The design of the battery pack is based on the energy required to travel a certain distance and the capacitor bank is designed as a power source to provide acceleration and power requirements. Fig. 3 shows the structure of the SC, bidirectional DC-DC interface converter, and its control system. The SC is connected to the common DC link through the power electronic converter. To show the generality of the proposed control method and is not dependent on the type of interface converter, two different DC-DC converters, buck and boost interface have been studied. The converters under study are considered to be bidirectional so that they pass current in both directions and the SC works well in charge and discharge modes. The proposed control circuit consists of three different loops. The voltage control loop is responsible for regulating the voltage of the SC and returns it to the nominal value in the charging and discharging modes. The proposed control loop is a virtual inertial loop. In DC microgrids, the size of the DC link capacitor is too small to provide inherent inertia to the system. As a result, in case of load changes or power fluctuations on the side of production sources, large and rapid voltage changes will occur in the DC link, which leads to a decrease in the quality of the system voltage. Energy storage systems are used to provide better performance, improved inertia and dynamic stability of the electric vehicle.

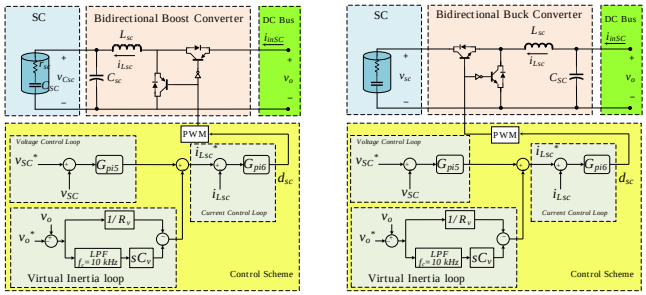

(a) (b)

Fig. 3. Configuration and control diagram of SC unit, a) interface boost converter, b) interface buck converter

C. PV Unit

The output power generated from the solar panel is very low to drive the powertrain in electric vehicle. Therefore, solar energy is used as an auxiliary source to reduce energy consumption from batteries and fuel sources and is used to charge batteries when needed. Evaluating the installation of solar arrays on the roof of cars, tracking the maximum power point to quickly track changes in conditions, and analyzing the effects of solar panels on improving the distance traveled are the challenges that exist in the development of solar panel-based car applications. In [26], the authors have presented the fuel cell/battery/solar panel structure in which the maximum power point tracking algorithm has not been considered. Therefore, for better performance of the solar panel and tracking the maximum power point (MPP), a unidirectional boost converter has been used. By applying the appropriate control method, the solar cell works at a specific voltage and current where the output power of the system is maximum for a given conditions. Fig. 4 shows the structure of the PV, unidirectional DC-DC interface converter, and its control system.

D. AC and DC Loads

The loads in electric vehicle can be considered as direct current (DC) loads connected to the common DC link and

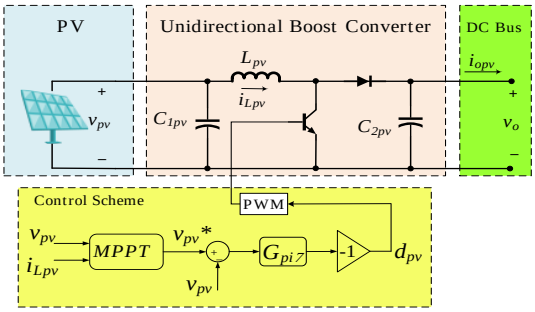

Fig. 4. Configuration and control diagram of PV unit.

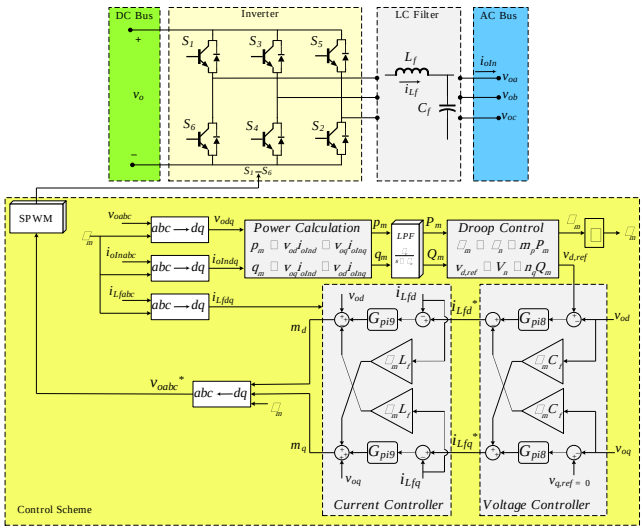

Fig. 5. Configuration and control diagram of inverter unit.

alternating current (AC) loads connected to the AC link. Most of the energy in hybrid cars is consumed by AC loads or the induction motors installed inside the wheels, which are responsible for moving the vehicle. In addition to this, there are internal loads and other loads when the cars are in parking mode and their collection provides the camp's energy needs in the form of a microgrid. Therefore, the existing loads are divided into two parts: motor loads and fixed impedance loads. The constant impedance loads connected to the DC link are assumed as pure resistance and the constant impedance loads connected to the AC link are assumed to be a combination of resistance, inductor and capacitor in series. An inverter with sinusoidal pulse width modulation is used to create an AC link with controllable constant voltage and frequency. By applying a suitable control method, the DC input of the inverter, which is connected to the DC link, is converted into a three-phase sine wave form with a certain voltage and frequency, and makes a controllable three-phase AC link available, which can be used to drive motors through this link. The three-phase induction fed the wheels as well as other AC loads. Fig. 5 shows the structure of the inverter and its related control circuit.

III. Small-Signal Modeling of Electric Vehicle

In this section, a detailed small-signal model of the EV system is obtained to demonstrate the effectiveness of the proposed method and to investigate the behavior of the system in the presence of energy storage devices and loads. In terms of small-signal stability, hybrid vehicle operation in pure electric mode is the worst-case scenario. Therefore, small-signal stability analysis has been investigated for this mode. Also, in this section, without loss of generality and for the simplicity of calculations, the internal resistances of the inductor and the line have been neglected.

A. Small-Signal Model of The Battery Unit

For the bidirectional boost converter between source bus (360 V) and main dc bus (800V) if the switch turns on, it yields

$$\begin{cases} L_{bat}\dfrac{di_{Lbat}}{dt} = v_{bat} \\ C_{bat}\dfrac{dv_o}{dt} = -i_{obat} \end{cases} \quad (1)$$

where i_{Lbat}, v_o and i_{obat} are the inductor current, the output voltage, the output current, respectively. If the switch turns off, it yields

$$\begin{cases} L_{bat}\dfrac{di_{Lbat}}{dt} = v_{bat} - v_o \\ C_{bat}\dfrac{dv_o}{dt} = i_{Lbat} - i_{obat} \end{cases} \quad (2)$$

By using state-space averaging, the state-space function is derived as

$$\begin{cases} L_{bat}\dfrac{di_{Lbat}}{dt} = v_{bat} - (1-d_{bat})v_o \\ C_{bat}\dfrac{dv_o}{dt} = (1-d_{bat})i_{Lbat} - i_{obat} \end{cases} \quad (3)$$

where d_{bat} is the duty cycle for on-state of the switch. Based on the results given in (3), the small-signal model is achieved as

$$\begin{cases} L_{bat}\dfrac{d\hat{i}_{Lbat}}{dt} = \hat{v}_{bat} - D'_{bat}\hat{v}_o + \hat{d}_{bat}V_o \\ C_{bat}\dfrac{d\hat{v}_o}{dt} = D'_{bat}\hat{i}_{Lbat} - \hat{d}_{bat}I_L - \hat{i}_{obat} \end{cases} \quad (4)$$

where the variables appear in capital letter represent the steady-state values and the variables with "^" indicate the small-signal deviation. Meanwhile, $D'_{bat}=(1-D_{bat})$ By considering the control diagram in Fig. 3 and assuming power sharing loop is off ($R_d = 0$), the small signal model in frequency domain is achieved

$$\hat{d}_{bat}(s) = \hat{v}^*_o(s)G_{pi3}G_{pi4} - \hat{v}_o(s)G_{pi3}G_{pi4} - \hat{I}_{Lbat}(s)G_{pi4} \quad (5)$$

By integrating the two equations (4) and (5) it yields

$$\hat{v}_o(s) = G_{11}.\hat{v}_{bat}(s) + G_{12}.\hat{v}^*_o(s) - Z_{o1}.\hat{i}_{obat}(s) \quad (6)$$

where

$$G_{11} = \frac{D'_{bat} + I_{Lbat}G_{pi4}}{T_1}, Z_{o1} = \frac{L_{bat}s + V_{bat}G_{pi4}}{T_1},$$

$$G_{12} = \frac{(V_oD'_{bat} - I_{Lbat}L_{bat}s)G_{pi3}G_{pi4}}{T_1}$$

$$T_1 = D_{bat}^{\phi\,2} + L_{bat}C_{bat}s^2 + G_{pi3}G_{pi4}(V_o D_{bat}^{\phi} - I_{Lbat}L_{bat}s) + G_{pi4}(V_o C_{bat}s + D_{bat}^{\phi} I_{Lbat}). \quad (7)$$

For the bidirectional boost converter used for SC, the analysis is presented in the next subsection.

B. Small-Signal Model of The Supercapacitor Unit

For the bidirectional boost converters used for SC, the converter topology is shown in Fig. 3. In order to avoid repetition, no detailed procedure is shown below. By using the similar procedure in III-A, one can obtain the final small-signal model of the boost converter as

$$\begin{cases} L_{SC}\dfrac{d\hat{i}_{Lsc}}{dt} = D_{SC}\hat{v}_o + V_o\hat{d}_{sc} - \hat{v}_{Csc} \\ C_{sc}\dfrac{d\hat{v}_{Csc}}{dt} = \hat{i}_{LSC} - \hat{i}_{SC} \\ C_{SC}\dfrac{d\hat{v}_{CSC}}{dt} = \hat{i}_{SC} \\ \hat{i}_{inSC} = D_{SC}\hat{i}_{LSC} + I_{LSC}\hat{d}_{sc}, \hat{i}_{SC} = \dfrac{\hat{v}_{Csc} - \hat{v}_{CSC}}{r_{SC}} \end{cases} \quad (8)$$

where i_{Lsc}, v_{CSC}, v_{Csc} and d_{sc} are the inductor current, the SC voltage, the capacitor voltage, the duty cycle for on-state of the switch, respectively. A virtual capacitance and resistance control strategy is implemented in inductor current loop as follows

$$\hat{i}_{LSC}^{\ *} = C_v\frac{d\hat{v}_o}{dt} + \frac{1}{R_v}\hat{v}_o \quad (9)$$

where C_v and R_v are the virtual capacitance and virtual resistance, respectively. Because the proposed control is at the inner current control loop, it needs to be faster than the outer voltage level control. This control also ensures a rapid response to changes in load, providing fast inertia response. The equation (9) demonstrates that the rate of voltage change ($d\hat{v}_o/dt$) and voltage deviation ($\hat{v}_o$) decrease when $C_v>0$ and $0<R_v<1$ during load changes. This leads to an improvement in the inertia and damping of the EV. Fig. 3 illustrates the implementation of the proposed inertia response control loop within the inner current control loop. However, it should be noted that the pure differentiation of the virtual capacitance in the proposed inertia response strategy may introduce unwanted high frequency noises to the system. A first-order low-pass filter (LPF) is constructed in series with the virtual capacitance feedback to solve this problem. By considering the control diagram in Fig. 3, the small signal model in frequency domain is achieved

$$\hat{d}_{sc}(s) = \hat{v}_o(s)G_{pi6}(C_v sG_{LPF} + 1/R_v) - \hat{i}_{LSC}(s)G_{pi6} - \hat{v}_o^*(s)G_{pi6}(C_v sG_{LPF} + 1/R_v) - \hat{v}_{Csc}(s)G_{pi5}G_{pi6} \quad (10)$$

By analyzing the simultaneous equations of (8) and (10), it yields

$$\hat{v}_o(s) = G_{21}.\hat{v}_o^*(s) + Z_{in,SC}\hat{i}_{inSC}(s) \quad (11)$$

where

$$G_{21} = \frac{V_o G_{pi6}\left(C_v sG_{LPF} + 1/R_v\right)}{T_3},$$
$$Z_{in,SC} = \frac{(L_{SC}s + V_o G_{pi6})T_2 + (1 + r_{SC}C_{SC}s)(1 + V_o G_{pi5}G_{pi6})}{T_2 T_3 D_{SC}} \quad (12)$$
$$T_2 = (C_{sc} + C_{SC})s + r_{SC}C_{sc}C_{SC}s^2$$
$$T_3 = D_{SC} + V_o G_{pi6}\left(C_v sG_{LPF} + 1/R_v\right).$$

For the unidirectional boost converter used for PV, the analysis is presented in the next subsection.

C. Small-Signal Model of The PV Unit

For the unidirectional boost converters used for PV, the converter topology is shown in Fig. 4. In order to avoid repetition, no detailed procedure is shown below. By using the similar procedure in III-A, one can obtain the final small-signal model of the boost converter as

$$\begin{cases} L_{pv}\dfrac{d\hat{i}_{Lpv}}{dt} = \hat{v}_{pv} - D_{pv}^{\phi}\hat{v}_o + V_o\hat{d}_{pv} \\ C_{2pv}\dfrac{d\hat{v}_o}{dt} = D_{pv}^{\phi}\hat{i}_{Lpv} - I_{Lpv}\hat{d}_{pv} - \hat{i}_{opv} \\ C_{1pv}\dfrac{d\hat{v}_{pv}}{dt} = -\dfrac{1}{r_{pv}}\hat{v}_{pv} - \hat{i}_{Lpv} \end{cases} \quad (13)$$

where i_{Lpv}, i_{opv}, r_{pv} and d_{pv} are the inductor current, the output current, the output resistance of PV, the duty cycle for on-state of the switch, respectively. By considering the control diagram in Fig. 4, the small signal model in frequency domain is achieved

$$\hat{d}_{pv}(s) = -\hat{v}_{pv}^*(s)G_{pi7} + \hat{v}_{pv}(s)G_{pi7} \quad (14)$$

By analyzing the simultaneous equations of (13) and (14), it yields

$$\hat{v}_o(s) = G_{31}.\hat{v}_{pv}^*(s) - Z_{o2}.\hat{i}_{opv}(s) \quad (15)$$

where

$$G_{31} = I_{Lpv}G_{pi7} - T_4 V_o G_{pi7}, Z_{o2} = \frac{1}{C_{2pv}s + T_4 D_{pv}^{\phi}}$$
$$T_4 = \frac{D_{pv}^{\phi}(C_{2pv}s + 1/r_{pv}) + I_{Lpv}G_{pi7}}{1 + V_o G_{pi7} + L_{pv}s(C_{2pv}s + 1/r_{pv})} \quad (16)$$

For the AC load connected to inverter, the analysis is presented in the next subsection.

D. Small-Signal Model of The Inverter

The single-phase equation of a three-phase system can be obtained on the output side of the inverter, including the three-phase input voltage, the filter consists of an inductor and a capacitor, and the motor load is a resistive-inductive load as follows

$$\begin{cases} L_f \dfrac{di_{La}}{dt} = v_a - v_{ca} \\ C_f \dfrac{dv_{ca}}{dt} = i_{La} - i_{oa} \\ L_o \dfrac{di_{oa}}{dt} = v_{ca} - R_o i_{oa} \end{cases} \tag{17}$$

where L_f , C_f , L_o , R_o , i_{La} , v_a , v_{ca} , and i_{oa} are the filter inductance, the filter capacitance, the load inductance, the load resistance, the filter inductance current, the filter capacitance voltage, the input voltage and the load current, respectively. According to Fig. 5 and using circuit laws, Park transformation, and Taylor series-based linearization, A state space representation can be given as follows

$$\begin{aligned} \dot{X} &= AX + B_1 \hat{V}_o \\ Y &= CX + D\hat{V}_o \end{aligned} \tag{18}$$

where

$$\begin{aligned} X &= \begin{bmatrix} \hat{i}_{Ld} & \hat{i}_{Lq} & \hat{v}_{cd} & \hat{v}_{cq} & \hat{i}_{od} & \hat{i}_{oq} & \hat{a}_1 & \hat{a}_2 & \hat{a}_3 & \hat{a}_4 \end{bmatrix}^T \\ B_1 &= \begin{bmatrix} \dfrac{M_d}{2L_f} & \dfrac{M_q}{2L_f} & 0 & 0 & 0 & 0 & 0 & 0 & 0 & 0 \end{bmatrix}^T \\ C &= \frac{3}{2V_o} \begin{bmatrix} 0 & 0 & I_{od} & I_{oq} & V_{cd} & V_{cq} & 0 & 0 & 0 & 0 \end{bmatrix} \\ D &= -\frac{I_{in,IN}}{V_o} \end{aligned} \tag{19}$$

By analyzing the simultaneous equations of (18) and (19), it yields

$$\hat{i}_{in,IN}(s) = \frac{1}{Z_{in,In}} \hat{v}_o(s) \tag{20}$$

where

$$Z_{in,IN} = \frac{\hat{V}_o}{\hat{i}_{in,IN}} = \left[C\left(sI - A\right)^{-1} B_1 + D \right]^{-1} \tag{21}$$

By summarizing the results in (6), (11), (15) and (20), the small-signal model of the multistage configuration of electric vehicle is obtained, as shown in Fig. 6. The closed-loop transfer function between the main DC bus voltage and the load current is obtained as

$$TF(s) = \frac{\hat{v}_o(s)}{\hat{i}_{Load}(s)} = \frac{-1}{Z_{o1}^{-1} + Z_{o2}^{-1} + Z_{in,SC}^{-1} + Z_{in,IN}^{-1} + R_L^{-1}} \tag{22}$$

IV. Stability Analysis and Parameter Selection

In this section, small-signal stability of the hybrid vehicle, is studied via analysis of the system eigenvalues using the transfer function derived in (22). Therefore, for AC load and the proposed control strategy, there are three parameters to be considered, namely, active power (R_o), virtual resistance (R_v), the virtual capacitance (C_v). The system parameters are given in Table I and Table II. The active power load connected to the inverter has a negative effect on the damping of the system. In Fig. 7, the eigenvalues of the entire system are plotted when R_o decreases. By decreasing R_o, damping ratio of the complex conjugate eigenvalues (λ_3 and λ_4) continual decrease, so the system is more prone to low-frequency oscillation. The selected R_o should ensure the stable operation of the whole system, i.e., all the dominant poles are located in left side of s domain. Therefore, the acceptable rang is $1.5 < R_o$. For load resistance values less than $R_o = 1.5\ \Omega$, the system becomes unstable. In Fig. 8(a), the eigenvalues of the entire system are plotted when C_v increases. By increasing C_v, damping ratio of the complex conjugate eigenvalues (λ_1 and λ_2) continual decrease, so the system is more prone to low-frequency oscillation. The selected C_v should ensure the stable operation of the whole system, i.e., all the dominant poles are located in left side of s domain. Therefore, the acceptable rang is $0 < C_v < 0.004$ (for $R_v = 8$). Fig. 8(b) shows the trajectory of dominant poles when R_v decreases from 50 to 0.5. By increasing $1/R_v$, the damping factor of the system is improved. As it is observed, there is also an inflection point for the virtual resistance in the system root-locus diagram. Therefore, the inflection point of system root-locus will be the optimal one for R_v, namely,

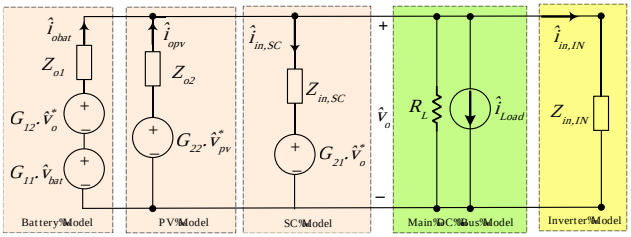

Fig. 6. Small-signal model of electric vehicle.

TABLE 1
SYSTEM PARAMETERS OF THE HYBRID VEHICLE

system	Parameters	Values	Parameters	Values
PV system	L_{pv}	5mH	v_{pv}	109.4V
	C_{1pv}	0.1 mF	C_{2pv}	0.5mF
Battery system	L_{bat}	50 mH	V_{bat}	360V
	C_{bat}	0.1 mF	V_{Cbat}	800V
SC system	L_{SC}	10 mH	V_{SC}	250V
	C_{SC}	0.01 F	C_{sc}	0.5 mF
Inverter	L_f	5 mF	$v_{o,abc}$	220V-AC
	C_f	1 mF	V_n	311.12V
	ω_n	100π	m_p , n_q	0, 0
AC Load	L_o	17.7 mH	R_o	28 Ω
DC Load	R_L	128Ω	Load power	5 kW

TABLE 2
CONTROLLER PARAMETERS OF THE HYBRID VEHICLE

system	Parameters	Values	Parameters	Values
Battery system	K_{p3}	0.1	K_{i3}	7
	K_{p4}	0.1	K_{i4}	30
SC system	K_{p5}	0.6	K_{i5}	5
	K_{p6}	0.1	K_{i6}	15
PV system	K_{p7}	0.01	K_{i7}	2
inverter	K_{p8}	1	K_{i8}	50
	K_{p9}	1	K_{i9}	30

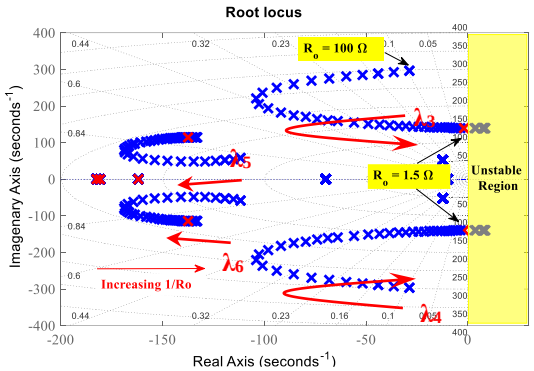

Fig. 7. Trace of the dominant poles for varying R_o

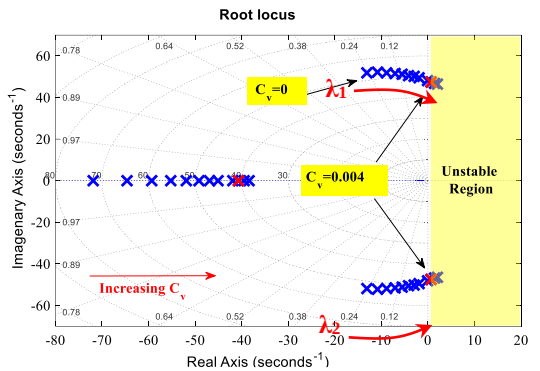

(a)

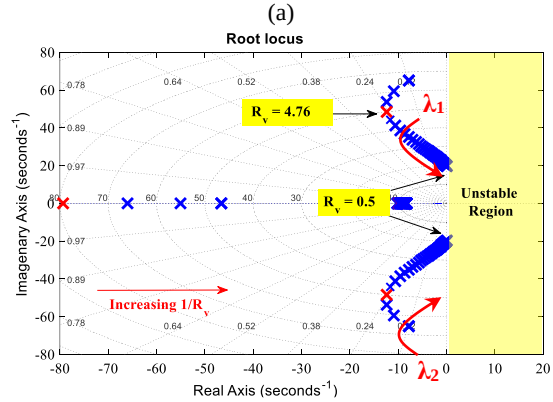

(b)

Fig. 8. Trace of the dominant poles for: (a) varying C_v while R_v=8, (b) varying R_v while C_v=0.001

R_v=4.76.

V. Simulation Results

In order to validate the effectiveness of the proposed virtual inertia control, the EV system, is simulated in MATLAB/Simulink. The system parameters can be found in Table I and Table II. The battery employs a bidirectional boost converter to establish the regulated main DC bus through control loops. The main DC bus and SC voltage are regulated at the rated value of 800 V and 250 V, respectively. It is assumed that a DC load with power rate of 5kW is directly connected to the main DC bus. the man AC bus is controlled at 220 V-rms and 50Hz and 5kW and 1 kvar AC load is connected to the main AC bus. Fig. 9 shows the main dc bus

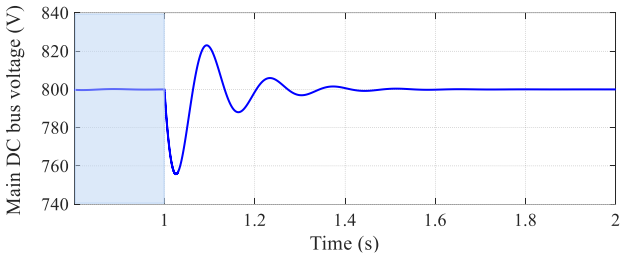

(a)

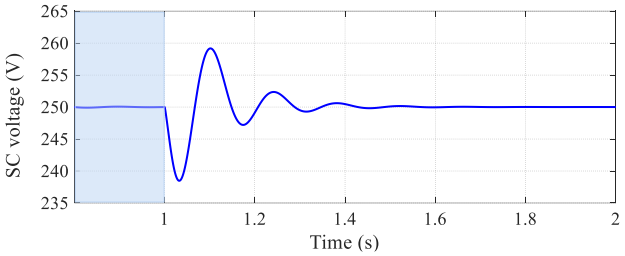

(b)

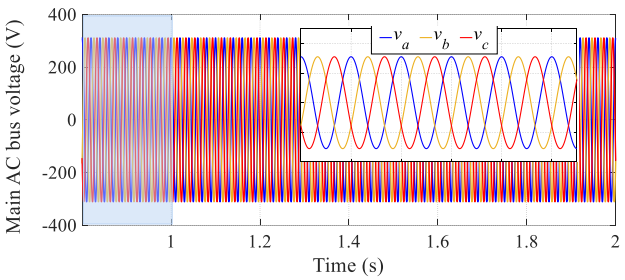

(c)

Fig. 9. Voltage response based on proposed method to step changes in the DC load power: a) main DC bus voltage, b) SC voltage, c) main AC bus voltage.

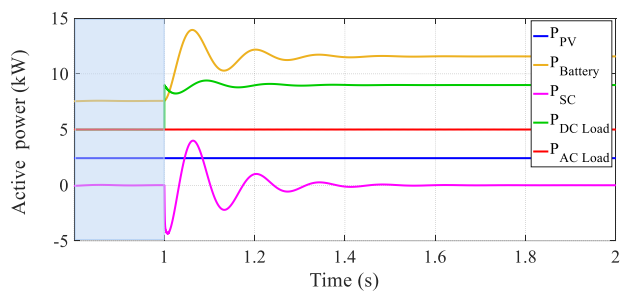

Fig. 10. Active power based on proposed method to step changes in DC load power.

voltage, SC voltage and main AC bud voltage when DC load power (at *t=1s*) changes. Fig. 10 shows the PV output power, battery output power, SC output power, DC load power and active power of AC load when DC load power changes. As can be seen, using the proposed virtual inertia ensures stable operation. To evaluate its effectiveness, a +80% change in DC load power from P_{Load} = 5 kW to P_{Load} = 9 kW at t=1s was investigated, with C_v=0.001 and R_v=4.76.

Fig. 11 shows the main DC bus voltage for varying in virtual inertia loop parameters. In Fig. 11 when *C*v and/or *1/R*v increase (decrease), the voltage deviation and RoCoV will

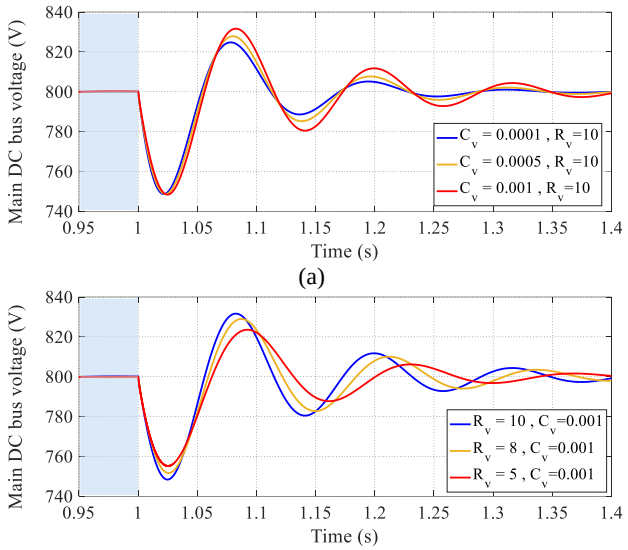

Fig. 11. Main DC bus voltage after a step change in load power, a) varying *Cv* for R_v=10, b) varying R_v for *Cv* =0.001.

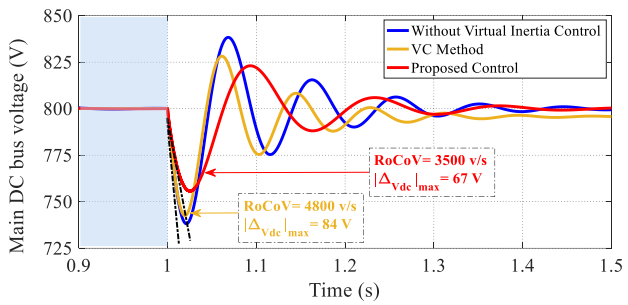

Fig. 12. Main DC bus voltage response based on basic, VC [27] and proposed methods.

decrease (increase), respectively. Meanwhile, the parameters of inertia response have no influence on the steady-state performance.

Fig. 12 compare the virtual capacitance (VC) method from [27] with the proposed virtual inertia loop method. Additionally, the result without an additional control loop is shown. Fig. 12 demonstrates that the virtual inertia controller improves the main dc bus voltage performance by reducing RoCoV, overshoot, and oscillations. This leads to an improved stability margin for the EV.

VI. Conclusions

This paper presents a solution to address the issues of low inertia and significant dc bus voltage fluctuations in an EV due to limited system capacitance. The proposed approach involves implementing a virtual inertia control using an ESS based on SC. By introducing virtual capacitance, the inertia of the dc bus is increased, resulting in a reduction in the required capacitance and voltage drop in the EV. This is achieved by providing instantaneous current during step-load changes. The increase in virtual capacitance leads to a decrease in the RoCoV during variations in load power. However, it is important to note that a larger virtual capacitance can cause larger low-frequency oscillations and reduced damping. To mitigate this issue, a proportional feedback gain (1/*R*v) is implemented to mimic the damping factor and decrease the oscillations. This approach also improves the battery lifetime by reducing the rate of charge and discharge. A comprehensive small-signal model is derived, and the selection of parameters is discussed based on eigenvalues analysis. Simulation results demonstrate that the proposed method, which utilizes proportional-derivative feedback, outperforms other methods in terms of performance.

References

[1] T. Mesbahi, P. Bartholomeus, N. Rizoug, R. Sadoun, F. Khenfri and P. Le Moigne, “Advanced model of hybrid energy storage system integrating lithium-ion battery and supercapacitor for electric vehicle applications,” *IEEE Trans. Ind. Electron.*, vol. 68, no. 5, pp. 3962-3972, May 2021.

[2] A. K. Podder, O. Chakraborty, S. Islam, N. Manoj Kumar and H. H. Alhelou, “Control strategies of different hybrid energy storage systems for electric vehicles applications,” *IEEE Access*, vol. 9, pp. 51865-51895, 2021.

[3] M. Carignano, V. Roda, R. Costa-Castelló, L. Valiño, A. Lozano, and F. Barreras, “Assessment of energy management in a fuel cell/battery hybrid vehicle,” *IEEE Access*, vol. 7, pp. 16110-16122, 2019.

[4] A. Tahri, H. El Fadil, F. Z. Belhaj, K. Gaouzi, A. Rachid, F. Giri, and F. Z. Chaoui, “Management of fuel cell power and supercapacitor state-ofcharge for electric vehicles,” *Electr. Power Syst. Res.*, vol. 160, pp. 89-98, Jul. 2018.

[5] S. Ahmadi, S. Bathaee, AH. Hosseinpour, “Improving fuel economy and performance of a fuel-cell hybrid electric vehicle (fuel-cell, battery, and ultracapacitor) using optimized energy management strategy,” *Energy Conversion and Management*, vol. 160, pp. 74-84, 2018.

[6] J. P. Torreglosa, P. García, L. M. Fernández, and F. Jurado, “Predictive control for the energy management of a fuel-cell-battery-supercapacitor tramway,” *IEEE Trans Ind. Informat.*, vol. 10, no. 1, pp. 276-285, Feb. 2014.

[7] S. Ahmadi and S. M. T. Bathaee, “multi-objective genetic optimization of the fuel cell hybrid vehicle supervisory system: Fuzzy logic and operating mode control strategies,” *Int. J. Hydrogen Energy*, vol. 40, no. 36, pp. 12512-12521, Sep. 2015.

[8] J. Chen, C. Xu, C. Wu, and W. Xu, “Adaptive fuzzy logic control of fuel-cell battery hybrid systems for electric vehicles,” *IEEE Trans. Ind. Informat.*, vol. 14, no. 1, pp. 292-300, Jan. 2018.

[9] L. Samaranayake and S. Longo, “Degradation control for electric vehicle machines using nonlinear model predictive control,” *IEEE Trans. Control Syst. Technol.*, vol. 26, no. 1, pp. 89-101, Jan. 2018.

[10] M. H. K. Tushar, C. Assi, M. Maier, M. F. Uddin, “Smart Microgrids: optimal joint scheduling for electric vehicles and home appliances”, *IEEE Trans. on Smart Grid*, vol. 5, no. 1, pp. 239 – 250, Jan. 2014.

[11] K. W. Hu, C. M. Liaw, "Incorporated Operation Control of DC Microgrid and Electric Vehicle", *IEEE Trans. on Ind. Electron*., vol. 63, no. 1, pp. 202 – 215, Jan. 2016.

[12] J. Fang, H. Li, Y. Tang, and F. Blaabjerg, "On the inertia of future more-electronics power systems," *IEEE J. Emerg. Sel. Topics Power Electron.*, vol. 7, no. 4, pp. 2130–2146, Dec. 2019.

[13] M. Su, Z. Liu, Y. Sun, H. Han, X. Hou, "Stability analysis and stabilization methods of DC microgrid with multiple parallel-connected DC–DC converters loaded by CPLs," *IEEE Trans. Smart Grid*, vol. 9, no. 1, pp.132-142, Mar. 2016.

[14] W. Yu, Z. Liu, and I. A. Tasiu, "Virtual inertia control strategy of traction converter in high-speed railways based on feedback linearization of sliding mode observer," *IEEE Trans. Veh. Technol.*, vol. 70, no. 11, pp. 11390–11403, Nov. 2021.

[15] G. Lin, J. Liu, C. Rehtanz, C. Li, Y. Li, and P. Wang, "Inertia droop control and stability mechanism analysis of energy storage systems for dc-busbar electric vehicle charging station," *IEEE Trans. on Transp. Electrific.*, vol. 9, no. 1, pp. 266-282, Mar 2023.

[16] H. Ali, "A hybrid energy storage system based on supercapacitor and electric vehicle batteries for frequency stability improvement of islanded microgrids," in *2022 23rd International Middle East Power Systems Conference (MEPCON)*, 2022, pp. 1-6.

[17] H. Jafari, M. Moghaddami, T. O. Olowu, A. Sarwat and M. Mahmoudi, "Virtual inertia-based multi-power level controller for inductive electric vehicle charging systems," *IEEE Trans. Emerg. Sel. Topics Power Electron.*, vol. 9, no. 6, pp. 7369-7382, Dec. 2021.

[18] L. Huang, H. Xin, H. Yuan, G. Wang, and P. Ju, "Damping effect of virtual synchronous machines provided by a dynamical virtual impedance," *IEEE Trans. Energy Convers.*, vol. 36, no. 1, pp. 570–573, Mar. 2021.

[19] A. Karimipouya, S. Karimi, H. Abdi, "Microgrid frequency control using the virtual inertia and ANFIS-based controller," *International Journal of Industrial Electronics, Control and Optimization*, vol. 2, no. 2, pp. 145-154, Apr. 2019.

[20] A. Karimi, Y. Jafarian, H. Bevrani, R. Mirzaei, "Frequency response improvement in microgrids: a fuzzy–based virtual synchronous generator approach," *International Journal of Industrial Electronics, Control and Optimization*, vol. 3, no. 2, pp.147-158, Apr. 2020.

[21] Y. Zhang, Q. Sun, J. Zhou, L. Li, P. Wang, and J. M. Guerrero, "Coordinated control of networked AC/DC microgrids with adaptive virtual inertia and governor-gain for stability enhancement," *IEEE Trans. Energy Convers.*, vol. 36, no. 1, pp. 95–110, Mar. 2021.

[22] Y. Yang, C. Li, J. Xu, F. Blaabjerg, and T. Dragiˇcevi´c, "Virtual inertia control strategy for improving damping performance of DC microgrid with negative feedback effect," *IEEE J. Emerg. Sel. Topics Power Electron.*, vol. 9, no. 2, pp. 1241–1257, Apr. 2021.

[23] Q. Ye, R. Mo, and H. Li, "Impedance modeling and DC bus voltage stability assessment of a solid-state-transformer-enabled hybrid AC–DC grid considering bidirectional power flow," *IEEE Trans. Ind. Electron.*, vol. 67, no. 8, pp. 6531–6540, Aug. 2020.

[24] W. Du, Q. Fu and H. F. Wang, "Small-signal stability of a DC network planned for electric vehicle charging," *IEEE Trans. Smart Grid*, vol. 11, no. 5, pp. 3748-3762, Sep. 2020.

[25] R. Shi, S. Semsar and P. W. Lehn, "Single-stage hybrid energy storage integration in electric vehicles using vector controlled power sharing", *IEEE Trans. Ind. Electron.*, vol. 68, no. 11, pp. 10623-10633, 2021.

[26] J.-L. Kuo, K.-L. Chao, and L.-S. Lee, "Dual mechatronic MPPT controllers with PN and OPSO control algorithms for the rotatable solar panel in PHEV system," *IEEE Transactions on Industrial Electronics*, vol. 57, no. 2, pp. 678–689, 2009.

[27] E. Unamuno, J. A. Barrena, "Design and small-signal stability analysis of a virtual-capacitor control for dc microgrids," *Proc. 19th Eur. Conf. Power Electron. Appl. (EPE ECCE Eur.)*, pp.1-10, 2017.

Mehran Jami was born in Marivan, Iran (1986). He received the B.Sc. degree from University of Tehran, Tehran, Iran, and the M.Sc. degree from Tarbiat Modares University (TMU), Tehran, Iran, and the Ph.D. degree from University of Kurdistan, Sanandaj, Iran, all in Power Electrical Engineering in 2012, 2014, and 2020 respectively. He is currently an Assistant Professor in the Department of Electrical Engineering, Islamic Azad University, Marivan Branch, Marivan, Iran. His research interests include modeling, analysis, design, and control of power electronic devices.

International Journal Of
Industrial Electronics Control and Optimization
Print ISSN: 3517-2645
Online ISSN: 3568-2645
Homepage: https://ieco.usb.ac.ir/

An Effective Damping Control Approach in Grid-Connected Converters

Anwer J. Ali[1] | Sirwan Shazdeh[1] | Hassan Bevrani[1] | Rahmatollah Mirzaei[1] | Qobad Shafiee[1] |

Smart/Micro Grids Research Center (SMGRC), University of Kurdistan, Sanandaj, Iran.[1]
Corresponding author's email: a.jalalali@uok.ac.ir.

Article Info

Article type:
Research Article

Article history:
Received: 24- July -2023
Received in revised form: 15-October -2023
Accepted: 04- November -2023
Published online: 26- November -2023

Keywords:
grid connected converters, virtual synchronous generator, swing equation, damping control.

ABSTRACT

The primary objective of this paper is to address the adverse effects of active power fluctuations on grid-connected converters. One of the challenges in integrating high levels of solar photovoltaic power into the utility grid is the lack of inertia from converter-based resources. This paper proposes a solution to this challenge by synthesizing additional inertia and damping properties using power electronics converters. They emulate the inertia and damping properties of synchronous generators. The paper discusses different approaches to achieving effective damping control in grid-connected converters. It proposes a genetic algorithm optimization tool to optimize virtual damping and inertia parameters. The goal is to suppress oscillations and ensure stable grid operation. The proposed method is evaluated in both time-domain and frequency-domain analyses. The simulation results demonstrate the validity of the optimization technique and implementation procedure. Using virtual inertia and damping properties ensures stable grid operation and improves the integration of solar photovoltaic power into the utility grid. The paper provides a detailed discussion of the approach, optimization tool, and simulation results, highlighting the effectiveness of the proposed method.

I. Introduction

In the global energy market, renewable energy sources such as solar systems are increasingly considered as viable alternatives to conventional sources of energy for power generation. The growing demand for energy and the environmental concerns associated with fossil fuels are the main reason for this revolution in energy production [1]. The integration of PV power into the utility grid has become a significant area of research and has garnered substantial public attention [2]. This interest is fueled by the decreasing costs of solar PV panels and the fast growth of related technologies [3]. In PV systems, converters are commonly used as interfaces between the PV arrays and the grid. However, converter-based resources (CBRs) introduce zero/low inertia dynamics into the grid due to the absence of rotating masses, which typically serve as sources of inertia. As a result, the overall inertia of the integrated power system is reduced due to the high penetration of CBRs [4]. To address this challenge and enhance power system stability with high PV penetration, the synthesis additional inertia and damping properties virtually has emerged as a promising solution [5].

Power electronic converters, equipped with short-term energy storage and appropriate control mechanisms, can be employed to emulate inertia and damping properties within the power system, thereby ensuring stable grid operation [6]. Unlike an actual synchronous generator (SG), the dynamic response of the system can be improved by manipulating the parameters of a virtual dynamic system. In addition to the virtual inertia control [7], other SG dynamics can be emulated on the converter control which is known as virtual synchronous machine (VSM) [8], [9], virtual synchronous generator (VSG) [10], [11], or synchronverter [12], [13].

Grid-connected converters (GCCs) with dynamic characteristics emulation features have gained significant interest on a global scale, as they offer power systems with desirable dynamics. GCCs possessing these properties are referred to as grid-forming converters [14]. It is important to note that the term “grid-forming” can be used to describe voltage and frequency control as a voltage source converter, and it can operate in both grid-connected and islanded scenarios [15]. For the sake of simplicity, the term "GCC" instead of “grid-forming GCC” will be used throughout the rest of this paper. GCCs play a crucial role in the future power grids due to the advancement of renewable energy generation. Since GCCs lack a rotating mass to provide inertia support for the grid, a virtual governor droop characteristic is employed to automatically track frequency changes, and a damping property is incorporated to mitigate undesirable oscillations [16]. Thus, the concept of VSG control, which emulates the swing equation of a synchronous generator to provide inertia and damping support for the power grid, offers a viable solution [17]. As a result, a new type of grid-forming control with an enhanced P-ω control loop is implemented. In recent years, various methods for emulating the swing equation with different damping techniques have been proposed [14], [18].

Despite sharing similar foundational principles, the control strategies employed in GCCs exhibit significant differences, leading to various approaches for achieving inertia and damping effects [19]. While the differential swing equation of SGs is commonly utilized to emulate inertia, alternative methods have been explored for virtual damping. Early studies in the literature focused on damping-free (DF) GCC control [11], [12]. Subsequent investigations introduced different techniques to enhance the GCC control structure, such as virtual damper windings (VDW) [20], [21], damping correction loops (DCL) [22], state feedback (SF)[23], and low-pass filtered state feedback (LPFSF) [24]. Additional damping techniques have been proposed, including the use of virtual power system stabilizers, artificial intelligence-based methods [25], output reactance boosting through virtual impedance control [26], fuzzy control strategies[27]. These approaches offer a broader range of options for achieving effective damping control in GCCs. Parameter-based approaches with self-adaptation have shown promising potential in enhancing the dynamic responses of active power and/or frequency by appropriately tuning the parameters in the VSG. [28]. These approaches encompass various techniques, including the incorporation of virtual inertia [29], [30], adjustment of damping factor [31], and simultaneous optimization of both parameters [32]–[34]. In [9], an effective damping method to improve VSM responses is proposed, while the stability of the DC-link voltage is not considered. The study in [28] presents a simple improved virtual inertia strategy based on a differential compensation model, addressing the issue of governor removal. Meanwhile, [29] introduces an approach to enhance oscillation damping and increase power system stability, but lacks a detailed consideration of certain parameters like the inertia coefficient. Additionally, the authors of [30] propose an adaptive virtual inertia control strategy, acknowledging its potential to improve the frequency response, but highlighting the need for optimization.

In this paper, the primary objective is to mitigate the adverse active power fluctuations observed at the output of a typical GCC. Therefore, the contributions of this paper can be summarized as follows:

The implementation of a virtual dynamic loop that includes damping and inertia to suppress oscillations and ensure proper coordination between virtual damping and virtual inertia.

The use of a genetic algorithm optimization tool to optimize both damping and inertia parameters. This method offers a simple and accurate approach to fine-tuning the control parameters, leading to improved system response and performance.

comprehensive analysis in both the time-domain and frequency-domain, include examining step response characteristics and pole locations, providing insights into the system's stability and dynamic behavior.

Briefly, this paper contributes to the understanding of how to mitigate active power fluctuations in GCCs using a virtual dynamic loop with optimized virtual damping and virtual inertia parameters, and provides a method for evaluating the effectiveness of this approach.

The remaining sections of the paper are organized as follows: Section 2 provides an overview of the grid-forming converter concept. The operation principles of GCCs are explained in detail in Section 3. In Section 4, a proper linear dynamic model for active power and frequency response, as well as damping control synthesis, is presented. Section 5 explains the proposed design methodology for parameter optimization. Simulation results and discussion are presented in Section 6. Finally, the paper is concluded in Section 7.

II. Concept and Structure of GCCs

Based on their control strategies, Grid-connected converters can be classified into two primary topologies: grid-following and grid-forming [35], [36]. A grid-following converter uses a Phase-Locked Loop (PLL) and current loop to achieve rapid control of the converter's output current. The output characteristic of a grid-following converter can be

visualized as an ideal AC current source connected in parallel with an admittance associated with the grid. Fig. 1(a) depicts a simplified equivalent model of this configuration.

In contrast, grid-forming converters regulate the output active and reactive power by controlling the voltage magnitude and frequency. They can be represented as an ideal AC voltage source connected in series with impedance. The simplified equivalent model of a grid-forming converter is illustrated in Fig. 1(b). GCCs have the capability to adjust their output power to accommodate loads and maintain local voltage and frequency at desired levels, even in unexpected scenarios. One notable advantage of dynamic characteristic-based GCCs is their rapid response to changes in output power and frequency. Unlike SGs, the transition time between such changes is significantly reduced in GCCs. This enhanced response enables GCCs to adapt to various conditions and react more efficiently compared to SGs. Although grid-following converters can regulate the output of real and reactive power by injecting a current with a specific phase angle, they do not have direct control over system voltage and frequency. In grid-following converters, the voltage and frequency references are typically provided externally, either by a GCC or the connected power grid.

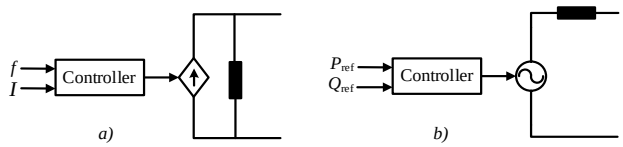

Fig. 1. Simplified equivalent models of power converters: (a) grid-following converter, (b) grid-forming converter.

Fig. 2 depicts a simplified control system of a GCC, comprising two primary subsystems: a voltage controller and a dynamic characteristic emulator unit. These subsystems provide the main reference signals to the voltage controller. The dynamic characteristic emulator unit consists of a control mechanism designed to replicate the necessary dynamics, allowing it to fulfill various functions such as virtual damping control, droop control, VSG, or any other desired dynamic behavior [19].

To accomplish dynamic characteristic emulation in GCCs, the control system incorporates several blocks. Fig. 3 illustrates a representative GCC along with its detailed control system. The “P-droop, inertia, and damping emulator” block is the core of the GCC control system, responsible for emulating the desired droop characteristics, inertia, and damping effects. Another critical block is the “output impedance emulator” which applies a virtual impedance control loop to enable the GCC to exhibit an equivalent output impedance characteristic.

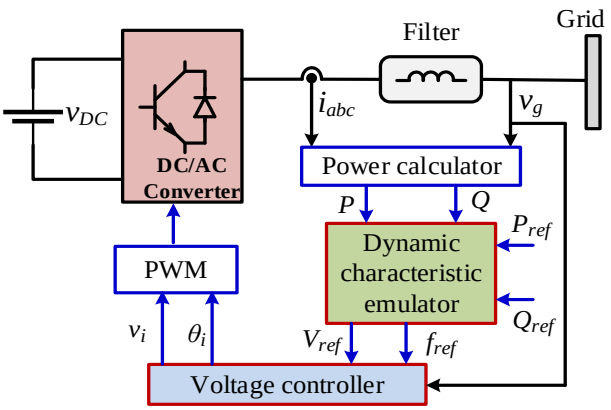

Fig. 2. Simplified GCC structure.

the “Q-droop emulator” block is also crucial in the dynamic characteristic emulation system of GCCs. It enables the implementation of the droop relationship between voltage and reactive power, ensuring that the reactive power output of the GCC follows the desired droop characteristics. This block plays a significant role in maintaining proper voltage regulation and reactive power support within the power system. Collectively, these blocks enable the GCC to exhibit the desired control behaviors and characteristics [26].

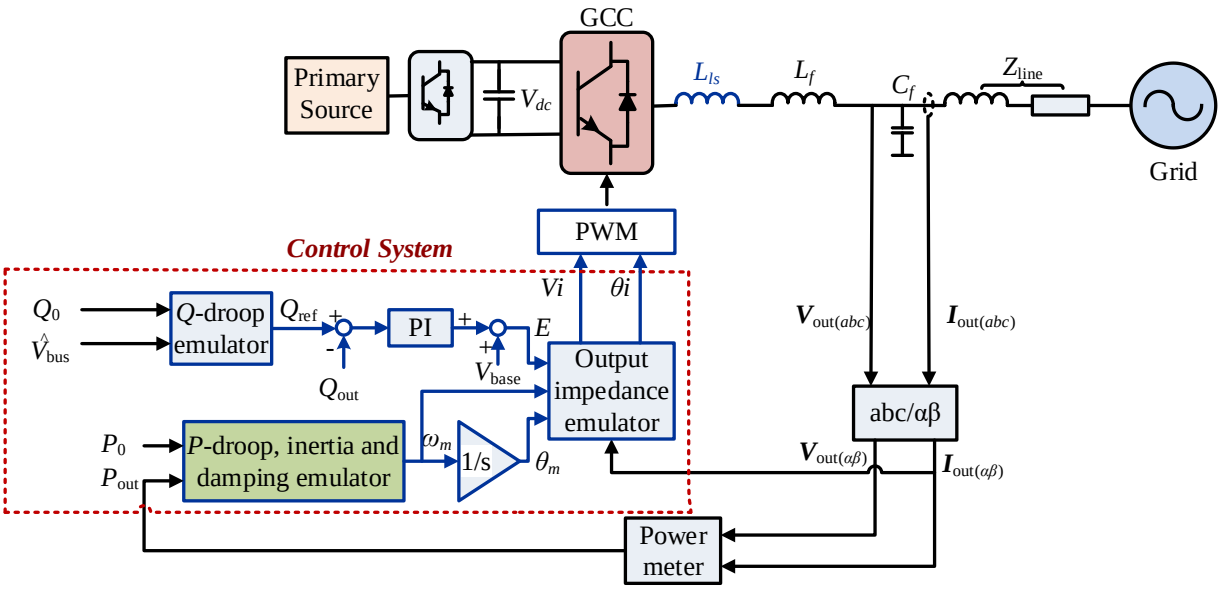

Fig. 3. Basic control structure of a grid-forming GCC.

III. Operation Principles of GCCs

In a GCC, the swing equation of SG can be emulated using a power controller. This emulation enables the implementation of frequency droop, power-oscillation damping, and/or virtual inertia characteristics [37]. A comprehensive control scheme for a VSG that incorporates virtual inertia control, droop control, and damping control can be represented mathematically as [18]

$$P_{out} - P_0 = J\omega_0 \frac{d\omega_m}{dt} + k_p(\omega_m - \omega_0) + D(\omega_m - \omega_g) \quad (1)$$

where P_0 denotes the reference power determined by the governor, P_{out} represents the measured output power, J is the moment of inertia, D is the damping factor, ω_m represents the rotor angular frequency, ω_g represents the angular frequency of the grid where the voltage sensor is installed, k_p is the droop coefficient, and ω_0 represents the nominal angular frequency.

The angular momentum (M) can be expressed as the product of the moment of inertia (J) and the angular synchronous velocity (ω_0). Hence, (1) can be modified as follows:

$$P_{out} - P_0 = M \frac{d\omega_m}{dt} + k_p(\omega_m - \omega_0) + D(\omega_m - \omega_g) \quad (2)$$

Since it can be challenging to measure ω_g directly, it is commonly approximated by $\tilde{\omega}_g$, which represents the angular frequency estimated through the use of a PLL with the output voltage V_{out} [18] .Fig. 4(a) illustrates this process.

The Non-PLL method has emerged as the preferred choice for damping control over the PLL-based method. Among the various techniques, the Non-PLL method has gained popularity and is illustrated in the block diagram shown in Fig. 4(b). The primary difference between the PLL-based and Non-PLL damping techniques lies in the way damping power is generated. In the Non-PLL approach, damping power is derived using the nominal frequency rather than the grid frequency [38]. Consequently, equation (2) can be modified as follows:

$$P_{out} - P_0 = M \frac{d\omega_m}{dt} + k_p(\omega_m - \omega_0) + D(\omega_m - \omega_0) \quad (3)$$

As per the given information, the mathematical expressions for droop control and damping power, as described in equation (3), are identical. This suggests that the droop coefficient and damping factor are equivalent and serve the same purpose within the control loop. The damping factor is intended to mitigate oscillation modes within the control system, while the droop coefficient is responsible for maintaining the required frequency levels in power systems and ensuring the proper distribution of power among converters in a proportional manner [28].

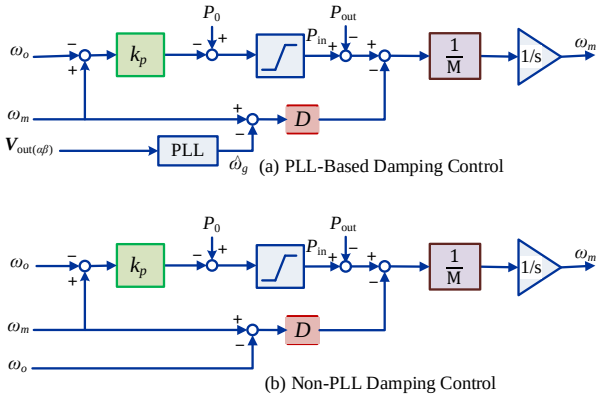

Fig. 4. Swing Equation emulation of GCC using traditional damping control. (a) PLL-based damping control. (b) Non-PLL damping control.

IV. Dynamic expressions

This section outlines a basic dynamic model that describes the active power-frequency response of the GCC. This model is essential for designing damping control strategies. Fig. 5 depicts a simplified diagram of the GCC system.

The synchronizing power coefficient K_s of the GCC is commonly represented as follows [24]:

$$K_s = \frac{\partial P_{out}}{\partial \delta} \approx \frac{EV_g cos\delta_0}{X_T} \approx \frac{V_{base}^2 \sqrt{1 - {X_T}^{*2}}}{X_T} \quad (4)$$

where, E represents the electromotive force, V_g denotes the grid voltage, V_{base} represents the rated voltage, S_{base} is the rated power, and ${X_T}^*$ denotes the per unit value of total reactance as depicted in Fig. 5.

The derivative of the power angle δ can be expressed as

$$\frac{d\delta}{dt} = \left(\omega_m - \omega_g\right) \quad (5)$$

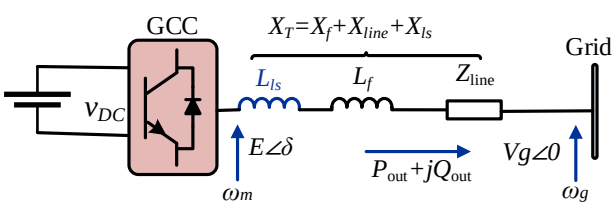

Fig. 5. Simplified diagram of a grid-connected GCC.

The GCC closed-loop transfer functions of the active power, and frequency related to the input active power (ΔP_0) and disturbance input grid frequency ($\Delta\omega_g$) can be obtained by deriving (3) to (5). The resulting expressions are given by (6) to (9). It should be noted that the dynamics of the PLL are disregarded. Consequently, the GCC system will be a typical second-order system, and both the PLL-based and Non-PLL systems exhibit identical characteristics.

$$\frac{\Delta P_{out}}{\Delta P_0} = \frac{K_s}{Ms^2 + \left(k_p + D\right)s + K_s} \quad (6)$$

$$\frac{\Delta \omega_m}{\Delta P_0} = \frac{s}{Ms^2 + \left(k_p + D\right)s + K_s} \quad (7)$$

$$\frac{\Delta P_{out}}{\Delta \omega_g} = \frac{K_s k_p + K_s M s}{Ms^2 + \left(k_p + D\right)s + K_s} \quad (8)$$

$$\frac{\Delta \omega_m}{\Delta \omega_g} = \frac{K_s + ds}{Ms^2 + \left(k_p + D\right)s + K_s} \quad (9)$$

The characteristic equations of (6)-(9) is

$$Ms^2 + \left(k_p + D\right)s + K_s = 0 \quad (10)$$

Thus, the undamped natural frequency (ω_n) and the damping ratio (ζ) can be found as

$$\omega_n = \sqrt{\frac{K_s}{M}} \quad (11)$$

$$\zeta = \frac{k_p + D}{2\sqrt{MK_s}} \quad (12)$$

The transient response performance of a control system can be assessed by parameters such as overshoot, rise time, delay time, and settling time. The natural frequency, ω_n, directly influences the rise time, delay time, and settling time, but it does not affect the overshoot. On the other hand, the maximum overshoot is solely dependent on the damping ratio, ζ, and can be controlled independently. Consequently, in practice, the settling time can be reduced by increasing ω_n while keeping ζ constant. For $0.7 < \zeta < 1$, the step response is oscillatory, but the oscillations are well-damped and are hardly perceptible [39], [40].

V. Proposed Method for Parameters Optimization

Parameter-based techniques with self-adaptation possess the capability to enhance the dynamic responses of active power and/or frequency by effectively adjusting the parameters within the VSG. By appropriately tuning these parameters, the dynamic behavior of the VSG can be optimized, leading to improved performance in terms of active power and frequency control.

There are numerous techniques available for finding optimal

solutions that can work efficiently, including artificial intelligence, neural networks, fuzzy systems, and soft computing. Among these techniques, the Genetic Algorithm (GA) stands out as a robust method that consistently produces the best possible solutions for optimization [41]. The GA is well-suited for solving numerous practical optimum design problems that are characterized by a combination of continuous and discrete variables, as well as discontinuous and nonconvex design spaces, which cannot be effectively addressed using standard nonlinear programming techniques [42]. Consequently, the GA is considered an optimal choice for optimization.

In this study, the optimal values of M and D (M^* and D^*) are obtained for different scenarios through the implementation of the GA using MATLAB codes. Subsequently, the performance and stability of the system are analyzed. The proposed method of using the GA optimization tool to optimize virtual damping and virtual inertia parameters in GCCs has moderate computational complexity.

The important key points of the GA process of obtaining M^* and D^*, include; the cost-function (or objective function), M and D variation bounds, and the desired prescribed performance.

The cost-function (*cf*) is defined based on the settling time (t_s) and Maximum overshoot (M_p) tolerances as

$$cf = \left(t_{s_{Desired}} - t_{s_{Actual}}\right)^2 + \left(M_{p_{Desired}} - M_{p_{Actual}}\right)^2 \quad (13)$$

where, $t_{s_{Desired}}$ is the desired settling time that can be calculated as,

$$t_{s_{Desired}} = \frac{4}{\zeta \omega_n} \quad (14)$$

$t_{s_{Actual}}$ is the actual settling time measured from the step response of the system,

$M_{p_{Desired}}$ is the desired overshoot indicated based on the desired ζ, as

$$M_{p_{Desired}} = e^{-\left(\frac{\zeta}{\sqrt{1-\zeta^2}}\right)\pi} \quad (15)$$

and $M_{p_{Actual}}$ is the actual overshoot measured from the step response of the system.

The optimal values can be obtained based on the minimization of the objective function. The flow chat of the GA based optimization algorithm is illustrated in Fig. 6.

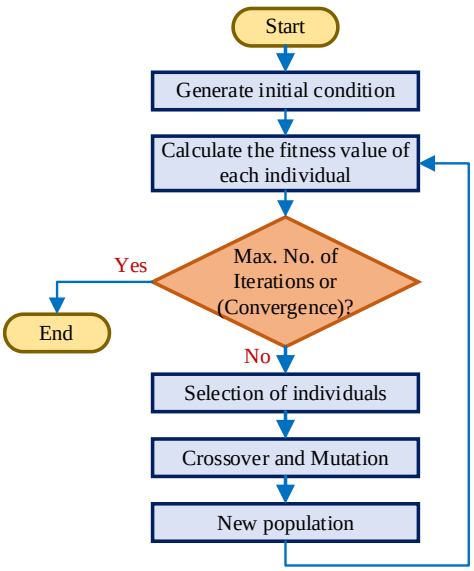

Fig. 6. Flowchart of the GA optimization algorithm.

VI. Simulation Results and Discussion

In Table 1, the control parameters of the GCC are considered and designed. Notably, the per unit values of the parameters are defined such as ratios relative to a specified base value as.

$$k_p{}^* = k_p \frac{\omega_0}{S_{base}}, and\ X_T{}^* = X_T \frac{S_{base}}{V_{base}^2}$$

TABLE 1
GCC's PARAMETERS

Parameter	Value	Parameter	Value
V_{base}	200 V	$P_0{}^*$	1 pu
S_{base}	5 kVA	$X_T{}^*$	0.3 pu
ω_0	377 rad/s	$k_p{}^*$	20 pu

The primary objective of this design is to enhance damping. Therefore, an overshoot value of 0.0015, which corresponds to a damping ratio of ζ =0.9, is selected. Different settling times and, consequently, different pole locations are considered. The obtained optimized results are presented in Table 2.

TABLE 2
SYSTEM BEHAVIOR WITH OPTIMAL VALUES OF D AND M

Case	Desired t_s(s)	Desired M_p	Desired ζ	D^*	M^*
1	0.2	0.0015	0.9	1.19	0.041
2	0.3	0.0015	0.9	1.7	0.075
3	0.4	0.0015	0.9	2	0.1
4	0.5	0.0015	0.9	2.42	0.14

The corresponding step response and pole

locations of the system depicted by (6) can be observed in Figs. 7 and 8 respectively.

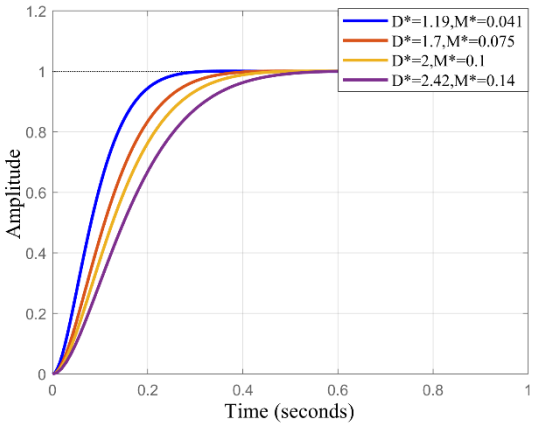

Fig. 7. Step responses of the GCC with damping.

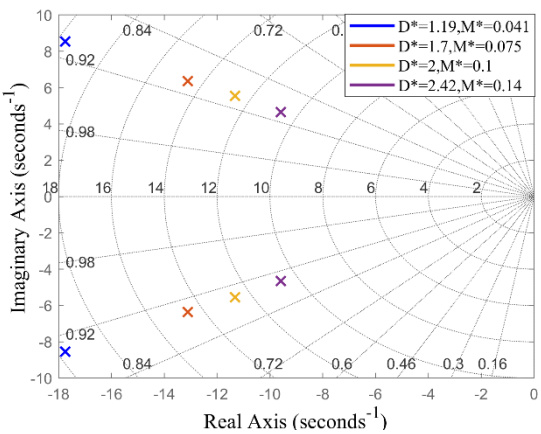

Fig. 8. Pole locations of the GCC with damping.

When the damping coefficient D is disregarded (D = 0), the system depicted by (6) become oscillatory and the system parameters are changed accordingly to the new values given in Table 3, with the same previous values of M*.

The corresponding step response and pole locations of the system can be found in Figs. 9 and 10 respectively. The comparative pole locations of the system with and without damping is illustrated in Fig. 11.

TABLE 3
THE SYSTEM'S BEHAVIOR WITH D=0.

Case	Actual t_s(s)	Actual M_p	D	M^*
1	1.1678	0.5895	0	0.041
2	2.1981	0.6806	0	0.075
3	2.8111	0.7171	0	0.1
4	3.9136	0.7554	0	0.14

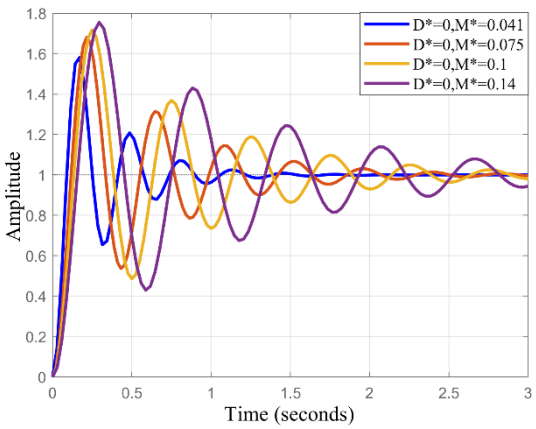

Fig. 9. Step response of the GCC without damping.

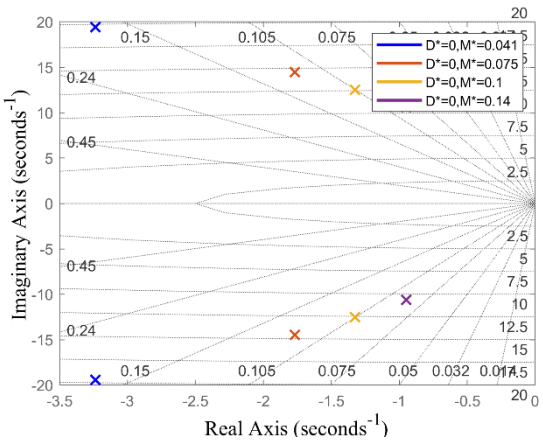

Fig. 10. Pole locations of the GCC without damping.

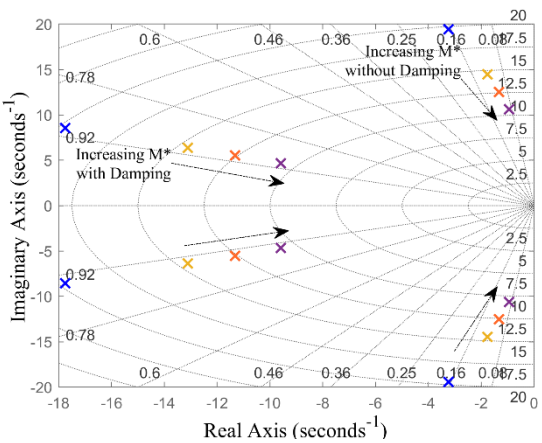

Fig. 11. Pole locations of the GCC with and without damping.

To further highlight the effect of the damping term on the system, the comparative step response and pole locations of the GCC system depicted by (6) to (9) are provided in Figs. 12, 13 and 14, respectively, when D^*=1.19 and M^*=0.041 with damping, and D=0 and M^*=0.041 without damping.

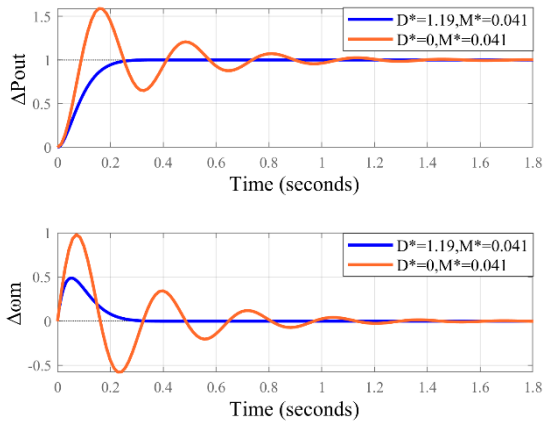

Fig. 12. Step response of the GCC with and without damping related to the set input active power (ΔP_0).

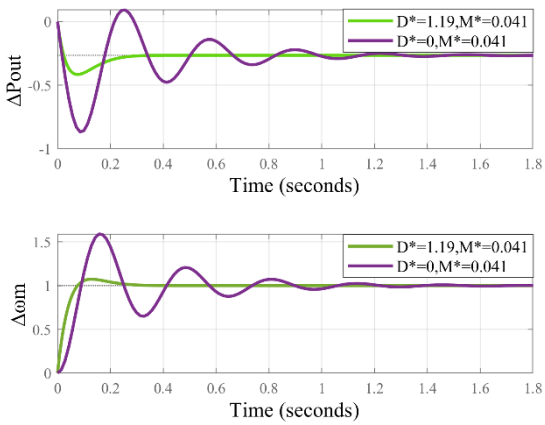

Fig. 13. Step response of the GCC with and without damping related to disturbance input grid frequency ($\Delta\omega_g$).

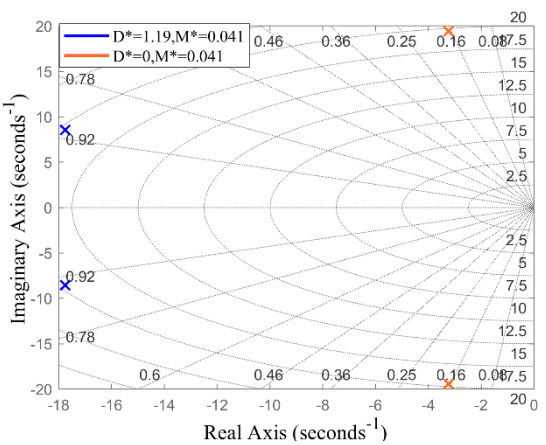

Fig. 14. Pole locations of the GCC with and without damping.

The system is tested again with the optimal values of M* and D*, when ζ changing from 0.7 to 1 and t_s =0.4 s. the obtained results are given in table 4. The corresponding system responses are shown in Figs.15 and 16 respectively.

TABLE 4
THE SYSTEM'S BEHAVIOR WHEN ζ CHANGING FROM 0.7 TO 1 AND T_S=0.4S.

Case	Desired t_s(s)	Desired M_p	Desired ζ	D^*	M^*
1	0.4	0.046	0.7	1.5	0.1
2	0.4	0.0152	0.8	1.75	0.1
3	0.4	0.0015	0.9	2	0.1
4	0.4	0	1	2.42	0.1

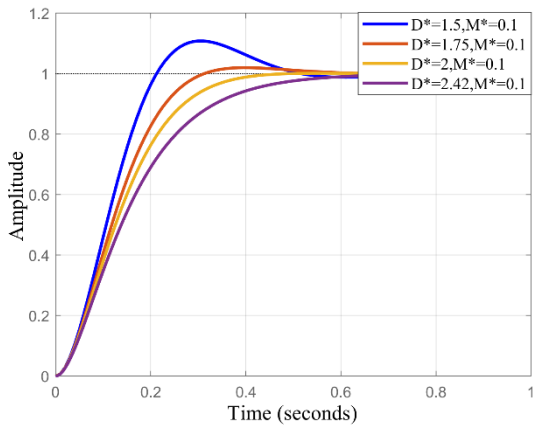

Fig. 15. Step response of the GCC with damping when ζ changing from 0.7 to 1.

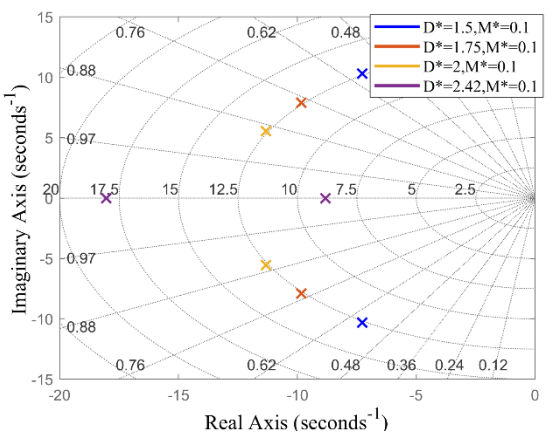

Fig. 16. Pole locations of the GCC with damping when ζ changing from 0.7 to 1.

These simulation results illustrate the step response and pole locations of the GCC under different damping conditions, highlighting the impact of damping on the system's behavior and stability. They also depict the importance of properly tuning and optimizing the GCC parameters. The performance improvement can be easily discerned from the step response, which shows a shorter settling time and decreased overshoot, while the poles settle at more stable positions.

To verify the effectiveness of the proposed optimal damping control design method, simulations were conducted in the MATLAB/Simulink environment. Fig. 17 provides an overview of the case study, serving as the simulation setup. The circuit parameters are displayed in Fig. 17, and additional system parameters can be found in Table 1. Fig. 18 presents the simulation results, illustrating the GCC output power and frequency fluctuations in two scenarios: with the optimal damping control loop and without damping control. It is evident that the desired performance can be achieved with the optimal damping control loop, in contrast to the case where no damping characteristics are present. These findings support the effectiveness of the proposed optimal damping control design method.

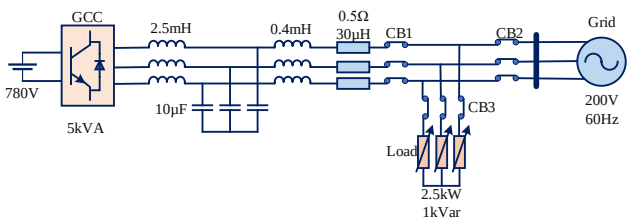

Fig. 17. The schematic of a grid-connected GCC case study in MATLAB/Simulink environment.

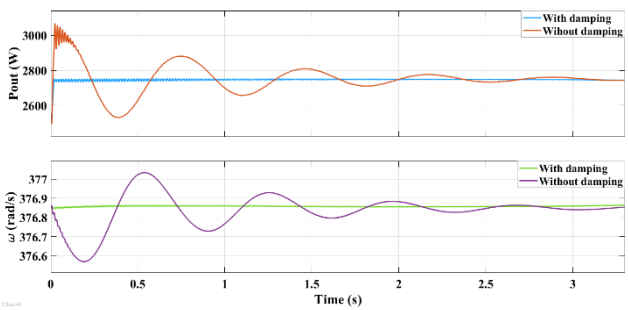

Fig. 18. The GCC output power and frequency in grid connected mode.

Since the proposed method is performance-index based, to compare its dynamic performance with existing methods, similar analyses to (6) are applied to the following methods. The performance indices for this comparative study are shown in Table 5. It is important to note that a large inertia is desired for better inertia support. However, insufficient damping can lead to significant oscillations and overshoot, which may damage the GCC, as demonstrated in the DF method. On the contrary, the VDE methods exhibit good damping ability. As mentioned earlier, the VDE methods can provide better dynamic responses if their parameters are properly chosen, as we have done in our optimization approach. The effectiveness of the proposed approach can be clearly observed by demonstrating better dynamic performance, such as shorter rising (t_r) and settling times (t_s) or overshoot (M_p), compared to other methods given in [11], [20], [22], [23] and summarized in [24].

TABLE 5
COMPARISON OF THE PERFORMANCE INDICES OF DYNAMIC RESPONSES.

DF			Proposed method				
t_r(s)	t_s(s)	M_p	t_r(s)	t_s(s)	M_p	D^*	M^*
0.0922	3.12	0.724	0.0898	2.811	0.71713	0	0.1
VDE			Proposed method				
t_r(s)	t_s(s)	M_p	t_r(s)	t_s(s)	M_p	D^*	M^*
0.236	0.384	0.00152	0.2287	0.372	0.001503	2	0.1
DCL			Proposed method				
t_r(s)	t_s(s)	M_p	t_r(s)	t_s(s)	M_p	D^*	M^*
0.236	0.386	0.00152	0.2427	0.395	0.001534	2.143	0.112
SF			Proposed method				
t_r(s)	t_s(s)	M_p	t_r(s)	t_s(s)	M_p	D^*	M^*
0.166	0.263	0.00537	0.1601	0.252	0.005342	1.352	0.056
LPFSF			Proposed method				
t_r(s)	t_s(s)	M_p	t_r(s)	t_s(s)	M_p	D^*	M^*
0.162	0.254	0.00603	0.1582	0.248	0.006101	1.337	0.055

VII. Conclusion

This paper proposes a solution of synthesizing additional inertia and damping properties virtually using power electronic converters. The paper explores different approaches to achieve effective damping control in GCCs and proposes a genetic algorithm optimization tool to optimize virtual damping and virtual inertia parameters. The primary objective of the paper is to mitigate adverse active power fluctuations in GCCs. The proposed method is evaluated in both the time-domain and frequency-domain analyses. Overall, the proposed method uses virtual inertia and damping properties to ensure stable grid operation and improve the integration of solar PV power into the utility grid. The simulation results emphasize the validity of the optimization technique and implementation procedure.

References

[1]S.-J. Yoon and K.-H. Kim, “Harmonic Suppression and Stability Enhancement of a Voltage Sensorless Current Controller for a Grid-Connected Inverter Under Weak Grid,” *IEEE Access*, vol. 10, pp. 38575–38589, 2022, doi: 10.1109/ACCESS.2022.3166592.

[2]Y. Tu, J. Liu, T. Liu, and X. Cheng, “Impedance-Based Stability Analysis of Large-Scale PV Station under Weak Grid Condition Considering Solar Radiation Fluctuation,” in *2018 International Power Electronics Conference (IPEC-Niigata 2018*

-*ECCE Asia)*, 2018, pp. 3934–3939. doi: 10.23919/IPEC.2018.8507415.

[3]M. M. Gulzar, A. Iqbal, D. Sibtain, and M. Khalid, "An Innovative Converterless Solar PV Control Strategy for a Grid Connected Hybrid PV/Wind/Fuel-Cell System Coupled With Battery Energy Storage," *IEEE Access*, vol. 11, pp. 23245–23259, 2023, doi: 10.1109/ACCESS.2023.3252891.

[4]T. Kerdphol, F. S. Rahman, M. Watanabe, and Y. Mitani, *Virtual Inertia Synthesis and Control*. in Power Systems. Springer International Publishing, 2020. [Online]. Available: https://books.google.com/books?id=UTGjzQEACAAJ

[5]P. Unruh, M. Nuschke, P. Strauss, and F. Welck, "Overview on Grid-Forming Inverter Control Methods," *Energies*, vol. 13, p. 2589, 2020, doi: 10.3390/en13102589.

[6]G. Kryonidis, K.-N. Malamaki, J. M. Mauricio, and C. Demoulias, "A new perspective on the synchronverter model," *Int. J. Electr. Power Energy Syst.*, vol. 140, p. 108072, 2022, doi: 10.1016/j.ijepes.2022.108072.

[7]J. Fang, H. Li, Y. Tang, and F. Blaabjerg, "Distributed Power System Virtual Inertia Implemented by Grid-Connected Power Converters," *IEEE Trans. Power Electron.*, vol. 33, no. 10, pp. 8488–8499, 2018, doi: 10.1109/TPEL.2017.2785218.

[8]L. Huang, H. Xin, H. Yuan, G. Wang, and P. Ju, "Damping Effect of Virtual Synchronous Machines Provided by a Dynamical Virtual Impedance," *IEEE Trans. Energy Convers.*, vol. 36, no. 1, pp. 570–573, 2021, doi: 10.1109/TEC.2020.3040605.

[9]M. Ebrahimi, S. A. Khajehoddin, and M. Karimi-Ghartemani, "An Improved Damping Method for Virtual Synchronous Machines," *IEEE Trans. Sustain. Energy*, vol. 10, no. 3, pp. 1491–1500, 2019, doi: 10.1109/TSTE.2019.2902033.

[10]U. Markovic, N. Früh, P. Aristidou, and G. Hug, "Interval-Based Adaptive Inertia and Damping Control of a Virtual Synchronous Machine," in *2019 IEEE Milan PowerTech*, 2019, pp. 1–6. doi: 10.1109/PTC.2019.8810640.

[11]H. Wu *et al.*, "Small-Signal Modeling and Parameters Design for Virtual Synchronous Generators," *IEEE Trans. Ind. Electron.*, vol. 63, no. 7, pp. 4292–4303, 2016, doi: 10.1109/TIE.2016.2543181.

[12]Q.-C. Zhong and G. Weiss, "Synchronverters: Inverters That Mimic Synchronous Generators," *IEEE Trans. Ind. Electron.*, vol. 58, no. 4, pp. 1259–1267, 2011, doi: 10.1109/TIE.2010.2048839.

[13]V. Natarajan and G. Weiss, "Synchronverters With Better Stability Due to Virtual Inductors, Virtual Capacitors, and Anti-Windup," *IEEE Trans. Ind. Electron.*, vol. 64, no. 7, pp. 5994–6004, 2017, doi: 10.1109/TIE.2017.2674611.

[14]H. Bevrani, B. Francois, and T. Ise, *Microgrid Dynamics and Control*. 2017. doi: 10.1002/9781119263739.

[15]Z. Zhao, Z. Sun, Y. Feng, B. Ji, S. Wang, and J. Zhao, "High-Performance Resonant Controller Implemented in the Discrete-Time Domain for Voltage Regulation of Grid-Forming Converters," *IEEE Trans. Power Electron.*, vol. 37, no. 4, pp. 3913–3926, 2022, doi: 10.1109/TPEL.2021.3120426.

[16]H. Bevrani, *Robust Power System Frequency Control*. 2009. doi: 10.1007/978-0-387-84878-5.

[17]J. Driesen and K. Visscher, "Virtual synchronous generators," in *2008 IEEE Power and Energy Society General Meeting - Conversion and Delivery of Electrical Energy in the 21st Century*, 2008, pp. 1–3. doi: 10.1109/PES.2008.4596800.

[18]J. Liu, Y. Miura, H. Bevrani, and T. Ise, "A Unified Modeling Method of Virtual Synchronous Generator for Multi-Operation-Mode Analyses," *IEEE J. Emerg. Sel. Top. Power Electron.*, vol. 9, no. 2, pp. 2394–2409, 2021, doi: 10.1109/JESTPE.2020.2970025.

[19]H. Bevrani, J. Liu, and T. Kato, "Robust Optimal Damping Control Design For Grid-Forming Converters," in *2021 9th International Renewable and Sustainable Energy Conference (IRSEC)*, 2021, pp. 1–6. doi: 10.1109/IRSEC53969.2021.9741217.

[20]T. Shintai, Y. Miura, and T. Ise, "Oscillation Damping of a Distributed Generator Using a Virtual Synchronous Generator," *IEEE Trans. Power Deliv.*, vol. 29, no. 2, pp. 668–676, 2014, doi: 10.1109/TPWRD.2013.2281359.

[21]L. Huang, H. Xin, and Z. Wang, "Damping Low-Frequency Oscillations Through VSC-HVdc Stations Operated as Virtual Synchronous Machines," *IEEE Trans. Power Electron.*, vol. 34, no. 6, pp. 5803–5818, 2019, doi: 10.1109/TPEL.2018.2866523.

[22]S. Dong and Y. C. Chen, "Adjusting Synchronverter Dynamic Response Speed via Damping Correction Loop," *IEEE Trans. Energy Convers.*, vol. 32, no. 2, pp. 608–619, 2017, doi: 10.1109/TEC.2016.2645450.

[23]J. Liu, Y. Miura, and T. Ise, "A Novel Oscillation Damping Method of Virtual Synchronous Generator Control Without PLL Using Pole Placement," in *2018 International Power Electronics Conference (IPEC-Niigata 2018 -ECCE Asia)*, 2018, pp. 775–781. doi: 10.23919/IPEC.2018.8508003.

[24]J. Liu, Y. Miura, and T. Ise, "Fixed-Parameter Damping Methods of Virtual Synchronous Generator Control Using State Feedback," *IEEE Access*, vol. 7, pp. 99177–99190, 2019, doi: 10.1109/ACCESS.2019.2930132.

[25]F. Blaabjerg, *Control of Power Electronic Converters and Systems Vol 1*. 2018.

[26]J. Liu, Y. Miura, H. Bevrani, and T. Ise, "Enhanced Virtual Synchronous Generator Control for Parallel Inverters in Microgrids," *IEEE Trans. Smart Grid*, vol. 8, no. 5, pp. 2268–2277, 2017, doi: 10.1109/TSG.2016.2521405.

[27]A. Karimi, Y. Jafarian, H. Bevrani, and R. Mirzaei, "Frequency Response Improvement in Microgrids: A Fuzzy–based Virtual Synchronous Generator Approach," *Int. J. Ind. Electron. Control Optim.*, vol. 3, no. 2, pp. 147–158, 2020, [Online].Available:https://ieco.usb.ac.ir/article_5084.html%0Ahttps://ieco.usb.ac.ir/article_5084_ec47895f67ba5dd947f10ef414763fa1.pdf

[28]M. Li *et al.*, "Phase Feedforward Damping Control Method for Virtual Synchronous Generators," *IEEE Trans. Power*

Electron., vol. 37, no. 8, pp. 9790–9806, 2022, doi: 10.1109/TPEL.2022.3150950.
[29]J. Alipoor, Y. Miura, and T. Ise, "Power System Stabilization Using Virtual Synchronous Generator With Alternating Moment of Inertia," *IEEE J. Emerg. Sel. Top. Power Electron.*, vol. 3, no. 2, pp. 451–458, 2015, doi: 10.1109/JESTPE.2014.2362530.
[30]X. Hou, Y. Sun, X. Zhang, J. Lu, P. Wang, and J. M. Guerrero, "Improvement of Frequency Regulation in VSG-Based AC Microgrid Via Adaptive Virtual Inertia," *IEEE Trans. Power Electron.*, vol. 35, no. 2, pp. 1589–1602, 2020, doi: 10.1109/TPEL.2019.2923734.
[31]M. Li, Y. Wang, N. Xu, W. Wang, and J. Li, "A consistent dynamic response control strategy for virtual synchronous generator," in *2017 IEEE 3rd International Future Energy Electronics Conference and ECCE Asia (IFEEC 2017 - ECCE Asia)*, 2017, pp. 1570–1574. doi: 10.1109/IFEEC.2017.7992280.
[32]D. Li, Q. Zhu, S. Lin, and X. Y. Bian, "A Self-Adaptive Inertia and Damping Combination Control of VSG to Support Frequency Stability," *IEEE Trans. Energy Convers.*, vol. 32, no. 1, pp. 397–398, 2017, doi: 10.1109/TEC.2016.2623982.
[33]M. A. Torres L., L. A. C. Lopes, L. A. Morán T., and J. R. Espinoza C., "Self-Tuning Virtual Synchronous Machine: A Control Strategy for Energy Storage Systems to Support Dynamic Frequency Control," *IEEE Trans. Energy Convers.*, vol. 29, no. 4, pp. 833–840, 2014, doi: 10.1109/TEC.2014.2362577.
[34]S. Qu and Z. Wang, "Cooperative Control Strategy of Virtual Synchronous Generator Based on Optimal Damping Ratio," *IEEE Access*, vol. 9, pp. 709–719, 2021, doi: 10.1109/ACCESS.2020.3046626.
[35]X. Liu *et al.*, "Stability Assessment of A Radial Grid With Power Converters," *IEEE Open J. Power Electron.*, vol. 3, pp. 61–74, 2022, doi: 10.1109/OJPEL.2021.3138509.
[36]M. Li *et al.*, "Unified Modeling and Analysis of Dynamic Power Coupling for Grid-Forming Converters," *IEEE Trans. Power Electron.*, vol. 37, no. 2, pp. 2321–2337, 2022, doi: 10.1109/TPEL.2021.3107329.
[37]L. Harnefors, M. Schweizer, J. Kukkola, M. Routimo, M. Hinkkanen, and X. Wang, "Generic PLL-Based Grid-Forming Control," *IEEE Trans. Power Electron.*, vol. 37, no. 2, pp. 1201–1204, 2022, doi: 10.1109/TPEL.2021.3106045.
[38]Q. Taoufik, E. Rokrok, A. Bruyere, B. Francois, and X. Guillaud, "A PLL-Free Grid-Forming Control With Decoupled Functionalities for High-Power Transmission System Applications," *IEEE Access*, vol. 8, 2020, doi: 10.1109/ACCESS.2020.3034149.
[39]F. Golnaraghi and B. C. Kuo, *Automatic Control Systems*, 10th Editi. New York: McGraw-Hill Education, 2017. [Online]. Available: https://www.accessengineeringlibrary.com/content/book/9781259643835
[40]K. Ogata, *Modern control engineering*. 2010.
[41]O. Kramer, *Genetic Algorithm Essentials*. 2017. doi: 10.1007/978-3-319-52156-5.
[42]S. S. Rao, *Engineering Optimization: Theory and Practice*. Wiley,2019.[Online].Available:https://books.google.nl/books?id=oG21DwAAQBAJ

Anwer J. Ali received his B.E. degree in Electrical Engineering from the Salahaddin University, Hawler, Iraq, in 2000 and his M.Sc. degree in Power Engineering from the University of Sulaimani, Sulaimani, Iraq in 2008. He is currently Ph.D. Student of Control of Power Systems and a member of the Smart/Micro Grids Research Center (SMGRC) at the University of Kurdistan, Sanandaj, Iran. His current research interests include power electronics and virtual dynamics.

Sirwan Shazdeh received PhD degree in electrical engineering from University of Kurdistan (Iran) in 2022. Currently, he is an associate research fellow with Smart/Micro Grids Research Center (SMGRC) at the University of Kurdistan. His current research interests include microgrid dynamics and control, smart grid wide-area protection and control.

Hassan Bevrani (Fellow, IEEE) received the Ph.D. degree in electrical engineering from Osaka University, Osaka, Japan, in 2004. He is currently a Professor and the Program Leader of Smart/Micro Grids Research Center with the University of Kurdistan, Sanandaj, Iran. Over the years, he has worked as a Senior Research Fellow and a Visiting Professor with Osaka University, Kumamoto University, Kyushu Institute of Technology, Doshisha University, Nagoya University (Japan), Queensland University of Technology (Australia), Centrale Lille (France), and Technical University of Berlin (Germany). He is the author and coauthor of 9 international books, 15 book chapters, and more than 500 journal/conference papers. His current research interests include smart grid operation and control, power systems stability and optimization, microgrid dynamics and control, and intelligent/robust control applications in power electric industry.

Rahmatollah Mirzaei received the B.E. degree in electronic engineering from Tabriz University, Tabriz, Iran, in 1987, the M.Sc. degree in control engineering from Tehran University, Tehran, Iran, in 1991, and the Ph.D. degree in the Power Electronics from Indian Institute of Science in Bangalore, India, in 2007. He is currently an Assistant Professor, and a member of the Smart/Micro Grids Research Center at the University of Kurdistan, Sanandaj, Iran, where he was a Lecturer from 1993.

His research interests include design, analysis, control, and modeling of power converters for PFC circuits, soft switching and active filter systems.

Qobad Shafiee (Senior Member, IEEE) received the M.Sc. degree in electrical engineering from the Iran University of Science and Technology, Tehran, Iran, in 2007, and the Ph.D. degree in electrical engineering and microgrids from the Department of Energy Technology, Aalborg Univeristy, Aalborg, Denmark, in 2014. He was with the Department of Electrical and Computer Engineering, University of Kurdistan, Sanandaj, Iran, from 2007 to 2011, where he taught several electrical engineering courses and conducted research on load frequency control of power systems. From March 2014 to June 2014, he was a Visiting Researcher with the Electrical Engineering Department, University of Texas-Arlington, Arlington, TX, USA. He was a Postdoctoral Fellow with the Department of Energy Technology, Aalborg University, in 2015. He is currently an Assistant professor with the Department of Electrical and Computer Engineering, University of Kurdistan. His research interests include modeling, power management, hierarchical and distributed control applied to distributed generation in microgrids.

International Journal Of
Industrial Electronics Control and Optimization
Print ISSN: 3517-2645
Online ISSN: 3568-2645
Homepage: https://ieco.usb.ac.ir/

Design and Optimization of a Very High-speed Three-phase Bearingless Induction Motor

Hamed Azadrou

Faculty of Engineering, Islamic Azad University, Salmas Branch, Salmas, Iran.
Corresponding author's email: azadrou.elec@gmail.com

Article Info

Article type:
Research Article

Article history:
Received: 06 May 2023
Received in revised form:
30 August 2023
Accepted: 22 September 2023
Published online: 26- Nov -2023

Keywords:
Bearingless motor,
finite element analysis,
high-speed compressors.

ABSTRACT

This paper explores the application of high-speed bearingless induction motors within compressor systems. These motors utilize two distinct electromagnetic fields to generate both torque and suspension forces, making them suitable for applications requiring high speed with efficient operation. However, a significant challenge arises from the interference between these fields, which can negatively impact motor performance. To address this issue, we propose a new rotor structure that mitigates the interference problem. Subsequently, we focus on optimizing the motor's dimensions to enhance both torque generation and suspension force capabilities. To achieve this optimization, a modern genetic algorithm is employed, allowing for a comprehensive exploration of the design space. The results of the proposed optimized motor are compared with those of a motor optimized using a conventional algorithm. The findings affirm the effectiveness of our approach in improving motor performance.

NOMENCLATURE

W_m	Magnetic energy
i_{ab}	two-phase current vector
L_{ab}	inductance matrix
F_x and F_y	suspension forces in x and y directions
ω_{rm}	mechanical rotor speed
ω_{2s}	two pole slip frequency
ω_{4s}	four pole slip frequency
i_{2ds}, i_{2qs}	two pole stator constant dc currents
i_{2dr}, i_{2qr}	two pole rotor constant dc currents
i_{4ds}, i_{4qs}	four-pole stator constant dc currents
i_{4dr}, i_{4qr}	four pole rotor constant dc currents
M'_{24}	mutual inductance between torque and force windings
L_{2s}	torque windings self-inductances
L_{4s}	force windings self-inductances
$\underline{U}(\underline{X})$	objective function
$U_i(\underline{X})$	decision space
$\underline{X}$	state related to the Q-dimensional decision space
F_{av}	average suspension force
T_{av}	average electromagnetic torque
x	set of variables that can be adjusted
f	multi-objective optimization
P	power
N	speed (rpm)
P_t	torque winding pole number
P_f	force winding pole number
Q_s	stator slots
Q_r	rotor slots
V_L	supply voltage
I_t	Torque winding current
I_s	Force winding current
h_{rp}	Rotor slot depth
f_f	Stator slot fill factor
g	airgap

I. INTRODUCTION

Bearingless motors (BLM) are electromagnetic devices that have a function of magnetic rotor levitation as conventional magnetic bearings [1]. One electromagnetic unit of the bearingless drives provides radial forces in two perpendicular axes as well as rotational torque. The active magnetic bearing uses the windings to generate a magnetic force. Different types of electrical motors such as switched reluctance [2] and synchronous motors [3] can use magnetic bearing technology. Induction motors have many advantages that make them more popular in various industries. The advantages are also available in the bearing-less induction motors (BLIMs). In a BLIM there are two distinct magnetic fields, which create the electromagnetic torque and suspension force simultaneously. The basic method to create two independent fields is to use separate windings in common stator slots [4]. This structure is simple but especially in high-speed and high-power applications due to occupying the space of the slots and significantly reducing the torque density of the motor, this method is not very effective. Another construction is the combined winding, in which both fields are produced by a single set of windings. This structure has been used in a slotless disc drive in [5] and in a conventional induction motor in [6]. This increases significantly the torque density of the motor. However, the power electronic converter in this structure is more complicated and the interference between the fields is also high [7]. To overcome this problem, a special type of combined winding is presented in [8], called dual purpose no voltage structure. The distinctive feature of this structure is that the current of the force field does not create a back electromotive force in the rotor, and therefore the interference between the fields is almost eliminated.

High-speed electrical machines have advantages such as high efficiency, compact design, and low material consumption. So they can be very useful in various industries [9]. Bearingless motors with very low and predictable friction can run without lubrication and in a vacuum. So, they can be good candidates for industrial applications with high-speed requirements such as turbochargers, micro-turbines, and spindles. In [10], the design of a high-speed induction motor for gas compressor applications has been presented. The electrical, mechanical, and metallurgical design, construction, and testing of another high-speed induction motor to drive a small centrifugal compressor has been shown in [11]. The electrical and mechanical design strategies and limits for high-speed induction motors have been discussed in [12]. Laminated and solid rotor applications have been compared in [13]. Design and performance evaluation techniques for bearingless induction motors and their difference from conventional induction motors have been investigated in [14]. Another optimized BLIM with different magnetic slot wedges has been proposed in [15]. Modeling and performance analysis of two types of bearingless induction motors have been discussed in [20]. An active magnetic bearing design and optimization in a high-speed motor has been presented in [16]. The electrical machines can be optimized using computation intelligence-based techniques, such as genetic algorithm (GA) [17] and [18] and seeker optimization algorithm (SOA) [19].

This work covers high-speed compressors in section II, followed by an examination of bearingless induction motors. The corresponding equations for these motors are presented in this section and a new rotor structure for the motor is presented. In Section III, the optimization of the proposed bearingless motor is discussed, and the optimization objective function is derived. The optimization results and motor performance evaluation are presented in Section 4.

II. BEARING-LESS INDUCTION MOTORS

A. Oil and gas industry drivers

Traditional compressor systems are constructed based on gas turbines as displaced in Fig. 1 (a). Although these systems are independent of electrical instruments and power supply, they have weak speed control, low efficiency, environmental emissions, noise pollution, and maintenance requirements. Gas turbines are more difficult to start and their efficiency is low. Further, the use of a gas turbine as a compressor drive requires keeping multiple spare parts available and scheduling more shutdowns for maintenance. Electrical motor drive systems have greater availability, while they could operate within a wider speed control range. Thus, they can be used as a driver for gas compressors, as shown in Fig. 1. (b). Conventional electrical motors work based on the available limited voltage and frequency power supply, while they have a limited speed range. To adapt the characteristics of these motors as gas compressor drivers, an incremental gearbox is required to bring the speed to the acceptable range. This would lower the system's efficiency. The use of an appropriate high-speed electrical motor eliminates the need for mechanical converters, as depicted in Fig. 1. (c). These systems have many advantages such as improved speed control, higher efficiency, no site emissions, reduced site noise impact, less maintenance, dynamic braking capability, and short startup time. By eliminating the mechanical bearing, high-speed electric motors would have high efficiency and reliability with reduced maintenance costs.

B. Structure of the BLIM

The design of the BLIMs is similar to that of conventional induction motors. The most important difference is in the

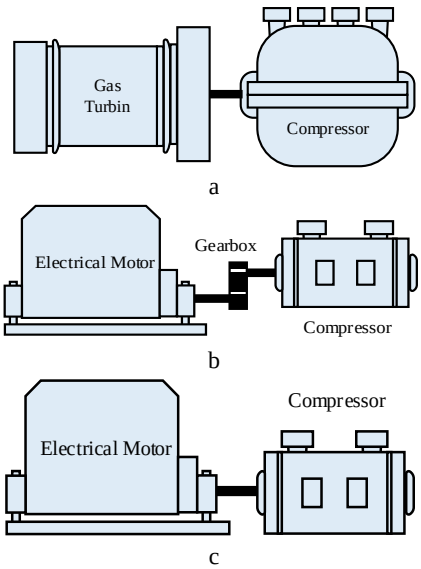

Fig. 1. Gas compression systems, (a) traditional system, (b) low

design of the bearing, so that in BLIMs, the design process is slightly different due to the need for suspension force. speed electric motor and gearbox, (c) high-speed electric motor.

Therefore, the stator windings in BLIMs must be designed more carefully because, in addition to producing motor torque, they must also produce the shaft suspension force. On the other hand, the torque and force fields should have the least interference. Each BLIM requires two distinct fields. One is the "P" pole, called the torque or motoring field that produces torque similar to normal motors, and the other is the "P±2" pole called the force or suspension field.

The proposed motor is a three-phase bearing-less squirrel cage induction motor. These motors have a simple and robust structure with easy construction. But, in a bearing-less motor both torque and force magnetic fields induce currents in rotor bars. In low-speed applications, the negative effect of the torque field on the suspension force is negligible, while in high-speed and high-power motors, it is complicated. To overcome this problem, a BLIM with multi cage rotor structure as shown in Fig. 2 is proposed in this work. As shown in the figure, the rotor consists of several two-pole cages. The rotor has 32 slots so, there is 16 distinct two pole path in the proposed rotor. The proposed motor has a two-pole magnetic field for torque production and a four-pole field for force creation. Using the proposed rotor structure, only two pole currents could be induced in the rotor. Then, the force-generating system will be independent of the torque as much as possible. The torque and force of the induction motor with the conventional squirrel cage rotor are shown in Fig. 3. The data have been obtained based on 3-D finite element analysis (FEA) with ANSYS Electronics. As the speed of the rotor increases, the force also decreases until it reaches almost zero. The unsuitability of the conventional squirrel cage rotor for high speeds is clear from these results.

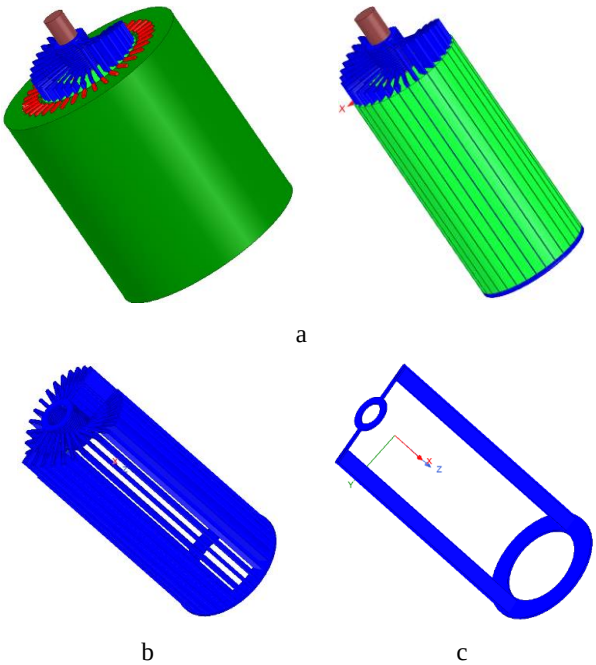

Fig. 2. Proposed BLIM, a) the motor and rotor, b) multi cage, c) one cage structure.

C. Mathematical equations of the BLIM

To design the proposed motor, equations illustrated in [13] have been used in this work. Initial obtained dimensions for a 2 Mega-Watt BLIM with a 15000 rpm speed motor have been listed in Table 1. This motor can be used in gas compressor systems [16]. To optimize the BLIM, some parameters have been considered variable and the influence of them on the motor performance has been studied in the next section.

A complete analysis of magnetic force in a BLIM with a squirrel cage rotor has been presented in [3]. The magnetic energy is expressed as:

$$W_m = \frac{1}{2}[i_{ab}]^t[L_{ab}][i_{ab}] \tag{1}$$

Suspension forces in $the\ x$ and y directions can be written by partial derivatives of the energy concerning the corresponding radial displacement

$$\begin{bmatrix} F_x \\ F_y \end{bmatrix} = \begin{bmatrix} \dfrac{\partial w_m}{\partial x} \\ \dfrac{\partial w_m}{\partial y} \end{bmatrix} \tag{2}$$

considering $\theta_{rm} = \int \omega_{rm} dt$, slip frequencies can be written as

$$\left.\begin{aligned} \omega_{2s} &= \omega_2 - \omega_{rm} \\ \omega_{4s} &= \omega_4 - 2\omega_{rm} \end{aligned}\right\} \tag{3}$$

The suspension force matrix is obtained as follows

$$\begin{bmatrix} F_x \\ F_y \end{bmatrix} = M'_{24} \begin{bmatrix} i_{2ds} + i_{2dr} & i_{2qs} + i_{2qr} \\ -(i_{2qs} + i_{2qr}) & i_{2ds} + i_{2dr} \end{bmatrix} \begin{bmatrix} i_{4ds} + i_{4dr} \\ i_{4qs} + i_{4qr} \end{bmatrix} \tag{4}$$

The electromagnetic torque can be expressed as follows [17].

$$T_e = \partial w_{mech}/\partial x = L_{2s}\left(i_{2dr} i_{2qs} - i_{2ds} i_{2qr}\right) + L_{4s}\left(i_{4dr} i_{4qs} - i_{4ds} i_{4qr}\right) \tag{5}$$

III. OPTIMIZATION

A. Multi-Objective Optimization Problem

A MOOP is a Q-dimensional decision space with objective function $\underline{U}(\underline{X}) = \{U_1(\underline{X}), U_2(\underline{X}), \dots, U_q(\underline{X})\}$ in the feasible set of decision vectors $\underline{X}$, where $q > 1$. In this algorithm, an optimized one replaces a set of non-dominated solutions. The problem is to minimize the value of the MOOP and to achieve this goal, the objective functions must be minimized.

$$Minimize\ \underline{U}(\underline{X}) = \{U_1(\underline{X}), U_2(\underline{X}), \dots, U_q(\underline{X})\} \quad (6)$$

where $\underline{X} = [\underline{X}_1, \underline{X}_2, \dots, \underline{X}_Q] \in R^Q$ is a state related to the Q-dimensional decision space (R^Q), and $\underline{U} = [U_1, U_2, \dots, U_q] \in \Omega^q$ is the objective space that contains q objective functions.

B. Objective Functions

BLIM has a specific structure and performance is more complicated than conventional induction motors. Torque and force-producing units have undesirable influences together that decrease motor performance. To optimize the BLIM dimensions, an appropriate objective function consisting of the optimization parameters should be determined. In the first step, the average suspension force (F_{av}), the average electromagnetic torque (T_{av}), and force ripple (RF) must be optimized. For this purpose, the objective functions including the parameters are defined as follows:

$$u_1(\underline{x}) = \frac{1}{F_{av}} \quad (7)$$

$$u_2(\underline{x}) = \frac{1}{T_{av}} \quad (8)$$

$$u_3(\underline{x}) = RF \quad (9)$$

where x indicates a set of variables that can be adjusted to minimize the functions $u_i(x)$. Torque production with a lower weight is an important benefit in all electrical machines. In this work, the fourth objective function is defined as the motor's total weight.

$$u_4(\underline{x}) = M \quad (10)$$

To minimize the objective functions, suitable variable parameters should be optimized. Some of the motor dimensions are dependent. In this case, choosing both parameters makes the optimization process more complicated. Therefore, independent parameters are considered as the variable, x. In this work, the optimization parameters are selected as shown in Fig. 3. The proposed method in [13] was used to design the motor, and the initial dimensions were obtained. These values are the starting point for optimization. Some of the obtained dimensions are not considered in the optimization process. These parameters along with the other fixed parameters are shown in Table 1.

In this section, optimization of the designed BLIM using the MOOP method is presented. Adjustable parameters are specified in Fig. 4. Thus, we can choose x as (11).

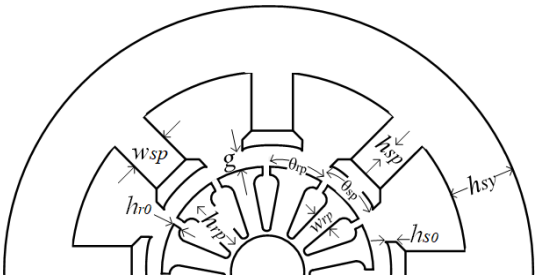

Fig. 3. The optimization parameters of the BLIM

TABLE 1
FIXED PARAMETERS OF THE BLIM

Parameter	Symbol	Constraints
Power	P	2 MW
Speed	N	15000 rpm
Torque winding poles	P_t	2
Force winding poles	P_f	4
Supply frequency	f	250 Hz
Stator slots	Q_s	60
Rotor slots	Q_r	54
Voltage	V_L	4 kV
Torque winding current	I_t	320 A
Force winding current	I_s	70 A
Stack length	l	220 cm
Rotor slot depth	h_{rp}	8 cm
Stator slot fill factor	f_f	0.6

TABLE 2
CONSTRAINTS OF OPTIMIZATION

Symbol	Constraints	
$\boldsymbol{g}$	0.2 – 4	mm
$\boldsymbol{w_{sp}}$	5 – 30	mm
$\boldsymbol{w_{rp}}$	5 – 30	mm
$\boldsymbol{h_{sp}}$	50 – 150	mm
$\boldsymbol{h_{s0}}$	2 – 10	mm
$\boldsymbol{h_{r0}}$	2 – 10	mm
$\boldsymbol{h_{sy}}$	50 – 250	mm
$\boldsymbol{\theta_{sp}}$	1 – 6	deg
$\boldsymbol{\theta_{rp}}$	1– 6	deg

$$\underline{x} = (g, w_{sp}, w_{rp}, h_{sp}, h_{rp}, h_{s0}, h_{r0}, h_{sy}, \theta_{sp}, \theta_{rp}) \quad (11)$$

There are limitations in the optimization of the above dimensions. For example, the poles of the stator and rotor cannot overlap. Thus, each parameter was considered in a specified region as listed in Table 2. At each optimization stage, the suspension force, the electromagnetic torque, the force ripple, and the total mass of the motor are calculated for a set of x. The optimization continues until the objective function in (12) reaches a minimum value. The multi-objective optimization can be defined as

$$f = min\{u_1, u_2, u_3, u_2\} \quad (12)$$

TABLE 3
ADJUSTABLE VARIABLES OF BLIM

Symbol	Initial value	NSGA-II	NSGA-III
g	1 mm	1 mm	0.9 mm
w_{sp}	15 mm	13.7 mm	14.3 mm
w_{rp}	10 mm	12 mm	12.2 mm
h_{sp}	110 mm	1.2 mm	97.5 mm
h_{s0}	7 mm	7.2 mm	7.5 mm
h_{r0}	5 mm	5.8 mm	5.8 mm
h_{sy}	170 mm	168 mm	167.4 mm
θ_{sp}	4.4 deg	4.4 deg	4.45 deg
θ_{rp}	5.5 deg	5.6 deg	5.74 deg

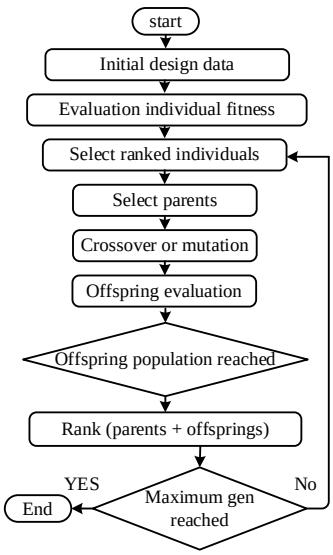

Fig. 4. Flowchart of the genetic algorithm

IV. SIMULATION RESULTS

The design of the proposed BLIM was done based on the analytical approach presented in [19] and [20]. The achieved initial dimensions were optimized using the NSGA-II and NSGA-III and the optimization dimensions were obtained. The initial and optimized dimensions are shown in Table 3. The computational flowchart and algorithm steps are depicted in Fig. 4.

3-D finite element analysis of the proposed motor was done in ANSYS Electronics software and the results were extracted. To have a better evaluation, the characteristics of the motor with a conventional squirrel cage rotor, the initially designed motor, and the optimized motor are compared. F_x and F_y indicate the suspension force in the x and y axes, respectively. Under normal conditions, when the rotor is completely centered on the axis, there is only F_y, which is produced to

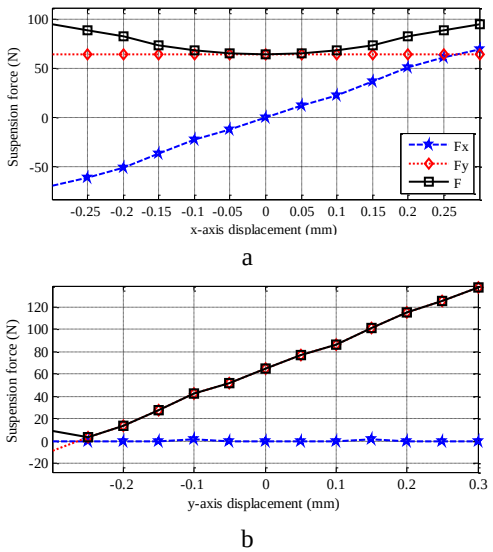

Fig. 5. 2-D suspension forces, a) x-axis, b) y-axis.

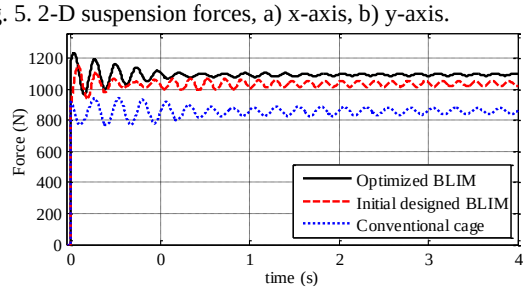

Fig. 6. Suspension force comparison at speed 15000 rpm.

hold the rotor, while F_x is zero. If the rotor deviates from the center, an appropriate force must be generated to bring it back. The suspension force produced for different values of the distance of the rotor from the center is shown in Fig. 5.

Fig. 6 shows the suspension force for the BLIM with a conventional squirrel cage rotor, initially designed proposed BLIM, and optimized BLIM. This is the sum of the two axes' force vectors and has been obtained by applying the corresponding rated currents to both torque and force windings.

Comparing the curves indicates that the suspension force in the optimized structure is better than the other two structures in terms of value and ripple.

The curves of average suspension force and average torque variations about the force winding current and for different values of the torque winding current (I_t) are shown in Fig. 7. The curves indicate that the average force is proportional to the force winding current.

To have a better study, rated currents are fed into both torque and force windings with different current phases λ. The obtained results are shown in Fig. 8. It can be seen that F_x and F_y are sine and cosine curves, respectively. Fig. 8 (b) indicates the relationship between two direction forces and the final produced suspension force vector. According to the relationship. It can be understood that the direction of the total force can be controlled by adjusting the winding currents.

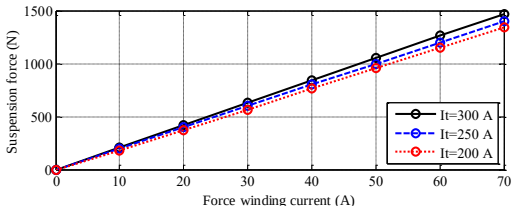

a

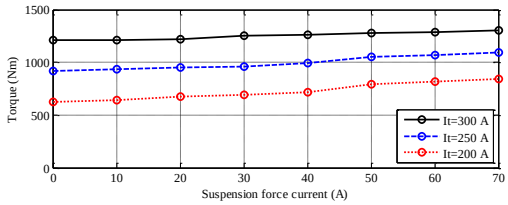

b

Fig. 7. Force and torque curves for different currents, a) suspension force, b) torque.

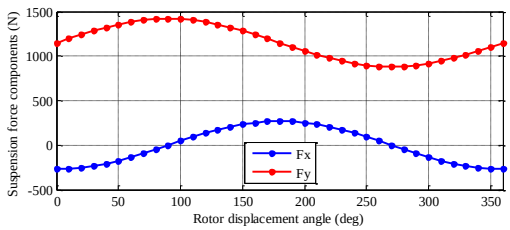

a

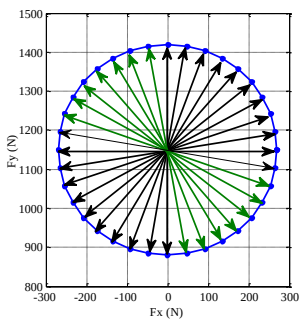

b

Fig. 8. Suspension force, (a) components, (b) relationship.

The performance of the proposed motor during startup and under load conditions is depicted in Fig. 9. The obtained results are for a speed of 15000 rpm, while following the motor's initial run in the no-load state, a nominal load is applied to it at 1.2 seconds. The acquired outcomes clearly illustrate the motor's commendable performance at high speeds.

In Fig 10, a comparison is presented between an unoptimized motor, an optimized motor with an algorithm employed in [21], and the proposed approach. It is assumed that the rotor is not initially positioned at the center of the stator but rather has initial positions of $x = +1\ mm$ and $y = -1\ mm$. Consequently, forces in both horizontal and vertical directions are necessary to reposition the rotor to the center. A comparison of these curves illustrates that the motor optimized through the proposed method exhibits superior performance in comparison to others.

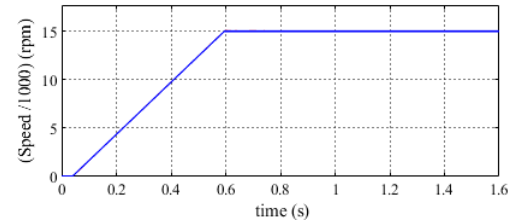

a

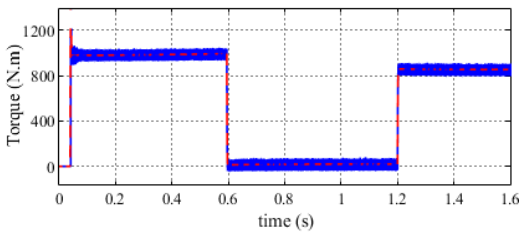

b

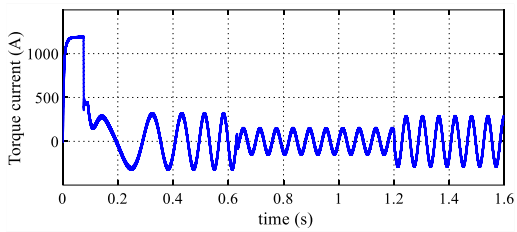

c

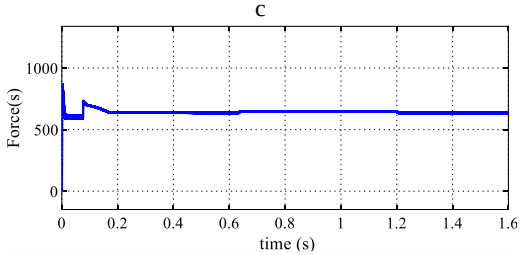

d

Fig. 9. Motor performance at high speed, (a) speed, (b) torque, (c) torque current, (d) suspension force.

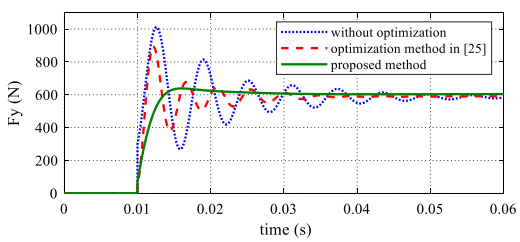

a

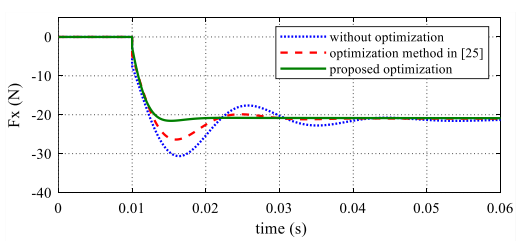

b

Fig. 10. Horizontal and vertical force production in the BLIM, (a) Fy, (b) Fx.

V. CONCLUSIONS

In this paper, we have demonstrated the application of high-speed bearingless induction motors in compressor systems. These motors, leveraging distinct electromagnetic fields for torque and suspension forces, present a promising solution for applications requiring precise control and operational efficiency. However, the challenge of interference between these fields significantly affects motor performance. To overcome this challenge, we introduced a new rotor structure that effectively minimizes the interference issue. Additionally, we conducted a comprehensive optimization of the motor's dimensions to enhance torque and suspension force generation. Utilizing a modern genetic algorithm, we achieved remarkable improvements in motor performance. Through a comparative analysis, we established the superiority of our proposed optimized motor over a motor optimized by conventional means. The results underscore the significance of our approach in enhancing motor efficiency and performance within compressor applications.

REFERENCES

[1] A. Chiba, T. Fukao, O. Ichikawa, M. Oshima, M. Takemoto, and D. G. Dorrel, "Magnetic bearings and bearingless drives," in Proc. Liacre House, Joordan Hill. Oxford OX2 8DP, 30 Corporate Drive, Burlington, MA 01803, DOI: 10.1016/B978-0-7506-5727-3.X5000-7.

[2] J. Chen, J. Zhu, and E. L. Severson, "Review of bearingless motor technology for significant power application," IEEE Trans. on Ind. Appl., vol. 56, no. 2, pp. 1377-1388, 2021.

[3] T. Pei, D. Li, J. Liu, J. Li, and W. Kong, "Review of bearingless synchronous motors: principle and topology," IEEE Trans. on Trans. Electrification, vol. 8, no. 3, pp. 3489-3502, 2022.

[4] T. Tera, Y. Yamauchi, A. Chiba, T. Fukao, and M. A. Rahman, "Performances of bearingless and sensorless induction motor drive based on mutual inductances and rotor displacements estimation," IEEE Trans. on Ind. Elec., vol. 53, no. 1, pp. 187-195, 2006.

[5] D. Steinert, T. Nussbaumer, and J. W. Kolar, "Concept of a 150 krpm bearingless slotless disc drive with combined windings," in Proc. IEEE Int. Electric Mach. Drives Conf., pp. 311-318, 2013.

[6] J. Chen, Y. Fujii, M. W. Johnson, A. Farhan, and E. L. Severson, "Optimal design of the bearingless induction motor," IEEE Trans. on Ind. Appl., vol. 57, no. 2, pp. 1375-1389, 2021.

[7] Y. Jiang and E. L. Severson, "Floating capacitor suspension inverter for parallel combined winding bearingless motors," IEEE Trans. on Ind. Appl., vol. 56, no. 2, pp. 1518–1528, 2020.

[8] E. L. Severson, S. Gandikota, and N. Mohan, "Practical implementation of dual-purpose no-voltage drives for bearingless motors," IEEE Trans. on Ind. Appl., vol. 52, no. 2, pp. 1509–1518, 2016.

[9] R. Abebe, M. D. Nardo, D. Gerada, G. L. Calzo, L. Papini, and C. Gerada, "High-speed drives review: machines, converters, and applications," in Proc. IECON 42nd Annual Conf., IEEE Ind. Elec. Society, 2016.

[10] P. Beer, J. E. Tessaro, B. Eckels, and P. Geberson, "High-speed motor design for gas compressor applications," in Proc. Proceedings of the thirty-fifth turbomachinery symposium, 2006.

[11] W. L. Soong, G. B. Kliman, R. N. Johnson, R. A. White, and J. E. Miller, "Novel high-speed induction motor for a commercial centrifugal compressor," IEEE Trans. on Ind. Appl., vol. 36, no. 3, pp. 706-714, 2000.

[12] J. J. Guerrero, A. Wright, and N. Bhatia, "LNG compressor driver trends gas turbines vs. electric motors," in Proc. IEEE IAS Petroleum and Chemical Industry Technical Conference (PCIC), 2021.

[13] R. Lateb, J. Enon, L. Durantay, "High-speed, high-power electrical induction motor technologies for integrated compressors," in Proc. International Conf. on Elec. Machines and Sys., ICEMS, 2009.

[14] J. Pyrhonen, T. Jokinen, and V. Hrabovcová, "Design of Rotating Electrical Machines," Hoboken, NJ, USA: Wiley, ISBN: 978-1-118-58157-5, 2009.

[15] J. Chen, and E. L. Severson, "Design and modeling of the bearingless induction motor," in Proc. IEEE International Elec. Machines Drives Conf. (IEMDC), 2019.

[16] K. Li, G. C, X. Sun, Z. Yang, and Y. Fan, "Performance optimization design and analysis of bearingless induction motor with different magnetic slot wedges," Results in Physics, vol. 12, pp. 349-356, 2019.

[17] A. Smirnov, N. Uzhekov, T. Sillanpaa, J. Pyrhonen, and O. Pyrhonen, "High-speed electrical machine with active magnetic bearing system optimization," IEEE Trans. on Ind. Elec., vol. 64, no. 12, pp. 9876-9886, 2017.

[18] M. Soltanpour, H. Abdollahi, and S. Masoudi, "Optimisation of Double Sided Linear Switched Reluctance Motor for Mass and Force Ripple Minimization," IET Science, Measurement and Technology, vol. 13, no. 4, pp. 509-517, 2019.

[19] K. Deb, A. Pratap, S. Agarwal, "A fast and elitist multi-objective genetic algorithm: NSGA-II," IEEE Trans. on Evolutionary Computation, vol. 6, no. 2, pp. 182-197, 2002.

[20] A. Teymourifar, A. M. Rodrigues, J. S. Ferreira, "A comparison between NSGA-II and NSGA-III to solve multi-objective sectorization problems based on statistical parameter tuning," in Proc. 24th International Conference on Circuits, Systems, Communications, and Computers (CSCC), 2020.

[21] A. Azadrou, S. Masoudi, Sh. Gharaati, "An improved linear switched reluctance motor for elevator application," in Proc. International of Industrial Electronics Control and Optimization (IECO), pp. 297-304, 2022.

Hamed Azadrou was born in Salmas, Iran, in 1983. He received his B.S. degree in electrical engineering from Islamic Azad University, Abhar Branch, Abhar, Iran, and M.S. degree from Dezful Branch, Dezful, Iran, and PhD degree from Islamic Azad University, Urmia Branch, Urmia, Iran. He is a member of science in Islamic Azad University, Salmas Branch, Iran since 2012.

IECO

This page intentionally left blank.

International Journal Of
Industrial Electronics Control and Optimization
Print ISSN: 3517-2645
Online ISSN: 3568-2645
Homepage: https://ieco.usb.ac.ir/

De-Noising of Partial Discharge Signals in HV XLPE Cables by Reference Noise based on the Wavelet Transform

Amir Ghaedi[1] | Reza Sedaghati[2] | Mehrdad Mahmoudian[3]| Shahriar Bazyari[4]

Department of Electrical Engineering, Dariun Branch, Islamic Azad University, Dariun, Iran.[1]
Department of Electrical Engineering, Beyza Branch, Islamic Azad University, Beyza, Iran.[2]
Department of Electrical Engineering, Iran University of Science and Technology, Tehran, Iran.[3]
Department of Electrical Engineering, Kazerun Branch, Islamic Azad University, Kazerun, Iran.[4]

Corresponding author's email: amir.ghaedi@miau.ac.ir

Article Info

Article type:
Research Article

Article history:
Received: 2023-08-06
Received in revised form: 2023-11-02
Accepted: 2023-11-13
Published online: 2023-11-18

Keywords:
De-noising,
On-line detection,
Partial discharge,
Wavelet Transform,
XLPE cable.

ABSTRACT

The use of underground XLPE cables in power systems is increasing due to the problems associated with overhead lines. However, insulation failure, primarily caused by partial discharge (PD) phenomenon, remains a major concern. Monitoring the insulation condition of XLPE cables, particularly the magnitude and trend of PDs, is crucial. Detecting and localizing PDs online pose a significant challenge due to the presence of various environmental noises that must be eliminated. In recent years, power system-introduced noises like impulse noises generated by power electronic devices have become prevalent. Therefore, effective de-noising techniques are required to filter out the noises and interferences from the detected PD signals. This paper proposes the use of wavelet transform, which encompasses both time and frequency domains, to remove various noises from PDs, considering their non-stationary nature. To determine the suitable mother wavelet transform, threshold, and number of decompositions, experimental tests are conducted to investigate the characteristics of PD signals in the cables. Additionally, background noise at the measurement site, which varies in substations, is recorded as reference noise for the wavelet-based noise removal process. Using MATLAB software, reference noises and noisy PD signals are measured in substations, and the de-noising process is executed. The proposed method is evaluated on a sample cable, and the results are discussed. Furthermore, the method is applied to detect PD signals in multiple 20 kV substations in Iran, utilizing high-frequency current transformers connected to shield wires, oscilloscopes with high-frequency bandwidth, and MATLAB software.

I. Introduction

A. Research Motivation

XLPE cables are commonly utilized in power systems as an alternative to overhead lines. The reliability of high-voltage equipment often hinges on the condition of its insulation. The primary cause of insulation failure in high-voltage devices is the occurrence of partial discharge within the insulation. Therefore, monitoring high-voltage equipment, such as cables, while they are operational, is crucial to timely detect any partial discharge and protect the cable insulation from further deterioration. Offline detection methods can also be employed for PD detection. However, applying offline methods is impractical for cables and other high-voltage equipment that cannot be easily de-energized during operation, and it may be

too late by the time offline PD measurements are conducted. When online monitoring is employed for PD measurement, the presence of environmental noises and electromagnetic interference (EMI) can make it challenging to detect the PD signals. Thus, the removal of noise from PD signals is an essential task that must be carried out in the online monitoring of high-voltage equipment.

B. Literature Review

Due to the critical importance of detecting PD signals in high-voltage equipment, such as high-voltage XLPE cables, extensive research has been dedicated to denoising PD signals in these contexts. In reference [1], a novel wavelet selection scheme is introduced for detecting PDs that occur in environments with low signal-to-noise ratio conditions. This research recommends the use of a wavelet entropy-based wavelet selection scheme to eliminate noise from PD signals. In paper [2], a technique employing wavelet transform with histogram-based threshold estimation is applied for online noise removal from PD signals. The proposed approach determines two distinct threshold values for each wavelet sub-band and applies a significant threshold that preserves the original signal energy. The wavelet transform has proven to be a powerful tool, and as a result, it has been applied in various contexts, including the operation of networks comprising wind and photovoltaic units, detection of transmission line faults, and classification of power quality events [3-5]. In reference [3], a prediction method based on the wavelet transform, an artificial neural network with a nonlinear structure for enhanced training and learning, and the imperial competition algorithm is employed to conduct operational studies of wind farms, cascade hydro systems, photovoltaic units, and pumped-storage systems. Paper [4] introduces a single-ended approach for detecting the protection zone and identifying faults occurring behind the relays used in transmission lines. This paper utilizes the wavelet transform to classify different types of faults that may occur in transmission lines. In [5], a novel method based on discrete wavelet transform and correlation coefficient is implemented to detect and classify a wide range of power quality events. In [6], an improved generalized cross-correlation time delay estimation approach is utilized to locate partial discharge signals occurring in AC XLPE cables. Given the influence of electromagnetic noise and other factors, this paper suggests an online localization technique based on the generalized correlation algorithm for estimating the signal time delay. Paper [7] applies an improved wavelet spectrum segmentation algorithm based on the spectral kurtogram to detect partial discharge signals. This research presents an approach that eliminates the need for human intervention in selecting threshold parameters or decomposition layer numbers when detecting PDs in noisy environments. In [8], a novel adaptive method based on the total least-squares with Matern Kernel is proposed for locating partial discharges in cable systems. The algorithm is designed to suppress environmental noise from both the direct and reflected waves of the PD source while estimating the time difference used for locating PDs. Paper [9] employs a recursive continuous S-shaped approach to denoise PD signals occurring in cables. This research develops an adaptive filtering method to address both Gaussian and impulsive noises in PD signals. In [10], a partial discharge detection system is introduced for detecting PDs in XLPE cables. This research involves the development of an acoustic wave sensing system based on a fiber optic Mach-Zehnder interferometer to enhance the anti-interference capabilities and real-time performance of PD detection.

Paper [11] investigates the background noises, mechanisms, and coupling paths of partial discharge detection through experiments conducted in complex electromagnetic environments. Several denoising methods, including improved grounding, power isolation, and optimized wiring layouts, are analyzed in this paper. Paper [12] introduces a combined ultra-high frequency noise removal approach that integrates waveform correlation analysis, time-domain windowing techniques considering external noise signals, and a clustering approach based on the magnitude ratio associated with two consecutive sensors.

In [13], a deep learning method is applied for detecting partial discharge signals occurring in power lines. This paper suggests a novel end-to-end framework based on convolutional neural network methods to identify the pulses associated with partial discharges. Paper [14] utilizes the convolutional neural network method for classifying the noises present in the background of partial discharge signals. In this paper, a modified 10-fold cross-validation approach is proposed, where the convolutional neural network-based partial discharge classifier is trained using clean partial discharge data and tested with noisy partial discharge signals. In [15], power spectral subtraction is applied to eliminate different types of acoustic partial discharge signal noises. This method is used to detect partial discharge signals contaminated with white noises and study other discharges, including corona, surface, parallel, and void discharges.

In [16], the detection of partial discharge signals in environments with radio frequency noises is performed using multiple narrow-band antennas. This method is applied to detect partial discharge signals occurring in SF6 gas, and the results of this approach are compared with a standard wide-band Horn antenna. In [17], a review of radiometric approaches used for detecting partial discharge signals is conducted. The paper studies radiofrequency bands, including high frequency, very high frequency, and ultra-high frequency bands, used for partial discharge detection in cables and transformers. Finally, in [18], the detection and location of partial discharge signals occurring in medium-voltage cables in noisy industrial environments are performed. This paper

describes the application of high-resolution data acquisition devices for detecting PDs in medium-voltage cables equipped with high-frequency current transformers.

C. The Necessity of the Research based on Challenges of the Literature

According to the papers reviewed in the literature, various techniques such as wavelet transform, deep learning methods, convolutional neural network approaches, power spectral subtraction methods, multiple-narrow band antennas, radiometric approaches, and high-resolution data acquisition techniques are employed to detect PDs in high voltage apparatus.

TABLE 1
SUMMARY OF LITERATURE REVIEW

References	Description	Challenges
[1-2]-[7]-[19-20]	Wavelet transform is used for de-noising of PDs	Reference noise is not implemented
[3-5]	Wavelet transform is used for operation, transmission line fault detection and power quality event classification.	Detection and localization of PDs occurred in the XLPE cables are not performed.
[6]	Generalized cross-correlation method is used to locate PDs in cables.	Unlike the wavelet, transformation of PD signal in the time and frequency domains is not available, and so, noise removal is less accurate.
[8-9]	An adaptive method is used for de-noising PDs occurred in cables.	Reference noise is not implemented, and so, the accuracy of the method is low.
[10]	Acoustic wave sensing system based on fiber optic Mach-Zehnder interferometer is used for PDs detection.	Unlike the wavelet, transformation of PD signal in the time and frequency domains is not available, and so, noise removal is less accurate.
[11]	The type of background noises is studied	De-noising of PDs is not performed
[12]	Ultra-high frequency noise removing approach is studied	Reference noise is not implemented
[13]	Deep learning method is used for detecting PDs.	De-noising of PD signals is not performed.
[14]	Classification of background noises is performed.	De-noising of PD signals is not performed.
[15]	Power spectral subtraction is used for de-noising PDs.	Reference noise is not implemented
[16]	Multiple-narrow band antenna is used for de-noising PDs.	Only radio frequency noises are considered.
[17]	Radiometric methods for PD detection are reviewed.	De-noising of PD signals is not performed.
[18]	High resolution data acquisition device is used for detection of PDs.	De-noising of PD signals is not performed.

The main challenges associated with these reviewed papers are presented in Table 1. According to the literature review, various methods are available for denoising PD signals detected in cables installed within energized substations. However, when the precise location of a failure or PD along the cable's length is a concern, a specialized denoising method becomes necessary. In certain PD localization methods, one must consider the reflection of the wave from the cable's end, where its travel time depends on the wave propagation speed at a specific frequency. Consequently, some denoising methods require the separation of PD-related frequencies from the frequencies associated with environmental noise. Therefore, an effective denoising method that encompasses both time and frequency domains becomes essential, and the wavelet transform has proven to be suitable for this purpose.

In this paper, we introduce PD detection circuits applied for online PD detection in XLPE cables, employing the wavelet transform for denoising. The method introduced by Shim et al [19] and Ma et al [20] does not employ reference noise; instead, it uses a Gaussian model to characterize various noise distributions. Given that a significant portion of environmental noise resembles white noise with a distribution similar to the standard Gaussian model, this approach appears suitable. However, in modern power systems equipped with power electronic devices, other noise distributions, such as impulsive noises generated by these devices, are prevalent. Therefore, because some of the existing noises do not follow a Gaussian distribution, this paper utilizes an antenna to capture the waveform of existing noises as reference noise. These reference noises are then utilized to remove noise from the PD signals.

D. Novelty and Main Contributions of the Paper

Based on the literature review and the identified research gap in the field of detecting PD signals in high voltage XLPE cables, this paper makes the following contributions:

- Investigation of the characteristics of partial discharge signals occurring in XLPE cables, with a particular focus on their frequency spectrum.
- Application of wavelet transform for denoising PD signals in high-voltage XLPE cables.
- Exploration of the characteristics of detected PD signals in XLPE cables within a high-voltage laboratory setting, aiming to determine the suitable mother wavelet, appropriate decomposition level, and the most effective denoising techniques.
- Introduction of a practical method that utilizes reference noise for denoising PD signals.
- Validation of the proposed method's effectiveness through several case studies.

E. Organization and Structure of the Paper

In accordance with the study's objectives, the paper is structured as follows:

In the second section, we introduce the detection circuit, including various sensors that can be utilized. The third section

is dedicated to the proposed method based on wavelet transform for addressing reference noises. Simulation results are presented in the fourth section. Finally, a summary of the paper in the last section is provided.

II. PD Phenomenon

Medium and high-voltage cables are widely used in power systems today. This is due to the improvement of their reliability in comparison with overhead lines. Many natural events interfere with the operation of power systems, such as lightning, tower breaking, and falling due to the snowfall, among others, but they do not have any effect on the operation of power systems when power cables are used and installed underground. Cross-linked polyethylene cables are one of the most reliable types of underground cables used in high voltage or extra-high voltage power system distribution and transmission networks. The specific structure of the polyethylene material allows this insulation to withstand high temperatures, reaching up to nearly 900 °C [21]. In electrical markets, the reliability of power systems is crucial, and customers are even willing to pay higher prices to ensure uninterrupted service. Thus, utilities should improve their system's reliability. One of the problems that increase the risk of failure in a power system is the failure of cable insulation. It is understood from experience that the occurrence of a partial discharge often leads to major insulation failure and service interruption if not detected through an online monitoring system.

Partial discharge is due to the existence of voids in the cable insulation. Air fills these voids, and since the dielectric resistance of air is lower than that of polyethylene, partial discharge occurs when the voltage over the void is higher than the air discharge inception voltage. However, if the magnitude of the partial discharge is kept lower than the permissible value, it poses no harm to the insulation. Serious increases in the magnitude of partial discharge over the life of the insulation can result in a breakdown.

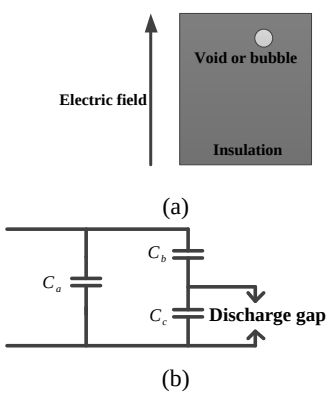

Fig. 1. The a-b-c model of PD (a) void or bubble in insulation, (b) a-b-c model [22]

The partial discharges that occur in high voltage XLPE cables arise from the presence of cavities, impurities, water drops, and air bubbles in the insulation, which reduce the insulation strength of the cable. By applying a high voltage across the cable insulation, the intensity of the created electric field may exceed the insulation strength, leading to currents with high-frequency impulses called PD. To study the partial discharges that occur in cables, the a-b-c model is used, as presented in Fig. 1. In this model, the cavity or bubble is presented by capacitor C_c, insulation placed in top and bottom of the cavity is modeled by C_b, and the insulation placed in right and left of the cavity is modeled by C_a. When, high voltage with magnitude V_a is applied to the insulation, according to the voltage division theorem, voltage with magnitude V_c is applied on capacitor C_c (cavity or bubble) that is calculated by:

$$V_c = \frac{C_b}{C_c + C_b} V_a \tag{1}$$

If the magnitude of voltage applied on cavity or bubble is more than the insulation strength, short circuit is occurred. Thus, the impulse currents are resulted as presented in Fig. 2. The amplitude of these impulse currents is calculated as:

$$i_{PD} = C_c \frac{dV_c}{dt} \tag{2}$$

When PDs occur in polymeric materials, due to the erosion of dielectric materials caused by physical and chemical mechanisms, they lead to the formation of pits and craters on the cavity surface. Some physical and chemical mechanisms created by PDs include the bombardment of the cavity surface by photons and charge carriers, an increase in the local temperature resulting from high-temperature discharge gases, and chemical reactions activated by excited molecules or chemical compounds in the gas and solid phases, especially ozone and oxygen [24].

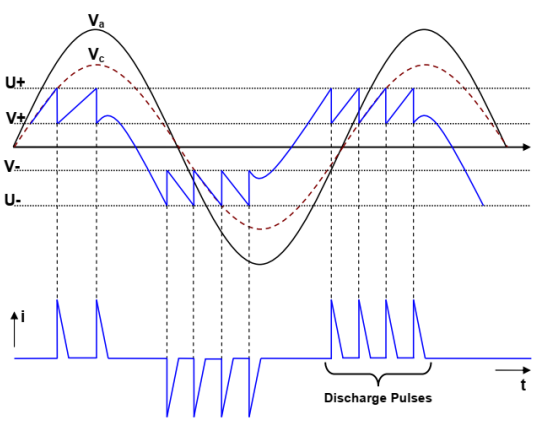

Fig. 2. The impulse currents of PDs [23]

III. The Circuit for Detecting PDs

After measuring the magnitude of the PD, if it exceeds the permissible value, it should be located along the length of the

cable where it is occurring. Subsequently, necessary actions must be taken to prevent its extension to other parts of the cable system. Online detection and location of partial discharge are imperative for this purpose. In online cable monitoring, the PD magnitude can be continuously measured while the power system is operational, and if necessary, warnings can be issued. To successfully measure online PD signals, it is essential to distinguish between the noises present at the measurement site (i.e., a substation) that can interfere with the PD signals. The differentiation between the detected signal and a genuine PD is necessary. Therefore, de-noising should be performed to extract the partial discharge signal from the detected signal.

The circuit utilized for PD measurement is depicted in Fig. 3. This system comprises several components. The sensor is an inductive type with a bandwidth of 100 MHz, essentially functioning as a high-frequency current transformer that detects the PD signal. This high-frequency PD signal is then amplified by a wide-band amplifier. An oscilloscope is employed to observe and record the waveform of the PD signal, with a bandwidth of 250 MHz. In this method, there is only one sensor for measuring the PD signal, which may pick up various environmental noises. There is no additional sensor in this circuit for measuring reference environmental noises. The length of the 11 kV XLPE cable used in this experiment is 2.4 meters. According to the rated values of the detection devices and the frequency characteristics of PD signals, the sampling rate for this experiment is set at 100 Mega samples per second.

Several sensors can be used for the detection of PD signals. In this section, two types of these sensors are introduced [24-26]. Inductive sensors detect the PD signals through the induced current, which is proportional to the magnetic field of this signal. The PD signal is a high-frequency current that has two components in the shield of the cables, as shown in Fig 4. One of these components is the current IZ that induces the current in the rectangular coil.

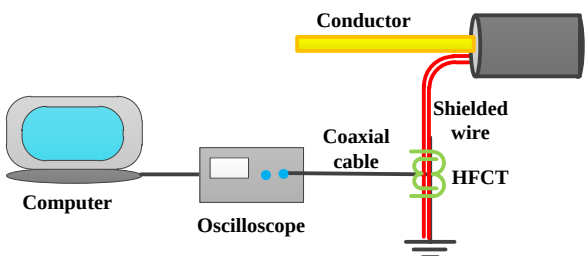

Fig. 3. The circuit for PD detection [25]

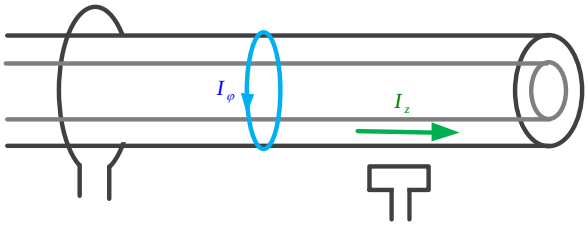

Fig. 4. Principle of an inductive sensor [25]

The other component of PD signal is I_φ that inducts a current in the circular coil as shown in Fig 4. The disadvantage of this sensor is its significant pick up of the external noises which affect the detected signals. In Fig 3, another type of inductive sensor (HFCT) is used for detection of PD signals in HV XLPE cables.

The various layers of XLPE cables consist of capacitive elements. These layers include an inner semi-conducting layer, insulation or dielectric, and an outer semi-conducting layer. The shield is connected to the ground. When a metallic ring is placed over the sheath, there will be four capacitive layers, and the PD signal voltage will be divided among them. By detecting the voltage on this ring, the PD signal can be identified. These sensors are also used to detect PD signals in power transformers. The copper strip serves as the capacitive sensor and is placed on the transformer HV bushing. The HV conductor of the transformer bushing and this copper strip create a capacitance that picks up the PD signal. By connecting this copper strip to the ground, the PD signal can be detected, initially by passing this connection through a high-frequency current transformer (Fig 5), and subsequently by adding a resistor in series and measuring its voltage (Fig 6).

In the high-voltage lab, voltages up to 20 kV were applied to an 11 kV XLPE cable with a 2.4 m length, connected as shown in Fig. 7, and the PD signal was detected. Fig. 8 presents the results of this experiment. Fig. 8.a shows the PD signal versus time. This signal is a damped oscillatory pulse in which a main oscillating signal with a period of 50 ns can be recognized. Its frequency spectrum is shown in Fig. 8.b.

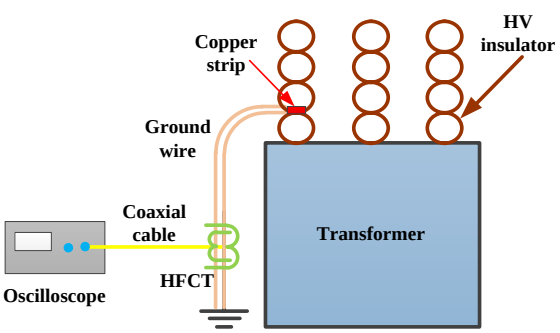

Fig. 5. Capacitive sensor in the power transformer and a HFCT for detection of partial discharge [26-27]

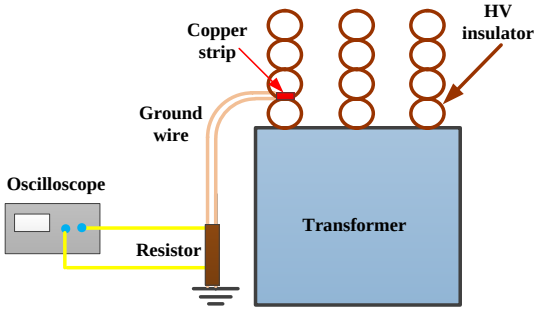

Fig. 6. Capacitive sensor in the power transformer and a HFCT for detection of partial discharge [26-27]

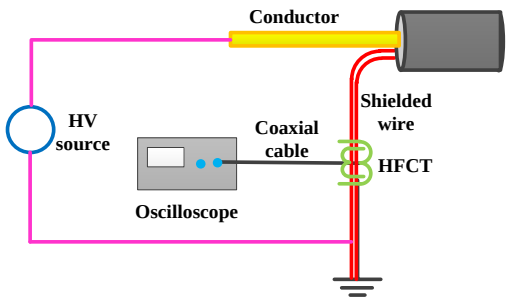

Fig. 7. The circuit employed in high voltage lab for PD detection in XLPE cable [25]

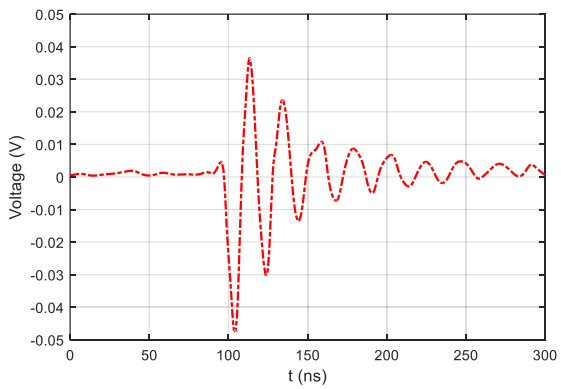

(a)

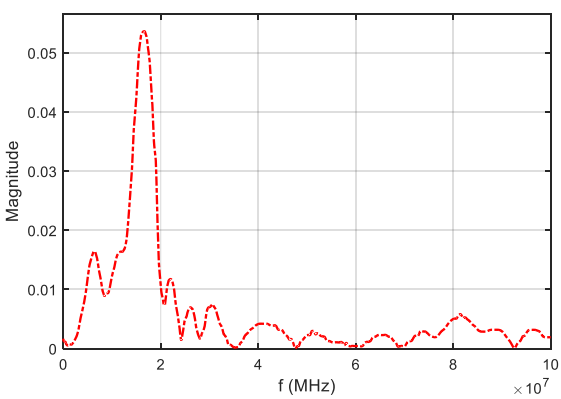

(b)

Fig. 8. (a)- PD signal in XLPE cable, (b)- Frequency spectrum PD signal in XLPE cables [25]

The PD signal of this XLPE cable involves a frequency spectrum around 20 MHz and it may have some higher frequencies. As can be seen in the figure, the amplitude of frequency components higher than 30 MHz is low. Thus, the sampling frequency for detecting PD signals occurred in the XLPE cables can be less than 30 MHz. For enhancing the accuracy of the proposed method, the HFCT used in this experiment have an acceptable transfer function up to 100 MHz.

IV. Wavelet Transform Method for PD De-Noising

In the Fourier transform, a function is converted from the time domain to the frequency domain, and the time parameter is not present in the final domain. De-noising a signal using the Fourier transform involves identifying the frequency spectrum that corresponds to the noise and distinguishing it from the PD signal. By applying filters, the frequencies associated with noise are removed, leaving only the PD signal. The results of the PD measurement are also used to determine the location of the PD. This is achieved by calculating the time between the detection of the signal and its reflection from the end of the cable, taking into account the propagation speed of the PD signal in the cable shield.

As previously mentioned, the Fourier transform has been the most commonly used tool for analyzing the frequency characteristics of a given signal. However, after transformation, time information is lost, making it difficult to determine when a specific frequency occurs [28]. Traditional approaches for signal processing are generally based on either the time or frequency domain for analyzing and extracting PD events. In the case of the frequency domain, the Fourier transform assumes that signals can be represented as a sum of sine and cosine waveforms. While the signal can be analyzed throughout the frequency domain following the Fourier transform, time information is lost.

Partial discharge signals often exhibit non-periodic and fast transient features, which are not effectively revealed by the Fourier transform. This limitation has led to the recognition of the need for more powerful mathematical tools in signal analysis and processing by researchers and engineers. Among these tools, wavelet and Gabor transforms are employed to obtain two-dimensional information about PD pulses in both the time and frequency domains, allowing for the extraction of features from measurement data.

The Gabor transform is a special case of the short-time Fourier transform, which extracts sinusoidal frequency and phase content from local sections of a signal as they vary over time. The signal is first multiplied by a Gaussian function, acting as a window function, and then transformed using a Fourier transform to provide time-frequency analysis. The window function gives higher weight to the signal near the time being analyzed [30]. The Gabor transform represents a

signal as a set of properly shifted and modulated Gaussian elementary signals. However, its effectiveness is limited when dealing with PD signals containing non-Gaussian noise, and it can be computationally challenging to compute Gabor coefficients. For de-noising PD signals in power substations that involve various types of noise, the wavelet transform is a more suitable choice.

The continuous wavelet transform for a function, such as $f(t)$, is defined as follows [31].

$$CWT_{\psi}f\ (a,b) = W_f\ (b,a) = |a|^{\frac{1}{2}} \int_{-\infty}^{\infty} f(t)\psi^*(\frac{t-b}{a})dt \qquad (3)$$

In this equation $a,b \in R.\ a \neq 0$, 'b' is the value by which the function is shifted in the time domain and 'a' is the scale that multiplies by time and is used as the frequency factor. The function $\Psi(t)$ is mother wavelet and it has several different types such as Haar, Daubechies family, Coiflet1, Symlet2, Meyer, Morlet and Mexican Hat that the different types of wavelets are resulted of these types of mother wavelet functions [31]. For different application the specific types of this mother wavelet is used and for removing the noises from the PD signal Daubechies family can be applied. It is suitable for this purpose, since the waveforms of partial discharge signal is similar to these mother wavelet functions and the noises have the different characteristic that it is easy to remove them from the partial discharge signal. The waveform of the Daubechies mother wavelet functions is presented in Fig 9. In [31], discrete time wavelet transform definition is given.

Due to the similarity between PD signals occurring in HV cables as presented in Fig 7 and the mother wavelet of Daubechies7, Daubechies7 is applied for PD signal denoising in HV XLPE power cables in this paper.

For denoising using the wavelet transform method, there are three stages: First, the conversion of the waveform of the signal and noise to the wavelet domain is performed, and the level and the coefficients in this domain are determined. Then, in the wavelet domain, the separation of noise and PD is carried out, and finally, the denoised PD signal is reconstructed in the time domain. The procedure is illustrated in Fig 10.

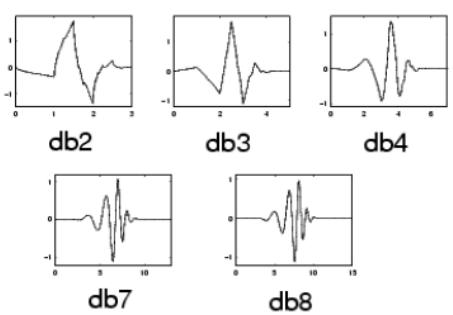

Fig. 9. Daubechies mother wavelet functions family [31]

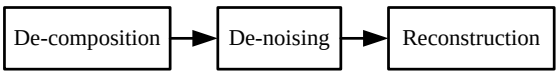

Fig. 10. De-noising procedure [27]

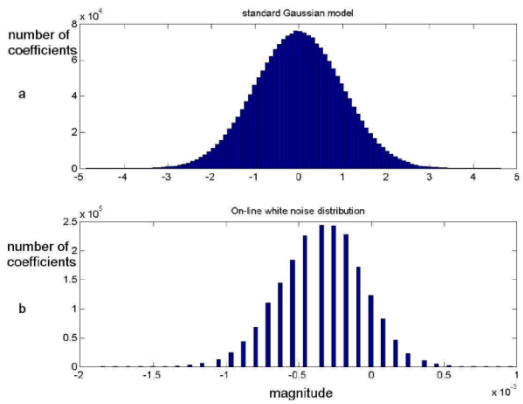

Fig. 11. Gaussian distribution function of white noise [32]

In the old method employed by Shim et al [19] and Ma et al [20], a Gaussian model is utilized to represent the noise distribution. Based on this model, noise removal is performed in the wavelet domain. This model is well-suited for white noises, such as ambient and random noises like thermal noise, and so on. However, in modern power substations, there exist various noises for which the standard Gaussian distribution is not suitable for modeling. These noises often exhibit amplitudes that may exceed the magnitude of partial discharge signals, making it challenging to detect partial discharge signals in their presence.

In the substations of power system, there are four types of noise that include [32]:

1- White noise: the environmental noises and the noises associated with amplifiers are placed in this category. This type of noises named white noise has Gaussian distribution function as presented in Fig. 11. To removing this type of noises from PD signals, the previous methods based on Gaussian noises that do not require to the reference noise can be used.

2- Discrete spectral interference (DSI) that includes telecommunication and radio signals such as modulated AM and FM signals. This type of noises has narrow band specification and to remove them from PD signals, digital filters such as notch filter and spectrum analysis method can be implemented.

3- Repetitive or pulse type noises that include the pulses are arisen from power electronic devices such as thyristor fire pulses. This type of noises has repetitive nature and is repeated regularly at each cycle of power frequency. The band width of these noises is wide and for removing them from PD signals, the methods in time domain such as gate circuits are applied.

4- Switching noises that are random high frequency

pulses. This type of noises is arisen from switching occurrence of different devices, lightning and corona discharge of high voltage apparatus. The switching pulses have wide bandwidth and are typical source of disturbances. The most problem for de-noising PD signals are arisen from this type of noises. The frequency characteristic of these noises is very similar to the PD signals, and so, the notch filters cannot be used for removing of them. On the other hand, due to the random nature of these noises, the gate circuits cannot be used for removing them.

By studying different types of noises, it is concluded that some of these noises do not have Gaussian model and we cannot apply the Gaussian model for them, thus the old method is not suitable for modeling all noises in substations. Fig. 12 presents the distribution of real noises in the substations and compares it with Gaussian distribution function that is suitable for modeling white noises. In the proposed method there are two sensors. One of them such as an antenna is applied for measurement of only noises. It samples the noises when the cable is out of the system and the breaker of this bay is disconnected. Thus the results of this sensor are only the noises that are used for the reference noises.

The second sensor is applied for measurement of the partial discharge signal that is noisy. This sensor records the signal by a specific sampling rate when that cable is alive. There are several options for measurements of the background noises; one is that the sensor measures the signals when the cable is out of service, second is to measure the signal when there are two bays and one of them is out of service, and in the last option, an antenna can be used to detect the noises available in the environment. Then conversion of the measured signal by the sensors to the wavelet domain is done and in this domain the coefficient of the reference noise is applied on the threshold to remove the noises from the detected signal.

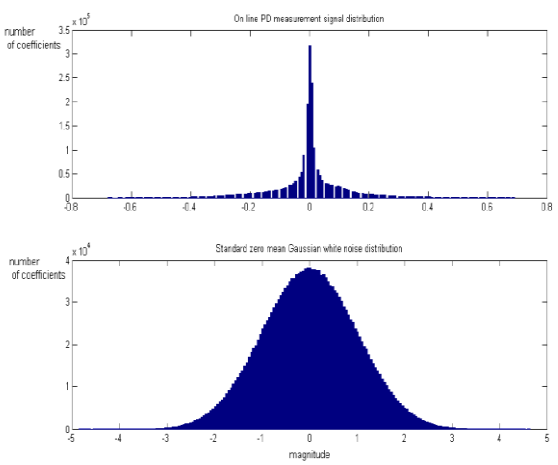

Fig. 12. Distribution function of white and real noises [32]

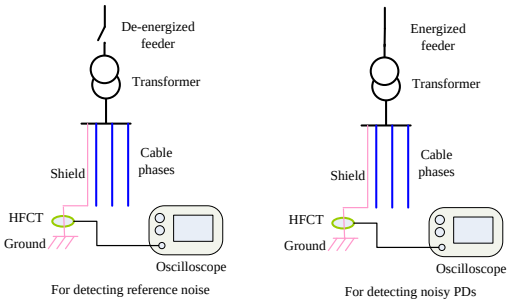

Fig. 13. Single line diagram of circuits proposed for detecting PDs

Thus, according to the proposed method, de-noising of PD signals is performed by following steps:

Step1. Using of HFCT, the noisy PD signals are detected and presented on oscilloscope. Then, data of noisy PDs is transferred to the computer.

Step 2. Reference noise is detected by an antenna or by HFCT when the feeder is de-energized. The single-line diagram of PD detecting system is presented in Fig. 12. As can be seen in the figure, when, the feeder is de-energized, the HFCT placed on cable shield detects noises, and when the feeder is energized, the HFCT detects noisy PDs.

Step 3. The reference noise is transferred to wavelet transform. The suitable mother wavelet, number of de-composition levels and de-noising technique are determined in the next part. The outcomes present that for de-noising PDs occurred in XLPE cables, db7 is an appropriate mother wavelet, between 5 to 20 decomposition levels is suitable and hard type de-noising technique is better than soft type de-noising method.

Step 4. The threshold level required for de-noising PDs is selected based on the reference noise.

Step 5. The noisy PD signal is transferred to the wavelet domain by considering suitable mother wavelet and appropriate de-composition level.

Step 6. By threshold determined in step 4, using hard de-noising technique, de-noising process is performed.

Step 7. The de-noised PD signals are reconstructed in time domain.

To compare the suitability of different mother wavelet for de-noising PD signals from noises, SNR index is calculated as:

$$SNR = 10 \log \frac{\sum_{i=1}^{n} y^2(i)}{\sum_{i=1}^{n} (x(i) - y(i))^2} \quad (4)$$

In (4), *x(i)* is the initial PD signal and *y(i)* is the de-noised PD signal. For de-noising by wavelet transform, two approaches including hard and soft techniques presented in Fig. 14 can be applied. According to the literature review, hard de-noising technique is better than soft de-noising technique [31].

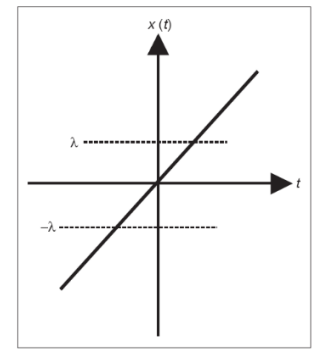

(a)

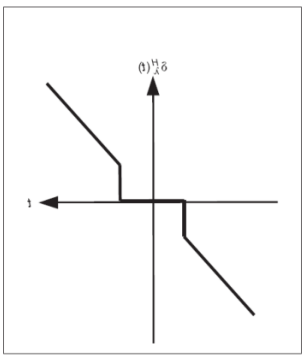

(b)

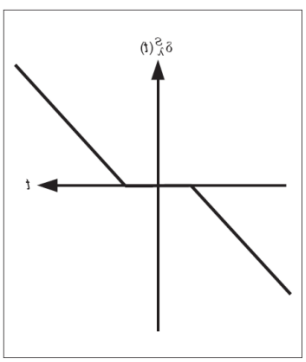

(c)

Fig. 14. (a) initial signal (b) hard de-noising method (c) soft de-noising method [32]

V. Case Studies

In the first study, the following steps were performed to determine the suitable mother wavelet and de-noising technique:

1. A sample of partial discharge signals related to a specific cable, tested under the application of high voltage, was recorded by a digital scope with a 250 MHz bandwidth.

2. Based on the characteristic of PD signals occurring in XLPE cables, four samples were simulated using a mathematical function obtained by multiplying a sinusoidal function and an exponential function. These functions were combined with the noises measured in a substation to create a noisy signal.

3. Different mother wavelet functions were employed to de-noise these noisy signals.

4. The de-noised signals were then compared with the corresponding original signals.

5. The signal-to-noise ratio (SNR) factor was used as a measure to evaluate the performance of the different mother wavelet functions. It was found that db7 had the highest SNR factor.

Fig. 15 presents the initial PD signals, the added noise, and the extracted PD signals for different mother wavelet applications. Additionally, in Figure 16, the steps of the proposed method performed in MATLAB software for de-noising PD signals with reference noise are presented. As shown in the figure, the proposed method follows seven steps to de-noise PD signals.

Table 2 presents the values of SNR obtained for different mother wavelet functions. The results present db7 is a suitable mother wavelet for de-noising PDs occurred in XLPE cables.

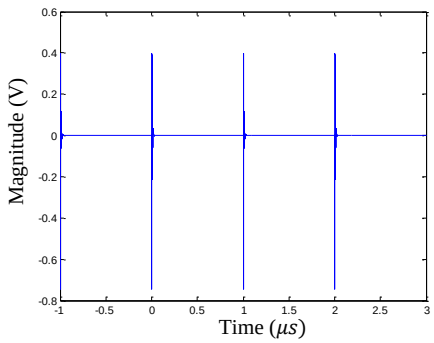

(a)

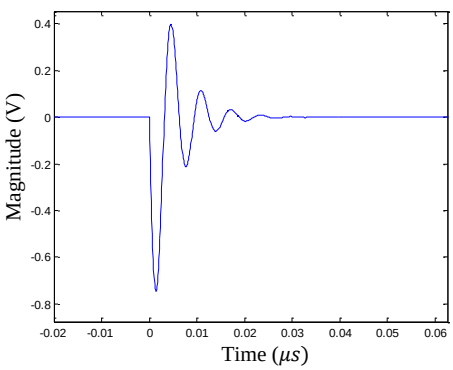

(b)

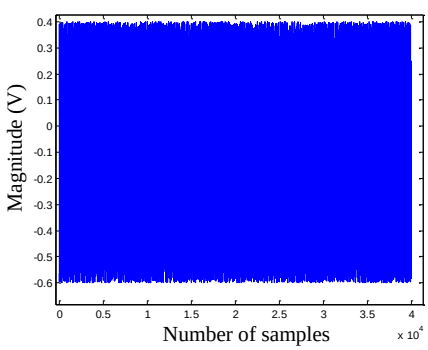

(c)

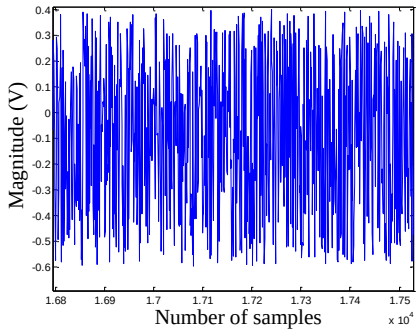

(d)

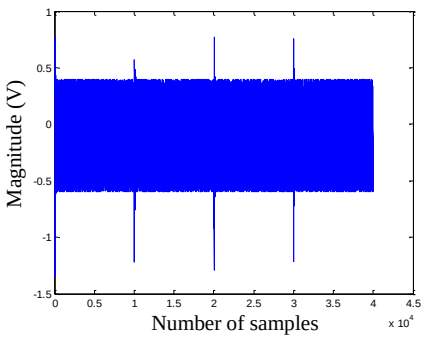

(e)

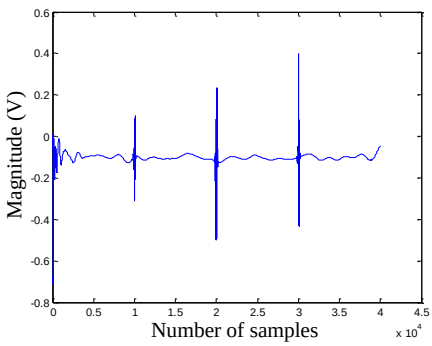

(f)

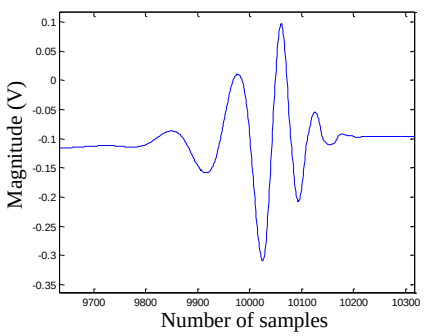

(g)

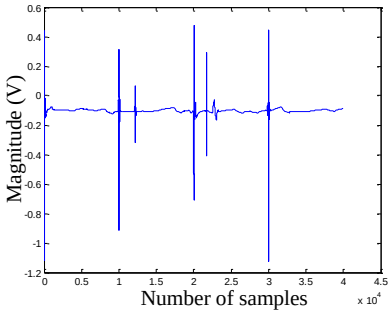

(h)

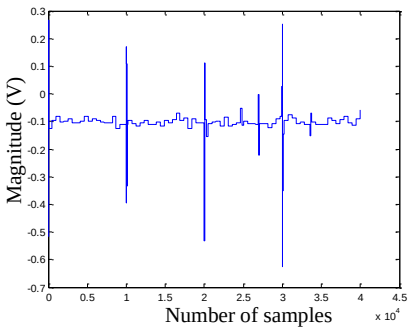

(i)

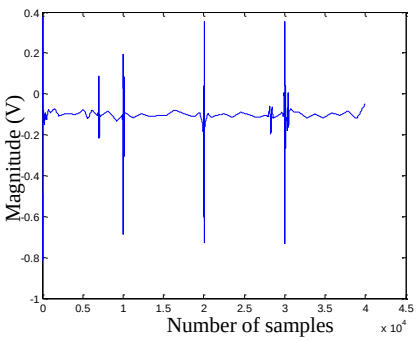

(j)

Fig. 15. (a) initial PDs (b) enlarged figure of PD (c) noises (d) enlarged figure of noises (e) noisy PDs (f) extracted PDs by db7 (g) enlarged extracted PD by db7 (h) extracted PDs by db2 (i) extracted PDs by Haar (j) extracted PDs by coiflet1

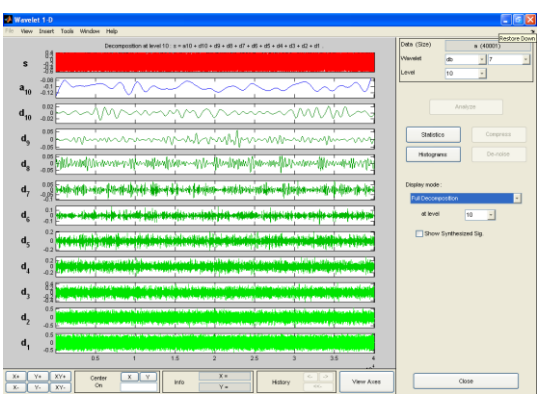

(a)

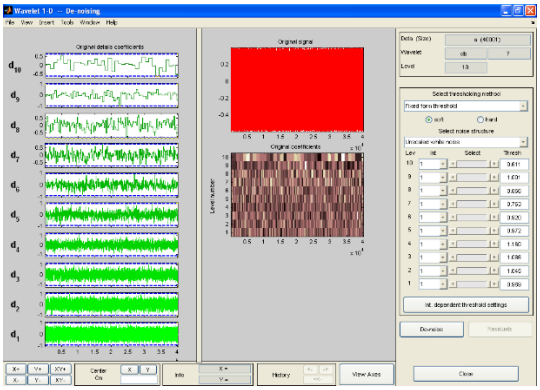

(b)

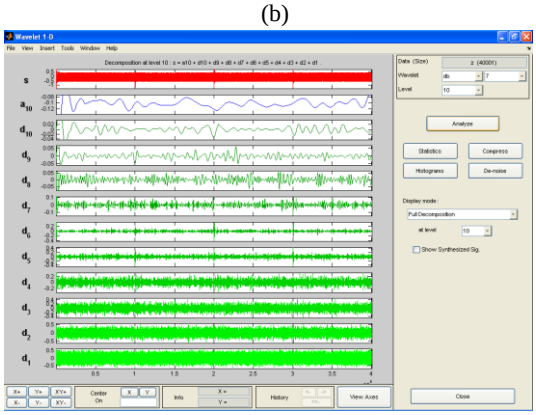

(c)

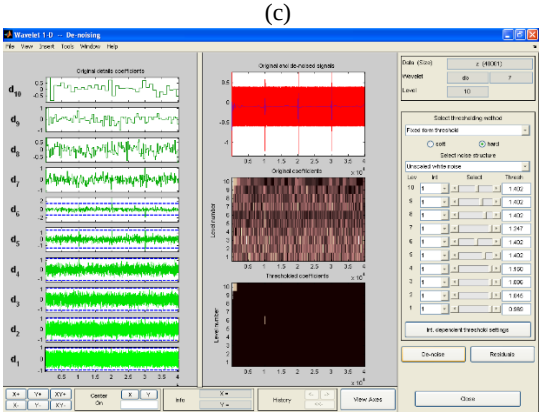

(d)

Fig. 16. (a) wavelet transform of reference noise (b) threshold determination by reference noise (c) wavelet transform of noisy PDs (d) noise removing of PDs

TABLE 2
SNR FOR DIFFERENT MOTHER WAVELET FUNCTIONS

Mother wavelet function	SNR (dB)
Haar	24.7
Coiflet1	19.6
Symlet2	27.1
Meyer	22.8
Morlet	36.5
Mexican Hat	40.1
Daubechies 2	37.3
Daubechies 3	38.2
Daubechies 4	43.5
Daubechies 7	49.6
Daubechies 8	45.2

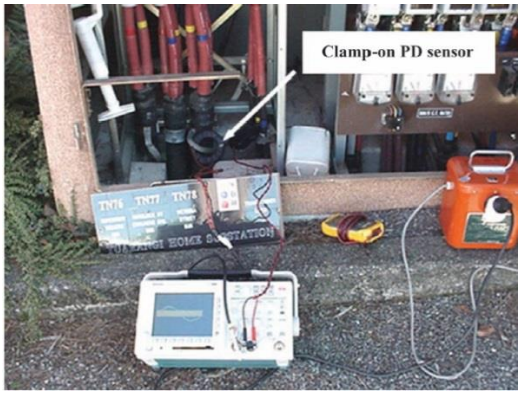

(a)

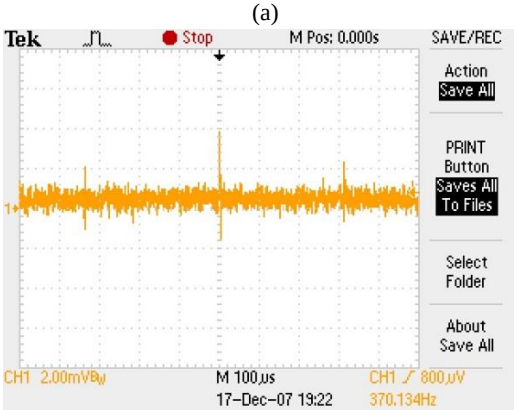

(b)

Fig. 17. (a) Test system used for detecting PDs in Poonak substation and (b) presented signal on oscilloscope

As for the second case study, in this section, the recorded measurements of a substation are utilized to be de-noised using the suggested method. The following presents the results of a PD test conducted on a 20 kV XLPE cable for the Nahal feeder in Poonak substation in Tehran.

During this test, the first stage involves de-energizing the feeder, and the HFCT connected to the shield detects the reference noise. In the second stage, the feeder is energized, and the HFCT connected to the shield detects the PD signals along with the accompanying noises. The oscilloscope used in this experiment has a bandwidth of 250 MHz, while the HFCT has a bandwidth of 100 MHz. The HFCT is connected to the oscilloscope via a coaxial cable, which includes a low-pass filter that filters out frequencies above 30 MHz. Fig. 17 presents the test system set up for this experiment.

In Fig 18, a, b and c are the noisy PD signal, the reference noise signal, and the PD signals after de-noising, respectively. In this method db7 mother wavelet up to level 10, hard threshold approach based on the reference noise and the wavelet toolbox of MATLAB are applied. As for the third case study, a substation in Fars province is being examined. The results of the PD measurement of the XLPE cable in Kheir-Abad substation are presented in the following figures. In this substation, a similar procedure to the one used in Poonak substation is being followed. The oscilloscope and HFCT used in this experiment have bandwidths of 250 and 100 MHz,

respectively. In this test, the db7 wavelet up to level 6, a hard threshold based on the reference noise, and the wavelet toolbox of MATLAB are being applied. Fig. 19 displays the detected signal (a), the reference noise (b), and the PD signal after de-noising (c). These coefficients represent the maximum magnitudes obtained from the wavelet decomposition of the reference noise.

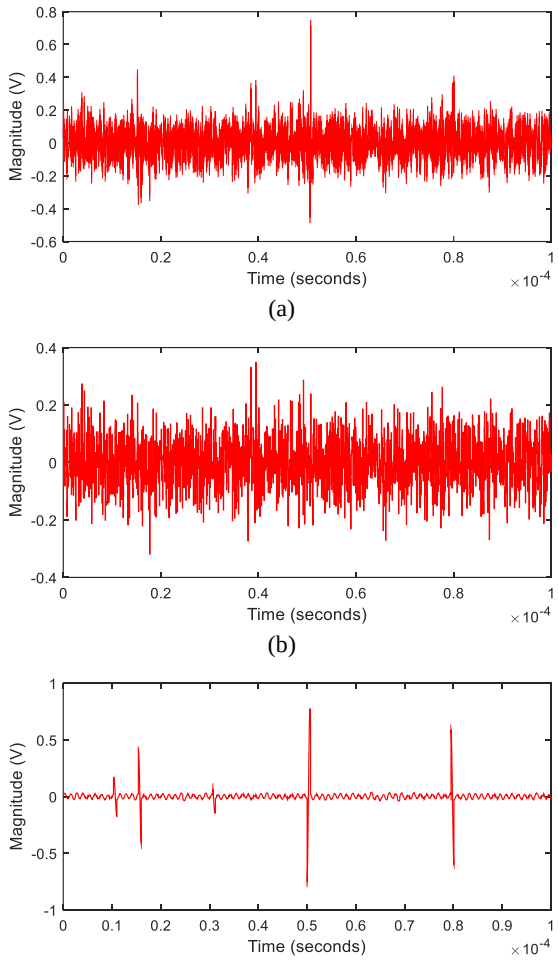

(a)

(b)

(c)

Fig. 18. Poonak substation (a)- Detected signal, (b)- Reference noise, (c)- PD signals after noise removing

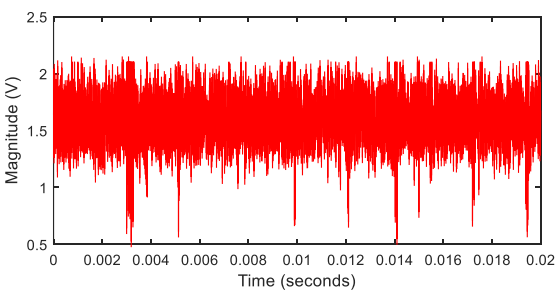

(a)

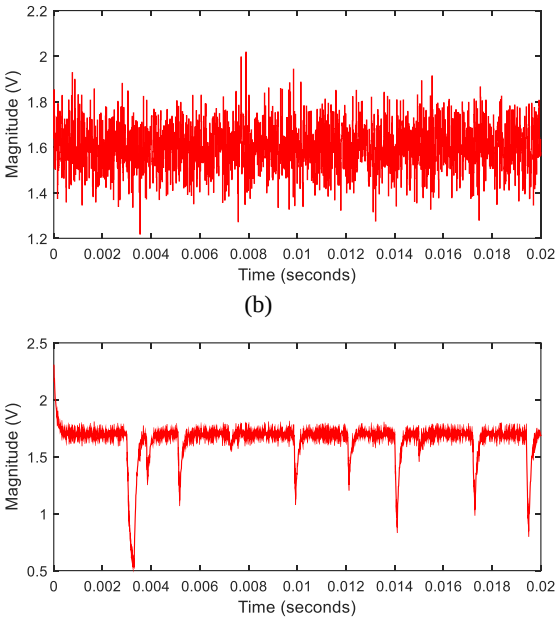

(b)

(c)

Fig. 19. Kheir-Abad substation (a)- The detected signal, (b)- Reference noise, (c)- The PD signal after noise removing

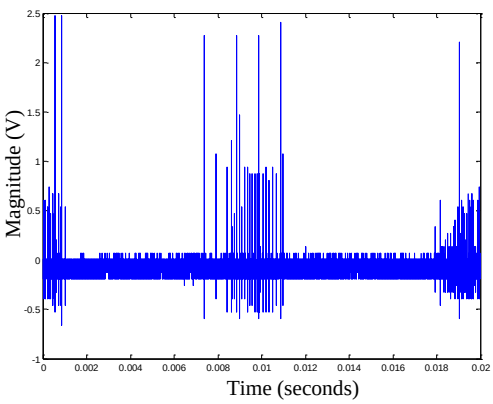

(a)

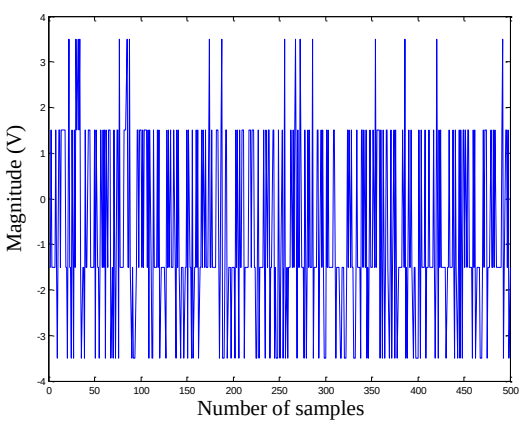

(b)

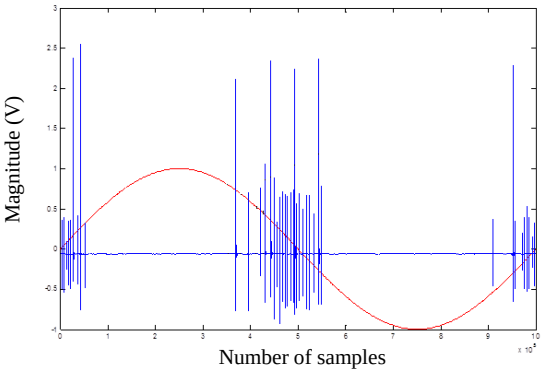

(c)

Fig. 20. Afsarieh Substation (a)- The detected signal, (b)- Reference noise, (c)- The PD signal after noise removing

For detecting PD signals in Afsarieh substation, similar procedure used in previous case studies is followed. The Afsarieh substation located in Tehran is a 230kv/63kv substation. The measurement devices are placed on 63 kv side. The noisy PDs, reference noise and PDs extracted from noisy signals are presented in Fig. 20. As can be seen in the figure, the proposed technique with good accuracy removes the noises of PDs.

VI. Sensitivity Analysis

To select the suitable de-noising method, we perform the de-noising of noisy PD signals using the soft de-noising approach based on the db7 mother wavelet. The initial PD signals, as presented in Fig. 15, are contaminated with noise. Then, following the soft de-noising method, we determine and present the extracted PD signals in Fig. 21. From the figure, it is evident that the performance of the hard de-noising method in removing noise from PD signals is superior to the soft de-noising approach. The SNR index associated with the soft de-noising method is 38.1, which is lower than the SNR index associated with the hard de-noising method, which is 49.6. In this stage, the impact of number of de-composition level on performance of PD signals de-noising is investigated.

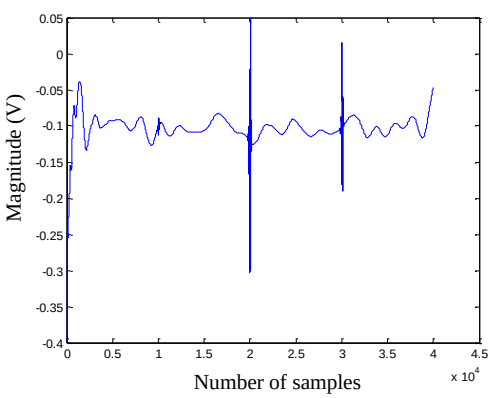

Fig. 21. PDs extracted by soft de-noising method

TABLE 3
SNR FOR DIFFERENT NUMBER FOR DE-COMPOSITION LEVEL

Number of de-composition	SNR (dB)	Number of de-composition	SNR (dB)
2	11.82	13	50.04
3	25.77	14	50.18
4	39.26	15	50.24
5	42.65	16	50.33
6	46.72	17	50.47
7	48.53	18	50.69
8	48.80	19	50.74
9	49.34	20	50.82
10	49.61	21	50.98
11	49.78	22	51.06
12	49.89	23	51.12

For this study, the number of de-composition level for de-noising of PD signals polluted by noises (presented in Fig. 15), is changed from 2 to 23, and by hard de-noising technique and db7 mother wavelet, the PD signals are extracted. The SNR indices associated with this study are calculated and presented in table 3. As can be seen in the table, for understudied PDs and noises, when the number of de-composition level increases from 7 to 2023 the value of SNR index do not change significantly. Thus, for preventing from high volume of computation, the suitable number of de-composition level is between 7 and 10.

VII. Discussion

To study the effectiveness of the proposed method, de-noising of PD signals occurred in this substation is performed by old method that do not use the reference noise. By wavelet transform and without reference noise, de-noising of noisy PD signals presented in Figs. 18, 19 and 20 is performed. The results are presented in Fig. 22. As can be seen in the figure, the de-noised PD signal is still noisy. Thus, the proposed method has been able to separate the noise from the PD signals better than the method without reference noise.

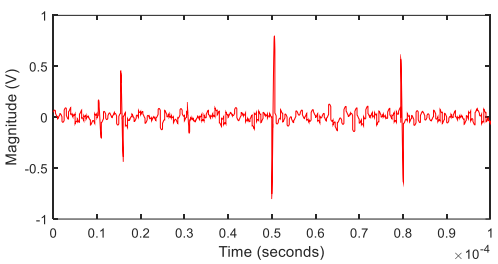

(a)

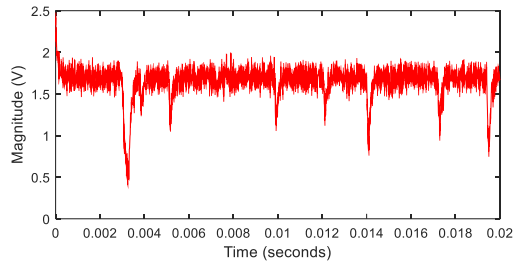

(b)

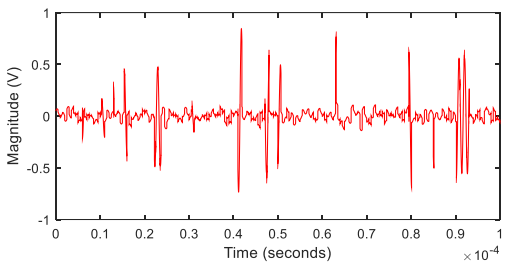

(c)

Fig. 22. PD signals after noise removing without reference noise (a) Poonak substation (b) Kheir-Abad substation (c) Afsarieh substation

For comparing different methods mentioned in the literature review that can be used for de-noising of PDs with the proposed method based on the wavelet transform, the PD signals of first case study are used. According to the first case study, the PD signals are polluted with different noises. Then, by different methods including improved generalized cross-correlation time delay estimation approach as method 1, total least-square with Matern Kernel as method 2 and recursive continuous s-shaped approach as method 3, de-noising of polluted PDs is performed. The SNR related to the outcomes of these methods as well as the SNR related to the outcome of de-noising by proposed method are presented in table 4. As can be seen in the table, the accuracy of the proposed technique is more than other methods.

TABLE 4
SNR FOR DIFFERENT DE-NOISING METHODS

Methods	SNR (dB)
Proposed method	49.6
Method 1	39.2
Method 2	42.6
Method 3	39.8

VIII. Conclusions

In this paper, a method based on the wavelet transform approach, considering the reference noise, is employed to remove different noises from recorded partial discharge signals occurring in XLPE cables. This method utilizes the MATLAB toolbox associated with wavelet transform. The suitable mother wavelet, threshold for de-noising, number of decompositions, and noise rejection technique are selected based on the characteristics of PDs occurring in XLPE cables. The waveform of PDs leads to the selection of the db7 mother wavelet. Additionally, the background noise is obtained through off-line measurement, another sensor placed on a de-energized feeder, or an antenna, and is applied as the reference noise. The proposed approach effectively performs noise rejection on PD signals occurring in XLPE cables. It accurately detects the pulses of PDs, which can be used to determine the location of partial discharge. This method relies on the available data regarding the time between the PD signal and its reflection from the end of the cable. Two sensors are used in this method: one for measuring the PD signal mixed with noise and the other solely for measuring the background noises. For future work, one can explore other new methods introduced in the communication field for de-noising, such as blind source method, SVD method, adaptive filter, non-adaptive filter, and more.

Appendix

The characteristics of test systems and devices applied in the paper for detecting PDs occurred in XLPE cables are presented in Table 4.

TABLE 4
CHARACTERISTIC OF TEST SYSTEMS AND APLIED DEVICES

Characteristic	**Value**
Rated voltage of sample XLPE cable	11 kv
Poonak substation voltage	63kv/20kv
Kheir-Abad substation voltage	63kv/20kv
Afsarieh substation voltage	230kv/63kv
Oscilloscope bandwidth	250 MHz
HFCT bandwidth	100 MHz
Length of sample XLPE cable	2.4 m
Sampling rate	100 Msample/s
Used software for simulation	MATLAB
Used sensor for PD detection	HFCT

References

[22] J. Liu, W.H. Siew, J.J. Soraghan, E.A. Morris, A novel wavelet selection scheme for partial discharge signal detection under low SNR condition, *2018 IEEE Conference on Electrical Insulation and Dielectric Phenomena (CEIDP)*. IEEE, 2018.

[23] R. Hussein, K.B. Shaban, A.H. El-Hag, Wavelet transform with histogram-based threshold estimation for online partial discharge signal denoising, *IEEE Transactions on Instrumentation and Measurement*, vol. 64, no. 12, pp. 3601-3614, 2015.

[24] E. Jafari, Ehsan, Coordinated operation of Wind Farms, Cascaded Hydro, Photo-voltaic and Pump-storage Units by WT-ANN-ICA Prediction Method, *International Journal of Industrial Electronics Control and Optimization*, vol. 4, no. 1, pp. 127-139, 2021.

[25] I. Mousaviyan, S.G. Seifossadat, and M. Saniei, A new and very fast fault detection and classification method based on traveling wave in transmission lines, *International Journal*

of Industrial Electronics Control and Optimization, vol. 4, no. 4, pp. 377-385, 2021.

[26] N. Ghaffarzadeh, A New Method for Power Quality Events Detection and Classification using Discrete Wavelet Transform and Correlation Coefficients, *International Journal of Industrial Electronics Control and Optimization*, vol. 4, no. 1, pp. 47-57, 2021.

[27] M. Guo, J. Xu, Y. Zhang, X. Xiao, Z. Yang, Z. Wu, A partial discharge localization method for AC XLPE cable based on improved GCC algorithm, *IEEE Open Access Journal of Power and Energy*, vol. 10, pp. 605-616, 2023.

[28] J. Zhong, X. Bi, Q. Shu, D. Zhang, X. Li, An improved wavelet spectrum segmentation algorithm based on spectral kurtogram for denoising partial discharge signals, *IEEE Transactions on Instrumentation and Measurement*, vol. 70 pp. 1-8, 2021.

[29] L. Lu, K. Zhou, G. Zhu, X. Yang, B. Chen, Partial discharge location algorithm based on total least-squares with Matern kernel in cable systems, *IEEE Transactions on Industrial Informatics*, vol. 19, no. 3, pp. 2421-2431, 2022.

[30] L. Lu, K. Zhou, G. Zhu, B. Chen, X. Yana, Partial discharge signal denoising with recursive continuous S-shaped algorithm in cables, *IEEE Transactions on Dielectrics and Electrical Insulation*, vol. 28, no. 5, pp. 1802-1809, 2021.

[31] Y. Hao, Y. Chen, Y. Chen, T. Huang, J. Xiao, L. Yang, A partial discharge detection system for XLPE cable terminals and acoustic wave sensing characteristics based on fiber optic mach-zehnder interferometer, *IEEE Sensors Journal*, vol. 21, no. 19, pp. 21782-21790, 2021.

[32] C. Ma, H. Li, W. Zhou, J. Yu, L. Wang, S. Yang, S. Hu, Background noise of partial discharge detection and its suppression in complex electromagnetic environment, *2018 IEEE International Conference on High Voltage Engineering and Application (ICHVE)*. IEEE, 2018.

[33] Z. Tang, C. Wang, W. Chang, C. Li, Q. Lu, J. Qu, A combined noise-rejection method for UHF PD detection on-site, *IEEE Transactions on Dielectrics and Electrical Insulation*, vol. 19, no. 3, pp. 917-924, 2012.

[34] G. Michau, C.C. Hsu, and O. Fink, Interpretable detection of partial discharge in power lines with deep learning, *Sensors*, vol. 21, no. 6, 2154, 2021.

[35] W.J.K. Raymond, C.W. Xin, L.W. Kin, H.Z. Illias, Noise invariant partial discharge classification based on convolutional neural network, *Measurement*, vol. 177, 109220, 2021.

[36] R. Hussein, K.B. Shaban, and A.H. El-Hag, Denoising different types of acoustic partial discharge signals using power spectral subtraction, *High voltage*, vol. 3, no. 1, pp. 44-50, 2018.

[37] T. Bandi, and S. Ohtsuka, Partial Discharge Detection of Multiple-Narrow Band Antenna under the Radio Communication Noise, *IEEJ Transactions on Electrical and Electronic Engineering*, vol. 16, no. 5, pp. 715-721, 2021.

[38] S. Kaziz, M.H. Said, A. Imburgia, B. Mammer, D. Flandre, P. Romano, F. Tounsi, Radiometric Partial Discharge Detection: A Review, *Energies*, vol. 16, no. 4, 1978, 2023.

[39] C. Eastham, Carl, C.D. Smith, and F.C. Chen, Detection and location of PD in MV cables in electrically noisy industrial environments, *21st International Conference on Electrical Distribution*. 2011.

[40] I. Shim, J.J. Soraghan, and W.H. Siew, Digital signal processing Applied to the detection of partial discharge: an overview, *IEEE Electrical Insulation Magazine*, vol. 16, no.3, pp. 6-12, 2000.

[41] X. Ma, C. Zhou and I.J. Kemp, Interpretation of wavelet analysis and its application in partial discharge detection, IEEE Transactions on Dielectrics and Electrical Insulation, vol. 9, no. 3, pp.446-457, 2002.

[42] B. Jahnke and H. Memmer, Installation of the first 400 kV XLPE Cable in Berlin, *Modem Power Systems*, vol. 18, no. pp. 4749, March 1998.

[43] A. Ghaedi, R. Sedaghati, and M. Mahmoudian. "A Complete Analysis for Detection and Localization of Partial Discharges in XLPE Cables, Power Transformers and Generators." Accepted in *Journal of Southern Communication Engineering* (2023).

[44] H. Fadaeeasrami, F. Faghihi, and H. Mohammadnezhad. "A Review of Partial Discharge Signals Occurrence in Polluted High Voltage Insulator." *Signal Processing and Renewable Energy*, vol. 5, no.1, pp. 51-78, 2021

[45] J. M. Rodríguez-Serna, and R. Albarracín-Sánchez. "A study on the life estimation and cavity surface degradation due to partial discharges in spherical cavities within solid polymeric dielectrics using a simulation based approach." *Polymers*, vol. 13, no. 3, 2021.

[46] A. Ghaedi, M. Moeini Aghtaie, and A. Ghaffari, Detection of online PD signals in XLPE cables using the Bhattacharyya distance, *Turkish Journal of Electrical Engineering and Computer Sciences*, vol. 24, no. 5, pp. 3552-3563, 2016.

[47] A. Alesaadi, A. Ghaedi, A. Ghaffari, V. Parvin, De-noising of Online PD Signals in Power Transformers Using the Bhattacharyya Distance, *Trends in Applied Sciences Research*, vol. 7, no. 10, 813, 2012.

[48] M. Ghaffarian, M., V. Vakilian, V. Parvin, A. Ghaedi, Investigation of online detected partial discharges in power transformer, *2008 Australasian Universities Power Engineering Conference*. IEEE, 2008.

[49] W. Chao, "Gabor wavelet transform and its application." *R98942073 (TFA&WT final project)* (2010).

[50] K. Ramprasad, "de-noising of partial discharge signals generated in high voltage power transformer using Gabor wavelet transform" *International Journal of Computers Electrical and Advanced Communication Engineering*, Vol. 1 no. 9, pp. 40-46, 2016.

[51] L. Debnath, et al. "The Gabor Transform and Time–Frequency Signal Analysis." *Wavelet Transforms and Their Applications*, vol. 1, no. 1, pp. 243-286, 2015.

[52] R.S. Pathak, *The wavelet transform*, vol. 4. Springer Science & Business Media, 2009.

[53] H. Zhang, et al. "A novel wavelet transform technique for on-line partial discharge measurements. 1. WT de-noising algorithm." *IEEE transactions on dielectrics and electrical insulation*, vol. 14, no. 1, pp. 3-14, 2007.

Amir Ghaedi was born in 1984 in Kheirabad, a village of Shiraz, and received the M.Sc., and Ph.D. degrees in electrical engineering, power field, from Sharif University of Technology, Tehran, Iran, in 2008, and 2013, respectively. He is currently associate professor in Department of Electrical Engineering, Dariun Branch, Islamic Azad University, Dariun, Iran. His main research interests are the power quality, power system reliability, smart grids, renewable resources and high voltage engineering.

Reza Sedaghati was born in Kazeroon, Iran, on September 21, 1983. He received his PhD degree in Electrical Engineering in 2019. He is assistant professor in Department of Electrical Engineering, Beyza Branch, Islamic Azad University, Beyza, Iran. His research interests include renewable energies, optimization, FACTS devices and power system dynamics.

Mehrdad Mahmoudian was born in Iran, in 1990. He received the B.Sc. degree in Electrical Engineering from Shahid Bahonar University, Kerman, Iran, and M.S. degree in Electrical Engineering from Iran University of Science and Technology (IUST), Tehran Iran, in 2012 and 2014 respectively. His research interests include DC/DC Converters, Energy Conversion and Photovoltaic Power System.

Shahriar Bazyari was born in 1986 in Fasa, Iran. He received the BA degree in electrical engineering and the M.Sc. degree in mechatronic engineering, in 2009, and 2012, respectively. He is currently PhD student in Department of Electrical Engineering, Kazerun Branch, Islamic Azad University, Kazerun, Iran. His main research interests are the medical equipment, optimization, and renewable energies.

International Journal Of
Industrial Electronics Control and Optimization
Print ISSN: 3517-2645
Online ISSN: 3568-2645
Homepage: https://ieco.usb.ac.ir/

Tail Gas Quality Warning System in a Sulfur Recovery unit based on H_2S and SO_2 Concentration Soft Sensor utilizing Multi-State-Dependent Modeling Method

Fereshte Tavakoli Dastjerd[1] | Farhad Shahraki[*1] | Jafar Sadeghi[1] | Mir Mohammad Khalilipour[1]| Bahareh Bidar[1]

Center for Process Integration and Control (CPIC), Department of Chemical Engineering, University of Sistan and Baluchestan, Zahedan 98164, Iran.[1]

Corresponding author's email: fshahraki@eng.usb.ac.ir

Article Info

Article type:
Research Article

Article history:
Received: 13-August-2023
Received in revised form: 19-November-2023
Accepted: 23-November-2023
Published online: 10- Dec -2023

Keywords:
Pollutants,
Data-Driven Soft Sensor,
Sulfur Recovery Unit,
Multi-State-Dependent Parameter,
Generalized Random Walk

ABSTRACT

The design and development of data-driven soft sensors is important to predict the concentration of perilous pollutants in industry effluents to protect environmental health. The aim of this research is to design a tail gas quality warning system in the sulfur recovery unit (SRU) based on H_2S and SO_2 concentration soft sensor utilizing multi-state-dependent modeling method. The SRU in the petrochemical plant of ERG PETROLI, located in Italy, is selected as the study region for implementation of the warning system. The generalized random walk- multi-state-dependent parameter method (GRW-MSDP) for soft sensor design is proposed. The GRW-MSDP estimation system is based on multi-state-dependent modeling method by utilizing the extension of the generalized random walk model. The method has been developed by utilizing the algorithms of extended Kalman filter (EKF) and fixed interval smoothing (FIS). The quality warning system of tail gas based on the estimated concentrations of SO_2 and H_2S sends instructions to adjust the ratio of air to feed flow in the reaction furnace of SRU by plant operators. The results indicate that the proposed estimation system can be efficient in dealing with process non-linearity, high-dimensional values, and random missing data. The comparative discussion of GRW-MSDP technique performance with different soft sensing methods shows that the designed soft sensor model is more reliable with fewer input variables, lower complexity and relatively higher prediction accuracy. Furthermore, the great efficiency of the designed quality warning system is obvious from the good accuracy and F1-score values of 99.4% and 0.8951, respectively.

Nomenclature

e	Observation error	R	Covariance of one-step-ahead prediction error
$\mathbf{F}$	The SDP's coefficient matrix	$\mathbf{s}$	States that SDP is a function of them
$\mathbf{G}$	The SDP's coefficient matrix	t	Time numerator
$\mathbf{H}$	The SDP's coefficient vector	u	Input variable

j	Regressor numerator	$\mathbf{X}$	Stochastic state vector
$\mathbf{L}_p$	Predecessor set	y	Output variable
$\mathbf{L}_f$	Successor set	z	Regressor
m	Number of delay inputs	α	Hyper-parameters
N	Number of data points in time series	β	Hyper-parameters
n	Number of delay outputs	γ	Hyper-parameters
n_p	Number of parameters	δ	Hyper-parameters
n_s	Number of state that SDP is a function of them	δ	Pure time delay
$\mathbf{P}$	Covariance matrix	ε	Hyper-parameters
$\mathbf{Q}$	Noise variance matrix	ε	One-step-ahead prediction error
q	Polynomial order of the SDP	$\boldsymbol{\eta}$	White noise vector with zero mean

I. Introduction

In this modern epoch, a significant concern to mankind is environmental pollution. Industrialization in developing and developed countries is the main reason for environmental pollution. The poor air quality in urban environments can create chronic and acute sickness in people [1]. Therefore, keeping good air quality has become an important concern for most economies. H_2S and SO_2 are the conventional gaseous pollutants which can damage people's health and atmosphere significantly. One of the emission reasons for these gases is from industrial activities. Recently, studies have been carried out about the adequate treatment of gas containing the environmental pollutant H_2S from industrial activities before discharge into the environment [2-4]. The sulfur recovery unit is a refinery processing unit which eliminates H_2S from refinery gas flows before being delivered into the atmosphere. However, there are remaining SO_2 and H_2S from the reactions in the output gas flow from the SRU (tail gas). Hence it is important to determine the tail gas quality of SRU as a safety concern issue. Estimating the tail gas quality and sending out warning signals based on the tail gas quality value is necessary to control the ratio of air to feed flow to SRU and thus avoid exposure to hazardous pollutants [5]. Many factors like the regional environmental issues and characteristics of the instruments might impress the variance of the data collected from traditional instruments, thus the costly traditional instrumentation can be replaced by soft sensors to estimate the H_2S and SO_2 concentration. The historical data can be employed by machine learning and statistical methods to get important information that can be utilized to make decisions for safe and robust process operation. The online prediction of the product quality variables is one type of this information which can be achieved using data-driven soft sensors. The popularity of data-driven soft sensors is rising with the accessibility of stored data in industries and the accessibility of computational potency for data processing [6,7].

The first data-driven soft sensors were designed by the traditional offline modelling methods. The most popular linear offline approaches include multivariate linear regression (MLR) [8], partial least squares (PLS) [9], principal component analysis (PCA) [10] and canonical coordinates regression (CCR) [11] while the nonlinear offline approaches include support vector machine (SVM) [12] artificial neural networks (ANN) [13], neuro-fuzzy (NF) system [14] and Gaussian process regression (GPR) [15]. The nonlinear and linear offline approaches can be merged to improve the soft sensor performance such as nonlinear PLS (NNPLS) [16], nonlinear principal component regression (NNPCR) [17], kernel PLS (KPLS) [18], dynamic kernel PCA (DKPCA) [19] and least squares support vector regression (LSSVR) [20].

Catalyst activity changes, Changes of process input materials, changes in external environment and production of different grades of product quality can lead to time-varying behavior of processes thus a methodology is needed to adapt the model online [21]. Adaptive soft sensing methods are used to update the soft sensor model frequently. The moving window (MW) models [22] and the recursive updates of the PLS, least squares (LS), and PCA methods are the first adaptive soft sensors [23]. Although these methods can cope with slow process changes, they cannot adapt soft sensors with sudden changes of process. Thus, the local learning modeling methods are introduced. The popular local modeling methods include the just-in-time learning (JITL) method [24], correlation based just-in-time learning (CoJIT) method [25], locally weighted regression (LWR) [26].

If the models are adapted using faulty data, the estimation accuracy of the soft sensor reduces. Therefore, data pre-processing is employed to address data quality challenges

such as high dimensionality, inconsistencies, outliers and missing data [27]. In addition, there are methods to select contamination-free and comprehensive data from large data sets [28] and to deal with missing values such as automatically excluding the missing data and employing data imputation algorithms [29, 30].

Varying parameter models present a precise physical interpretation for the real variables of process and can be used instead of adaptive approaches [31, 32]. The models of time variable parameter (TVP) and state dependent parameter (SDP) are definitions of linear and nonlinear time-varying systems, respectively. Each parameter of univariate SDP models is varying with only one state variable and is stated utilizing the generalized random walk (GRW) model, estimated utilizing Kalman filter (KF) technique, with the implementation of fixed interval smoothing (FIS), data sorting and back-fitting algorithms [31].

The SDP-based soft sensor extension which includes the nonlinearities of multi-state dependent parameter (MSDP) is necessary for a large category of dynamic, stochastic nonlinear systems. Two best-known multi-state-dependent modeling methods are the MSDP [33] and local instrumental variable (LIV) [34] methods. In the MSDP method, the parameters are estimated using an expansion of the GRW model with the carrying out of extended FIS, data sorting and back-fitting algorithms. In the MSDP approach due to the presence of the Lagrange multipliers in the extended FIS formulation, relationships achieved by the method need to be parameterized for interpolation and dealing with the missing data. If the model parameters depend on three or more state variables, it will be difficult or impossible to parameterize the model. Also, the MSDP method cannot decrease the effect of outliers on estimation of parameters. The instrumental variable (IV) technique is employed to design the LIV method and in the LIV method, the estimate of each MSDP is not impressed by other states and regressors. But if there is a linear correlation between the model regressors, the LIV method cannot be used practically. The interpolation is performed directly without parameterization in the LIV method but the method cannot handle the missing data and cannot reduce the effect of outliers on estimated parameters. Therefore, MSDP and LIV methods need data pre-processing prior to use of the methods.

The contribution of this paper is to design and implement a new data-driven soft sensor which estimates the concentration of SO_2 and H_2S in the tail gas flow from the SRU based on the structure of multi-state-dependent parameter (MSDP) and technique of generalized random walk. The method, termed GRW-MSDP, estimates the parameter values in the form of multivariable state space utilizing the algorithms of extended Kalman filter (KF) and fixed interval smoothing (FIS), combined with data sorting procedure and back-fitting algorithm. The extended KF decreases the effect of outlier data by assigning small weight to them and the FIS algorithm handles the missing data as a predictor-corrector type estimator. Therefore, the main advantage of GRW-MSDP method is the not-requirement of data pre-processing techniques. In the proposed method, the prediction step of the FIS algorithm is used to interpolate directly without parameterization. GRW-MSDP method can be used in the presence of linear correlation between the model regressors, due to the use of the back-fitting algorithm in accordance with the single-parameter approach. Separate from estimation, the design of a quality warning system is important to analyze the tail gas quality and to take precautionary actions to reduce the content of pollutants in the tail gas stream. Therefore, the innovation of this research is the design of a tail gas quality warning system based on H_2S and SO_2 concentration soft sensor. In order to design the tail gas quality warning system, a classifier has been modeled based on the estimated concentration of H_2S and SO_2.

This research mostly concentrates on the importance of the tail gas quality warning system in the SRU in the petrochemical plant of ERG PETROLI placed in Italy and the GRW-MSDP estimation system is used to achieve accurate determination of SO_2 and H_2S concentration. Also, the SRU model prediction capability and the performance of the tail gas quality warning system are evaluated by the existence of the missing values in the industrial dataset and a comparison is conducted between the proposed approach and other soft sensing techniques.

In the rest of this article, the study region, data analysis, GRW-MSDP method and tail gas quality warning system will be given in Section II. Section III presents the results and discussions. Finally, conclusion is drawn in Section IV.

II. Analysis and method

D. Study Region

In this paper, the sulfur recovery unit in the petrochemical plant of ERG PETROLI, located in Italy, is selected as the

study region. The SRU is a refinery processing unit which recovers the elemental sulfur as a valuable byproduct from acid gases such as H_2S and eliminates the H_2S pollutant from

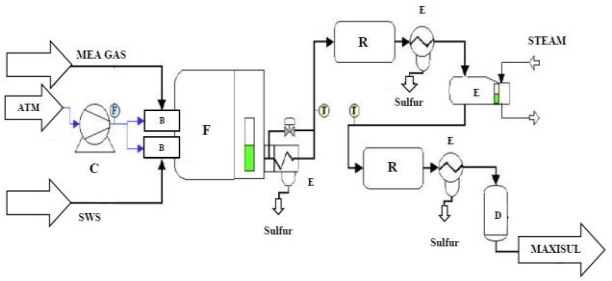

Fig. 1. Block diagram of sulfur recovery unit [5]

TABLE 1
INPUTS AND OUTPUTS OF SULFUR RECOVERY UNIT

Variable	Description	Unit
u_1	MEA gas flow	m^3/hr
u_2	First air flow (AIR MEA 1)	m^3/hr
u_3	Second air flow (AIR MEA 2)	m^3/hr
u_4	Air flow in SWS zone (AIR SWS)	m^3/hr
u_5	Gas flow in SWS zone	m^3/hr
y_1	H_2S concentration	-
y_2	SO_2 concentration	-

gas streams. The final gas flow from the SRU (tail gas) contains remaining SO_2 and H_2S created by reactions.

The block diagram of the SRU is demonstrated in Fig. 1. The acid gases containing H_2S from the MEA plant and the acid gases containing NH_3 and H_2S from the SWS plant are fed to a reaction furnace (F). According to the reaction (1), one third of H_2S is burned in the furnace to obtain H_2S/SO_2 stoichiometric ratio of 2 to 1. This proportion is kept fixed during the entire process by adjusting air content in the reaction furnace.

$$H_2S + \frac{3}{2} O_2 \rightarrow SO_2 + H_2O \quad (1)$$

The exhaust gases from the furnace are sent to a water condenser. Then, in order to achieve elemental sulfur at 90% according to reaction (2), two catalytic reactors (R) and two condensers (E) are utilized.

$$2H_2S + SO_2 \rightarrow 3S + 2H_2O \quad (2)$$

Air supplies O_2 for the reaction (1). If the air in the reaction furnace is very little, there will be very much H_2S in the tail gas. But if the air is very much, there will be very much SO_2 in the tail gas. Therefore, the air is an important factor in the H_2S conversion. If the reactants are in stoichiometric ratio in the reaction (2), the total sulfur compounds are removed in the catalytic converters and the tail gas becomes free of pollutants. The $[H_2S]$-$2[SO_2]$ value is zero in the optimal state and is utilized as the process variable to control the ratio of air to feed flow. Thus, adjusting the air flow rate (AIR MEA 1 and AIR SWS) is manually done by the unit operators to ensure the second reaction occurs in stoichiometric proportion. The second air flow is controlled using an automatic feedback loop [5].

The concentrations of H_2S and SO_2 residuals should be monitored due to considerable hazard for process equipment, the environment safety, and human health. Since direct measurement of their concentrations during the processing is difficult, the soft sensor methodology is suggested to estimate SO_2 and H_2S contents.

E. Data analysis

The soft sensor model of the sulfur recovery unit is designed based on MSDP methodology and input and output variables provided in Table 1. The benchmark dataset for the SRU contains 10081 samples, and in this paper the first 5000 samples are utilized as the train and test datasets. By the consideration of process dynamics and expert knowledge analysis, Fortuna et al. [5] presented a soft sensing model of quality parameters of SRU as follow: In order to make it easier to express, previous outputs $y_i(t\text{-}j)$ and previous inputs $u_i(t\text{-}j)$ are shown as $y_i d_j$ and $u_i d_j$ in tables and models.

$$\hat{y}_1 , \hat{y}_2 = g \{u_1, u_2, \ldots, u_5, u_1 d_5, u_1 d_7, u_1 d_9, \ldots, u_5 d_5, u_5 d_7, u_5 d_9 \} \quad (3)$$

where $\hat{y}_1$ and $\hat{y}_2$ are the predicted values of y_1 and y_2 for the t^{th} sample, respectively.

Given that the total time of reaction (2) is large and the process dynamic is slow [5], the present output value depends on the values of previous inputs. Therefore, the present inputs are eliminated and one-step delayed outputs are added in set of input variables. In order to determine the most impressive input variables, the analysis of correlation is done between the outputs and the new set of inputs using the training dataset that is shown in Table 2.

TABLE 2
CORREATION COEFFICIENTS BETWEEN OUTPUTS AT TIME t AND t-1 AGAINST INPUT DELAY VALUES

	u_{1d5}	u_{1d7}	u_{1d9}	u_{2d5}	u_{2d7}	u_{2d9}
y_1	-0.089	-0.132	-0.152	-0.158	-0.162	-0.154
y_2	0.141	0.175	0.191	0.202	0.206	0.198
	u_{3d5}	u_{3d7}	u_{3d9}	u_{4d5}	u_{4d7}	u_{4d9}
y_1	-0.083	-0.120	-0.139	-0.095	-0.096	-0.098
y_2	0.035	0.072	0.098	0.056	0.056	0.057
	u_{5d5}	u_{5d7}	u_{5d9}	y_{1d1}	y_{2d1}	
y_1	-0.080	-0.077	-0.073	0.951		
y_2	0.043	0.039	0.036	_	0.944	

Based on the maximum correlation coefficient in every input variable, a set of 6 impressive variables is chosen for every output variable to model the soft sensor (gray cells in Table 2). In the following, the structures of the MSDP model for output variables are given.

$$\hat{y}_1 = g \{ u_1 d_9, u_2 d_7, u_3 d_9, u_4 d_9, u_5 d_5, y_1 d_1 \} \quad (4)$$

$$\hat{y}_2 = g \{ u_1 d_9, u_2 d_7, u_3 d_9, u_4 d_9, u_5 d_5, y_2 d_1 \} \quad (5)$$

The training flowchart for soft sensor modeling based on

MSDP shown in Fig. 2 is utilized to achieve the best structure of MSDP model.

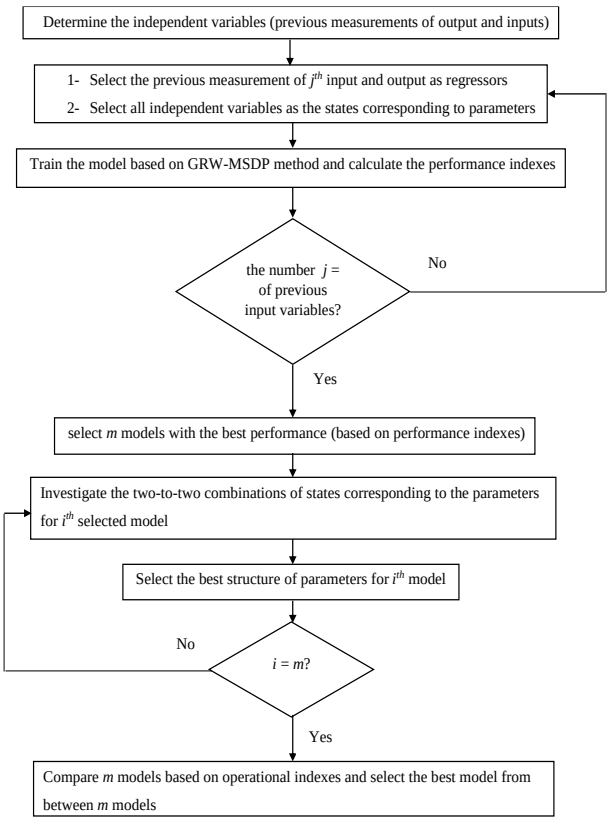

Fig. 2. Proposed flowchart for soft sensor modeling

F. Generalized random walk-multi-state dependent parameter method

The generalization of state-dependent auto-regressive with exogenous variables models (SDARX) which includes the nonlinearities of multi-state-dependent parameter is defined as,

$$y_t = \sum_{j=1}^{n+m+1} x_j\left(\mathbf{s}_t^{(j)},t\right) z_{j,t} + e_t \quad \text{with} \quad \begin{cases} e_t \sim \mathrm{N}(0,\sigma^2) \\ \mathbf{s}_t^{(j)} = \left[\mathrm{s}_{1,t}^{(j)}\ \mathrm{s}_{2,t}^{(j)} \cdots \mathrm{s}_{n_{sj},t}^{(j)}\right] \end{cases} \tag{6}$$

$$z_{j,t} = \begin{cases} y_{t-j} & j \le n \\ u_{t-\delta+n+1-j} & j > n \end{cases}$$

$$x_j = \begin{cases} -\alpha_j & j \le n \\ \beta_{j-(n+1)} & j > n \end{cases}$$

y_t and u_t are the outputs and inputs, respectively. $z_{j,t}$ is the j^{th} regressor and $n+m+1$ is the number of regressors in the model. n and m are the number of delay outputs and delay inputs, respectively. $x_j\left(\mathbf{s}_t^{(j)},t\right)$, a function of n_{sj} corresponding states $(\mathrm{s}_{i,t}^{(j)}\ i = 1, 2, \ldots, n_{sj})$, is the j^{th} multi-state dependent parameter, e_t is a Gaussian white noise with zero mean and variance σ^2, δ is pure time delay, $\beta_{j-(n+1)}$ is the coefficient of delay $(j\text{-}n\text{-}1)^{th}$ measurement of input and α_j is the coefficient of delay j^{th} measurement of output.

The GRW model for each SDP in a (q_j+1) dimensional observation space defined as the state space form in Eq. (7) is appropriate for recursive optimal estimation of multi-state-dependent parameters (MSDPs).

$$\mathbf{X}_{j,t} = \mathbf{F}_j\,\mathbf{X}_{j,t-1} + \mathbf{G}_i \tag{7}$$

$$\boldsymbol{\eta}_{j,t-1} \qquad j = 1, 2, \ldots, m+n+1 \quad , \quad t = 1, 2, \ldots, N$$

$$\mathbf{F}_j = \begin{bmatrix} \alpha & \beta \\ 0 & \gamma \end{bmatrix} \quad ; \quad \mathbf{G}_j = \begin{bmatrix} \delta & 0 \\ 0 & \varepsilon \end{bmatrix}$$

$$\mathbf{X}_{j,t} = \left[x_j\left(\mathbf{s}_t^{(j)},t\right), \nabla x_j\left(\mathbf{s}_t^{(j)},t\right), \cdots, \nabla^{q_j} x_j\left(\mathbf{s}_t^{(j)},t\right)\right]$$

where $\mathbf{X}_{j,t} = [l_{j,t},\ d_{j,t}]^{\mathrm{T}}$ is the stochastic state vector associated to j^{th} state dependent parameter at t^{th} sample. $d_{j,t}$ and $l_{j,t}$ are the slope change and magnitude change of correspondent SDP, respectively. q_j (q_j = 0, 1, 2, 3, . . .) is the polynomial order of the j^{th} SDP in GRW. $\boldsymbol{\eta}_{j,t} = \left[\eta_{1j,t}\ \eta_{2j,t}\right]^T$ characterized by a covariance matrix $\mathbf{Q}_{\eta j}$ allows stochastic changes in the parameters and is a white noise vector with zero mean. The GRW model parameters are known as hyper-parameters (α, β, γ, δ, ε, $\mathbf{Q}_{\eta j}$). Integrated random walk (IRW) (q_j=1, α=1, β=1, γ=1, δ=0, ε=1) and random walk (RW) (q_j=0, α=1, β=0, γ=0, δ=1, ε=0) are two cases of GRW general model.

The observation equation is as follow,

$$y_t = \sum_{j=1}^{n+m+1} \mathbf{H}_{j,t}\,\mathbf{X}_{j,t} + e_t \tag{8}$$

where $\mathbf{H}_{j,t}$ represents the regressor vector $\mathbf{H}_{j,t} = [z_{j,t}\ 0]$. The formulation of state space in Eqs. (7) and (8) is appropriate to estimate the MSDPs using two passes, "forward pass filtering" and "backward pass smoothing" by the carrying out of the extended Kalman filter and recursive fixed interval smoothing (FIS), respectively. Fast changes of state variables cannot be traced by GRW model. Therefore, prior to estimation of parameters, the variables are sorted in a non-time order according to the specific state variable. In this method, Delaunay triangulation is utilized as the algorithm of data sorting. After sorting N samples, the sets of predecessor ($\mathrm{L}_{p,k}$) and successor ($\mathrm{L}_{f,k}$) are defined for each k^{th} sample. $n_{p,k}$ and $n_{f,k}$ are the number of the closest p and f samples to the k^{th} sample in $\mathrm{L}_{p,k}$ and $\mathrm{L}_{f,k}$, respectively. The following numbered paragraphs display the step by step calculations of forward-pass filtering algorithm:

(1) KF algorithm includes two steps of prediction and correction. For each k = 1, 2, . . . , N, follow the steps below.

(1-1) For each $n_{p,k}$, calculate Eqs. (9) and (10).

$$\mathbf{X}_{k,p} = \mathbf{F}\ \mathbf{X}_p \tag{9}$$

$$\mathbf{P}_{k,p} = \mathbf{F}\ \mathbf{P}_p\ \mathbf{F}^T + \mathbf{G}\,\mathbf{Q}_r\,\mathbf{G}^T \tag{10}$$

where $\mathbf{P}_{k,p}$ and $\mathbf{X}_{k,p}$ are the covariance matrix of predicted parameter vector and parameter vector prediction from every $n_{p,k}$, respectively. $\mathbf{G}$ and $\mathbf{F}$ are obtained by Eq. (7) and $\mathbf{Q}_r$ is the noise variance ratio matrix (NVR).

(1-2) Estimate the predictive parameter vector using Eqs.

(11) and (12). Then, correct the predictive parameter vector using Eqs. (13) and (14).

$$\mathbf{P}_{k|p}=\left[\frac{1}{n_{p,k}}\sum_{p\in \mathrm{L}_{p,k}}\mathbf{P}_{k,p}^{-1}\right]^{-1} \tag{11}$$

$$\mathbf{X}_{k|p}=\mathbf{P}_{k|p}\left[\frac{1}{n_{p,k}}\sum_{p\in \mathrm{L}_{p,k}}\mathbf{P}_{k,p}^{-1}\ \mathbf{X}_{k,p}\right] \tag{12}$$

$$\mathbf{P}_k=\mathbf{P}_{k|p} - \mathbf{P}_{k|p}\ \mathbf{H}_k^T\ R_k{}^{-1}\ \mathbf{H}_k\ \mathbf{P}_{k|p}\quad,\ R_k=1+\mathbf{H}_k\ \mathbf{P}_{k|p}\ \mathbf{H}_k^T \tag{13}$$

$$\mathbf{X}_k=\mathbf{X}_{k|p}+\mathbf{P}_k\ \mathbf{H}_k^T\ \varepsilon_k\quad,\quad \varepsilon_k=y_k-\mathbf{H}_k\ \mathbf{X}_{k|p} \tag{14}$$

$\mathbf{P}_{k|p}$ and $\mathbf{X}_{k|p}$ are the covariance matrix of predicted parameter vector and parameter vector prediction, respectively. $\mathbf{X}_k$ and $\mathbf{P}_k$ are the covariance matrix of Estimated parameter vector and parameter vector estimate, respectively. The estimate of Eqs. (11) and (12) is based on entire points that are less than *k* in sorted order and, the estimation of Eqs. (13) and (14) is based on entire points that are less than or equal to *k* in sorted order. ε_k (one-step-ahead prediction error) and R_k are the residual at k^{th} sample and its covariance, respectively.

The EKF algorithm is just used in the process of optimizing the hyper-parameters. $\mathbf{Q}_r^{\mathrm{opt}}$ is the optimum NVR matrix and the maximum likelihood (ML) or cross validation (CV) approaches can be employed to optimize NVR hyper-parameters [33, 35]. The optimization is started with the primary values for the hyper-parameters, which either are set to default values or are chosen by the user. The concentrated likelihood and CV functions are expressed as:

$$\log(L_c)=\frac{1}{2}\left[\frac{1}{N}\sum_{k=1}^{N}\log(R_k)+\log\left(\frac{1}{N}\sum_{k=1}^{N}\frac{\varepsilon_k^2}{R_k}\right)\right] \tag{15}$$

$$\mathrm{CV}=\frac{1}{N}\sum_{k=1}^{N}\varepsilon_k{}^2 \tag{16}$$

The EKF algorithm is utilized frequently to generate ε_k and R_k. The optimization functions are numerically minimized relative to the unknown hyper-parameters to find minimum L_c and CV.

The backward pass smoothing for MSDPs estimation is carried on the following procedure:

(1) The FIS algorithm obtains a smooth estimation based on entire points in the time series and eliminates any lag effect. For each $k = N, ..., 2, 1$, estimate the smoothed parameter vector by Eqs. (17) – (20).

$$\mathbf{P}_k^*=\mathbf{Q}_P-\mathbf{Q}_P\ \mathbf{F}^T\left(\mathbf{Q}_F+\mathbf{F}\mathbf{Q}_P\mathbf{F}^T\right)^{-1}\mathbf{F}\ \mathbf{Q}_P \tag{17}$$

$$\mathbf{Q}_P=\frac{1}{n_{p,k}}\ \mathbf{G}\ \mathbf{Q}_r^{\mathrm{opt}}\ \mathbf{G}^T\quad;\quad \mathbf{Q}_F=\frac{1}{n_{f,k}}\ \mathbf{G}\ \mathbf{Q}_r^{\mathrm{opt}}\ \mathbf{G}^T$$

$$\mathbf{P}_{k|N}=\mathbf{P}_k^*-\mathbf{P}_k^*\ \mathbf{H}_k^T\left(1+\mathbf{H}_k\ \mathbf{P}_k^*\ \mathbf{H}_k^T\right)^{-1}\mathbf{H}_k\ \mathbf{P}_k^* \tag{18}$$

$$\mathbf{X}_k^*=\mathbf{F}\ \bar{\mathbf{X}}_P+\mathbf{P}_k^*\ \mathbf{F}^T\ \mathbf{Q}_F^{-1}\left(\bar{\mathbf{X}}_F-\mathbf{F}^2\ \bar{\mathbf{X}}_P\right) \tag{19}$$

$$\bar{\mathbf{X}}_P=\frac{1}{n_{p,k}}\sum_{p\ \in \mathrm{L}_{p,k}}\mathbf{X}_{p|N}\quad;\quad \bar{\mathbf{X}}_F=\frac{1}{n_{f,k}}\sum_{f\in \mathrm{L}_{f,k}}\mathbf{X}_{f|N}$$

$$\mathbf{X}_{k|N}=\mathbf{X}_k^*+\mathbf{P}_{k|N}\ \mathbf{H}_k^T\left(y_k-\mathbf{H}_k\ \mathbf{X}_k^*\right) \tag{20}$$

$\mathbf{P}_{k|N}$ and $\mathbf{X}_{k|N}$ are the covariance matrix of the smoothed parameter vector and the smoothed estimate of the parameter vector, respectively. Interpolation and missing data prediction are performed directly without parameterization by the prediction step ($\mathbf{X}_k^*$) of FIS. The iterative Gauss-Seidel technique is used to solve the system of FIS algorithm linear equations. After estimating each MSDP, the estimated parameters need to be reordered in time order before the back-fitting algorithm carries on for the subsequent parameter.

GRW-MSDP modeling method is utilized as the core of a data-driven soft sensor for prediction of concentration of SO_2 and H_2S in the tail gas stream.

The prediction efficiency of soft sensing models is determined using four performance indexes; determination coefficient (R^2), mean absolute error (MAE), root mean squares error (RMSE), and young information criterion (YIC) as follows:

$$\mathrm{R}^2=1-\frac{\sum_{j=1}^{N}\left(\hat{y}_j-\bar{y}\right)^2}{\sum_{j=1}^{N}\left(y_j-\bar{y}\right)^2} \tag{21}$$

$$\mathrm{MAE}=\frac{\sum_{j=1}^{N}\left|y_j-\hat{y}_j\right|}{N} \tag{22}$$

$$\mathrm{RMSE}=\sqrt{\frac{\sum_{j=1}^{N}\left(y_j-\hat{y}_j\right)^2}{N}} \tag{23}$$

$$\mathrm{YIC}=\log_e^{\left\{\frac{\sigma^2}{\sigma_y^2}\right\}}+\log_e^{\mathrm{EVN}} \tag{24}$$

$$\mathrm{EVN}=\frac{1}{n_p}\sum_{j=1}^{j=n_p}\frac{\sigma^2\ p_j}{\rho_j^2}$$

y_j, $\hat{y}_j$ and $\bar{y}$ are the actual value, predicted value and mean values of *y*, respectively. ρ_j, $\sigma^2\ p_j$ and n_p are parameter estimates, the estimated error variance on the j^{th} parameter and the number of parameters, respectively. The YIC, a negative value, evaluates the relationship between over parameterization and model fit. The best model has the lowermost YIC, MAE and RMSE values and the highest R^2.

G. Tail gas quality warning system

The designed tail gas quality warning system is demonstrated in Fig. 3 as a block diagram. The air and feed flow rates are fed as inputs to the designed GRW-MSDP estimation system. Then, the concentration of H_2S and SO_2 computed by GRW-MSDP approach are given as inputs to a computational block as a classifier. The class assignment for the classifier is performed based on the criteria presented as follows, which are created according to the change in air flow rate to minimize pollutants in the tail gas stream.

Class +1: H_2S concentration-2(SO_2 concentration) > 0

Class -1: H_2S concentration-2(SO_2 concentration) < 0

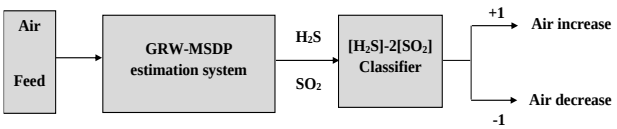

Fig. 3. Block flow diagram of tail gas quality warning system

If the classifier provides class +1 as output signal, the tail gas quality warning system produces an alarm showing that the air in the furnace is too little and tail gas contains too much of H_2S. Therefore, in order to adjust the H_2S/SO_2 stoichiometric ratio and reduce pollutants in the tail gas, the air flow must be manually increased by the unit operators to occur second reaction in the stoichiometric proportion. If the air in the furnace is too high, tail gas contains too much SO_2 and the classifier returns class -1 as the output. Therefore, in order to occur reaction (2) in the stoichiometric proportion and reduce pollutants in the tail gas, the air flow must be decreased manually by the operators.

The classifier performance evaluation is indicated by calculating accuracy and F1-score [36] based on the following equations.

$$\text{Accuracy} = \frac{\textit{Correct classifications}}{\textit{Number of observations}} \times 100 \quad (25)$$

$$\text{F1-score} = 2\times \frac{\textit{Precision} \times \textit{Recall}}{\textit{Precision} + \textit{Recall}} \quad (26)$$

$$\text{Recall} = \frac{\textit{True positive}}{\textit{True positive} + \textit{False negative}}$$

$$\text{Precision} = \frac{\textit{True positive}}{\textit{True positive} + \textit{False positive}}$$

III. Result and discussion

The model identification is performed based on RW parameter variation model and CV optimization criterion. The soft sensor model structure is obtained using the training flowchart. The training results for y_1 and y_2 are demonstrated in Table 3 and Table 4, respectively. First, all possible combinations of the regressors and states for soft sensor modeling are specified. Secondly, the models are trained based on GRW-MSDP method and the models with the best performance are selected which are shown by *. In fact, a model with a high R^2 and a quite low YIC is chosen, since a quite big YIC shows the possibility of over-parameterization. Then, the two-to-two combinations of states corresponding to the parameters for selected models are investigated and the best parameter structure for models are Selected (see colored cells in Table 3 and Table 4). Finally, the best configuration of the MSDP model is chosen by comparison between selected structures. Due to the use of the RW parameter variation model, when the value of the parameter NVR is very small, the parameter can be assumed to be constant. Thus, structures 6, 8, and 10 in Table 3 and Table 4 transform into 7, 9, and 11, respectively. Since the concentration of H_2S and SO_2 in tail gas is dependent on H_2S and air input to the process, the regressors and states of three mentioned structures in Table 3 are acceptable and logical in terms of expert knowledge. In Table 3, structure 11 increases the model accuracy on training data by increasing the NVR value, but it decreases the predictability of test data (R^2_{test} is low). By comparing structures 7 and 9, 7 is selected as the best model structure for predicting the H_2S concentration due to its lower RMSE, MAE and YIC and higher R^2. Since in structure 7 in Table 4, the SO_2 concentration is calculated by delayed amount of incoming air and one-step delayed output, this structure isn't acceptable in terms of expert knowledge. Finally, by comparing acceptable structures 9, 11 in Table 4, 11 is selected as the best model structure due to its lowest YIC, and R^2, RMSE, MAE and R^2_{test} almost identical to the 9 structure.

The best structures of MSDP models for estimating the concentrations of H_2S and SO_2 are determined as:

$$\hat{y}_1 = a_1\{u_3 d_9, y_1 d_1\}\ u_1 d_9 + b_1\ y_1 d_1 + e_t \quad (27)$$

$$\hat{y}_2 = a_2\{u_2 d_7, u_3 d_9\}\ u_5 d_5 + b_2\ y_2 d_1 + e_t \quad (28)$$

Where a_1 and a_2 are MSDPs and b_1 and b_2 are constant parameters.

In the unfavorable conditions, the designed estimation system is a better alternative than costly traditional instruments to achieve fast and precise results and has too low RMSE of 0.01836 and 0.01549 for H_2S and SO_2, respectively. When the missingness is not random, missing at random (MAR) happens in a dataset, and in this case the missingness is totally accounted for by variables that contain complete information. To demonstrate the robustness of the proposed soft sensor modeling method, the output value of 550 random samples from the training dataset of y_1 and y_2 are missing according to the MAR mechanism. Figs. 4 and 5 show the real and predicted values of y_1 and y_2 on the training dataset, respectively. The missing values are indicated by regions marked by rectangles. According to the results, the estimated and real values agree well with each other in both y_1 and y_2 and the used method can accurately predict the missing values.

Among the total of 2500 data samples utilized for classifier in the presence of missing values, there are 17 misclassifications and 2483 data samples are classified correctly. In the 17 misclassifications, 10 are false negatives and 7 are false positives. In the 2483 correct classifications, there are 2419 true negatives and 64 true positives. Accuracy and F1-score are obtained as 99.32% and 0.8828, respectively for the tail gas quality warning system demonstrating that the designed quality warning system is reliable in the presence of missing values.

TABLE 3
TRAINING RESULTS FOR y_1 WITH VARIOUS REGRESSORS AND STATES

	regressors	states	NVR	R^2	RMSE	MAE	YIC	R^2_{test}
1*	u_1d_9	u_1d_9, u_2d_7, u_3d_9, u_4d_9, u_5d_5 , y_1d_1	4.95305	0.90608	0.02053	0.00582	-63.1956	0.88536
	y_1d_1	u_1d_9, u_2d_7, u_3d_9, u_4d_9, u_5d_5 , y_1d_1	1.20519e-18					
2	u_2d_7	u_1d_9, u_2d_7, u_3d_9, u_4d_9, u_5d_5 , y_1d_1	1.93132e+1	0.90818	0.02029	0.00580	-53.7448	0.88350
	y_1d_1	u_1d_9, u_2d_7, u_3d_9, u_4d_9, u_5d_5 , y_1d_1	1.63352e-14					
3*	u_3d_9	u_1d_9, u_2d_7, u_3d_9, u_4d_9, u_5d_5 , y_1d_1	3.77913	0.90480	0.02068	0.00628	-58.6019	0.88291
	y_1d_1	u_1d_9, u_2d_7, u_3d_9, u_4d_9, u_5d_5 , y_1d_1	1.18134e-16					
4	u_4d_9	u_1d_9, u_2d_7, u_3d_9, u_4d_9, u_5d_5 , y_1d_1	2.38604e+1	0.90975	0.02015	0.00585	-54.8812	0.88479
	y_1d_1	u_1d_9, u_2d_7, u_3d_9, u_4d_9, u_5d_5 , y_1d_1	5.32083e-15					
5*	u_5d_5	u_1d_9, u_2d_7, u_3d_9, u_4d_9, u_5d_5 , y_1d_1	1.58471	0.90512	0.02067	0.00604	-64.6855	0.88552
	y_1d_1	u_1d_9, u_2d_7, u_3d_9, u_4d_9, u_5d_5 , y_1d_1	2.65594e-19					
6	u_1d_9	(u_3d_9, y_1d_1)	2.13511	0.92297	0.01859	0.00519	-66.4423	0.87593
	y_1d_1	(u_4d_9, u_5d_5)	2.86497e-21					
7	u_1d_9	(u_3d_9, y_1d_1)	1.80000	0.92477	0.01836	0.00502	-20.9464	0.88787
	y_1d_1	(-)	0					
8	u_3d_9	(u_1d_9, u_2d_7)	8.12757e-1	0.91196	0.01987	0.00560	-57.7681	0.88787
	y_1d_1	(u_1d_9, u_3d_9)	1.77828e-17					
9	u_3d_9	(u_1d_9, u_2d_7)	3.14381e-1	0.91077	0.02002	0.00559	-20.6170	0.89052
	y_1d_1	(-)	0					
10	u_5d_5	(u_2d_7, u_3d_9)	3.82804	0.94626	0.01552	0.00458	-53.4242	0.89056
	y_1d_1	(u_1d_9, y_1d_1)	3.13960e-15					
11	u_5d_5	(u_2d_7, u_3d_9)	3.48962	0.94654	0.01548	0.00475	-21.4786	0.86515

TABLE 4
TRAINING RESULTS FOR y_2 WITH VARIOUS REGRESSORS AND STATES

	regressors	states	NVR	R^2	RMSE	MAE	YIC	R^2_{test}
1	u_1d_9	u_1d_9, u_2d_7, u_3d_9, u_4d_9, u_5d_5 , y_2d_1	3.29193	0.99342	0.00447	0.00169	-19.8493	0.88826
	y_2d_1	u_1d_9, u_2d_7, u_3d_9, u_4d_9, u_5d_5 , y_2d_1	1.21432e+4					
2	u_2d_7	u_1d_9, u_2d_7, u_3d_9, u_4d_9, u_5d_5 , y_2d_1	1.11852e+1	0.98359	0.00706	0.00283	-18.1709	0.88801
	y_2d_1	u_1d_9, u_2d_7, u_3d_9, u_4d_9, u_5d_5 , y_2d_1	4.88249e+3					
3*	u_3d_9	u_1d_9, u_2d_7, u_3d_9, u_4d_9, u_5d_5 , y_2d_1	5.47454	0.99704	0.00300	0.00104	-21.3284	0.88868
	y_2d_1	u_1d_9, u_2d_7, u_3d_9, u_4d_9, u_5d_5 , y_2d_1	2.43154e+4					
4*	u_4d_9	u_1d_9, u_2d_7, u_3d_9, u_4d_9, u_5d_5 , y_2d_1	1.61668	0.99743	0.00279	0.00093	-21.5301	0.88617
	y_2d_1	u_1d_9, u_2d_7, u_3d_9, u_4d_9, u_5d_5 , y_2d_1	2.94792e+4					
5*	u_5d_5	u_1d_9, u_2d_7, u_3d_9, u_4d_9, u_5d_5 , y_2d_1	1.06796	0.99599	0.00349	0.00122	-20.7206	0.88684
	y_2d_1	u_1d_9, u_2d_7, u_3d_9, u_4d_9, u_5d_5 , y_2d_1	1.97858e+4					
6	u_3d_9	(u_4d_9, u_5d_5)	8.53372e-19	0.96103	0.01088	0.00525	-55.2530	0.88752
	y_2d_1	(u_2d_7, u_4d_9)	5.98381e+1					
	u_3d_9	(-)	0					

7	y_2d_1	(u_2d_7, u_4d_9)	5.30959e+1	0.95882	0.01118	0.00528	-18.0488	0.88722
8	u_4d_9	(u_1d_9, u_5d_5)	3.86188e-21	0.92065	0.01552	0.00652	-57.0638	0.88715
	y_2d_1	(u_1d_9, u_5d_5)	4.61123					
9	u_4d_9	(-)	0	0.92165	0.01542	0.00658	-18.2832	0.88716
	y_2d_1	(u_1d_9, u_5d_5)	4.86968					
10	u_5d_5	(u_2d_7, u_3d_9)	1.20091	0.91762	0.01581	0.00640	-56.5420	0.88809
	y_2d_1	(u_4d_9, y_2d_1)	9.29781e-17					
11	u_5d_5	(u_2d_7, u_3d_9)	1.43076	0.92094	0.01549	0.00640	-22.2774	0.88739
	y_2d_1	(-)	0					

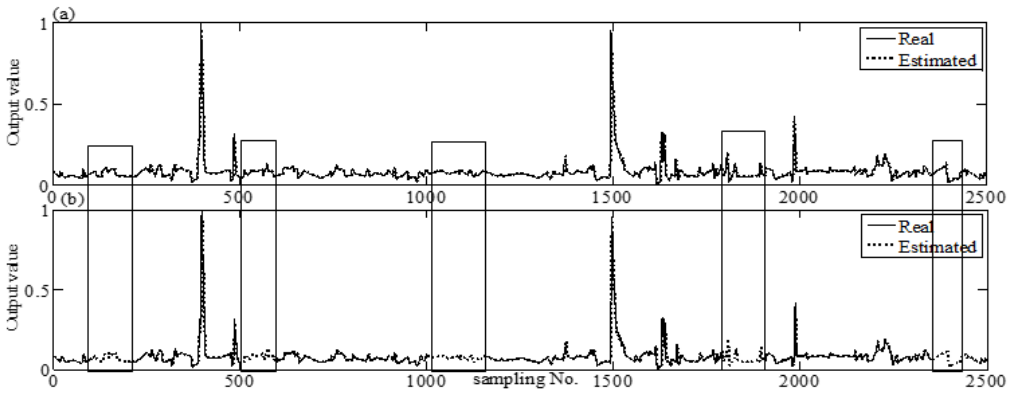

Fig. 4. H_2S concentration prediction results on train dataset (a) free of missing data, (b) with missing data

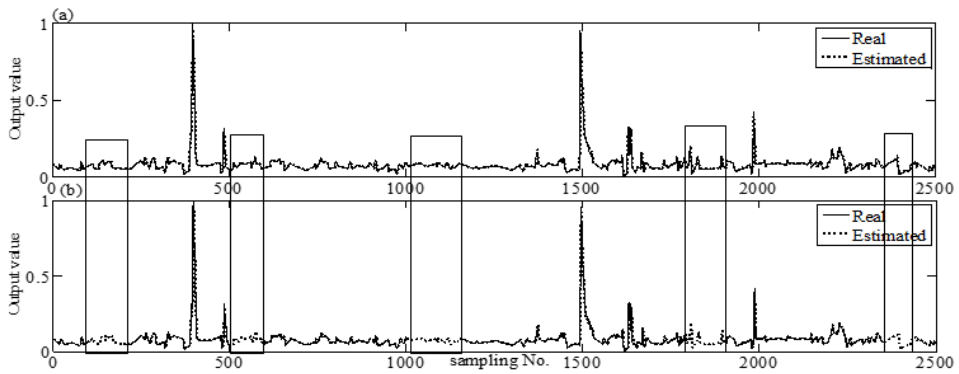

Fig. 5. SO_2 concentration prediction results on train dataset (a) free of missing data, (b) with missing data

Figs. 6(a) and 6(b) display the real and estimated values of y_1 and y_2 on the testing dataset. Since the estimated and real values agree well with each other in both y_1 and y_2, the GRW-MSDP method can properly model the nonlinearity. Among a total of 2500 samples utilized for the classifier in the testing dataset, there are 15 misclassifications and 2485 data samples are classified correctly. In the 15 misclassifications, 10 are false negatives and 5 are false positives. In the 2485 correct classifications, there are 2421 true negatives and 64 true positives. Accuracy and F1-score are obtained as 99.4% and 0.8951, respectively for the tail gas quality warning system demonstrating that the designed warning system is reliable in testing dataset.

The scatter plots of output concentration estimations against real values are presented in Figs. 7(a) and 7(b). The estimated and real values are in good compromise with each other and most of the data samples are situated along the diameter line, which displays great prediction accuracy of the soft sensor.

The average relative error between the predicted and actual output values of y_1 and y_2 for the whole set of 5000 samples are 5.54% and 6.28%, respectively, which show the proper performance of soft sensor prediction. The GRW-MSDP method prediction performance is compared with different soft sensing approaches for the SRU in Table 5.

According to the performance indexes presented in Table 5, linear models such as MLR, PCR and PLS have a relatively high RMSE and have displayed undesirable performance in dealing with the nonlinear data. The RMSE of several models such as LASS, OLPLS, SELPLS, ELFIR-SKRLS, MWtrPBC, MWAdp –JITL, $JITL_{TT}$ –MWt, SDP, MSDP, C-vine CR, D-vine CR, R-vine CR, JITL-GRNN and SCN are too close to the GRW-MSDP approach. In the mentioned models (With the

exception of SDP, MSDP, MWAdp –JITL, C-vine CR, D-vine CR, R-vine CR and JITL-GRNN), the output variables are predicted using 20 or more input variables, while more input variables lead to high model complexity and high computational load.

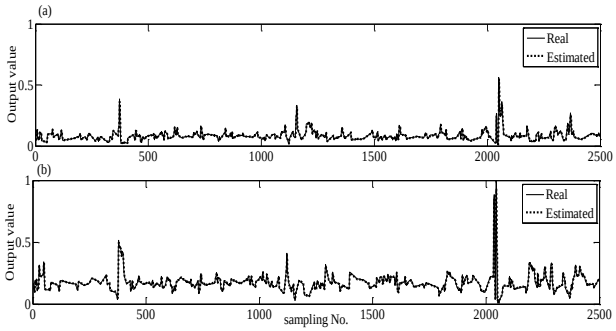

Fig. 6. Estimated output results on test dataset (a) y_1, (b) y_2

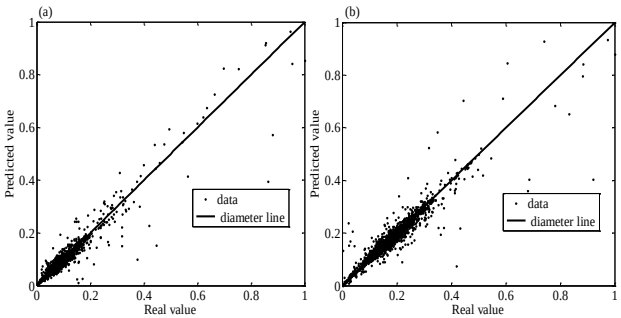

Fig. 7. Estimated values against real values of output concentration (a) y_1, (b) y_2

In MWAdp –JITL, C-vine CR, D-vine CR, R-vine CR and JITL-GRNN, the input delay values were not considered as input variables, so the designed soft sensor models are not appropriate for control aims. None of the mentioned soft sensors except SDP and MSDP were considered the system dynamic (delayed outputs), while if the previous information of the output variable is considered, it has a significant effect on improving the quality prediction with fewer input variables. The current modeling method can be included in the category of the best methods due to few inputs, simple model, low computational load, suitable performance indicators, direct interpolation without parameterization and automatic dealing with missing data.

IV. Conclusions

H_2S and SO_2 are dangerous air pollutants and their estimation is important for keeping environmental health. The tail gas stream from the industrial sulfur recovery unit contains remaining SO_2 and H_2S created by reactions and it is significant to design an efficient tail gas quality warning system. The SRU in the petrochemical plant of ERG PETROLI in Italy is selected as the study region for implementation of the warning system. A machine learning approach namely GRW-MSDP is suggested for the development of an efficient soft sensor to compute the concentration of SO_2 and H_2S. The performance evaluation of the designed estimation system based on GRW-MSDP demonstrates that the suggested method is more efficient in modeling nonlinear systems and in dealing with random missing values, and high-dimensional data. A comparative study between different estimation methods for SRU has shown that the proposed method considerably reduces the error while is more robust and reliable with fewer input variables, less complexity, and relatively higher prediction accuracy over other presented estimation approaches. A fast classifier is utilized to design the tail gas quality warning system based on the suggested soft sensor and the accuracy and F1-score of the warning system are obtained as 99.4% and 0.8951, respectively. The precise results for GRW-MSDP estimate system and classifier indicate that the designed tail gas quality warning system is reliable.

TABLE 5
COMPARSION OF PREDICTION RESULTS OF VARIOUS SOFT SENSORS FOR SRU

Publication	Model type	No. of variables	H_2S concentration			SO_2 concentration		
			R^2	RMSE	MAE	R^2	RMSE	MAE
Fortuna et al. [5]	MLP[1]	20	-	0.0300	-	-	0.0200	-
	RBF[2]	20	-	0.0424	-	-	0.0387	-
	NF	20	-	0.0346	-	-	0.0283	-
	Nonlinear LSQ[3]	20	-	0.0283	-	-	0.0200	-
Ge and Song [37]	PLS	5	-	0.0528	-	-	0.0563	-
	LSSVM[4]	5	-	0.0401	-	-	0.0512	-
	RVM[5]	5	-	0.0397	-	-	0.0511	-
Shao et al. [38]	JITPLS	20	-	0.0210	-	-	0.0238	-
	RPLS[6]	20	-	0.0196	-	-	0.0209	-

[1] Multi-Layer Perceptrons
[2] Radial Basis Function
[3] Nonlinear Least Square
[4] Least-Squares Support Vector Machine
[5] Relevance Vector Machine
[6] Recursive PLS

	OLPLS[7]	20	-	0.0162	-	-	0.0142	-
Shao and Tian [39]	LWPLS[8]	20	-	0.0181	-	-	0.0179	-
	MWPLS[9]	20	-	0.0246	-	-	0.0230	-
	LASS[10]	20	-	0.0172	-	-	0.0168	-
	SELPLS[11]	20	-	0.0130	-	-	0.0119	-
Jain et al. [40]	SSVR[12]	5	-	0.068	0.032	-	0.067	0.045
	LSSVR[13]	5	-	0.078	0.051	-	0.123	0.094
	MLR	5	-	0.069	0.037	-	0.07	0.048
	PCR	5	-	0.060	0.037	-	0.051	0.048
Shao and Tian [41]	PLS	20	-	0.0519	-	-	0.0573	-
	LSSVR	20	-	0.0415	-	-	0.0517	-
	JITL LSSVR	20	-	0.0401	-	-	0.0475	-
	EnLSSVR[14]	20	-	0.0382	-	-	0.0477	-
	SEnL-DM[15]	20	-	0.0376	-	-	0.0421	-
	S^3EnL-DM[16]	20	-	0.0367	-	-	0.0408	-
Bidar et al. [33]	SDP	4	-	0.0139	0.0055	-	0.0144	0.0073
	MSDP	3 and 4	-	0.0119	0.0034	-	0.0121	0.0065
Chen et al. [42]	ELFIR-LS[17] (N^S=5)	150	-	0.0216	-	-	-	-
	ELFIR-PLS (N^S=5)	150	-	0.0219	-	-	-	-
	ELPLS (N^S=5)	150	-	0.02125	-	-	-	-
	EL*FIR-SKRLS[18] (N^S=5)	150	-	0.0215	-	-	-	-
	ELFIR-SKRLS (N^S=5)	150	-	0.01975	-	-	-	-
Alakent [43]	MW_{tr}^{PBC}	30	0.910	0.0153	-	0.931	0.0135	-
Urhan and Alakent [44]	MW_{Adp} -JITL	5	0.932	0.0136	0.0081	-	-	-
Alakent [45]	$JITL_{TT}$ -MW_tr	30	0.914	0.0159	-	0.934	0.0138	-
Liu et al. [46]	C-vine CR[19]	5	-	-	-	0.9556	0.0101	-
	D-vine CR	5	-	-	-	0.9519	0.0106	-
	R-vine CR	5	-	-	-	0.9625	0.0093	-
Vijayan et al.[47]	JITL-GRNN[20]	7	-	0.0180	0.0064	-	0.0165	0.0080
Zhang et al. [48]	CDADPLS[21]	5	-	0.5855	-	-	0.3821	-
Zhao et al. [49]	SCN[22]	20	-	-	-	0.9524	0.0105	0.0077
	CTSCN[23]	20	-	-	-	0.8396	0.0224	0.0164
	LPSCN[24]	20	-	-	-	0.8408	0.0205	0.0161
This work	GRW-MSDP	4	0.92477	0.01836	0.00502	0.92094	0.01549	0.00640

References

[1] H. Xu, Y. Jia, Z. Sun, J. Su, Q.S. Liu, Q. Zhou, and G. Jiang, "Environmental pollution, a hidden culprit for health issues, " Eco-Environment & Health, Vol.1, No.1, pp.31-45, 2022.

[2] Z. Zhao, J. Yang, Z. Zhang, S.Wang, Z. Zhang, and J. Lu, "New method for efficient control of hydrogen sulfide and methane in gravity sewers: Combination of NaOH and Nitrite, " Front. Environ. Sci. Eng., Vol. 16, No. 6, pp. 1-14, 2021.

[3] Y. Wang, P. Ning, R. Zhao, K. Li, C. Wang, X. Sun, X. Song, and Q. Lin, "A Cu-modified active carbon fiber significantly promoted H2S and PH3 simultaneous removal at a low reaction temperature, " Front. Environ. Sci. Eng., "Vol. 15, No. 6, pp. 1-10, 2021.

[7] Online Local PLS
[8] Locally Weighted PLS
[9] Moving Window PLS
[10] Localized Adaptive Soft Sensor
[11] Selective Ensemble of Local PLS
[12] Smooth SVR
[13] Least Square SVR
[14] Ensemble of SSVR
[15] Supervised Ensemble Learning Based on Distance to Model
[16] Selective Semi-Supervised EnL-DM
[17] Ensemble Local Global Finite Impulse Response-LS
[18] Stable Kernel-based Regularized LS
[19] Vine Copula Regression
[20] JITL-Generalized Regression Neural Network
[21] Concept Drift Adaptive Dynamic PLS
[22] Stochastic Configuration Network
[23] Co-Training SCN
[24] Locality Preserving SCN

[4] S. Sun, T. Jia, K. Chen, Y. Peng, and L. Zhang, "Simultaneous removal of hydrogen sulfide and volatile organic sulfur compounds in off-gas mixture from a wastewater treatment plant using a two-stage bio-trickling filter system, " Front. Environ. Sci. Eng., Vol. 13, No. 4, pp. 1-13, 2019.
[5] L. Fortuna, A. Rizzo, M. Sinatra, and M.G. Xibilia, "Soft analyzers for a sulfur recovery unit, " Control Engineering Practice, Vol. 11, No. 12, pp. 1491-1500, 2003.
[6] Y. Yu, M. Peng, H. Wang, Z. Ma, and W. Li, "Improved PCA model for multiple fault detection, isolation and reconstruction of sensors in nuclear power plant, " Annals of Nuclear Energy, Vol. 148, p. 107662, 2020.
[7] Y.S. Perera, D.A.A.C. Ratnaweera, C.H. Dasanayaka, and C. Abeykoon, "The role of artificial intelligence-driven soft sensors in advanced sustainable process industries: A critical review, " Engineering Applications of Artificial Intelligence, Vol. 121, p.105988, 2023.
[8] G.K. Uyanık and N. Güler, "A study on multiple linear regression analysis, " Procedia-Social and Behavioral Sciences, Vol. 106, pp. 234-240, 2013.
[9] Q. Zhu, "Dynamic Autoregressive Partial Least Squares for Supervised Modeling, " IFAC-PapersOnLine, Vol, 54, No. 7, pp. 234-239, 2021.
[10] D. Yan, F.Yang, F.Yang, H. Zhang, Z. Guo, J. Li, and Y. Wu, "Identifying the key system parameters of the organic Rankine cycle using the principal component analysis based on an experimental database, " Energy Conversion and Management, Vol. 240, p. 114252, 2021.
[11] A.J. Burnham, R. Viveros, and J.F. MacGregor, "Frameworks for latent variable multivariate regression, " Journal of chemometrics, Vol. 10, No. 1, pp. 31-45, 1996.
[12] J. Huang, T. Jin, M. Liang, and H. Chen, "Prediction of heat exchanger performance in cryogenic oscillating flow conditions by support vector machine, " Applied Thermal Engineering, Vol. 182, p. 116053, 2021.
[13] S. Kamat and K. Madhavan, "Developing ANN based virtual/soft sensors for industrial problems, " IFAC-PapersOnLine, Vol. 49, No. 1, pp. 100-105, 2016.
[14] P.V. de Campos Souz, "Fuzzy neural networks and neuro-fuzzy networks: A review the main techniques and applications used in the literature, " Applied soft computing, Vol. 92, p. 106275, 2020.
[15] J. Chen, J. Yu, and Y. Zhang, "Multivariate video analysis and Gaussian process regression model based soft sensor for online estimation and prediction of nickel pellet size distributions, " Computers & Chemical Engineering, Vol. 64, pp. 13-23, 2014.
[16] E. Zamprogna, M. Barolo, and D.E. Seborg, "Development of a soft sensor for a batch distillation column using linear and nonlinear PLS regression techniques, " IFAC Proceedings Volumes, Vol. 35, No. 1, pp. 431-436, 2002.
[17] Q.X. Zhu, X. Wang, Y.L. He, and Y. Xu, "An improved extreme learning machine integrated with nonlinear principal components and its application to modeling complex chemical processes, " Applied Thermal Engineering, Vol. 130, pp. 745-753, 2018.
[18] X. Zhang, W. Yan, and H. Shao, "Nonlinear multivariate quality estimation and prediction based on kernel partial least squares, " Industrial & engineering chemistry research, Vol. 47, No. 4, pp. 1120-1131, 2008.
[19] S.W. Choi and I.B. Lee, "Nonlinear dynamic process monitoring based on dynamic kernel PCA, " Chemical engineering science, Vol. 59, No. 24, pp. 5897-5908, 2004.
[20] W. Zhou, Y. Cheng, S. Ding, L. Chen, and R. Li, "A grey seasonal least square support vector regression model for time series forecasting, " ISA transactions, Vol. 114, pp. 82-98, 2021.
[21] P. Kadlec, R. Grbić, and B. Gabrys, "Review of adaptation mechanisms for data-driven soft sensors, " Computers & chemical engineering, Vol. 35, No. 1, pp.1-24, 2011.
[22] Y. Liu, D. Huang, B. Liu, Q. Feng, and B. Cai, "Adaptive ranking based ensemble learning of Gaussian process regression models for quality-related variable prediction in process industries, " Applied Soft Computing, Vol. 101, p. 107060, 2021.
[23] I. Portnoy, K. Melendez, H. Pinzon, and M. Sanjuan, "An improved weighted recursive PCA algorithm for adaptive fault detection, " Control Engineering Practice, Vol. 50, pp. 69-83, 2016.
[24] W.S. Yeo, A. Saptoro, P. Kumar, and M. Kano, "Just-in-time based soft sensors for process industries: A status report and recommendations, " Journal of Process Control, Vol. 128, p.103025, 2023.
[25] K.Fujiwara, M. Kano, S. Hasebe, and A. Takinami, "Soft - sensor development using correlation - based just - in - time modeling, " AIChE Journal, No. 55, Vol. 7, pp. 1754-1765, 2009.
[26] K. Liu, W. Shao, and G. Chen, "Autoencoder-based nonlinear Bayesian locally weighted regression for soft sensor development, " ISA transactions, Vol. 103, pp. 143-155, 2020.
[27] M. Frye, J. Mohren, and RH. Schmitt, "Benchmarking of Data Preprocessing Methods for Machine Learning-Applications in Production, " Procedia CIRP, Vol. 104, pp. 50-55, 2021.
[28] S. Cohen, Dealing with data: strategies of preprocessing data. In: Artificial Intelligence and Deep Learning in Pathology, Amsterdam, Netherlands: Elsevier, 2021, pp. 77-92.
[29] Huber P.J., " Robust statistics " volume 523, John Wiley & Sons: Hoboken, New Jersey, United States (2004).
[30] L. Ma, M. Wang, and K. Peng, "A missing manufacturing process data imputation framework for nonlinear dynamic soft sensor modeling and its application," Expert Systems with Applications, Vol. 237, p. 121428, 2024.
[31] B. Bidar, J. Sadeghi, F. Shahraki, and M.M. Khalilipor, "Data-driven soft sensor approach for online quality prediction using state dependent parameter models, " Chemometrics and Intelligent Laboratory Systems, Vol. 162, pp. 130-141, 2017.
[32] R. Parvizi Moghadam, J. Sadeghi, and F. Shahraki, "Optimization of time - variable - parameter model for data - based soft sensor of industrial debutanizer, " Optimal Control Applications and Methods, Vol. 41, No.2, pp. 381-394, 2020.
[33] B. Bidar, F. Shahraki, J. Sadeghi, and M.M. Khalilipor, "Soft sensor modeling based on multi-state-dependent parameter models and application for quality monitoring in industrial sulfur recovery process, " IEEE Sensors Journal, Vol. 18, No. 11, pp. 4583-4591, 2018.
[34] B. Bidar, M.M. Khalilipor, F. Shahraki, and J. Sadeghi, "A data-driven soft-sensor for monitoring ASTM-D86 of CDU side products using local instrumental variable (LIV) technique, " Journal of the Taiwan Institute of Chemical Engineers, Vol. 84, pp. 49-59, 2018.
[35] DM. Hawkins, S.C. Basak, and D. Mills, "Assessing model fit by cross-validation, " Journal of chemical information and computer sciences, Vol. 43, No. 2, pp.579-586, 2003.
[36] B. Sprague, Q. Shi, M.T. Kim, L. Zhang, A. Sedykh, E.

Ichiishi, H. Tokuda, K.H. Lee, and H. Zhu, "Design, synthesis and experimental validation of novel potential chemopreventive agents using random forest and support vector machine binary classifiers, " Journal of computer-aided molecular design, Vol. 28, No. 6, pp. 631-646, 2014.
[37] Z. Ge and Z. Song, "Nonlinear soft sensor development based on relevance vector machine, " Industrial & engineering chemistry research, Vol. 49, No. 18, pp. 8685-8693, 2010.
[38] W. Shao, X. Tian, and P. Wang, "Local partial least squares based online soft sensing method for multi-output processes with adaptive process states division, " Chinese Journal of Chemical Engineering, Vol. 22, No. 7, pp. 828-836, 2014.
[39] W. Shao and X. Tian, "Adaptive soft sensor for quality prediction of chemical processes based on selective ensemble of local partial least squares models, " Chemical Engineering Research and Design, Vol. 95, pp.113-132, 2015.
[40] V. Jain, P. Kishore, R.A. Kumar, and A.K. Pani, "Inferential sensing of output quality in petroleum refinery using principal component regression and support vector regression, " In: 2017 IEEE 7th International Advance Computing Conference (IACC), Hyderabad, India, January 5-7, 2017, Piscataway: IEEE, 2017, pp. 461-465.
[41] W. Shao and X. Tian, "Semi-supervised selective ensemble learning based on distance to model for nonlinear soft sensor development, " Neurocomputing, Vol. 222, pp. 91-104, 2017.
[42] X. Chen, Z. Mao, R. Jia, and S. Zhang, "Ensemble regularized local finite impulse response models and soft sensor application in nonlinear dynamic industrial processes, " Applied Soft Computing, Vol. 85, p. 105806, 2019.
[43] B. Alakent, "Soft sensor design using transductive moving window learner, " Computers & Chemical Engineering, Vol. 140, p.106941, 2020.
[44] A. Urhan and B. Alakent, "Integrating adaptive moving window and just-in-time learning paradigms for soft-sensor design, " Neurocomputing, Vol. 392, pp. 23-37, 2020.
[45] B. Alakent, "Soft-sensor design via task transferred just-in-time-learning coupled transductive moving window learner, " Journal of Process Control, Vol. 101, pp. 52-67, 2021.
[46] S. Liu, and S. Li, "A semi-supervised soft sensor method based on vine copula regression and tri-training algorithm for complex chemical processes," Journal of Process Control, Vol. 120, pp.115-128, 2022.
[47] V. Vijayan, H.K. Mohanta, and A.K. Pani, " Adaptive non-linear soft sensor for quality monitoring in refineries using Just-in-Time Learning—Generalized regression neural network approach," Applied Soft Computing, Vol. 119, p.108546, 2022.
[48] T. Zhang, G. Yan, M. Ren, L. Cheng, R. Li, and G. Xie, " Dynamic transfer soft sensor for concept drift adaptation," Journal of Process Control, Vol. 123, pp.50-63, 2023.
[49] Y. Zhao, X. Deng, and S. Li, " A nonlinear industrial soft sensor modeling method based on locality preserving stochastic configuration network with utilizing unlabeled samples, " ISA transactions, 2023.

Fereshte Tavakoli Dastjerd received the B.S., M.S. and Ph.D. degrees in chemical engineering from University of Sistan and Baluchestan, Zahedan, Iran in 2013, 2016 and 2022, respectively. Her research interests include process modeling and simulation, process identification, process control and soft sensor design for chemical processes.

Farhad Shahraki received his B.S. degree in chemical engineering from the University of Sistan and Baluchestan, Zahedan, Iran in 1989, his M.S. degree in chemical engineering from Tarbiat Modares University, Tehran, Iran in 1992, and his Ph.D. degree in chemical engineering from The University of Manchester, Manchester, the U.K. in 2001. He is currently a professor of chemical engineering at the University of Sistan and Baluchestan. His research interests include process integration, process modeling, and optimization.

Jafar Sadeghi received his B.S. in chemical engineering from the Isfahan University of Technology, Isfahan, Iran, his M.S. degree in chemical engineering from the Sharif University of Technology, Tehran, Iran and his Ph.D. degree in chemical engineering from University of Lancaster, the U.K. in 1991, 1995, and 2007, respectively. He is currently an associate professor at the University of Sistan and Baluchestan, Zahedan, Iran. His research interests cover process modeling and simulation, process control, process identification, process intensification, automation, and instrumentation.

Mir Mohammad Khalilipour received his bachelor's degree in chemical engineering from Quchan University in 2004 and his master's and Ph.D. degrees in chemical engineering process design from the University of Sistan and Baluchistan, Iran in 2008 and 2016, respectively. He has been involved in safety management industrial projects for many Iranian oil and gas refineries from 2008 to 2011. He is currently an assistant professor at the Chemical Engineering Department, the University of Sistan and Baluchestan. His research interests are chemical safety, control, and process simulation especially with a focus on practical interesting of control, and soft sensors in chemical processes.

Bahareh Bidar received her bachelor's degree in chemical engineering from the Ferdowsi University of Mashhad, Iran, in 2007 and her master's and Ph.D. degrees in chemical engineering process design from the University of Sistan and Baluchistan, Iran in 2012 and 2018, respectively. Her main areas of research interest are process modeling and simulation, especially in soft sensor design for chemical process, process identification and control. She is currently an assistant professor in the chemical engineering department at the University of Sistan and Baluchestan.

IECO

This page intentionally left blank.

International Journal Of
Industrial Electronics Control and Optimization
Print ISSN: 3517-2645
Online ISSN: 3568-2645
Homepage: https://ieco.usb.ac.ir/

Advanced Inrush Current Mitigation Techniques for Microprocessor-Less High Power AC/DC/DC Synch-Buck Converters: A Start-up Perspective

Mohammad-Amin Baharamian[1] | Mazdak Ebadi[2] | Ali-Asghar Ghadimi[3]

Faculty of Engineering, Arak University, Arak, Iran.[1,2,3]
Corresponding author's email: m-ebadi@araku.ac.ir

Article Info

Article type:
Research Article

Article history:
Received: 17-Sep-2023
Received in revised form: 19-Nov-2023
Accepted: 22-Nov-2023
Published online: 10-Dec-2023

Keywords:
Synchronous Buck Converter,
Energization,
Soft Start-up,
Inrush current limiting.

ABSTRACT

This paper investigates the starting current of an AC/DC/DC converter, consisting of a three-phase diode bridge rectifier and a synchronous buck converter. The use of microprocessors in such converters increases the total cost and also reduces reliability due to EMI phenomena. For this reason, by removing the microprocessor, a start-up plan including a limiting starting resistor and then soft starting the switching module is proposed in this paper. By modeling the system under different operating modes, a solution is presented to minimize the circuit startup period, which includes minimizing the bypass time of the startup resistor and reducing the switching soft startup period as possible. The proposed method has been implemented on a 15-kW converter feeding from a three-phase 380 V power grid and provides up to 300 V_{dc}/50 A_{dc} to supply an electroplating pool. The results show that the sequential startup procedure, including using a 50 ohm/1500 w resistor for 3 seconds, and then bypassing it, then soft start switching after half a second and during 1.5 s, can move this circuit to a steady state in 5 seconds, keeping current in all parts below half rated current.

NOMENCLATURE

D_n	The final value of pulse width	V_m	Phase voltage peak value
f_n	The fundamental frequency of the power grid	V_S	Three-phase input voltage
fs	Switching frequency	α	Damping factor
Ip	C_1 Charging peak current	ω	Angular frequency of the power grid
T	Pulse-signal period	ω_0	Resonance frequency
t_0	The end time of the first phase	ω_n	Damped natural frequency
t_f	The end time of the second phase	V_m	Phase voltage peak value
t_p	The time when the current reaches its peak value in the second phase		
t_s	The time variable from the moment of triggering the main switches		
Δt_{ss}	Soft-start interval		
V_F	Capacitor steady-state voltage in each phase		
V_{in}	Diode bridge output voltage		

I. Introduction

Switching power supplies are widely used due to their high efficiency, compact size, and low weight. At lower power levels, higher switching frequencies (above 40kHz) allow the use of smaller inductors and capacitors. However, at high power levels, limitations of semiconductor devices necessitate lower switching frequencies. Larger inductors are then required, increasing costs. To mitigate this, lower inductance is utilized along with higher capacitor values. However, the resulting inrush current during start-up can damage semiconductors, circuitry, and capacitors. Methods to limit inrush current are thus needed which can be open or closed loop operation. While closed-loop operation enhances regulation, it necessitates a microprocessor for control. Without a microprocessor, staged start-up and shutdown procedures become challenging so a careful design is required to manage inrush current and transients during mode transitions without digital control capabilities. Overall, optimizing the switching topology and control scheme requires balancing frequency and component selections against complexity, performance, and cost.

Among the techniques that have been investigated in recent studies for AC-DC converters, the modulation method is based on an analytical expression for the MB-DAB half-bridge, which can be directly implemented on a microprocessor proposed in [1]. It can achieve almost full ZVS cycle brightness of all MOSFETs and unity power factor. Also, an overview of the power imbalance problem and the analysis of its reducing control technique for two-phase and single-phase isolated

MVAC-LVDC converters have been discussed in [2]. To achieve zero voltage switching (ZVS) in the full range of AC current, a combined phase shift and frequency modulation scheme of a double active bridge AC-DC converter (DAB) is presented in [3]. A directly applicable closed-form analytical solution for an efficient zero-voltage switching (ZVS) modulation scheme for DAB converters is also presented to minimize conduction losses under ZVS conditions [4]. A technique to limit the inrush current of an AC/DC converter is in [5], where the DC bus capacitor voltage is gradually increased to limit the charging current.

Among the widely used strategies for limiting the inrush current in DC-DC converters, modulation control topologies can be mentioned. Similarly, PWM mask [6] and investigating domain response of the system during start-up [7] have been introduced in

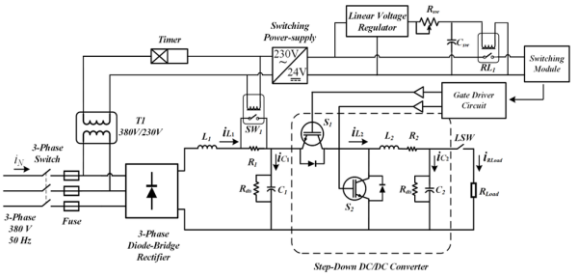

Fig. 1. Diagram of the under-study power circuit

this field. Also, as a new technique, a soft start modulation method is presented by Sante Pugliese et al. where a fast voltage balancing control is hired to prevent overvoltage and unbalanced voltage conditions [8]. Other soft start techniques include the methods of using auxiliary circuits to improve starting and limiting components [9, 10]. Despite the effectiveness, reliability, and efficiency of these procedures in limiting the current and achieving short start-up times, they are generally used at low power levels due to high working frequency, and their main limitation is their applicability in high powers. In addition, the use of an auxiliary circuit will increase the need for additional parts like sensors, power supplies, etc., and of course, the final cost of the circuit. Digital control schemes are also widely used to control inrush current in power converters including start-up response analysis or introducing digital soft-start circuits [11], [12]. Other control methods reviewed in the literature, are (VRSPV) [13] and (AGC) [14], which can provide soft-start without using high frequency and shorten converter settle time, respectively. To design a control algorithm, a new feeding strategy for a three-phase modular multilevel converter is proposed in [15]. Also, the control scheme based on passive communication and improved damping allocation is proposed in [16], which is used to adjust the dynamic characteristics of the system. In another approach, an offset-free model predictive control (MPC) has been proposed for a buck converter feeding a constant power load (CPL) [17]. Although prior literature references provide practical and accurate designs, due to the need to use microcontrollers and microprocessor-based auxiliary circuits, the limitation of implementing these methods at high power levels cannot be ignored. Another common control method is presented as a sliding mode control for efficient LLC resonant DC-DC converters in EV chargers, optimizing size and cost that achieves a notable peak efficiency [18]. Additionally, an

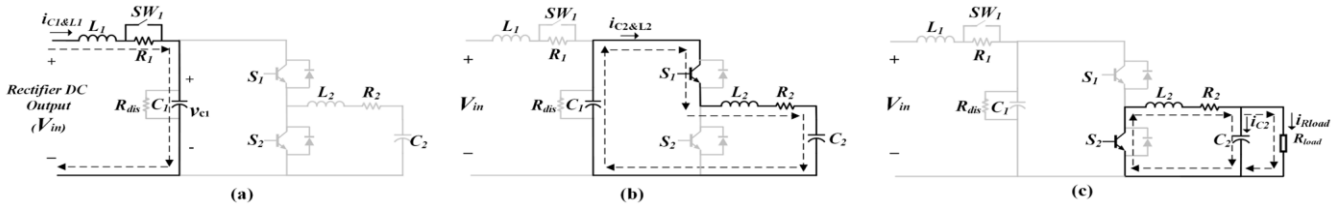

Fig. 2. The equivalent system circuit for a) phase 1, b) phase 2, c) phase 3

integrated bidirectional multiport DC-DC converter for plug-in EV charging, employing a half-bridge CLLC converter, ensures effective battery charge control and stable DC-link voltage [19]. A. Nabieh et.al proposed a simplified optimal path control (SOTC) to control a 1 MHz LLC converter. By implementing the proposed model, the optimal transient performance can be achieved and the settling time can be minimized [20]. Other soft start methods include the pulse jump control scheme to prevent inrush current and output voltage during the start-up period of DC-DC converters, which was presented by Pang-Jung Liu. [21]. Also, to eliminate the current and voltage stress in the resonance cycle during the soft start process, this process has been optimized based on the path condition analysis [22]. In another study, the differential evolution (DE) method was used to extract the parameters of the dynamic model of a converter, which is used to predict and model the inrush current phenomenon [23].

As mentioned, the precision regulation afforded by microprocessor-based digital control enables optimally efficient closed-loop operation in power supplies. However, at high power levels, microprocessor limitations can impede efficiency. The supplementary circuitry required further elevates complexity and expenditures. For applications without stringent regulation prerequisites, open-loop operation may suffice and eliminate the microprocessor. Devoid of a microprocessor, staged power-up and power-down sequences become challenging endeavors. Safely transitioning through these sequences without inrush currents necessitates meticulous design. Overall, the advantages of digital control must be weighed against its limitations at high power. Selecting topology and control schemes requires optimization across performance, complexity, and cost. Open or closed-loop configurations can be chosen to accommodate requirements while balancing capabilities, efficiency, and cost.

The focus of this paper is to provide a simple and efficient technique to restrict the inrush current in an industrial high-power AC/DC/DC converter. The circuit architecture includes a bridge rectifier, an LC filter, and a synchronous buck converter. The proposed start-up procedure includes three different phases, the pre-charge phase, the full charge phase, and the soft start switching phase.

This way, the converter moves from the zero initial state to the load connection state under nominal voltage, without any damaging inrush and transient.

II. System modeling

Fig. 1 shows the general outline of the system under study. At the input of the power circuit, a three-phase diode bridge and an LC filter consisting of an inductor L_1 and a capacitor bank with a total capacitance of C_1 are used. To limit the capacitor charging current, starting resistor R_1 is used, and to bypass this resistor, the contactor switch SW_1 is implemented in parallel with it. The power semiconductor switches of this circuit are S_1 and S_2, respectively, which usually come in a double-IGBT module. Considering that this converter operates in synchronous mode, both switches trigger with complementary pulses. Also, a high-frequency inductor L_2 has been used at the output of the power module and a capacitor set at the output of the converter with a total capacitance of C_2. It should be mentioned that using a diode bridge leads to undesirable harmonic content. If the THD and harmonic content of the AC side current should satisfy specific standards, using an additional Power-Factor-Correction circuit is recommended.

Fig. 1 also shows the proposed sequential start-up control circuit. A timer module activates the SW_1 contactor switch and the switching power supply. Then a linear regulator, feeding an $R_{SW}C_{SW}$ delay circuit, makes a tunable delay between activating SW_1 and relay switch RL_1. Closing RL_1 activates the switching module, which starts softly, in the pre–tuned time interval. This way, the start-up process of the power circuit consists of three different phases as follows:

A- The Pre-Charge phase

This phase starts from the moment the circuit is energized by connecting the three-phase switch 3phsw in Fig.1 and continues until the switch SW_1 is closed at $t=t_0$ by the timer module activation in Fig. 1. During this period, the capacitor C_1 is charged from the three-phase power supply, and the limiting resistor R_1, along with the inductor L_1, are in its current path. In this working mode, the switches S_1 and S_2 are both kept off, so the circuit is unloaded, and the capacitor C_2 remains uncharged. The equivalent circuit of the system in this working mode will be in the form of Fig. 2(a). Based on the maximum permissible current in this phase; the R_1 value will be:

$$R_1 = \frac{Vin}{Ip} \tag{1}$$

To determine the power rating of this resistor, the current RMS value and total power consumption will be:

$$i_{C1,rms} = \sqrt{\frac{1}{t_0}\int_0^{t_0} i^2(t)dt} \tag{2}$$

$$P = R_1 \cdot (i_{C1rms})^2 \tag{3}$$

The RLC loop current is equal to:

$$i_{C1} = C_1 \frac{dV_{C1}}{dt} \tag{4}$$

From Fig. 2(a), the KVL low gives:

$$L_1 \frac{dV_{C1}}{dt} + R_1 i_{C1} + V_{C1} = V_{in} \tag{5}$$

Considering that the value of the ripple coefficient of the output voltage of the three-phase diode rectifier is so negligible that it can be ignored, therefore, the value of V_{in} can be assumed to be constant in the upcoming calculations for the investigated circuit (cf. [24]). Also, the draining resistance of the R_{dis} capacitor bank is selected

to a large extent so that it does not affect the circuit's performance. For this reason, this resistance is ignored in the calculations. By inserting (4) in (5), the differential equation is obtained as follows:

$$\frac{d^2V_{C1}}{dt^2}+\frac{R_1}{C_1}\frac{dV_{C1}}{dt}+\frac{V_{C1}}{L_1C_1}=\frac{V_{in}}{L_1C_1} \quad (6)$$

The roots of the characteristic equation will be calculated as:

$$s_{1,2}=-\frac{R_1}{2L_1}\pm\sqrt{\left(\frac{R_1}{L_1}\right)^2-\frac{4}{L_1C_1}} \quad (7)$$

$$\Rightarrow s_{1,2}=-\alpha\pm\sqrt{\alpha^2-\omega_0^2}$$

$$\alpha=\frac{R_1}{2L_1} \quad (8)$$

$$\omega_0=\frac{1}{\sqrt{L_1C_1}} \quad (9)$$

If $\alpha>\omega_0$ will give:

$$V_C(t)=V_F+k_1e^{s_1t}+k_2e^{s_2t} \quad (10)$$

And for $\alpha=\omega_0$:

$$V_C(t)=V_F+k_1te^{-\alpha t}+k_2e^{-\alpha t} \quad (11)$$

For $\alpha<\omega_0$, the general form of the output voltage is:

$$V_C(t)=V_F+e^{-\alpha t}\left(k_1cos_nt+k_rsin_1\omega_nt\right) \quad (12)$$

Now the current equation can be driven using (1). R_1 is selected in a range that makes $\alpha>\omega_0$ to have a stable response. To determine k_1 and k_2 in (10), considering $V_{C1}(0)=0$ and $I_{C1}(0)=0$ in (10) gives:

$$V_{C1}(0)=V_F+k_1+k_2 \quad (13)$$

Using (1), the inductor L_1 current will be:

$$i_{C1}=i_{L1}=\left(k_1s_1e^{s_1t}+k_2s_2e^{st}\right)C_1 \quad (14)$$

Considering its initial state, (14) will give the following:

$$i_{L1}(0)=\left(k_1s_1+k_2s_2\right)C_1 \quad (15)$$

$$k_1=-(V_F+k_2) \quad (16)$$

$$k_2=\frac{V_Fs_1}{s_2-s_1} \quad (17)$$

Having k_1 and k_2, the C_1 voltage at the final moment of phase 1 (right before switching SW_1 on) will be:

$$V_{C1}(t_0)=V_{in}+k_1e^{s_1t_0}+k_2e^{s_2t_0} \quad (18)$$

Likely, the L_1 current at $t=t_0$ will be:

$$i_{C1}(t_0)=\left(k_1s_1e^{s_2t_0}+k_2s_2e^{s_2t_0}\right)C_1 \quad (19)$$

These two values are used as the initials for the second operating phase.

B- The Full-Charge phase

This phase starts when the R_1 resistor is bypassed by the SW_1 switch and continues until the capacitor C_1 reaches full charge, where the relay switch RL_1 in Fig. 1 is closed. According to the power circuit of this phase shown in Fig. 2(b):

$$L_1\frac{di_{L1}}{dt}+\frac{1}{C_1}\int i_1dt=\sqrt{3}V_m\cos(\omega t+\theta) \quad (20)$$

$$\Rightarrow\frac{d^2i_{L1}}{dt^2}+\frac{1}{L_1C_1}i_{L1}=-\frac{\sqrt{3}V_m\omega}{L_1}\sin(\omega t+\theta) \quad (21)$$

The roots of the characteristic equation will be:

$$s_{1,2}=\sqrt{-\omega_0^2}=\pm j\omega_0 \quad (22)$$

where:

$$\omega_0=\frac{1}{\sqrt{L_1C_1}} \quad (23)$$

And the final form of the current equation will be:

$$i_1(t)=k_1cos\ \omega_0t+k_2sin\ \omega_0t+Z\sin(\omega t+\theta) \quad (24)$$

where:

$$Z=\frac{\sqrt{3}V_m}{\sqrt{\left(\frac{1}{\omega C_1}-\omega L_1\right)^2}} \quad (25)$$

where $\omega=2\pi f_n$. Using initial state of $I_0=0$, k_1 and k_2 will be driven as:

$$k_1=-Z \quad (26)$$

$$\left(\frac{di}{dt}\right)_o=\frac{(V_s-V_{C1(to)})}{L_1} \quad (27)$$

$$\Rightarrow k_2=\frac{V_{L1}(0)-Z\omega}{\omega_0} \quad (28)$$

After determining k_1 and k_2 and replacing them in (24), the current equation of C_1 in phase 2 will be derived. From equalizing the I_{c1} derivative with zero, t_p the time for I_{c1} to get to its peak point is determined:

$$di(t)/dt=-k_1\omega_0\sin(\omega_0t_0)+k_2\omega_0\cos(\omega_0t_0)+...$$
$$...Z\omega\cos(\omega t_0+\theta)=0\rightarrow t_p=... \quad (29)$$

Replacing t_p into (24), the peak current in phase 2 will be determined:

$$i_{peak}=k_1\cos(\omega_0t_p)+k_2\sin(\omega_0t_p)+Z\sin(\omega t_p+\theta) \quad (30)$$

To limit the peak current in the second phase to the desired value, the time range of the first phase can be increased. This way, it is

possible to limit the value of I_p so that no destructive inrush current at the start of the second phase will happen. Also, by setting (24) equal to zero, the time range of the second phase can be obtained called t_f. The capacitor charge V_{C1} after the first cycle in the second phase, when the current reaches zero, will be:

$$\Delta V_{C1}\left(t_f\right)=\frac{1}{C_1}\int i_1 dt_f=\frac{1}{C_1}(\frac{k_1}{\omega}\sin\omega_0 t_f+... \\ ...Z\sin\left(\omega t_f+\theta\right)-\frac{k_2}{\omega}\cos\omega_0 t_f) \quad (31)$$

C- The Switching Soft-Start phase

This phase starts after the relay switch RL_1 in Fig. 1 is closed, and consists of two modes. The first mode is the L_2/C_2 charging mode, in which the S_1 switch is ON and feeds the output capacitor charging circuit. The second mode is called *the* L_2 discharging mode when S_2 gets ON.

Charging Mode

As the C_1 capacitor has reached its full charge, V_{C1} is assumed to be constant from now on. As the output voltage is lower than the rated, the load stands unconnected. So, based on Fig. 2(b):

$$L_2\frac{di_{C2}}{dt}+R_2 i_{C2}+V_{C2}=V_{C1} \quad (32)$$

Replacing $i_{C2}=C_2 dV_{C_2}/dt$ will give:

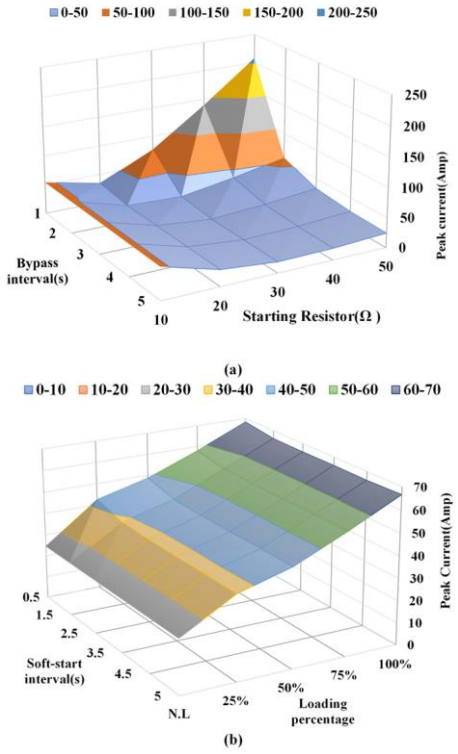

Fig. 3. Peak current in the DC link at the first and second phases a) Based on startup time and starting resistance value b) Based on system loading percentage

$$\frac{d^2V_{C2}}{dt^2}+\frac{R_2}{C_2}\frac{dV_{C2}}{dt}+\frac{V_{C2}}{L_2C_2}=\frac{V_{C1(t)}}{L_2C_2} \quad (33)$$

The roots of the characteristic equation will be:

$$s_{1,2}=-\frac{R_2}{2L_2}\pm\sqrt{\left(\frac{R_2}{L_2}\right)^2-\frac{4}{L_2C_2}} \\ \Rightarrow s_{1,2}=-\alpha\pm\sqrt{\alpha^2-\omega_0^2} \quad (34)$$

where α and ω_0 are:

$$\alpha=\frac{R_2}{2L_2} \quad (35)$$

$$\omega_0=\frac{1}{\sqrt{L_2C_2}} \quad (36)$$

The internal resistance of the HF inductor is very small, making $\alpha<\omega_0$, so:

$$V_{C2}(t)=V_F+e^{-\alpha t}\left(k_1 cos\omega_n t+k_2 sin_1\omega_n t\right) \quad (37)$$

where:

$$\omega_n=\sqrt{\omega_0^2-\alpha^2} \quad (38)$$

Using initial stats of $V_{C2}(0)=I_{C2}(0)=0$ will give:

$$k_1=-V_{C1} \quad (39)$$

$$L_2\frac{dV_{C2}}{dt}+R_2 i_{C2}+V_{C2}=0 \quad (43)$$

$$i_{C2(t)}=C_2\frac{dV_{C_2}}{dt} \quad (44)$$

$$\Rightarrow\frac{d^2V_{C2}}{dt^2}+\frac{R_2}{C_2}\frac{dV_{C2}}{dt}+\frac{V_{C2}}{L_2C_2}=0 \quad (45)$$

$$k_2=-\frac{\alpha V_{C1}}{\omega_n} \quad (40)$$

The output filter current will be:

$$i_{L2}(t)=i_{C2}(t)=C_2(-\alpha e^{-\alpha t}(k_1\cos(\omega_n t)+k_2\sin(\omega_n t))+... \\ ...e^{-\alpha t}(-k_1\omega_n\sin(\omega_n t)+k_2\omega_n\cos(\omega_n t))) \quad (41)$$

This operating mode will continue for $t=\%D/f_s$ and:

$$D=\left\lfloor t\frac{D_n}{\Delta t_{ss}}.100\right\rfloor \quad (42)$$

Discharge Mode

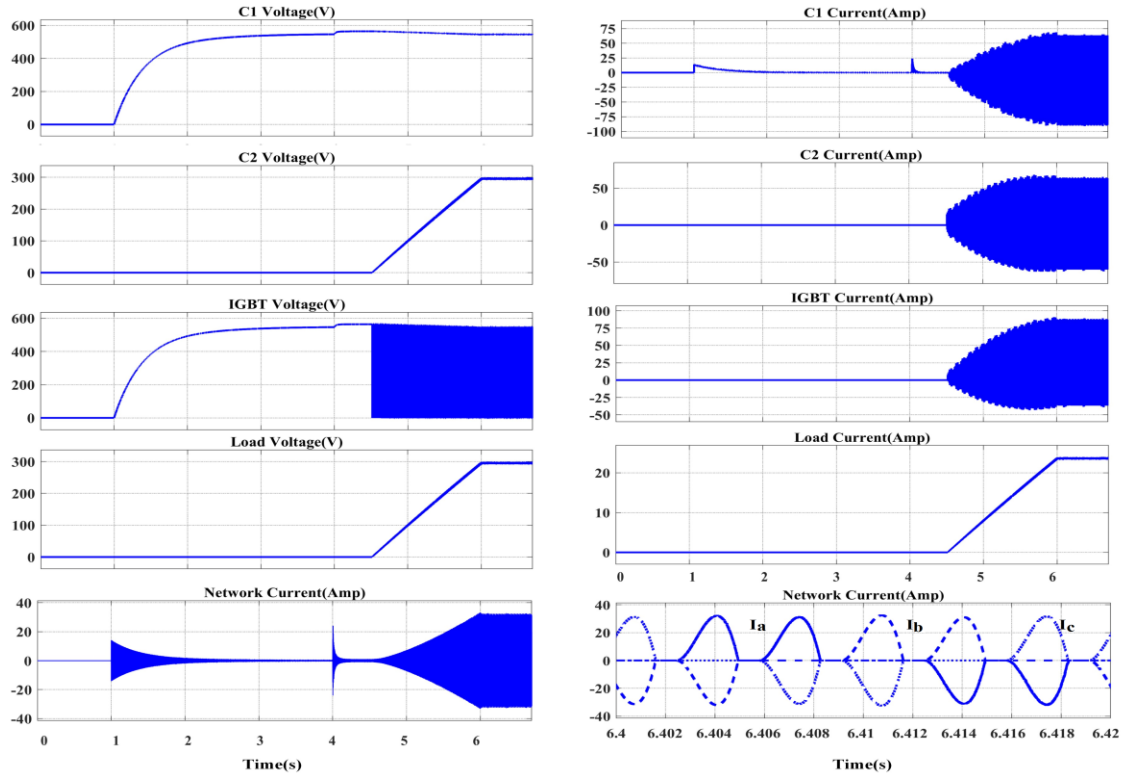

Fig. 4. Waveforms of simulation results of the proposed method

The equivalent circuit of this mode can be seen in Fig. 2(c). Since in this phase, the capacitor C_2 is not fully charged, the second-order RLC loop is formed to obtain the values of the capacitor voltage and the inductor current in this state, according to the KVL in Fig. 2(c):

Then the roots of the characteristic equation will be:

$$s_{1,2} = -\alpha \pm \sqrt{\alpha^2 - \omega_0^2} \tag{46}$$

Where:

$$\alpha = \frac{R_2}{2L_2} \tag{47}$$

$$\omega_0 = \frac{1}{\sqrt{L_2 C_2}} \tag{48}$$

As previously mentioned, in this phase $\alpha < \omega_0$, the output voltage and current will be:

$$V_{C2}(t) = V_F + e^{-\alpha t}\left(k_1 cos\omega_n t + k_2 sin\omega_n t\right) \tag{49}$$

$$i_{C2(t)} = C_2\left(-\alpha e^{-\alpha t}(k_1\cos(\omega_n t) + k_2\sin(\omega_n t)) + \ldots\right.$$
$$\left.\ldots e^{-\alpha t}(-k_1\omega_n\sin(\omega_n t) + k_2\omega_n\cos(\omega_n t))\right) \tag{50}$$

The initial states to determine k_1 and k_2 will be evaluated from (41) and (37) using $t=\%DT$, k_1 and k_2 will be driven as:

$$k_1 = V_{C_1}(DT - 1) \tag{51}$$

$$k_2 = \frac{\frac{DT(V_{C1})}{R_2} - \alpha C_2 V_{C1}(DT-1)}{C_2\omega_n} \tag{52}$$

The final values of C_2 voltage and current can be evaluated

TABLE I

PARAMETERS OF THE SYSTEM UNDER STUDY

Component	Parameter	Value
Grid	3 Phase	380 V 50 Hz
Buck-Converter	Rated power	15 KW
	Switching frequency	7.24 KHz
	Inductor L_1	300 µH
	Capacitor C_1	10000 µF
	Inductor L_2	189 µH
	Capacitor C_2	8000 µF
	R_1	50 Ω
	Inductor DC Resistance R_2	0.02 Ω
	R_{load}	8 Ω for a full load 15 Ω for a half load
	R_{dis1}, R_{dis2}	9400 Ω 100 W
	Nominal Output Voltage	300 V
	Nominal Output Current	50 A

from(49) and (50) with $t=T$.

start-up procedure.

TABLE II
PERFORMANCE COMPARISON WITH OTHER PUBLISHED DESIGNS

References	**Proposed converter**	[22]	[25]	[26]	[27]	[28]
Topology	**Step-down Buck Converter**	LLC Converter	Bidirectional Converter	GaN-based dual-output LLC Converter	DCM-Buck Converter	Phase-Shift Full-Bridge (PSFB) Converter
Input voltage (V_{DC})	**540**	400	400	600	500	400-600
Switching frequency (kHz)	**7.2**	120	100	600	50	18
No. of semiconductor switches	**2**	4	8	8	4	4
Output power (KW)	**15**	0.3	1.5	1.5	6.6	12
Output voltage (V)	**300**	12	200	250	200-450	40
Full load efficiency (%)	**96**	N.A	95.8	96.1	93	96
Soft-start interval(s)	**1.5**	1	2.7	20	2.2	2

The Same procedure can be followed for the next cycles with new values of *%D* from (42).

III. Results and discussion

The system under study consists of a 15 KW converter, which is fed by a three-phase 380 V power grid. The converter gives a nominal voltage of up to 300 V_{dc} with a maximum current of 50 A_{dc} to the load. Other parameters of this system are listed in detail in Table I. This set has been designed and implemented for a Car Shock-Absorber Manufacturing Company, as a power supply for the Electro-Plating Pool. Some of the designing constraints required by the client, like the set being designed on wheels, the cooling system to be air forced, etc., have reduced the power density. But the system still has better power density than thyristor-based rectifiers (which are usually used for this application), as it has removed the three-phase internal power transformer.

The system has been simulated in Matlab/Simulink first, with the same parameters as the experimental set, for the results to be comparable. Fig. 3(a) shows the peak of inrush current during phases 1 & 2 of the start-up procedure, concerning the starting resistor size and the phase#1 time duration. As illustrated by this figure, to keep current in the DC link under 15 A during start-up, a minimum starter resistor size of 35 Ω with a minimum time duration of 2.5 s is needed. On the other hand, Fig. 3(b) shows the peak current transient during the soft-start interval of the switching module. This figure shows that the current in this phase is highly dependent on load, but the minimum soft-start time of 1.2 s is enough to have the minimum transient current at no-load condition.

As a result, a 50 Ω/1500-watt resistor has been hired in the experimental set and also used in simulations. The time intervals for the three start-up procedure phases have taken 3, 0.5, and 1.5 seconds, respectively

To validate the modeling and the proposed approach, the simulation of this system has been performed in MATLAB/Simulink using the parameters of Table I.

The proposed start-up method, contains the pre-charge phase, full-charge phase, and the switching soft-start phase for 3, 0.5, and 1.5 s, respectively. Fig. 4 shows the system performance during the

According to Fig.4, after 1 second of energizing the circuit, the charging phase of capacitor C_1 starts and after 3 seconds at 540 voltage, it is fully charged. At the same time as the R_1 resistor is bypassed, a voltage jump up to 560 will occur in the C_1 capacitor, and after 0.5 s, the main switches will be switched with a soft start time of 1.5 s and 55% pulse width at t=4.5 s. Meanwhile, when the switch SW_1 is closed, the resistor R_1 is bypassed and the peak current of 25 amps is applied to the capacitor. Similarly, after the soft start switching at t=4.5 s, the maximum current of the capacitor is equal to 68 amps, and after passing the start-up period, it reaches stability in the range of 63 amps.

After R_1 resistance is bypassed, the soft start switching process takes place, and in this case, the maximum current passing through switch S_1 will be 91 amps. In this case, the main switch current changes will be continuous without abnormal spikes. The voltage remains at its maximum value at 562 and 545 during the start-up period and in the steady-state respectively.

The process of charging capacitor C_2 takes place completely linearly without any abnormality until it reaches full charge in t=6 seconds. During the charging process, the current of the capacitor is continuous and without destructive spikes, the maximum current applied to the capacitor in this case reaches 68 amps. Similarly to capacitor C_1, after passing the start-up period, the current will stabilize and be limited to 63 amps.

With the desired pre-charge resistor R_1, the charging current is limited to 14 amps at the beginning of the start-up and is limited to 3 amps within 1.7 s.

Considering the pre-charge phase as 3 seconds, after removing the limiting resistor R_1 at t=4 the current pulse at the beginning of the full charge phase is limited to 25 amps. After the soft start switching at t=4.5, the current stabilizes at 31 amps for 1.5 s, and no destructive current pulses are observed.

The experimental results on a 15 KW AC/DC/DC converter shown in Fig. 5 are presented in this section. The design preferences specifications, our design targeted a portable, air-cooled converter in a single enclosure. The final converter dimensions measured 80 by 75 by 110 cm and the mass was

approximately 80 kg, which has been acceptable according to the

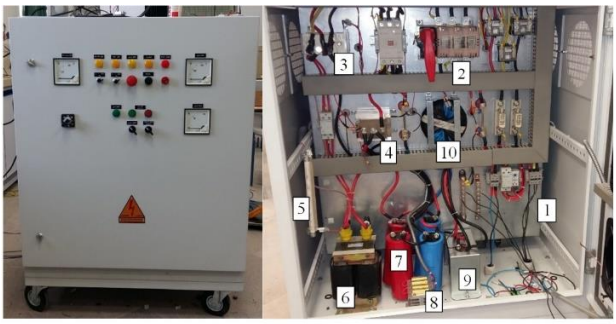

1: 3-Phase Input Voltage
2: Master Switch
3: Diode-Bridge Rectifier
4: IGBT Module
5: Charging Resistors
6: L1 Inductor
7: C1 Capacitor
8: Discharge Resistors
9: C2 Capacitor
10: L2 Inductor

Fig. 5 Experimental set

customer's needs. All the parameters of the system are listed in Table I. As seen in Fig. 3, the changes in the initial inrush current become insignificant compared to the increase in the duration of the soft start after the value of 1.2 s So, for the results to be compared with the simulations, the time duration of the three phases of the start-up process has been set to 3, 0.5, and 1.5 s, respectively. To protect the system, the charging resistor R_1 has chosen 50 Ω/ 1500 w in the experimental set.

Fig. 6 shows the results of phases 1 & 2, the energization period of capacitor C_1. The charging current with the R_1 resistor is limited to 10.5 amps. The transient of the resistor removal moment for t_0=3 is 15.7 amps, which is acceptable compared to 50 A nominal current. After bypassing R_1, the C_1 voltage jumps to 560 V in 0.5 s. It should be noted that in this test, to be able to recognize the start-up period, after bypassing the resistor R_1, the switching circuit is disabled.

Fig. 7 shows the voltage/ current of high/low IGBTs at the start of switching and the steady state. As the system starts no-loaded, the current average is zero. The peak-to-peak current in both switches remains under 65 amps (38 amps peak value at soft-start period). The DC link voltage has fallen to 544 V after switching start-up. Fig. 8(a) shows the HF inductor L_2 current at the soft starting period, which proves no transient inrush happened. The steady-state current of L_2 in Fig. 8(b) shows a continuous waveform with a 25 amps ripple amplitude. The system is now loaded with half nominal load (R_{load}=15 Ω). Figs 8(c) and 8(d) show the transient and steady-state waveform of the HF inductor L_2 current, which proves no transient current at the loading moment happened. The current ripple is also unchanged. Fig. 8(a) shows the HF inductor L_2 current at the soft starting period, which proves no transient inrush happened. The steady-state current of L_2 in Fig. 8(b) shows a continuous waveform with a 25 amps ripple amplitude. The system is now loaded with half nominal load (R_{load}=15 Ω). Figs 8(c) and 8(d) show the transient and steady-state waveform of the HF inductor L_2 current, which proves no transient current at the loading moment happened. The current ripple is also unchanged.

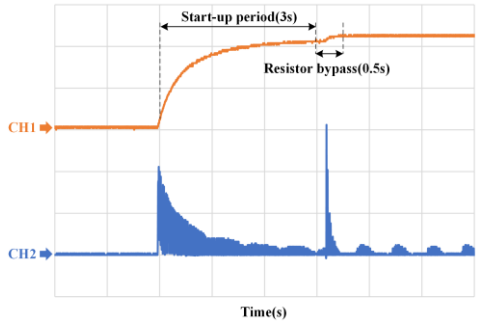

Fig. 6 Experimental results for capacitor C1 energization Ch1: voltage (250 V/div), Ch2: Current (5 A/div) for t_0=3

At last, the under-load soft-switching start-up test results are shown in Fig. 9. The soft-starting switching period happens in 1.5 s, no transient inrush current happens, and the voltage/current ripple at steady-state is 2.4V/ 1.1 A (lower than 1% / 2.5%). All the results prove that the proposed start-up strategy has conducted the system from an unloaded zero (initial) state to the loaded steady state, without any transient inrush current at any part of the circuit. It should be noted that the efficiency was calculated using the output power plus the total losses, which included the core losses multiplied by 1.5 to account for additional assembly losses. The core losses consisted of switching losses, iron core losses, and coil winding losses for this particular assembly.

The key parameters in this work and the performance comparison of the proposed method with prior literature are listed in Table II. It can be seen that compared with other published designs, the proposed converter has an obvious advantage in efficiency, without using a microcontroller or different sensors. Furthermore, it has a lower working frequency and higher power levels. Its 96% efficiency is higher compared to the Bidirectional (95.8%) and DCM-buck converter (93%) proposed in [25] and [27] respectively. Also, the use of fewer switches (2) compared to other references (4 and more), in addition to reducing the cost of construction, will increase the overall reliability of the converter. Its gain range is as good as the phase-shift converter in [28]. The rated power is larger than all listed literature. Therefore, the proposed method is a good choice for implementing a DC–DC converter with a high-power level and industrial application.

IV. Conclusion

In this paper, the problem of inrush current at the moment of energization and start-up of AC/DC/DC converters composed of a three-phase diode rectifier and synchronous buck converter at high powers was investigated. Due to the use of high-capacitance capacitors at the input and output of the converter, the direct drive of the circuit leads to a current up to several times the rated current and damages various parts, especially semiconductor switches. The proposed start-up method contains the application of a starting

resistor and soft starting of the switching circuit. The method of

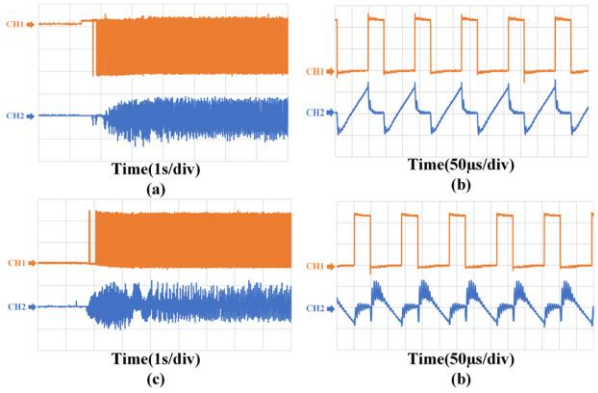

Fig. 7 Experimental results for IGBT switches, Ch1: voltage (250 V/div), Ch2: Current (25 A/div) a) high side switch start-up b) high side switch steady-state c) low side switch start-up d) low side switch steady-state

calculating and designing all parameters of the circuit start-up, including the size of the start-up resistor and the timing of the start-up phases, were described and analyzed in this paper. The simulation results and experimental tests of the proposed method on a 380Vac to 300VDC three-phase converter showed that the maximum time required between the circuit start-up and the start of feeding the load in this method is 5 seconds. The input current, IGBTs current, HF inductor current, and the capacitors are all well limited to less than half their nominal values in this period. No transient inrush happened on any part of the system, and the final loading output voltage/current has no ripple and transient.

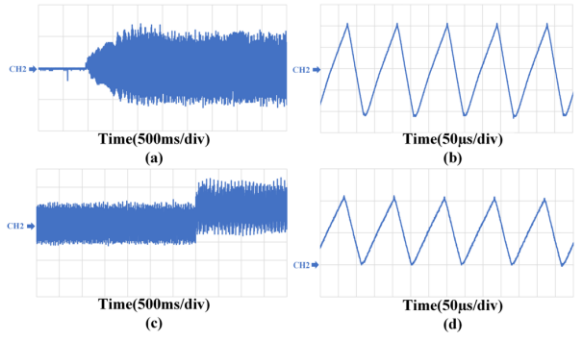

Fig. 8 Experimental results for HF inductor current a) switching start-up (25 A/div) b) no-load steady-state (12.5 A/div) c) half-loading (25 A/div) d) half-loaded steady-state (25 A/div)

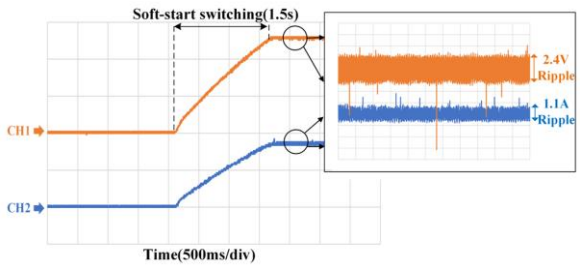

Fig. 9 Experimental results for Ch1: output voltage(120 V/div) Ch2: load current(15 A/div)

References

[1] Saha, J., Gorla, N.B.Y. and Panda, S.K., "Analytical expression-based modulation for soft-switched matrix-based dual-active-bridge (S2MB-DAB) single-phase AC-DC converter," *IEEE Journal of Emerging and Selected Topics in Power Electronics*, vol.10, DOI: 10.1109/TPEL.2016.2633507 , no.6, pp.6511-6522, Dec.2016.

[2] Saha, J., Gorla, N.B.Y. and Panda, S.K., "Comparative Overview of Power Balance Control for Two-stage and Single-stage Isolated MVAC-LVDC Cascaded Converters," In *2022 International Power Electronics Conference (IPEC-Himeji 2022-ECCE Asia)*, DOI: 10.23919/IPEC-Himeji2022-ECCE53331.2022.9807000, pp. 2465-2471, May.2022.

[3] Jauch, F. and Biela, J., "Combined phase-shift and frequency modulation of a dual-active-bridge AC–DC converter with PFC," *IEEE Transactions on Power Electronics*, vol.31, DOI: 10.1109/TPEL.2016.2515850, no.12, pp.8387-8397, Jan.2016.

[4] Everts, J., 2016. Closed-form solution for efficient ZVS modulation of DAB converters. *IEEE transactions on Power Electronics*, vol.32, DOI: 10.1109/TPEL.2016.2633507, no.10, pp.7561-7576, Dec.2016.

[5] Liu, P.J., Hsu, Y.C. and Chang, Y.H., "A current-mode buck converter with a pulse-skipping soft-start circuit" In 2013 IEEE 10th international conference on power electronics and drive systems (PEDS), DOI: 10.1109/PEDS.2013.6527025, pp. 262-265, April.2013.

[6] Li H, Gao Z, Ji S, Ma Y, Wang F. "An Inrush Current Limiting Method for Grid-Connected Converters Considering Grid Voltage Disturbances". *IEEE Journal of Emerging and Selected Topics in Power Electronics.*, vol. 10, DOI: 10.1109/JESTPE.2022.3147515, no. 2, pp. 2608-18, Jan 2022.

[7] Hu T, Huang M, Lu Y, Martins RP. "A Capacitor-Cross-Connected Boost Converter with Duty Cycle< 0.5 Control for Extended Conversion-Ratio and Soft Start-Up," *IEEE Transactions on Circuits and Systems I: Regular Papers.*, vol. 69, DOI: 10.1109/TCSI.2022.3189161, no. 10, pp. 4272-83, Jul 2022.

[8] Pugliese S, Buticchi G, Mastromauro RA, Andresen M, Liserre M, Stasi S. "Soft-start procedure for a three-stage smart transformer based on dual-active bridge and cascaded H-bridge converters," *IEEE Transactions on Power Electronics.*, vol. 35, DOI: 10.1109/TPEL.2020.2977226, no. 10, pp. 11039-52, Feb. 2020.

[9] Huang L, Luo P, Wang C, Zhou X. "A high speed on-chip soft-start technique with high start-up stability for current-mode DC-DC converter," *IEEE Access*, vol. 7, DOI: 10.1109/ACCESS.2019.2901529, pp. 27579-85, Feb. 2019.

[10] Jeong Y, Park MH, Moon GW. "High-efficiency zero-voltage-switching totem-pole bridgeless rectifier with integrated inrush current limiter circuit," *IEEE Transactions on Industrial Electronics.*, vol. 67, DOI: 10.1109/TIE.2019.2942559, no. 9, pp. 7421-9, Sep.2019.

[11] El Aroudi A, Martínez-Treviño BA, Vidal-Idiarte E, Martínez-Salamero L. "Analysis of start-up response in a digitally controlled boost converter with constant power load and mitigation of inrush current problems," *IEEE Transactions on Circuits and Systems I : Regular Papers.*, vol. 67, DOI: 10.1109/TCSI.2019.2939053, no. 4, pp. 1276-85, Sep.2019.

[12] Kurokawa F, Takano J, Takahashi T, Bansho K, Tanaka T, Hirose K. "A novel digital soft-start circuit for dc-dc converter," *In8th International Conference on Power Electronics-ECCE Asia*, DOI: 10.1109/ICPE.2011.5944479, pp. 1761-1766, May.2011.

[13] Fan S, Xue Z, Guo Z, Wang Y, Geng L. "VRSPV soft-start strategy and AICS technique for boost converters to improve the start-up performance," *IEEE Transactions on Power Electronics.*,

vol. 31, DOI: 10.1109/TPEL.2015.2461438, no. 5, pp. 3663-72, Jul.2015.
[14] Mohammadi M, Ordonez M. "Inrush current limit or extreme startup response for LLC converters using average geometric control," *IEEE Transactions on Power Electronics.*, vol. 33, DOI: 10.1109/TPEL.2017.2666803, no. 1, pp. 777-92, Feb.2017.
[15] Duarte SN, de Almeida PM, Barbosa PG. "A novel energizing strategy for a grid-connected modular multilevel converter operating as static synchronous compensator," *International Journal of Electrical Power & Energy Systems.*, vol. 109, DOI: doi.org/10.1016/j.ijepes.2019.02.028, pp. 672-84, Jul.2019.
[16] Pang S, Nahid-Mobarakeh B, Pierfederici S, Phattanasak M, Huangfu Y, Luo G, Gao F. "Interconnection and damping assignment passivity-based control applied to on-board DC–DC power converter system supplying constant power load," *IEEE Transactions on Industry Applications.*, vol. 55, DOI: 10.1109/TIA.2019.2938149, no. 6, pp. 6476-85, Aug.2019.
[17] Xu Q, Yan Y, Zhang C, Dragicevic T, Blaabjerg F. "An offset-free composite model predictive control strategy for DC/DC buck converter feeding constant power loads," *IEEE Transactions on Power Electronics.*, vol. 35, DOI: 10.1109/TPEL.2019.2941714, no. 5, pp. 5331-5342, Sep.2019.
[18] A. Taheri and N. Asgari, "Sliding mode control of LLC resonant DC-DC converter for wide output voltage range in battery charging applications," International Journal of Industrial Electronics Control and Optimization, vol. 2, DOI: doi.org/10.22111/ieco.2018.27333.1096, no. 2, pp. 127-136, Apr.2019.
[19] N. Bagheri, H. Alipour, L. Mohammadian, J. Beiza, and M. Ebadpour, "A Multiport Isolated Resonant LLC Converter for Grid-Tied Renewable Energy Powered Bidirectional EV Charger," International Journal of Industrial Electronics Control and Optimization, vol. 6, DOI: doi.org/10.22111/ieco.2023.43543.1447, no. 1, pp. 37-48, Mar. 2023.
[20] Nabih A, Ahmed MH, Li Q, Lee FC. "Transient control and soft start-up for 1-MHz LLC converter with wide input voltage range using simplified optimal trajectory control," *IEEE Journal of Emerging and Selected Topics in Power Electronics.*, vol. 9, DOI: 10.1109/JESTPE.2020.2973660, no. 1, pp. 24-37, Feb.2020.
[21] Liu PJ, Hsu YC, Chang YH. "A current-mode buck converter with a pulse-skipping soft-start circuit," *In2013 IEEE 10th international conference on power electronics and drive systems (PEDS).*, DOI: 10.1109/PEDS.2013.6527025, pp. 262-265, Apr.2013.
[22] Feng W, Lee FC. "Optimal trajectory control of LLC resonant converters for soft start-up," *IEEE Transactions on Power Electronics.*, vol. 29, DOI: 10.1109/TPEL.2013.2261094, no. 3, pp. 1461-1468, May.2013.
[23] Zhang D, Liu Y, Huang S. "Differential evolution based parameter identification of static and dynamic JA models and its application to inrush current study in power converters," *IEEE transactions on magnetics.*, vol. 48, DOI: 10.1109/TMAG.2012.2196984, no. 11, pp. 3482-3485, Oct.2012.
[24] Rashid, Muhammad H,1988, Power Electronics: Circuits, Devices & Applications, Pearson Education
[25] Wu, H., Jia, Y., Yang, F., Zhu, L. and Xing, Y. "Two-Stage isolated bidirectional dc–ac converters with three-port converters and two dc buses," *IEEE Journal of Emerging and Selected Topics in Power Electronics*., vol.8, DOI: 10.1109/JESTPE.2019.2936145, no.4 pp.4428-4439,Aug.2019.
[26] Ren R, Liu B, Jones EA, Wang FF, Zhang Z, Costinett D. Capacitor-clamped, three-level GaN-based DC–DC converter with dual voltage outputs for battery charger applications. *IEEE Journal of Emerging and selected topics in Power Electronics*., vol.4, DOI: 10.1109/JESTPE.2016.2586890,no.3, pp.841-53.Jun.2016.
[27] Lee JY, Chae HJ. "6.6-kW onboard charger design using DCM PFC converter with harmonic modulation technique and two-stage DC/DC converter," *IEEE Transactions on Industrial Electronics*., vol.61, DOI: 10.1109/TIE.2013.2262749, no.3, pp.1243-52, May.2013
[28] Shi Y, Feng L, Li Q, Kang J. "High power ZVZCS phase shift full bridge DC–DC converter with high current reset ability and no extra electrical stress," *IEEE Transactions on Industrial Electronics.*, vol. 69, DOI: 10.1109/TIE.2021.3130346, no. 12, pp.12688-12697, Dec.2021.

Mohammad Amin Bahramian received a B.Sc. degree in electrical engineering from Arak University, Arak, Iran, in 2020. He is now an M.Sc. student in electrical engineering at Arak University. His research interests include power electronics, DC-DC, and bidirectional converters

Mazdak Ebadi was born in Booshehr, Iran in 1983. He received a Ph.D. degree in electrical engineering from Shahid Chamran University, Iran in 2014. Since 2014, he is with the Department of Electrical Engineering, Arak University, Arak, Iran. His research interests include Power electronic circuit design, DC/DC Converters and Inverters, and their application in renewable energy resources like photovoltaics.

Ali Asghar Ghadimi was born in shazand, iran in 1976.received his M.Sc. and Ph.D. degrees in Power Engineering from Tehran Polytechnique University, Tehran, Iran in 2002 and 2008 respectively. He is currently an Associate Professor and research member in the Department of Electrical Engineering at Arak University, Arak, IRAN. His current research interests are in the area of Distributed Generation, Power system optimal planning, and Micro-Grid